Dynamics of underground tunnels

Semi-analytical solution for the response of the system under seismic waves and stability analysis of high-speed moving trains

Zhao, M.

DOI
10.4233/uuid:17180b63-ae91-4652-9294-726fecc182ba

Publication date
2024

Document Version
Final published version

Citation (APA)
Zhao, M. (2024). *Dynamics of underground tunnels: Semi-analytical solution for the response of the system under seismic waves and stability analysis of high-speed moving trains*. [Dissertation (TU Delft), Delft University of Technology]. https://doi.org/10.4233/uuid:17180b63-ae91-4652-9294-726fecc182ba

DYNAMICS OF UNDERGROUND TUNNELS

SEMI-ANALYTICAL SOLUTION FOR THE RESPONSE OF THE SYSTEM UNDER SEISMIC WAVES AND STABILITY ANALYSIS OF HIGH-SPEED MOVING TRAINS

DYNAMICS OF UNDERGROUND TUNNELS

SEMI-ANALYTICAL SOLUTION FOR THE RESPONSE OF THE SYSTEM UNDER SEISMIC WAVES AND STABILITY ANALYSIS OF HIGH-SPEED MOVING TRAINS

Dissertation

for the purpose of obtaining the degree of doctor
at Delft University of Technology,
by the authority of Rector Magnificus Prof. dr. ir. T.H.J.J. van der Hagen,
chair of the Board for Doctorates,
to be defended publicly on
Wednesday 11 September 2024 at 10:00 hours

by

Mingjuan ZHAO

Mastor of Science in Civil Engineering, Hunan University, Changsha, China
born in Kaifeng, China.

This dissertation has been approved by the promotors.

Composition of the doctoral committee:

Rector Magnificus,	Chairperson
Prof. dr. A.V. Metrikine,	Delft University of Technology, promotor
Dr. ir. K.N. van Dalen,	Delft University of Technology, promotor
Independent members:	
Dr. Z. Dimitrovová	Nova University of Lisbon, Portugal
Prof. dr. ir. C. Jommi	Delft University of Technology
Prof. dr. Q. Liu,	Hunan University, China
Prof. dr. R.R. Negenborn,	Delft University of Technology
Prof. dr. ir. E.C. Slob,	Delft University of Technology

The work presented in this thesis was conducted at Delft University of Technology, Delft, The Netherlands. The research was mainly funded by TU Delft and the China Scholarship Council (CSC) (file no. 201306110029).

Keywords: Underground tunnel, seismic waves, semi-analytical solution, method of conformal mapping, method of images, indirect BEM, high-speed oscillator, vibration instability, D-decomposition method, critical velocity for instability

Printed by: Gildeprint - Enschede

Cover: Designed by Mingjuan Zhao

ISBN 978-94-6496-196-6

To my family

CONTENTS

SUMMARY

Underground tunnels are important infrastructures due to diverse applications in civil engineering. The dynamic behavior of the underground tunnels when exposed to seismic waves or the passage of high-speed moving trains is of particular interest. Amplifications of displacements and stress concentrations may occur due to wave scattering and wave interference. Engineers concern about the vibration stability of moving trains as so-called anomalous Doppler waves may be generated when trains move at high speeds; the corresponding energy is fed into the vibration of the vehicle. Therefore, the train-track-soil interaction should be properly considered to predict when the vehicle vibration becomes unstable.

This thesis aims to present a semi-analytical solution for the response of a half-space with an embedded tunnel subject to seismic waves and to analyse the vibration stability of high-speed trains moving through that underground tunnel. Previous studies indicate that the method of conformal mapping is a promising analytical method to solve the two-dimensional (2D) wave scattering problem due to its computational efficiency and accuracy. Thus, the first objective of this thesis is to extend the method of conformal mapping to three-dimensional (3D) case and systematically evaluate its performance. Results reveal that inaccurate results maybe obtained, particularly at high frequencies. This observation motivates the second objective of this thesis, which focuses on verifying the accuracy of the specific application of the method of conformal mapping in which the waves scattered from the half-space surface are represented by cylindrical waves that originate from an image source of a priori unknown intensity. To this end, a simpler 2D model is considered, involving a cylindrical cavity embedded in an elastic half-space subject to a harmonic anti-plane shear wave. The performance of the indirect Boundary Element Method (indirect BEM) is evaluated too for this model in view of the choice of the appropriate solution method for the second type of dynamic problem considered in this thesis. For this second type of dynamic problem, due to the identified inaccuracies at high frequencies for the 3D problem, the indirect BEM is utilised to investigate the stability of vibrations of an oscillator moving at high speeds through a tunnel embedded in soft soil, which is the third objective of this thesis.

Regarding the first objective, the 3D problem of a cylindrical tunnel embedded in an elastic half-space subject to plane harmonic compressional and shear waves is considered. Both the tunnel and soil are modelled as an elastic continuum. Conformal mapping is employed to transform the original physical domain with boundary surfaces of two different types onto an image domain with surfaces of the same type. The total wave field in the half-space consists of incident and reflected (from the half-space surface) plane waves, as well as directly and secondary scattered cylindrical waves, while the total wave field in the tunnel consists of refracted cylindrical waves. The secondary scattered waves, generated when the cylindrical waves directly scattered from the tunnel meet the half-space surface, are represented by cylindrical waves that originate from an image source of a priori unknown intensity, which is in line with the spirit of the method of images. The unknown amplitude coefficients of the cylindrical waves are determined from the boundary and continuity conditions of the tunnel-soil system by projecting those onto the set of circumferential modes, which results in a set of algebraic equations. Results show that the present method converges for a small number of circumferential modes. A good agreement is observed between the obtained results and those in literature. It is shown in a systematic evaluation that the method works well for the frequency band of seismic waves, as well as for the complete considered ranges of the tunnel/soil stiffness ratio, the embedded depth of the tunnel, the vertical incident angle and the tunnel thickness. The reason for the inaccuracy at high frequencies probably lies in the fact that the secondary scattered waves in the soil are represented by cylindrical waves and not by plane waves, while the latter are most likely more suitable to represent the responses at the flat ground surface at high frequencies. In addition, the results obtained for a moderate tunnel-soil stiffness contrast under the incident compressional wave are inaccurate when Hankel functions are used to represent the cylindrical waves in the tunnel, which is due to the refracted shear waves in the tunnel transitioning from propagating to evanescent. These inaccuracies can be perfectly overcome by representing the waves in the tunnel by Bessel functions. Furthermore, the present method generally works better for the incident compressional wave than for the incident shear wave, as the condition number of the coefficient matrix (related to the mentioned algebraic equations) is often larger in the latter case. To conclude, the extension of the method of conformal mapping to the 3D case is successful and the present method can be used in preliminary design so as to avoid pronounced resonances, and to assess stress distributions and ground vibrations. In view of engineering practice, the tunnel is safer when the surrounding soil is stiffer, the tunnel is thicker and the vertical incident angle is larger.

With regard to the second objective, the 2D problem of a cavity embedded in an elastic half-space subjected to a harmonic anti-plane shear wave is considered. Main focus is the comparison of three methods: the method of images, the method of conformal mapping and the indirect BEM. The closed-form solutions obtained by the method of images serve as benchmark solutions for the other two methods. Convergence tests and validation examples are provided to assess the accuracy of the methods. It is shown in a comparative study that both the method of conformal mapping and the method of images require a similar number of circumferential modes to achieve converged results. In terms of computational efficiency, the method of images outperforms the method of conformal mapping, whereas the indirect BEM is the least efficient one among the three. A systematic evaluation demonstrates that both the method of conformal mapping and the indirect BEM accurately work within the complete considered ranges of the dimensionless frequency, the embedded cavity depth and the vertical incident angle. This is in contrast to the 3D case, where converged results could not be obtained at high frequencies for the method of conformal mapping. The findings suggest that representing the waves scattered from the free surface by cylindrical waves (originating from an image source of a priori unknown intensity) in the method of conformal mapping is indeed the cause of the inaccuracies at high frequency in the 3D problem. As no inaccuracies are observed for the current 2D anti-plane shear problem, the inaccuracy for the 3D problem is likely due to the use of cylindrical waves (instead of plane waves) that are apparently not fully able to capture all wave conversions taking place at the free surface. Furthermore, a parametric study reveals significant effects of the system parameters on the responses. The system response curves display nearly equally spaced resonances, which is in line with those of the one-dimensional (1D) shear layer subject to bedrock motion, while similar response curves for the 3D case do not display equally spaced resonances.

Regarding the third objective, the stability of vertical vibrations of an object moving at constant speed through a tunnel embedded in soft soil is investigated. The soil is modeled as an elastic continuum, while the tunnel is modelled by the Flügge shell. The moving object is modelled as a mass-spring system or as the limiting case of a single mass. By utilising the indirect BEM, the equivalent dynamic stiffness of the tunnel-soil system at the point of contact with the moving object is computed numerically. The concept of equivalent stiffness is employed to reduce the original 2.5D model to an equivalent discrete model, whose parameters depend on the vibration frequency and the object's velocity. The critical velocity beyond which the instability of the object vibration may occur is found, and it is the same for both models of the moving object. This critical velocity is much larger than the operational velocity of high-speed trains and ultra-high-speed transportation vehicles, which indicates that the model adopted in this thesis predicts the vibrations of Maglev and Hyperloop vehicles to be stable. Furthermore, the critical velocity for instability is found to be much larger than the critical velocity for resonance, contrary to the literature finding for the model of a railway track founded on top of the elastic half-space. For both models (i.e., tunnel embedded in the half-space, and track on top of the half-space), the critical velocity for resonance is slightly smaller than the velocity of Rayleigh waves, and the fact that the critical velocity for instability is so much larger in the current model is due to the large stiffness of the tunnel and the radiation damping of the waves excited in the tunnel. A parametric study shows that the thickness and material damping ratio of the tunnel, the stiffness of the soil and the burial depth have a stabilising effect, while the damping of the soil may have a slightly destabilising effect (i.e., lower critical velocity for instability). The D-decomposition method is utilised to investigate the stability of the moving object for velocities exceeding the identified critical velocity for instability. Instability domains in the space of system parameters are found, as well as the dependency of the critical mass and stiffness on the velocity. Results show that the higher the velocity, the smaller the mass of the object should be to ensure stability (single mass case); moreover, the higher the velocity, the larger the stiffness of the spring should be when a spring is added (oscillator case). Finally, in view of the stability assessment of Maglev and Hyperloop vehicles, the approach presented in this thesis can be applied to more advanced models with more points of contact between the moving object and the tunnel, which resembles reality even better.

SAMENVATTING

Ondergrondse tunnels zijn belangrijke infrastructuur wegens de diverse toepassingen binnen de civiele techniek. Het dynamische gedrag van ondergrondse tunnels is van belang met name wanneer ze blootgesteld worden aan seismische golven of wanneer een hogesnelheidstrein passeert. Verplaatsingen en spanningsconcentraties kunnen namelijk versterkt worden door weerkaatsing en interferentie van de seimische golven. Ingenieurs bekommeren zich verder om de stabiliteit van de trillingen van rijdende treinen omdat zgn. abnormale Dopplergolven kunnen worden gegenereerd bij hoge snelheden; de bijhorende energie voedt de trilling van het voertuig. Hierom moet de trein-spoorgrond interactie goed beschouwd worden om de mogelijke instabiliteit van het voertuig te voorspellen.

Deze dissertatie presenteert enerzijds een semi-analytische oplossing voor het gedrag van een halfruimte met ingebedde tunnel, geëxciteerd door seismische golven. Daarnaast wordt ook de stabiliteit van de trilling van hogesnelheidstreinen in een ondergrondse tunnel bestudeerd. Eerdere onderzoeken geven aan dat de methode van conforme afbeeldingen een veelbelovende analytische methode is om het twee-dimensionale (2D) golfweerkaatsingprobleem op te lossen vanwege de rekenkundige efficiëntie en nauwkeurigheid. Daarom is het eerste doel van deze dissertatie het uitbreiden van deze methode naar drie dimensies (3D) en het systematisch evalueren van hoe goed de methode presteert. Het blijkt dat de uitkomsten onnauwkeurig kunnen zijn, met name bij hoge frequenties. Dit gegeven is de motivatie achter het tweede doel van deze dissertatie. Dit tweede doel is het verifiëren van de nauwkeurigheid van de specifieke toepassing van de methode van conforme afbeeldingen. In deze toepassing worden golven die worden weerkaatst aan het oppervlak van de halfruimte namelijk gerepresenteerd door cilindrische golven gegenereerd door een gespiegelde bron met een a priori onbekende intensiteit. Voor dit tweede doel wordt een 2D model van een cilindrische holte ingebed in een elastische halfruimte gebruikt, dat geëxciteerd wordt door een harmonische uit-het-vlak-gepolariseerde afschuifgolf. Ten behoeve van de keuze voor een accurate oplossingsmethode voor het bovengenoemde tweede dynamische probleem wordt de nauwkeurigheid van de indirect Boundary Element Method (BEM) ook geëvalueerd voor dit model. Wegens de eerder genoemde onnauwkeurigheden bij hoge frequenties wordt voor het tweede dynamische probleem de indirect BEM gebruikt om de stabiliteit van de trilling van een op hoge snelheid bewegende oscillator door een in slappe grond ingebedde tunnel onderzocht; dit is het derde doel van deze dissertatie.

Met het oog op het eerste doel wordt het drie-dimensionaal (3D) model van een cilindrische, in een elastische halfruimte ingebedde tunnel geëxciteerd door vlakke harmonische druk- en afschuifgolven beschouwd. Zowel de tunnel als de grond worden gemodelleerd als een elastisch continuüm. De methode van conforme afbeeldingen wordt gebruikt om het originele fysieke domein met randoppervlakken van twee verschillende types te transformeren naar een afbeeldingsdomein met oppervlakken van hetzelfde type.

Het totale golfveld in de halfruimte bestaat uit inkomende en door het oppervlak van de halfruimte gereflecteerde vlakke golven alsmede uit direct en secundair weerkaatse cilindrische golven, terwijl het totale golfveld in de tunnel bestaat uit brekende cilindrische golven. De secundair weerkaatse golven, die ontstaan doordat cilindrische golven die direct door de tunnel weerkaatst zijn het oppervlak van de halfruimte bereiken, worden gerepresenteerd door cilindrische golven gegenereerd door een gespiegelde bron met een a priori onbekende intensiteit. Het gebruik van deze gespiegelde bron is geïnspireerd op de spiegelmethode ("method of images"). De onbekende amplitudecoëfficiënten van de cilindrische golven worden bepaald op basis van de rand- en continuïteitsvoorwaarden van het tunnel-grond systeem; door deze te projecteren op de set van omtrekstrilvormen wordt een stelsel van algebraïsche vergelijkingen verkregen. Volgens de resultaten convergeert de gebruike rekenmethode (van conforme afbeeldingen) bij een klein aantal omtrekstrilvormen. De verkregen resultaten komen goed overeen met die in de gerelateerde literatuur. In een systematische evaluatie wordt aangetoond dat de methode goed werkt voor frequenties die kenmerkend zijn voor seismische golven en ook voor het gehele beschouwde bandbreedtes van de verhouding tussen tunnel- en grondstijfheid, de ingebedde diepte van de tunnel, de verticale invalshoek en de tunneldikte. De reden voor de onnauwkeurigheid bij hoge frequenties ligt waarschijnlijk aan het feit dat de secundair weerkaatste golven in de grond worden beschreven door cilindrische golven en niet door vlakke golven. Vlakke golven zijn waarschijnlijk beter geschikt om het gedrag aan het vlakke grondoppervlak bij hoge frequenties te beschrijven. Resultaten verkregen voor een gematigde verhouding tussen tunnel- en grondstijfheid zijn ook onnauwkeurig bij een inkomende drukgolf in het geval dat Hankelfuncties gebruikt worden om de cilindrische golven in de tunnel te beschrijven. Dit gebeurt als brekende afschuifgolven in de tunnel overgaan van voortplatend naar 'evanescent'. De onnauwkeurigheid kan omzeild worden door Besselfuncties te gebruiken om de brekende golven in de tunnel te beschrijven. Verder werkt de gebruikte methode over het algemeen beter voor de inkomende drukgolf dan voor de inkomende afschuifgolf omdat het conditiegetal van de coëfficiëntenmatrix (gerelateerd aan de eerder genoemde algebraïsche vergelijkingen) vaak groter is in het laatste geval. Als conclusie kan gesteld worden dat de uitbreiding van de methode van conforme afbeeldingen naar het beschouwde 3D scenario succesvol is; de methode kan gebruikt worden voor het voorlopig ontwerp van tunnels om resonanties te voorkomen en ook om spanningsverdelingen en grondtrillingen te beoordelen. Met het oog op de praktijk kan verder gesteld worden dat de tunnel veiliger is bij een relatief stijvere grond, een dikkere tunnelwand en een grotere verticale invalshoek.

Met het oog op het tweede doel wordt het 2D probleem van een cilindrische holte ingebed in een elastische halfruimte beschouwd, geëxciteerd door een harmonische uit-het-vlak-gepolariseerde afschuifgolf. De nadruk ligt op de vergelijking tussen drie methodes: de spiegelmethode, de methode van conforme afbeeldingen en de indirect BEM. De analysitische oplossing verkregen met de spiegelmethode dient als referentie voor de andere twee methodes. Convergentietesten en validaties worden uitgevoerd om de nauwkeurigheid van de methodes te beoordelen. De vergelijking van de drie methodes laat zien dat zowel de methode van conforme afbeeldingen als de spiegelmethode een vergelijkbare hoeveelheid van omtrekstrilvormen nodig hebben om geconvergeerde resultaten te krijgen. In termen van numerieke efficiëntie overtreft de spiegelmethod de methode van conforme afbeeldingen, terwijl de indirect BEM in dat opzicht het minst presteert van de drie. Een systematische evaluatie laat zien dat zowel de methode van conforme afbeeldingen en de indirect BEM nauwkeurig zijn binnen de beschouwde bandbreedtes van de dimensieloze frequentie, de ingebedde diepte en de verticale invalshoek. Dit is in tegenstelling tot het 3D probleem, eerder beschouwd met het oog op het eerste doel. Daar kunnen geen geconvergeerde, en dus nauwkeurige, resultaten verkregen worden voor de hoge frequenties bij het gebruik van de methode van conforme afbeeldingen. De bevindingen suggereren dat het representeren van de weerkaatste golven afkomstig van het vrije oppervlak door cilindrische golven (afkomstig van een spiegelbron met a priori onbekende intensiteit) bij de methode van conforme afbeeldingen inderdaad de reden is voor de onnauwkeurigheden bij hoge frequenties in het 3D vraagstuk. Omdat geen onnauwkeurigheden zijn waargenomen voor het 2D probleem, wordt gesteld dat de onnauwkeurigheid in het 3D probleem waarschijnlijk veroorzaakt worden door het feit dat de gebruikte cilindrische golven (in plaats van vlakke golven) niet in staat zijn om alle optredende golfconversies bij het vrije oppervlak te beschrijven. Een parametrische studie m.b.v. het 2D model laat verder significante effecten zien van de systeemparameters op de responsies. De responsiecurves vertonen resonanties op nagenoeg gelijke afstanden van elkaar. Dit komt overeen met de responsiecurves van een één-dimensionale (1D) afschuifslaag geëxciteerd door een beweging van het onderliggende gesteente. De responsiecurves behorende bij het 3D model vertonen geen resonanties op gelijke afstanden van elkaar.

Met het oog op het derde doel wordt de stabiliteit van de verticale trilling beschouwd van een object dat met constante snelheid beweegt door een tunnel in slappe grond. De grond is gemodelleerd als een elastisch continuüm, terwijl de tunnel is gemodelleerd met behulp van de Flüggeschaal. Het bewegende object is gemodelleerd als een massa-veer-systeem, waarbij ook gekeken is naar het scenario van een enkele massa (zonder contactveer) als limietgeval. Door gebruik te maken van de indirect BEM wordt de equivalente dynamische stijfheid van het tunnel-grond-systeem op het contactpunt met het bewegende object numeriek berekend. Het concept van de equivalente stijfheid wordt gebruikt om het originele 2.5D model te reduceren tot een discreet model. De parameters van dit discrete model zijn afhankelijk van de trillingsfrequentie en de snelheid van het bewegende object. De kritische snelheid waarboven de trillingen van het object instabiel kunnen zijn wordt gevonden, en deze is hetzelfde voor beide modellen van het object (massa-veer-systeem en enkele massa). Deze kritieke snelheid (voor instabiliteit) is veel groter dan de operationele snelheid van hogesnelheidstreinen en van ultrahogesnelheid transportvoertuigen; het model gebruikt in deze dissertatie geeft dus aan dat de trillingen van Maglev en Hyperloop voertuigen stabiel zullen zijn. Verder is de kritieke snelheid (voor instabiliteit) veel groter dan de kritieke snelheid voor resonantie; dit correspondeert niet met bevindingen in de literatuur voor het model van een spoorweg bovenop een elastische halfruimte. Voor beide modellen (d.w.z. een tunnel ingebed in de halfruimte en een spoorweg bovenop de halfruimte) is de kritische snelheid voor resonantie iets kleiner dan de snelheid van Rayleighgolven. Het feit dat de kritieke snelheid voor instabiliteit zoveel groter is in het huidige model wordt veroorzaakt door de grote stijfheid van de tunnel en de stralingsdemping van de golven die zich langs tunnel voortplanten. Een parametrische studie toont dat de dikte en de materiaaldempingsratio van de tunnel, de stijfheid van de grond en de ingebedde diepte een stabiliserend effect hebben, terwijl de demping van de grond een licht destabiliserend effect heeft (d.w.z. een lagere kritische snelheid voor instabiliteit). Met behulp van de D-decompositiemethode is de stabiliteit van het bewegende object onderzocht voor snelheden boven de kritische snelheid. Het instabiliteitsdomein in de ruimte van de systeemparameters wordt gevonden, evenals de afhankelijkheid van de kritische massa en stijfheid van de snelheid. Resultaten tonen dat hoe hoger de snelheid is, hoe lager de massa van het object behoeft te zijn om de stabiliteit te garanderen (in het geval van de enkele massa). En hoe groter de snelheid, hoe groter de stijfheid van de veer moet zijn als deze wordt aangebracht (in het geval van het massa-veer systeem) om stabiliteit te garanderen. Tenslotte, met het oog op het beoordelen van de stabiliteit van Maglev- en Hyperlooptreinen, de methode ontwikkeld in deze dissertatie kan ook gebruikt worden voor geavanceerdere modellen waarbij meer contactpunten tussen de bewegende massa en de tunnel beschouwd worden; hierdoor de zou de realiteit nog beter beschreven worden.

1

INTRODUCTION

1.1. BACKGROUND AND MOTIVATION

Underground structures play a pivotal role in modern society, serving as vital infrastructures with a broad range of applications in civil engineering. The growth of rapid transit systems, commonly known as metro and high-speed trains, has led to the emergence of numerous embedded tunnels. These tunnels serve as efficient transportation networks within urban areas. Additionally, underground structures are utilised for housing and safeguarding utility infrastructure such as water and sewage pipelines, electrical cables, telecommunication networks and gas distribution systems. In most cases these systems are buried in the ground to prevent damages from external factors and reduce visual clutter in urban environment. Furthermore, underground structures are used to protect individuals or sensitive equipments as well as power plants. These are just a few examples of the diverse applications of underground structures in civil engineering. It is obvious that underground infrastructures are valuable assets in modern urban development. Therefore, it is of utmost importance to ensure the proper design of these structures, enabling them to withstand both externally and internally applied dynamics loads, including seismic waves and the passage of moving trains.

An earthquake, characterised by a sudden release of energy within the earth, generates seismic waves that propagate through the earth's layers. Such seismic events can cause severe damage to structures both above and beneath the ground surface. Recent examples include the occurrence of induced seismicity in the Netherlands. These induced events, although typically small with magnitudes not exceeding 4, possess the potential to inflict harm upon residential properties, infrastructures and public acceptance [Muntendam-Bos *et al.*, 2022]. The scattering of earthquake waves by embedded inclusions or local topographies in the ground has been an important topic in geotechnical engineering and seismology [Mow and Pao, 1971; Achenbach, 1973; Graff, 1975; Aki and Richards, 2002]. Extensive site investigations and theoretical studies have revealed that amplifications of displacements at the ground surface and dynamic stress concentrations at the surfaces of structures may occur due to the scattering of the incident and reflected waves (generated at the ground surface) by the embedded inclusions [Mow and Pao, 1971; Ariman and Muleski, 1981; Hashash *et al.*, 2001; Moore and Guan, 1996].

The fast development of high-speed trains makes the dynamics of moving loads another important research topic. The dynamic effects associated with modern high-speed trains are of significant importance due to the generation of propagating waves in both the railway track and subsoil. Engineers primarily focus on two main concerns: environmental vibrations induced by moving trains (e.g., [Kaynia *et al.*, 2000; Di *et al.*, 2016; Degrande *et al.*, 2006]) and the stability of moving trains themselves (e.g., [Denisov *et al.*, 1985; Bogacz *et al.*, 1986; Metrikine, 1994; Metrikine and Dieterman, 1997; Mazilu *et al.*, 2012]).

1.2. STATE OF THE ART

1.2.1. SCATTERING OF SEISMIC WAVES

It is widely acknowledged that the presence of underground structures can lead to substantial amplifications of ground motion and dynamic stress concentrations when subjected to seismic waves [Mow and Pao, 1971]. These dynamic responses arise from wave scattering and wave interference occurring between the ground surface and surfaces of the embedded inclusions [Lee and Trifunac, 1979].

The ground is often modelled by a half-space, which consists of an infinite domain beneath a flat stress-free surface. The challenges in solving the boundary value problem of a cylindrical tunnel embedded in a half-space are as follows: (1) The half-space domain is infinite, and it is often computationally expensive and challenging to satisfy the boundary conditions at large distance when applying numerical methods [Stamos and Beskos, 1995]; (2) The boundary surfaces are of two different types (i.e. flat and cylindrical), and it is difficult to deal with this issue especially when applying analytical methods; (3) It can be very difficult to get accurate results due to ill-conditioned matrices encountered for specific solution methods [Luco and de Barros, 1994a].

The existing approaches to study the scattering of waves by underground structures can be divided into two categories: analytical methods and numerical methods. These two types of methods have their own pros and cons. Analytical methods are computationally efficient but can only deal with structures of simple geometries. Numerical methods, on the other hand, can handle structures of complex geometries but are often computationally expensive because of the large domains that need to be discretised. In addition, when dealing with dynamic problems that involve nonlinear inelastic behaviour, one must turn to numerical methods for solutions. The most often used numerical methods are Finite Element Methods (FEM), Finite Difference Methods (FDM), Boundary Element Methods (BEM) and combinations of those. A comprehensive overview of the features of these different methods applied to the problem of wave scattering by underground structures in a half-space can be found in Stamos and Beskos [1995].

With the development of more powerful computers, numerical methods have been widely applied to investigate the dynamic amplifications induced by the scattering of plane waves by underground structures and canyons at the ground surface. In this context, the BEM has gained widespread application in the analysis of wave scattering in elastodynamics due to its ability to automatically satisfy the far-field wave radiation conditions by utilizing Green's functions of the full-space or the half-space medium. For example, Manolis and Beskos [1983] employed the isoparametric BEM formulated in the Laplace transformed domain to investigate the dynamic stress concentration in the lining of a tunnel. Luco and de Barros [Luco and de Barros, 1994a,b; de Barros and Luco, 1993; Luco and de Barros, 1993; de Barros and Luco, 1994] employed the indirect BEM to examine the two-dimensional (2D) and three-dimensional(3D) responses of infinitely long cylindrical inclusions embedded in a layered poroelastic half-space. A simplified Donnell shell theory was used to model pipelines. Applications of the indirect BEM to other wave scattering problems can be found in the work by Dravinski and Mossessian [1987]. The advantage of the indirect BEM is that (integrable) singularities of the Green's functions are eliminated by locating the source positions away from the integral surface at which the observation positions are located. A special direct BEM was used by Stamos and Beskos [1995, 1996] to determine the 3D dynamic response of underground structures in a half-space. In their paper, quadratic isoparametric boundary line elements and an advanced numerical integration technique for the treatment of singular integrals were used to produce results of high accuracy. Furthermore, the combination of BEM and FEM was applied by Liu *et al.* [1991] to study the 3D response of pipelines buried in a half-space. The above mentioned methods are all frequency-domain based. Some work conducted in the time domain employing FEM or BEM can be found on other references [Israil and Banerjee, 1990; Hatzigeorgiou and Beskos, 2010; Alielahi *et al.*, 2015, 2016; Panji and Ansari, 2017]. In the context of wave scattering problems in poroelastic media, Zimmerman and Stern [1993], and Liu *et al.* [2017] obtained boundary element solutions. Note that the BEM is often more efficient compared to other numerical methods, as explicit expressions for the employed Green's functions are available (in the frequency-wavenumber domain), and only surfaces need to be discretised. For that reason, the BEM in this thesis is perceived as semi-analytical method.

Analytical methods are usually based on wave-function expansions. Using the method of separation of variables, wave functions satisfying the wave or Helmholtz equations in Cartesian or cylindrical coordinates are obtained. The unknown coefficients in the wave-function expansions (i.e., general solutions) can be determined based on boundary conditions. Wave functions were first used by Mow and Pao [1971] to study the wave scattering from a cavity in a full-space. To solve the unknown coefficients for more complicated problems involving a half-space, additional techniques need to be employed. For the 2D SH wave scattering problem in a half-space with an embedded tunnel, the method of images was used to obtain a closed-form steady-state solution [Lee and Trifunac, 1979; Balendra *et al.*, 1984]. However, it is important to note that the application of the method of images is limited to the simple problem of the 2D anti-plane case only. The P-SV problem in a half-space is more complicated to solve due to mode conversions between the P and SV waves at the half-space surface and at the tunnel. To tackle this, Datta, EL-Akily and Shah [Datta and El-Akily, 1978; El-Akily and Datta, 1980, 1981; Datta and Shah, 1982] employed a method of matched asymptotic expansions and a method of successive reflections to calculate the response of the considered half-space system. Lee and Zhu [2014] employed Legendre polynomials to represent both P and S wave functions so that zero-stress boundary conditions at the half-space surface can be satisfied. Other examples of analytical solutions to solve the wave scattering problems can be found in Wong *et al.* [1986a,b].

To circumvent the difficulty arising due to the two different bounding surfaces in the problem of cylindrical structures embedded in a half-space, Cao and Lee [1990], and Lee and Karl [1992] proposed to approximate the flat half-space boundary by an almost flat circular boundary of a large radius. The aim of the current thesis is to present a semi-analytical solution without employing this approximation. To cope with the challenge of the two different boundary surfaces, the method of conformal mapping (which employs the complex-variable theory) is used; it transforms a domain with flat and cylindrical boundary surfaces into a domain with cylindrical surfaces only [Muskhelishvili, 1966]. Liu *et al.* [1982] were the first to apply the method of conformal mapping to solve the 2D full-space wave scattering by a cavity problem. Then, Verruijt [1998] also used this method to solve the problem of a circular cavity in an elastic half-space with prescribed static loads acting on the cavity surface. Later on, the method was used by Liu et al. to solve the 2D problem of two closely-spaced circular cavities subject to plane harmonic waves in a full-space [Liu and Wang, 2012], and to solve the 2D dynamic problem of a tunnel embedded in an elastic half-space subjected to seismic waves [Liu *et al.*, 2013]. The method of conformal mapping has also been applied to solve the wave scattering problems with non-circular tunnel [Kargar *et al.*, 2014; Zhang *et al.*, 2019] and in the poroelastic media[Wang *et al.*, 2009; Fang and Jin, 2017; Liu *et al.*, 2022; Yue and Liu, 2023a,b].

1.2.2. DYNAMICS OF HIGH-SPEED MOVING TRAINS

The study of dynamics of train-track-soil interactions has been of interest to researchers for decades. Popp *et al.* [1999] gave a comprehensive review of the existing models that can be used to study dynamic train-track-soil interaction.

In general, studies on moving trains fall into two categories. The first category is environmental vibrations induced by moving trains to assess vibration hindrance and to ensure the safety of nearby structures. The second category is the stability of vibrations of moving trains to ensure the safety and comfort of the passengers in the trains. For the former category, the steady-state regime is assumed when investigating the dynamic amplification due to resonance [Kaynia *et al.*, 2000; Di *et al.*, 2016; Degrande *et al.*, 2006]. Other studies in the first category are devoted to transition radiation which occurs when a train passes an inhomogeneity [Varandas *et al.*, 2017; Fărăgău *et al.*, 2019].

For studies falling into the second category, the train is usually modelled as a single- or muti-degree of freedom system [Ouyang, 2011]. When instability occurs, the free vibration (i.e., the vibration in the absence of an external force) of the train grows exponentially, resulting in an infinite displacement when time goes to infinity, which implies that a steady-state solution does not exist. This is very different from resonance, which happens when steady-state response as induced by an external moving load is extreme (either bounded or not depending on the presence of damping). Both phenomena come with a certain critical velocity. The critical velocity for resonance is defined as the velocity at which the steady-state response induced by a moving load is extreme (i.e., resonance takes place at certain specific velocities) [Dimitrovová, 2016, 2017], while the critical velocity for instability is defined as the velocity beyond which instability can occur (i.e., instability occurs in a range of velocities). Another crucial difference between resonance and instability is that resonance can be totally removed by increasing damping, while damping mostly shifts the instability domain, for example, to a region of larger velocities [Denisov *et al.*, 1985; Metrikine and Dieterman, 1997].

The first study on stability of vibrations is that of a mass that moves uniformly along an elastically supported beam [Denisov *et al.*, 1985]. The physical explanation of instability was given by Metrikine [1994] who argued that the instability is caused by the radiated anomalous Doppler waves [Ginzburg, 1979] which increase the energy of the vibrating object. In addition, the physical mechanism of instability was discussed using the laws of conservation of energy and momentum [Metrikine, 1994; Kononov and De Borst, 2002].

After the pioneering works on the instability phenomenon [Denisov *et al.*, 1985; Bogacz *et al.*, 1986], several aspects that influence the stability of an object have been discussed. For example, the effect of thermal stresses in the structure was studied considering different models of moving oscillators [Metrikine and Dieterman, 1997; Zheng *et al.*, 2000; Zheng and Fan, 2002]. Other papers considered the effect of more than one contact point between the object and the structure [Zheng and Fan, 2002], and of contact nonlinearities [Mazilu *et al.*, 2012]. Moreover, a more accurate beam model to represent the rail was considered and a comparison between the Timoshenko and Euler-Bernoulli beam models was given [Metrikine and Verichev, 2001]. Four different beam and plate models were considered in Kononov and De Borst [2002]. Furthermore, Verichev et al. introduced other complexities in their model, i.e., a bogie model which consists of a rigid bar of finite length on two identical supports [Verichev and Metrikine, 2002]. More recently, Mazilu studied the stability of a train of oscillators moving along an infinite Euler-Bernoulli beam on a viscoelastic foundation [Mazilu, 2013]. Another work focused on the stability of a moving mass in contact with a system of two parallel elastically connected beams, with one of them being axially compressed [Stojanović *et al.*, 2017]. Later, the stability of vibrations of a railway vehicle moving along an infinite three-beam/foundation system has been considered, with an emphasis on the effect of the damping and stiffness of the secondary suspension of the railway vehicle [Stojanović *et al.*, 2018]. For a more simple model, Dimitrovová presented a semi-analytical solution for the evolution of the beam deflection shapes and oscillator vibrations [Dimitrovová, 2019]. In that paper, not only the onset of instability, but also the severity is addressed.

1.3. AIM AND SCOPE

As discussed in Sections 1.1 and 1.2, this thesis is dedicated to addressing two distinct types of dynamic problems: the dynamic response of an elastic half-space with an embedded tunnel subjected to seismic waves, and the stability of vibrations of high-speed trains moving through that underground tunnel. The aim of this thesis is to present semi-analytical solutions to these problems. Spurred by its promising potential demonstrated in previous studies [Liu and Wang, 2012; Liu *et al.*, 2013, 2014, 2019], the method of conformal mapping is the first candidate to be applied for both problems.

With regard to the seismic wave scattering problem, the method of conformal mapping has already been employed to solve the 2D scenario involving a tunnel embedded in an elastic half-space [Liu *et al.*, 2013]. The accuracy and efficiency of the method of conformal mapping have been demonstrated for a particular set of material parameters.

Consequently, the first objective of this thesis is to extend the method of conformal mapping to 3D case. Additionally, this thesis aims to provide a comprehensive assessment of the method's performance across a wide range of system parameters, an aspect that is lacking in previous studies. The potential inaccuracies of the method that were found, particularly at high frequencies, motivate the second objective of this thesis to verify the accuracy of the specific application of the method of conformal mapping in which the waves scattered from the half-space surface are represented by cylindrical waves that originate from an image source of a priori unknown intensity. To this end, a simpler 2D model is considered, involving a cylindrical cavity embedded in an elastic half-space subject to a harmonic anti-plane shear wave. The performance of the indirect BEM is evaluated too for this model in view of the choice of the appropriate solution method for the second type of dynamic problem considered in this thesis.

Regarding this second type of dynamic problem concerning high-speed moving trains, the indirect BEM is employed due to the limitation of the method of conformal mapping in providing accurate solutions at high frequencies. Previous studies on stability analysis employing 3D models of railway tracks focused on trains moving on a track founded on the ground surface [Metrikine and Popp, 1999; Metrikine *et al.*, 2005]. It has been shown that, for such configurations, the critical velocity for instability of the moving object is close to the Rayleigh wave speed in the soil. However, the stability of trains moving through an underground tunnel using a 3D model has not been analysed yet. Therefore, the third objective of this thesis is to conduct a stability analysis for the vibration of an oscillator moving through a tunnel embedded in soft soil. It is of particular interest to investigate whether the critical velocity for instability of the moving object in both a shallow and deep tunnel is also close to the Rayleigh wave speed in the soil. These questions hold practical relevance, especially for contemporary high-speed railway tracks as well as for upcoming ultra-high-speed transportation systems such as Maglev and Hyperloop, respectively [Rote and Cai, 2002; Abdelrahman *et al.*, 2017; Janzen, 2017].

1.4. THESIS OUTLINE

The structure of this thesis is outlined as follows. Chapter 2 presents a semi-analytical solution for the 3D problem of a cylindrical tunnel embedded in an elastic half-space subject to plane harmonic compressional and shear waves. Both the tunnel and soil are modelled as an elastic continuum. The method of conformal mapping is employed to transform the original domain with boundary surfaces of two different types onto an image domain with surfaces of the same type. The total wave field in the half-space consists of incident and reflected plane waves, as well as directly and secondary scattered cylindrical waves, while the total wave field in the tunnel consists of refracted cylindrical waves. The unknown amplitude coefficients of the cylindrical waves are determined from the boundary and continuity conditions of the tunnel-soil system by projecting those onto the set of circumferential modes, resulting in a set of algebraic equations. Convergence tests and validations are given, as well as a systematic evaluation of the accuracy of the present method. The accuracy is analysed for varying dimensionless frequency, the stiffness ratio of the tunnel to soil, the embedded depth of the tunnel, the vertical incident angle and the thickness of the tunnel. The effects of these five important factors on the system response are briefly addressed.

In Chapter 3, the 2D dynamic response of an elastic half-space with a cylindrical cavity subject to a harmonic anti-plane shear wave is investigated. The soil is modelled as an elastic continuum. It is observed in Chapter 2 that inaccurate results may be obtained by the method of conformal mapping, particularly at high frequencies. This observation motivates the study in Chapter 3, which aims to verify the accuracy of the specific application of the method of conformal mapping (in which the waves scattered from the half-space surface are represented by cylindrical waves that originate from an image source of a priori unknown intensity) and of the indirect BEM. To achieve this aim, a comparison of three methods is conducted: the method of images, the method of conformal mapping and the indirect BEM. Convergence tests and validation examples are provided to assess the accuracy of these methods. The comparison of the three methods is made regarding two aspects: the requirement for converged results and the computational efficiency. The closed-form solutions obtained by the method of images serve as benchmark solutions for the other two methods. The study validates the accuracy of the specific application of the method of conformal mapping and of the indirect BEM, not only for specific parameters but also through a systematic evaluation. Specifically, the evaluation is conducted with respect to varying dimensionless frequency, the embedded depth of the cavity and the vertical incident angle. In addition, the effects of these three important factors on the system response are briefly discussed.

Chapter 4 is devoted to the stability analysis of vertical vibrations of an object moving through a tunnel embedded in soft soil. The soil is modelled as an elastic continuum, whereas the tunnel is modelled by an infinitely long cylindrical Flügge shell. The moving object is either modelled as a mass-spring system or as a limiting case of a single mass. The concept of the equivalent dynamic stiffness is employed, which reduces the original 2.5D model to an equivalent discrete model. As indicated in Chapter 3 that the method of conformal mapping is not applicable for high frequency loadings, we thus utilise the indirect BEM to obtain the equivalent dynamic stiffness of the tunnel-soil system at the point of contact with the moving object. Prior to that, the indirect BEM is validated for two specific problems. Using the equivalent stiffness, the critical velocity beyond which the instability of the object may occur is found. The critical velocity for instability is the most important result of the stability analysis. A parametric study is conducted to examine the effect of the tunnel thickness, the material damping ratio in the tunnel-soil system, the Lamé parameters of the soil and the burial depth of the tunnel on the critical velocity. The D-decomposition method is used to investigate the stability of the moving object for velocities exceeding the identified critical velocity for instability. The instability domains in the space of the system parameters is found, as well as the dependency of the critical mass and stiffness on the velocity.

Finally, in Chapter 5, all the important conclusions of this thesis and recommendations are presented.

2

SEMI-ANALYTICAL SOLUTION FOR THE 3D RESPONSE OF A TUNNEL EMBEDDED IN AN ELASTIC HALF-SPACE SUBJECT TO SEISMIC WAVES

This chapter presents a semi-analytical solution for the 3D problem of a cylindrical tunnel embedded in an elastic half-space subject to plane harmonic compressional and shear waves. Both the tunnel and soil are modelled as an elastic continuum. Conformal mapping is employed to transform the original physical domain with boundary surfaces of two different types onto an image domain with surfaces of the same type, which makes the problem easier to solve. The total wave field in the half-space consists of incident and reflected (from the half-space surface) plane waves, as well as directly and secondary scattered cylindrical waves, while the total wave field in the tunnel consists of refracted cylindrical waves. The secondary scattered waves, generated when the cylindrical waves directly scattered from the tunnel meet the half-space surface, are represented by cylindrical waves that originate from an image source, which is in line with the spirit of the method of images. The unknown amplitude coefficients of the cylindrical waves are determined from the boundary and continuity conditions of the tunnel-soil system by projecting those onto the set of circumferential modes, which results in a set of algebraic equations. Results show that the present method converges for a small number of circumferential modes. We observe very good agreement between the obtained results and those in literature. In a systematic evaluation, we demonstrate that the method works well for the frequency band

---

This chapter has been published as a journal paper in *Soil Dynamics and Earthquake Engineering* **174**, 108171 (2023) [Zhao *et al.*, 2023]. Minor changes have been made.

of seismic waves, as well as for the complete considered ranges of the tunnel/soil stiffness ratio, the embedded depth of the tunnel, the vertical incident angle and the tunnel thickness. However, the results obtained for a moderate tunnel-soil stiffness contrast under the incident compressional wave are inaccurate when Hankel functions are used to represent the cylindrical waves in the tunnel, which is due to the refracted shear waves in the tunnel transitioning from propagating to evanescent (in the 3D case). These inaccuracies can be perfectly overcome by representing the waves in the tunnel by Bessel functions. We also find that the present method generally works better for the incident compressional wave than for the incident shear wave, as the condition number of the matrix (related to the mentioned algebraic equations) is often larger in the latter case. In view of engineering practice, we conclude that the tunnel is safer when the surrounding soil is stiffer, the tunnel is thicker and the vertical incident angle is larger. Finally, the present method, which is in general fast, elegant and accurate, can be used in preliminary design so as to avoid pronounced resonances, and to assess stress distributions and ground vibrations.

2.1. INTRODUCTION

This chapter focuses on the dynamic problem of wave scattering caused by seismic waves interacting with an underground tunnel. Correctly understanding the dynamic behaviour of tunnel-soil system and efficiently obtaining reliable results are crucial for engineering practices. Consequently, the primary objective of this chapter is to present a semi-analytical solution for a three-dimensional (3D) problem.

The method of conformal mapping has been successfully employed to solve various two-dimensional (2D) wave scattering problems. For example, researchers utilised this method to solve the 2D full-space wave scattering by a cavity [Liu *et al.*, 1982], the scattering of plane harmonic waves by two closely-spaced circular cavities in a full-space [**?**], and the 2D dynamic problem of a tunnel embedded in an elastic half-space subjected to seismic waves [Liu *et al.*, 2013]. These studies have demonstrated the accuracy and computational efficiency of the method of conformal mapping. However, there remains a gap in the literature regarding the extension of this method to the 3D case and a systematic evaluation of its performance. Addressing this gap, the current chapter aims to extend the method of conformal mapping to a 3D problem and provide a comprehensive assessment of its capabilities. In addition, the extension of the conformal mapping method to 3D also serves the purpose ("second objective") of determining the right computation method for the stability analysis of high-speed trains moving through an underground tunnel in the Chapter 4.

This chapter is organised as follows. In Section 2.2, the statement of the considered problem is presented. Section 2.3 presents incident and reflected plane-wave fields in the soil, and scattered and refracted cylindrical-wave fields in the soil and tunnel, respectively. Stress and displacement expressions in terms of complex variables are given in Section 2.4. The conformal mapping functions are introduced in Section 2.5. In Section 2.6, the unknown coefficients of potentials related to the cylindrical waves are determined. After having solved the problem, convergence tests and validations of the proposed method are given in Section 2.7. Furthermore, an evaluation of the accuracy of the present method is given in Section 2.8. The accuracy is analysed for varying dimensionless frequency, the stiffness ratio of the tunnel to soil, the embedded depth of the tunnel, the vertical incident angle and the thickness of the tunnel. The effects of these five important factors on the response of the system are briefly addressed as well. Finally, Section 2.9 presents the conclusions.

2.2. PROBLEM STATEMENT

In this chapter, we consider the three-dimensional model shown in Fig. 2.1. An infinitely long tunnel embedded in an elastic half-space is subjected to seismic waves with the wave propagation direction being arbitrary. The tunnel has a circular cross-section, and the longitudinal axis of the tunnel is parallel to the half-space surface. Both the tunnel and the half-space are modelled as an elastic continuum which is assumed isotropic and linearly elastic.

Regions Ω_1 and Ω_2 shown in Fig. 2.1 refer to the domains of the soil and tunnel, respectively. For the analysis, it is convenient to use six coordinate systems: global Cartesian $(\tilde{y}, \tilde{z}, \tilde{x})$ and cylindrical $(\tilde{r}, \theta, \tilde{x})$ coordinates with origin at the free surface of the half-

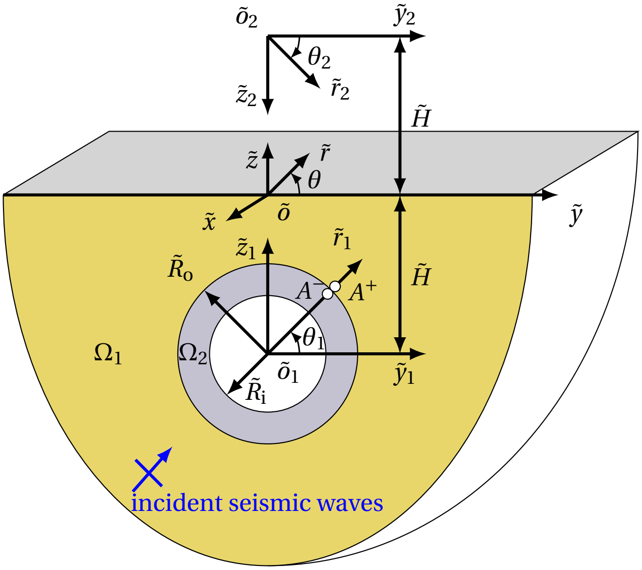

Figure 2.1: A 3D model of a tunnel embedded in an elastic half-space subjected to seismic waves and the employed coordinate systems.

space, local Cartesian ($\tilde{y}_1, \tilde{z}_1, \tilde{x}_1$) and cylindrical ($\tilde{r}_1, \theta_1, \tilde{x}_1$) coordinates with origin at the centre of the tunnel, and local Cartesian ($\tilde{y}_2, \tilde{z}_2, \tilde{x}_2$) and cylindrical ($\tilde{r}_2, \theta_2, \tilde{x}_2$) coordinates with origin at the centre of the image of the tunnel. The centre of the tunnel $\tilde{o}_1$ is located beneath the free surface at a depth of $\tilde{H}$, and the inner and outer radii of the tunnel are denoted as $\tilde{R}_\text{i}$ and $\tilde{R}_\text{o}$, respectively. The image of the tunnel is symmetrically positioned with respect to the free surface. As shown in Fig. 2.2, the vertical incident angle θ_v is defined as the angle between the wave propagation direction and the positive vertical $\tilde{z}$ axis, while the horizontal incident angle θ_h is the angle between the projection of the wave propagation direction on the horizontal plane (i.e., $(\tilde{x}, \tilde{y})$-plane) and the negative $\tilde{x}$ axis. Throughout this chapter, a tilde is used to denote that parameters, coordinates, variables and operators are dimensional.

2.2.1. GOVERNING EQUATIONS AND BOUNDARY CONDITIONS

As we are interested in the steady-state solution to the problem, we assume that both the excitations and the responses of the system are harmonic and proportional to $\text{e}^{+\text{i}\tilde{\omega}\tilde{t}}$, where i is the imaginary unit, $\tilde{t}$ time, $\tilde{\omega} = 2\pi\tilde{f}$ the angular frequency and $\tilde{f}$ the frequency in Hz. In what follows, the factor $\text{e}^{+\text{i}\tilde{\omega}\tilde{t}}$ is left out from all the expressions for brevity. The governing equations of motion of the soil medium and the tunnel in the frequency domain, without external forces, read [Achenbach, 1973; Aki and Richards, 2002]

$$\left(\tilde{\lambda}^{(i)} + \tilde{\mu}^{(i)}\right)\tilde{\nabla}\tilde{\nabla}\cdot\tilde{\mathbf{u}}^{(i)} + \tilde{\mu}^{(i)}\tilde{\nabla}^2\tilde{\mathbf{u}}^{(i)} = -\tilde{\omega}^2\tilde{\rho}^{(i)}\tilde{\mathbf{u}}^{(i)}, \tag{2.1}$$

where $\tilde{\lambda}^{(i)}$ and $\tilde{\mu}^{(i)}$ signify the Lamé constants, and $\tilde{\rho}^{(i)}$ the material density; the superscript $i = \{1,2\}$ indicates the soil or tunnel, respectively; $\tilde{\nabla}$ is the three-dimensional

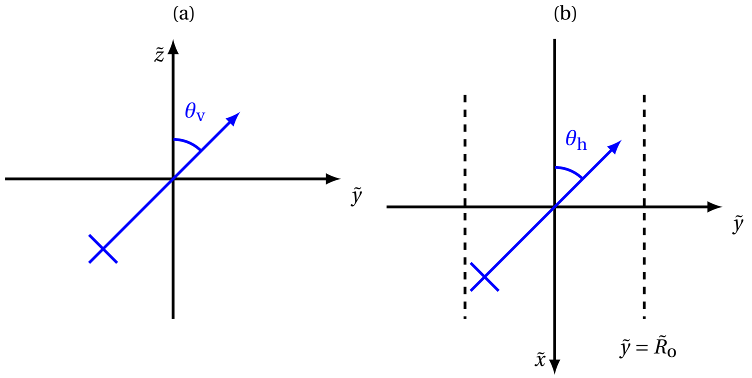

Figure 2.2: Incident angles: (a) vertical incident angle and (b) horizontal incident angle.

gradient vector (for Cartesian coordinates, as an example, $\tilde{\nabla} = (\partial_{\tilde{y}}, \partial_{\tilde{z}}, \partial_{\tilde{x}})$), $\tilde{\nabla}^2$ is the Laplace operator (e.g., $\tilde{\nabla}^2 = \partial^2_{\tilde{y}} + \partial^2_{\tilde{z}} + \partial^2_{\tilde{x}}$), and $\tilde{\mathbf{u}}^{(i)}$ is a displacement vector (e.g., $\tilde{\mathbf{u}}^{(i)} = (\tilde{u}^{(i)}_{\tilde{y}}, \tilde{u}^{(i)}_{\tilde{z}}, \tilde{u}^{(i)}_{\tilde{x}})$).

The excitations of the system are seismic waves coming from below the tunnel. Therefore, we have stress-free boundary conditions at both the free surface of the half-space and the inner surface of the tunnel. We assume that the soil and tunnel are perfectly bonded, which implies that we have continuity conditions at the tunnel-soil interface. Accordingly, these stress-free boundary and continuity conditions are written as follows:

$$\begin{array}{ll} \tilde{\sigma}^{(1)}_{\tilde{z}\tilde{z}} = \tilde{\sigma}^{(1)}_{\tilde{z}\tilde{y}} = \tilde{\sigma}^{(1)}_{\tilde{z}\tilde{x}} = 0, & \tilde{z} = 0, \\ \tilde{\sigma}^{(2)}_{\tilde{r}_1\tilde{r}_1} = \tilde{\sigma}^{(2)}_{\tilde{r}_1\theta_1} = \tilde{\sigma}^{(2)}_{\tilde{r}_1\tilde{x}_1} = 0, & \tilde{r}_1 = \tilde{R}_{\mathrm{i}}, \\ \tilde{u}^{(1)}_{\tilde{r}_1} = \tilde{u}^{(2)}_{\tilde{r}_1}, \quad \tilde{u}^{(1)}_{\theta_1} = \tilde{u}^{(2)}_{\theta_1}, \quad \tilde{u}^{(1)}_{\tilde{x}_1} = \tilde{u}^{(2)}_{\tilde{x}_1}, & \tilde{r}_1 = \tilde{R}_{\mathrm{o}}, \\ \tilde{\sigma}^{(1)}_{\tilde{r}_1\tilde{r}_1} = \tilde{\sigma}^{(2)}_{\tilde{r}_1\tilde{r}_1}, \tilde{\sigma}^{(1)}_{\tilde{r}_1\theta_1} = \tilde{\sigma}^{(2)}_{\tilde{r}_1\theta_1}, \tilde{\sigma}^{(1)}_{\tilde{r}_1\tilde{x}_1} = \tilde{\sigma}^{(2)}_{\tilde{r}_1\tilde{x}_1}, & \tilde{r}_1 = \tilde{R}_{\mathrm{o}}. \end{array} \tag{2.2}$$

2.2.2. APPLICATION OF THE HELMHOLTZ DECOMPOSITION

It is noted that the displacement components in Eq. (2.1) are coupled. For ease of finding solutions, we apply the Helmholtz decomposition $\tilde{\mathbf{u}}^{(i)} = \tilde{\nabla}\tilde{\phi}^{(i)} + \tilde{\nabla} \times \tilde{\mathbf{\Psi}}^{(i)}$, which reduces the elastodynamic equation of motion to two uncoupled Helmholtz equations:

$$\tilde{\nabla}^2 \tilde{\phi}^{(i)} + \left(\tilde{k}^{(i)}_{\mathrm{P}}\right)^2 \tilde{\phi}^{(i)} = 0, \tag{2.3}$$

$$\tilde{\nabla}^2 \tilde{\mathbf{\Psi}}^{(i)} + \left(\tilde{k}^{(i)}_{\mathrm{S}}\right)^2 \tilde{\mathbf{\Psi}}^{(i)} = 0, \tag{2.4}$$

where Eq. (2.3) is a scalar potential equation, and Eq. (2.4) is a vector potential equation; $\tilde{\phi}^{(i)}$ and $\tilde{\mathbf{\Psi}}^{(i)}$ are potentials related to dilatational and rotational motions, respectively; $\tilde{k}^{(i)}_{\mathrm{P}} = \tilde{\omega}/\tilde{c}^{(i)}_{\mathrm{P}}$ and $\tilde{k}^{(i)}_{\mathrm{S}} = \tilde{\omega}/\tilde{c}^{(i)}_{\mathrm{S}}$ are the compressional and shear wavenumbers; $\tilde{c}^{(i)}_{\mathrm{P}} = \sqrt{(\tilde{\lambda}^{(i)} + 2\tilde{\mu}^{(i)})/\tilde{\rho}^{(i)}}$ and $\tilde{c}^{(i)}_{\mathrm{S}} = \sqrt{\tilde{\mu}^{(i)}/\tilde{\rho}^{(i)}}$ are the propagation velocities of the compressional and shear waves.

The vector potential $\tilde{\mathbf{\Psi}}^{(i)}$ needs to satisfy the gauge condition $\tilde{\nabla}\cdot\tilde{\mathbf{\Psi}}^{(i)} = 0$, so that only two of the three components of $\tilde{\mathbf{\Psi}}^{(i)}$ are independent. We split up the vector potential $\tilde{\mathbf{\Psi}}^{(i)}$ as follows [Aki and Richards, 2002; Kausel, 2006]:

$$\begin{aligned}
\tilde{\mathbf{\Psi}}^{(i)} &= \tilde{\mathbf{\Psi}}_1^{(i)} + \tilde{\mathbf{\Psi}}_2^{(i)},\\
\tilde{\mathbf{\Psi}}_1^{(i)} &= \tilde{\psi}^{(i)}\mathbf{e}_{\tilde{x}} + \left(\tilde{k}_{\mathrm{S}}^{(i)}\right)^{-2}\tilde{\nabla}\left(\frac{\partial\tilde{\psi}^{(i)}}{\partial\tilde{x}}\right),\\
\tilde{\mathbf{\Psi}}_2^{(i)} &= \left(\tilde{k}_{\mathrm{S}}^{(i)}\right)^{-1}\tilde{\nabla}\times\left(\tilde{\chi}^{(i)}\mathbf{e}_{\tilde{x}}\right),
\end{aligned}\tag{2.5}$$

in which $\mathbf{e}_{\tilde{x}}$ is the unit vector along $\tilde{x}$ axis. The vector potential $\tilde{\mathbf{\Psi}}_1^{(i)}$ is defined such that the associated particle motion is polarized only in the vertical plane (i.e., $(\tilde{y},\tilde{z})$-plane); the other vector potential $\tilde{\mathbf{\Psi}}_2^{(i)}$ is defined such that the associated particle motion is polarized in all directions. This can be observed in the displacement expressions in Section 2.2.3 (see Eq. (2.10), contributions of $\psi^{(i)}$ and $\chi^{(i)}$).

By defining the vector potentials as in Eq. (2.5), the equation for the vector potential, Eq. (2.4), can be reduced to two uncoupled scalar potential equations:

$$\begin{aligned}
\tilde{\nabla}^2\tilde{\psi}^{(i)} + \left(\tilde{k}_{\mathrm{S}}^{(i)}\right)^2\tilde{\psi}^{(i)} &= 0,\\
\tilde{\nabla}^2\tilde{\chi}^{(i)} + \left(\tilde{k}_{\mathrm{S}}^{(i)}\right)^2\tilde{\chi}^{(i)} &= 0.
\end{aligned}\tag{2.6}$$

2.2.3. NON-DIMENSIONALISATION

For the analysis of the problem, we introduce non-dimensional parameters, coordinates, variables and operators. These are defined as

$$\begin{aligned}
&\{x,y,z,x_1,y_1,z_1,x_2,y_2,z_2,r,r_1,r_2\} = \{\tilde{x},\tilde{y},\tilde{z},\tilde{x}_1,\tilde{y}_1,\tilde{z}_1,\tilde{x}_2,\tilde{y}_2,\tilde{z}_2,\tilde{r},\tilde{r}_1,\tilde{r}_2\}/\tilde{H},\\
&\{H,R_{\mathrm{i}},R_{\mathrm{o}},\mathbf{u}^{(i)}\} = \{\tilde{H},\tilde{R}_{\mathrm{i}},\tilde{R}_{\mathrm{o}},\tilde{\mathbf{u}}^{(i)}\}/\tilde{H},\\
&\{c_{\mathrm{P}}^{(i)},c_{\mathrm{S}}^{(i)}\} = \{\tilde{c}_{\mathrm{P}}^{(i)},\tilde{c}_{\mathrm{S}}^{(i)}\}/\tilde{c}_{\mathrm{S}}^{(1)},\ t = \tilde{t}\tilde{c}_{\mathrm{S}}^{(1)}/\tilde{H},\ \omega = \tilde{\omega}\tilde{H}/\left(\pi\tilde{c}_{\mathrm{S}}^{(1)}\right),\\
&\{k_{\mathrm{P}}^{(i)},k_{\mathrm{S}}^{(i)}\} = \{\tilde{k}_{\mathrm{P}}^{(i)},\tilde{k}_{\mathrm{S}}^{(i)}\}\tilde{H},\ \{\phi^{(i)},\psi^{(i)},\chi^{(i)}\} = \{\tilde{\phi}^{(i)},\tilde{\psi}^{(i)},\tilde{\chi}^{(i)}\}/\tilde{H}^2,\\
&\{\lambda^{(i)},\mu^{(i)}\} = \{\tilde{\lambda}^{(i)},\tilde{\mu}^{(i)}\}/\tilde{\mu}^{(1)},\ \rho^{(i)} = \tilde{\rho}^{(i)}\left(\tilde{c}_{\mathrm{S}}^{(1)}\right)^2/\tilde{\mu}^{(1)}.
\end{aligned}\tag{2.7}$$

Accordingly, the dimensionless Helmholtz equations are obtained as

$$\begin{aligned}
\nabla^2\phi^{(i)} + \left(k_{\mathrm{P}}^{(i)}\right)^2\phi^{(i)} &= 0,\\
\nabla^2\psi^{(i)} + \left(k_{\mathrm{S}}^{(i)}\right)^2\psi^{(i)} &= 0,\\
\nabla^2\chi^{(i)} + \left(k_{\mathrm{S}}^{(i)}\right)^2\chi^{(i)} &= 0.
\end{aligned}\tag{2.8}$$

The boundary and continuity conditions (see Eq. (2.2)) of the problem in terms of dimensionless variables and parameters are as follows:

$$\begin{aligned}
&\sigma_{zz}^{(1)} = \sigma_{zy}^{(1)} = \sigma_{zx}^{(1)} = 0, && z = 0,\\
&\sigma_{r_1 r_1}^{(2)} = \sigma_{r_1 \theta_1}^{(2)} = \sigma_{r_1 x_1}^{(2)} = 0, && r_1 = R_{\mathrm{i}},\\
&u_{r_1}^{(1)} = u_{r_1}^{(2)}, \quad u_{\theta_1}^{(1)} = u_{\theta_1}^{(2)}, \quad u_{x_1}^{(1)} = u_{x_1}^{(2)}, && r_1 = R_{\mathrm{o}},\\
&\sigma_{r_1 r_1}^{(1)} = \sigma_{r_1 r_1}^{(2)}, \sigma_{r_1 \theta_1}^{(1)} = \sigma_{r_1 \theta_1}^{(2)}, \sigma_{r_1 x_1}^{(1)} = \sigma_{r_1 x_1}^{(2)}, && r_1 = R_{\mathrm{o}}.
\end{aligned} \tag{2.9}$$

Based on the dimensionless Helmholtz decomposition $\mathbf{u}^{(i)} = \nabla \phi^{(i)} + \nabla \times \mathbf{\Psi}^{(i)}$ and the definition of the vector potential (see Eq. (2.5)), the displacement components can be expressed in terms of the three dimensionless scalar potentials $\phi^{(i)}$, $\psi^{(i)}$ and $\chi^{(i)}$:

$$\begin{aligned}
u_y^{(i)} &= \frac{\partial \phi^{(i)}}{\partial y} + \frac{\partial \psi^{(i)}}{\partial z} + \frac{1}{k_{\mathrm{S}}^{(i)}} \frac{\partial^2 \chi^{(i)}}{\partial x \partial y},\\
u_z^{(i)} &= \frac{\partial \phi^{(i)}}{\partial z} - \frac{\partial \psi^{(i)}}{\partial y} + \frac{1}{k_{\mathrm{S}}^{(i)}} \frac{\partial^2 \chi^{(i)}}{\partial x \partial z},\\
u_x^{(i)} &= \frac{\partial \phi^{(i)}}{\partial x} + \frac{1}{k_{\mathrm{S}}^{(i)}} \left(\left(k_{\mathrm{S}}^{(i)} \right)^2 \chi^{(i)} + \frac{\partial^2 \chi^{(i)}}{\partial x^2} \right).
\end{aligned} \tag{2.10}$$

The 3D problem is reduced to a 2D one by letting $\partial/\partial x = 0$ (i.e., $k_x^{(1)} = 0$, $k_x^{(1)}$ is introduced later, in Eq. (2.13)), corresponding to the case when $\theta_{\mathrm{h}} = 90^{\circ}$ or $\theta_{\mathrm{v}} = 0^{\circ}$. From the displacement expressions shown in Eq. (2.10), we observe that the scalar potential $\psi^{(i)}$ in the 2D case is related to the well-known SV wave because $\psi^{(i)}$ only contributes to motions ($u_y^{(i)}$ and $u_z^{(i)}$) in the vertical plane (y, z); on the contrary, the other scalar potential $\chi^{(i)}$ is related to the SH wave because $\chi^{(i)}$ only contributes to the horizontally polarized out-of-plane motion $u_x^{(i)}$. Therefore, the 3D problem is reduced to decoupled 2D plane-strain (P-SV) and 2D anti-plane (SH) problems when $\partial/\partial x = 0$. However, in the 3D case, we cannot uniquely relate the potentials $\psi^{(i)}$ and $\chi^{(i)}$ to SV and SH waves, respectively, although $\psi^{(i)}$ still only contributes to motions in the (y, z)-plane for the 3D case (while the associated wave generally propagates in all directions).

The Cartesian stress components in terms of potentials can be easily obtained using the well-known Hooke's law [Graff, 1975]. The cylindrical displacement and stress components in terms of potentials could be derived in a similar way as demonstrated above (i.e., derived in Cartesian coordinates; see Eq. (2.10)). To do that, one would need to consider the gradient vector, the Laplace operator and the displacement vector in cylindrical coordinates (i.e., $\nabla = \left(\partial_r, (1/r)\,\partial_\theta, \partial_x\right)^{\mathrm{T}}$, $\nabla^2 = \partial_r^2 + (1/r)\,\partial_r + \left(1/r^2\right)\partial_\theta^2 + \partial_x^2$, $\mathbf{u}^{(i)} = \left(u_r^{(i)}, u_\theta^{(i)}, u_x^{(i)}\right)^{\mathrm{T}}$) instead of those in Cartesian coordinates shown in Section 2.2.1. As an alternative, we derive the cylindrical displacement and stress expressions by transforming the ones in Cartesian coordinates using the following relations for the displacement vector **u** and stress tensor $\boldsymbol{\sigma}$, respectively:

$$\begin{bmatrix} u_r \\ u_\theta \\ u_x \end{bmatrix} = \mathbf{T} \begin{bmatrix} u_y \\ u_z \\ u_x \end{bmatrix}, \ \mathbf{T} = \begin{bmatrix} \cos(\theta) & \sin(\theta) & 0 \\ -\sin(\theta) & \cos(\theta) & 0 \\ 0 & 0 & 1 \end{bmatrix}, \tag{2.11}$$

$$\begin{bmatrix} \sigma_{rr} & \sigma_{r\theta} & \sigma_{rx} \\ \sigma_{\theta r} & \sigma_{\theta\theta} & \sigma_{\theta x} \\ \sigma_{xr} & \sigma_{x\theta} & \sigma_{xx} \end{bmatrix} = \mathbf{T} \begin{bmatrix} \sigma_{yy} & \sigma_{yz} & \sigma_{yx} \\ \sigma_{zy} & \sigma_{zz} & \sigma_{zx} \\ \sigma_{xy} & \sigma_{xz} & \sigma_{xx} \end{bmatrix} \mathbf{T}^{\mathrm{T}}, \tag{2.12}$$

where the superscript "(i)" is omitted for brevity, the cylindrical coordinate system (r, θ, x) is defined based on $y = r\cos(\theta)$ and $z = r\sin(\theta)$, $\mathbf{T}$ is the transformation matrix, and $\mathbf{T}^{\mathrm{T}}$ is its transpose.

2.3. SOLUTIONS OF THE GOVERNING EQUATIONS

In this section, we aim to solve the governing equations specified in Eq. (2.8). These Helmholtz equations can be solved using the method of separation of variables in the Cartesian and cylindrical coordinate systems separately [Kausel, 2006]. The solutions are used to construct the complete wave field in the system [Graff, 1975].

2.3.1. INCIDENT AND REFLECTED PLANE WAVES

Our ultimate goal is to solve the dynamic problem shown in Fig. 2.1. As the problem of interest is linear, we first consider a submodel which is a half-space without a tunnel, subject to seismic excitations, and find the wave field in the half-space based on the stress-free boundary conditions at the free surface. Then, we add the embedded tunnel in the half-space, and find the additional wave field due to the presence of the tunnel; for this model the excitation is the response calculated in the previous submodel at the factitious tunnel-soil interface. The sum of the two wave fields obtained in both models form the total wave field.

Thus, considering first a half-space without the underground structure, we have harmonic plane waves as the solutions to Eq. (2.8). Reflected waves are generated when the incident wave meets the free surface of the half-space, and propagate away from the free surface. The sum of the incident and reflected plane waves form the wave field in the half-space. Three cases will be discussed in this subsection: incident compressional ($\phi^{(1)}_{\mathrm{inc}}$) and shear ($\psi^{(1)}_{\mathrm{inc}}$ and $\chi^{(1)}_{\mathrm{inc}}$) waves, where the subscript "inc" indicates the incident wave.

Case 1: Incident compressional wave. The plane-wave solutions for the incident ($\phi^{(1)}_{\mathrm{inc}}$) and reflected waves ($\phi^{(1)}_{\mathrm{ref}}$, $\psi^{(1)}_{\mathrm{ref}}$, $\chi^{(1)}_{\mathrm{ref}}$) are given as

$$\begin{aligned}
\phi^{(1)}_{\mathrm{inc}} &= \phi_0 \exp\left(-\mathrm{i}\,k^{(1)}_x x - \mathrm{i}\,k^{(1)}_y y - \mathrm{i}\,k^{(1)}_{z,\mathrm{P}} z\right), \\
\phi^{(1)}_{\mathrm{ref}} &= R_{\phi,\phi}\phi_0 \exp\left(-\mathrm{i}\,k^{(1)}_x x - \mathrm{i}\,k^{(1)}_y y + \mathrm{i}\,k^{(1)}_{z,\mathrm{P}} z\right), \\
\psi^{(1)}_{\mathrm{ref}} &= R_{\psi,\phi}\phi_0 \exp\left(-\mathrm{i}\,k^{(1)}_x x - \mathrm{i}\,k^{(1)}_y y + \mathrm{i}\,k^{(1)}_{z,\mathrm{S}} z\right), \\
\chi^{(1)}_{\mathrm{ref}} &= R_{\chi,\phi}\phi_0 \exp\left(-\mathrm{i}\,k^{(1)}_x x - \mathrm{i}\,k^{(1)}_y y + \mathrm{i}\,k^{(1)}_{z,\mathrm{S}} z\right),
\end{aligned} \tag{2.13}$$

where the subscript "ref" indicates the reflected wave; ϕ_0 is the amplitude of the incident compressional wave, $R_{\phi,\phi}$, $R_{\psi,\phi}$ and $R_{\chi,\phi}$ (given in Appendix A) are amplitude ratios of the reflected waves $\phi^{(1)}_{\text{ref}}$, $\psi^{(1)}_{\text{ref}}$ and $\chi^{(1)}_{\text{ref}}$, to the incident compressional wave $\phi^{(1)}_{\text{inc}}$, respectively. The wavenumbers $k^{(1)}_x$ and $k^{(1)}_y$ in the x and y directions are written as

$$k^{(1)}_x = k^{(1)}_{x,\text{P}} = -k^{(1)}_{\text{P}} \sin\left(\theta_{\text{v}}\right)\cos\left(\theta_{\text{h}}\right),\ k^{(1)}_y = k^{(1)}_{y,\text{P}} = k^{(1)}_{\text{P}} \sin\left(\theta_{\text{v}}\right)\sin\left(\theta_{\text{h}}\right). \tag{2.14}$$

The wavenumbers $k^{(1)}_{z,\text{P}}$ and $k^{(1)}_{z,\text{S}}$ in the z direction for compressional and shear waves in the soil medium are given as

$$k^{(1)}_{z,\text{P}} = \sqrt{\left(k^{(1)}_{\text{P}}\right)^2 - \left(k^{(1)}\right)^2},\ k^{(1)}_{z,\text{S}} = \sqrt{\left(k^{(1)}_{\text{S}}\right)^2 - \left(k^{(1)}\right)^2}, \tag{2.15}$$

where $\text{Re}\left(k^{(1)}_{z,\text{P}}\right) > 0$ and $\text{Re}\left(k^{(1)}_{z,\text{S}}\right) > 0$ are taken for propagating waves (assuming $\omega > 0$). Furthermore, the total wavenumber $k^{(1)}$ in the horizontal plane (x, y) is defined as

$$k^{(1)} = \sqrt{\left(k^{(1)}_x\right)^2 + \left(k^{(1)}_y\right)^2}. \tag{2.16}$$

According to Snell's law for elastic waves [Achenbach, 1973], the wavenumbers in the x direction of the reflected compressional and shear waves are the same (equal to that of the incident wave), that is, $k^{(1)}_{x,\text{P}} = k^{(1)}_{x,\text{S}} = k^{(1)}_x$, as well as the wavenumbers in the y direction, that is, $k^{(1)}_{y,\text{P}} = k^{(1)}_{y,\text{S}} = k^{(1)}_y$.

Case 2: Incident shear wave type ψ. The plane-wave solutions for the incident ($\psi^{(1)}_{\text{inc}}$) and reflected waves ($\phi^{(1)}_{\text{ref}}$, $\psi^{(1)}_{\text{ref}}$, $\chi^{(1)}_{\text{ref}}$) are given as

$$\begin{aligned}
\psi^{(1)}_{\text{inc}} &= \psi_0 \exp\left(-\text{i}\,k^{(1)}_x x - \text{i}\,k^{(1)}_y y - \text{i}\,k^{(1)}_{z,\text{S}} z\right),\\
\phi^{(1)}_{\text{ref}} &= R_{\phi,\psi}\psi_0 \exp\left(-\text{i}\,k^{(1)}_x x - \text{i}\,k^{(1)}_y y + \text{i}\,k^{(1)}_{z,\text{P}} z\right),\\
\psi^{(1)}_{\text{ref}} &= R_{\psi,\psi}\psi_0 \exp\left(-\text{i}\,k^{(1)}_x x - \text{i}\,k^{(1)}_y y + \text{i}\,k^{(1)}_{z,\text{S}} z\right),\\
\chi^{(1)}_{\text{ref}} &= R_{\chi,\psi}\psi_0 \exp\left(-\text{i}\,k^{(1)}_x x - \text{i}\,k^{(1)}_y y + \text{i}\,k^{(1)}_{z,\text{S}} z\right),
\end{aligned} \tag{2.17}$$

where ψ_0 is the amplitude of the incident shear wave; $R_{\phi,\psi}$, $R_{\psi,\psi}$ and $R_{\chi,\psi}$ (given in Appendix A) are amplitude ratios of the reflected waves $\phi^{(1)}_{\text{ref}}$, $\psi^{(1)}_{\text{ref}}$ and $\chi^{(1)}_{\text{ref}}$, to the incident shear wave $\psi^{(1)}_{\text{inc}}$, respectively. The wavenumbers in the x and y directions in this case are given as

$$k^{(1)}_x = k^{(1)}_{x,\text{S}} = -k^{(1)}_{\text{S}} \sin\left(\theta_{\text{v}}\right)\cos\left(\theta_{\text{h}}\right),\ k^{(1)}_y = k^{(1)}_{y,\text{S}} = k^{(1)}_{\text{S}} \sin\left(\theta_{\text{v}}\right)\sin\left(\theta_{\text{h}}\right). \tag{2.18}$$

Here, it is noted that under the incident shear waves ($\psi^{(1)}_{\text{inc}}$ and $\chi^{(1)}_{\text{inc}}$) there exists a critical vertical incident angle, beyond which the wavenumber $k^{(1)}_{z,\text{P}}$ becomes imaginary (see Eqs. (2.15) and (2.18)). This occurs when $k^{(1)}_{\text{P}} < k^{(1)} = k^{(1)}_{\text{S}} \sin(\theta_{\text{v}})$. Therefore, the critical vertical angle is defined as

$$\theta^{\text{crit}}_{\text{v}} = \arcsin\left(\frac{k^{(1)}_{\text{P}}}{k^{(1)}_{\text{S}}}\right) = \arcsin\left(\sqrt{\frac{1-2\nu^{(1)}}{2-2\nu^{(1)}}}\right). \tag{2.19}$$

Evanescent waves are generated when $\theta_{\mathrm{v}} > \theta_{\mathrm{v}}^{\mathrm{crit}}$, and for those waves it is required that $\mathrm{Im}\left(k_{z,\mathrm{P}}^{(1)}\right) < 0$.

Case 3: Incident shear wave type χ. The plane-wave solutions for the incident ($\chi_{\mathrm{inc}}^{(1)}$) and reflected waves ($\phi_{\mathrm{ref}}^{(1)}$, $\psi_{\mathrm{ref}}^{(1)}$, $\chi_{\mathrm{ref}}^{(1)}$) are given as

$$
\begin{aligned}
\chi_{\mathrm{inc}}^{(1)} &= \chi_0 \exp\left(-\mathrm{i}\, k_x^{(1)} x - \mathrm{i}\, k_y^{(1)} y - \mathrm{i}\, k_{z,\mathrm{S}}^{(1)} z\right), \\
\phi_{\mathrm{ref}}^{(1)} &= R_{\phi,\chi} \chi_0 \exp\left(-\mathrm{i}\, k_x^{(1)} x - \mathrm{i}\, k_y^{(1)} y + \mathrm{i}\, k_{z,\mathrm{P}}^{(1)} z\right), \\
\psi_{\mathrm{ref}}^{(1)} &= R_{\psi,\chi} \chi_0 \exp\left(-\mathrm{i}\, k_x^{(1)} x - \mathrm{i}\, k_y^{(1)} y + \mathrm{i}\, k_{z,\mathrm{S}}^{(1)} z\right), \\
\chi_{\mathrm{ref}}^{(1)} &= R_{\chi,\chi} \chi_0 \exp\left(-\mathrm{i}\, k_x^{(1)} x - \mathrm{i}\, k_y^{(1)} y + \mathrm{i}\, k_{z,\mathrm{S}}^{(1)} z\right),
\end{aligned}
\tag{2.20}
$$

where χ_0 is the amplitude of the incident shear wave; $R_{\phi,\chi}$, $R_{\psi,\chi}$ and $R_{\chi,\chi}$ (given in Appendix A) are amplitude ratios of the reflected waves $\phi_{\mathrm{ref}}^{(1)}$, $\psi_{\mathrm{ref}}^{(1)}$ and $\chi_{\mathrm{ref}}^{(1)}$, to the incident shear wave $\chi_{\mathrm{inc}}^{(1)}$, respectively. The wavenumbers in the x and y directions in this case are the same as that in case 2; see Eq. (2.18).

2.3.2. SCATTERING OF ELASTIC WAVES BY THE TUNNEL

The presence of the infinitely long cylindrical tunnel causes scattering of elastic waves. These scattered waves are denoted as $\phi_{\mathrm{s},1}^{(1)}$, $\psi_{\mathrm{s},1}^{(1)}$ and $\chi_{\mathrm{s},1}^{(1)}$. The subscript “s, 1" indicates the ‘directly scattered’ waves propagating away from the tunnel in the half-space. When these directly scattered waves meet the free surface of the half-space, secondary scattered waves are generated, which are denoted as $\phi_{\mathrm{s},2}^{(1)}$, $\psi_{\mathrm{s},2}^{(1)}$ and $\chi_{\mathrm{s},2}^{(1)}$. The subscript “s, 2" indicates the ‘secondary scattered’ waves. Based on the spirit of the method of images, these secondary scattered waves are considered to originate from an image source, but the intensity is a priori unknown. The image source is located at the centre of the image of the tunnel, positioned symmetrically with respect to the free surface.

To describe the waves propagating away from the tunnel and its image, we apply the method of separation of variables to solve the Helmholtz equations shown in Eq. (2.8), assuming a harmonic variation in the circumferential direction of the form $\exp(\mathrm{i}\, n\theta)$ [Graff, 1975; Kausel, 2006]. To satisfy the continuity condition at $\theta = 0$ and $\theta = 2\pi$, n is required to be an integer. It turns out that, for fixed n, the radial behaviour is described by a Hankel function. The general solution is then constructed as an infinite series (that is commonly referred to as a wave-function expansion), which represents the entire scattered wave field. The potentials related to the scattered wave fields in the half-space are given as follows:

$$
\begin{aligned}
\phi_{\mathrm{s},1}^{(1)} &= \sum_{n=-\infty}^{\infty} a_n H_n^{(2)}\left(k_{\mathrm{a}}^{(1)} r_1\right)\exp\left(\mathrm{i}n\theta_1 - \mathrm{i}k_x^{(1)}x\right),\\
\psi_{\mathrm{s},1}^{(1)} &= \sum_{n=-\infty}^{\infty} b_n H_n^{(2)}\left(k_{\mathrm{b}}^{(1)} r_1\right)\exp\left(\mathrm{i}n\theta_1 - \mathrm{i}k_x^{(1)}x\right),\\
\chi_{\mathrm{s},1}^{(1)} &= \sum_{n=-\infty}^{\infty} c_n H_n^{(2)}\left(k_{\mathrm{b}}^{(1)} r_1\right)\exp\left(\mathrm{i}n\theta_1 - \mathrm{i}k_x^{(1)}x\right),\\
\phi_{\mathrm{s},2}^{(1)} &= \sum_{n=-\infty}^{\infty} d_n H_n^{(2)}\left(k_{\mathrm{a}}^{(1)} r_2\right)\exp\left(\mathrm{i}n\theta_2 - \mathrm{i}k_x^{(1)}x\right),\\
\psi_{\mathrm{s},2}^{(1)} &= \sum_{n=-\infty}^{\infty} e_n H_n^{(2)}\left(k_{\mathrm{b}}^{(1)} r_2\right)\exp\left(\mathrm{i}n\theta_2 - \mathrm{i}k_x^{(1)}x\right),\\
\chi_{\mathrm{s},2}^{(1)} &= \sum_{n=-\infty}^{\infty} f_n H_n^{(2)}\left(k_{\mathrm{b}}^{(1)} r_2\right)\exp\left(\mathrm{i}n\theta_2 - \mathrm{i}k_x^{(1)}x\right),
\end{aligned}
\tag{2.21}
$$

where $a_n, ..., f_n$ denote the unknown coefficients which will be determined from the boundary and interface conditions, and $H_n^{(2)}(..)$ denotes the Hankel function of the second kind and n-th order, and represents outgoing waves (propagating away from the tunnel) considering the time dependent factor $\mathrm{e}^{+\mathrm{i}\omega t}$. $k_{\mathrm{a}}^{(1)}$ and $k_{\mathrm{b}}^{(1)}$ are the cylindrical wavenumbers of the compressional and shear waves in the soil, respectively:

$$
k_{\mathrm{a}}^{(1)} = \sqrt{\left(k_{\mathrm{P}}^{(1)}\right)^2 - \left(k_x^{(1)}\right)^2},\ k_{\mathrm{b}}^{(1)} = \sqrt{\left(k_{\mathrm{S}}^{(1)}\right)^2 - \left(k_x^{(1)}\right)^2},
\tag{2.22}
$$

where $\mathrm{Re}(k_{\mathrm{a}}^{(1)}) > 0$ and $\mathrm{Re}(k_{\mathrm{b}}^{(1)}) > 0$ are taken for the propagating cylindrical waves in the soil (assuming $\omega > 0$), while $\mathrm{Im}(k_{\mathrm{a}}^{(1)}) < 0$ is taken for the evanescent cylindrical waves. Note that cylindrical S waves in the soil never become evanescent because $k_{\mathrm{b}}^{(1)}$ is real valued as $k_{\mathrm{S}}^{(1)}$ is always larger than $k_x^{(1)}$.

The potentials related to refracted waves in the tunnel are constructed using Bessel functions, and are given as

$$
\begin{aligned}
\phi_{\mathrm{r}}^{(2)} &= \sum_{n=-\infty}^{\infty} \left[g_n J_n\left(k_{\mathrm{a}}^{(2)} r_1\right) + h_n Y_n\left(k_{\mathrm{a}}^{(2)} r_1\right)\right]\exp\left(\mathrm{i}n\theta_1 - \mathrm{i}k_x^{(2)}x\right),\\
\psi_{\mathrm{r}}^{(2)} &= \sum_{n=-\infty}^{\infty} \left[i_n J_n\left(k_{\mathrm{b}}^{(2)} r_1\right) + j_n Y_n\left(k_{\mathrm{b}}^{(2)} r_1\right)\right]\exp\left(\mathrm{i}n\theta_1 - \mathrm{i}k_x^{(2)}x\right),\\
\chi_{\mathrm{r}}^{(2)} &= \sum_{n=-\infty}^{\infty} \left[k_n J_n\left(k_{\mathrm{b}}^{(2)} r_1\right) + l_n Y_n\left(k_{\mathrm{b}}^{(2)} r_1\right)\right]\exp\left(\mathrm{i}n\theta_1 - \mathrm{i}k_x^{(2)}x\right),
\end{aligned}
\tag{2.23}
$$

where $g_n, ..., l_n$ denote the unknown coefficients; $J_n(..)$ and $Y_n(..)$ denote the Bessel functions of the first and second kind, respectively, and n-th order. $k_{\mathrm{a}}^{(2)}$ and $k_{\mathrm{b}}^{(2)}$ are the wavenumbers of the compressional and shear cylindrical waves in the tunnel, respectively:

$$
k_{\mathrm{a}}^{(2)} = \sqrt{\left(k_{\mathrm{P}}^{(2)}\right)^2 - \left(k_x^{(2)}\right)^2},\ k_{\mathrm{b}}^{(2)} = \sqrt{\left(k_{\mathrm{S}}^{(2)}\right)^2 - \left(k_x^{(2)}\right)^2},
\tag{2.24}
$$

The longitudinal wavenumber $k_x^{(2)}$ of the refracted waves is equal to $k_x^{(1)}$ according to Snell's law. Note that here we use Bessel functions to represent the cylindrical waves in the tunnel. Alternatively, we could use the Hankel functions of the first and second kind ($H_n^{(1)}$ and $H_n^{(2)}$) to represent the cylindrical ingoing and outgoing waves in the tunnel, like in Liu *et al.* [2013]. Mathematically, both representations of the waves in the tunnel are correct. However, it is found that the numerical results obtained by using Bessel functions are more accurate; see Sections 2.7.2 and 2.8.2.

2.3.3. TOTAL WAVE FIELDS

The incident and reflected plane waves together with the directly and secondary scattered cylindrical waves make up the total wave field in the half-space ($\phi^{(1)}$, $\psi^{(1)}$ and $\chi^{(1)}$):

$$\begin{aligned}\phi^{(1)} &= \phi^{(1)}_{\text{inc}} + \phi^{(1)}_{\text{ref}} + \phi^{(1)}_{\text{s},1} + \phi^{(1)}_{\text{s},2},\\ \psi^{(1)} &= \psi^{(1)}_{\text{inc}} + \psi^{(1)}_{\text{ref}} + \psi^{(1)}_{\text{s},1} + \psi^{(1)}_{\text{s},2},\\ \chi^{(1)} &= \chi^{(1)}_{\text{inc}} + \chi^{(1)}_{\text{ref}} + \chi^{(1)}_{\text{s},1} + \chi^{(1)}_{\text{s},2}.\end{aligned} \tag{2.25}$$

The total wave field in the tunnel consists of the refracted waves ($\phi^{(2)}$, $\psi^{(2)}$ and $\chi^{(2)}$):

$$\phi^{(2)} = \phi^{(2)}_{\text{r}},\ \psi^{(2)} = \psi^{(2)}_{\text{r}},\ \chi^{(2)} = \chi^{(2)}_{\text{r}}. \tag{2.26}$$

2.4. STRESS AND DISPLACEMENT EXPRESSIONS IN TERMS OF COMPLEX VARIABLES

To employ the complex-variable theory for determining the unknown coefficients in Eqs. (2.21) and (2.23), we introduce a complex variable $\kappa = y + \mathrm{i}z = r\mathrm{e}^{\mathrm{i}\theta}$ and its conjugate $\bar{\kappa} = y - \mathrm{i}z = r\mathrm{e}^{-\mathrm{i}\theta}$, where y, z and r, θ are the dimensionless Cartesian and cylindrical coordinates in the vertical plane, respectively, as introduced in Section 2.2. In line with the introduction of the image source, the local coordinate systems (y_1, z_1, x_1) and (y_2, z_2, x_2) are defined symmetrically with respect to the free surface of the half-space, with z_2 positive downward (see Fig. 2.1). The local coordinates r_1 and r_2 can be written in terms of complex variables κ and $\bar{\kappa}$ related to the global coordinate system using the relation between different coordinates:

$$\begin{aligned} r_1 &= |y_1 + \mathrm{i}z_1| = |y + \mathrm{i}(z + H)| = |\kappa + \mathrm{i}H|,\\ r_2 &= |y_2 + \mathrm{i}z_2| = |y + \mathrm{i}(-z + H)| = |\bar{\kappa} + \mathrm{i}H|.\end{aligned} \tag{2.27}$$

The exponential terms of the local coordinates θ_1 and θ_2, showing up in Eqs. (2.21) and (2.23), can also be written in terms of the complex variables κ and $\bar{\kappa}$ as

$$\mathrm{e}^{\mathrm{i}\theta_1} = \frac{y_1 + \mathrm{i}z_1}{r_1} = \frac{\kappa + \mathrm{i}H}{|\kappa + \mathrm{i}H|},\ \mathrm{e}^{\mathrm{i}\theta_2} = \frac{y_2 + \mathrm{i}z_2}{r_2} = \frac{\bar{\kappa} + \mathrm{i}H}{|\bar{\kappa} + \mathrm{i}H|}. \tag{2.28}$$

Substituting Eqs. (2.27) and (2.28) into the expressions for the potentials (see Eqs. (2.21) and (2.23)), we get the potentials in terms of the complex variables κ and $\bar{\kappa}$, which are not shown in this thesis for brevity.

Thereafter, the displacement (see Eq. (2.10)) and stress components in the Cartesian coordinates (y, z, x) can also be expressed in terms of the complex variables κ and $\bar{\kappa}$, and they are shown in Eqs. (B.1)-(B.9) in Appendix B. The expressions for the displacements and stresses in the cylindrical coordinate system (r,θ,x) can be derived in terms of the complex variables κ and $\bar{\kappa}$ as well by employing the transformation relations (see Eqs. (2.11)-(2.12)), and they are shown in Eqs. (B.10)-(B.16).

2.5. CONFORMAL MAPPING

As shown in Fig. 2.1, there are two different types of boundary surfaces in the model (i.e., a flat free surface and cylindrical surfaces of the tunnel). This makes the boundary value problem difficult to solve. In this chapter, we propose to use conformal mapping functions to circumvent this difficulty by mapping the original domain with boundary surfaces of two different types onto an image domain with boundary surfaces of the same type. The application of conformal mapping functions is demonstrated in this section.

We have introduced the complex variable κ and its conjugate $\bar{\kappa}$ in the original physical domain in Section 2.4. Here, we introduce a complex variable $\zeta = \xi + \mathrm{i}\eta = \rho \mathrm{e}^{\mathrm{i}\vartheta}$ and its conjugate $\bar{\zeta} = \xi - \mathrm{i}\eta = \rho \mathrm{e}^{-\mathrm{i}\vartheta}$, which are defined in the image domain. Two conformal mapping functions $w^{(1)}(\zeta)$ and $w^{(2)}(\zeta)$, one for the region of the half-space with a cavity and one for the tunnel region, defining the relations between the two complex variables κ and ζ in the original and image domains, are given as follows:

$$\kappa^{(1)} = w^{(1)}(\zeta) = -\mathrm{i}G\frac{1+\zeta}{1-\zeta}, \tag{2.29}$$

$$\kappa^{(2)} = w^{(2)}(\zeta) = -\mathrm{i}H + \frac{R_\mathrm{o}}{\beta_\mathrm{o}}\zeta, \tag{2.30}$$

where $G = H\left(1-\beta_\mathrm{o}^2\right)/\left(1+\beta_\mathrm{o}^2\right)$ and $\beta_\mathrm{o} = H/R_\mathrm{o} - \sqrt{\left(H/R_\mathrm{o}\right)^2 - 1}$. Using these two mapping functions, the two regions Ω_1 and Ω_2 in the physical domain (as shown in Fig. 2.1) are mapped onto two regions Γ_1 and Γ_2 in the image domain (as shown in Fig. 2.3), respectively. Accordingly, the free surface of the half-space $z = 0$, the outer surface $r_1 = R_\mathrm{o}$ and inner surface $r_1 = R_\mathrm{i}$ of the tunnel correspond to surfaces defined by circles $|\zeta| = 1$, $|\zeta| = \beta_\mathrm{o}$ and $|\zeta| = \beta_\mathrm{i} = \beta_\mathrm{o}R_\mathrm{i}/R_\mathrm{o}$. Clearly, the boundary surfaces in the image domain are of the same type.

The mappings of the regions Ω_1 and Ω_2 in the physical domain onto regions Γ_1 and Γ_2 in the image domain are conformal and reversible. It can be easily proven that the mapping functions $w^{(1)}(\zeta)$ and $w^{(2)}(\zeta)$ are analytic (except at one point $(\rho = 1, \vartheta = 0)$ corresponding to points at infinity in the physical domain), and their derivatives with respect to the complex variable ζ (i.e., $w^{(1)\prime}(\zeta)$ and $w^{(2)\prime}(\zeta)$) are nonzero.

In general, the mapping functions induce a phase change between the complex variables in the two domains. For a general conformal mapping function $\kappa = w(\zeta)$, the relation between the coordinate θ in the physical domain and the coordinate ϑ in the image domain is defined as [Muskhelishvili, 1966]

$$\exp(\mathrm{i}\theta) = \frac{\zeta}{\rho}\frac{w'(\zeta)}{|w'(\zeta)|} = \exp(\mathrm{i}\vartheta)\frac{w'(\zeta)}{|w'(\zeta)|}. \tag{2.31}$$

The first conformal mapping function $w^{(1)}(\zeta)$ indeed induces a phase change because $w^{(1)\prime}(\zeta)$ is a complex number. On the contrary, the second mapping function $w^{(2)}(\zeta)$

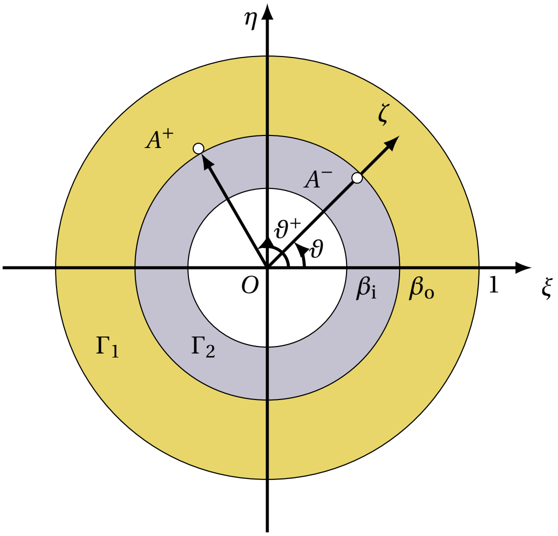

Figure 2.3: Image domain.

does not induce a phase change because the $w^{(2)\prime}(\zeta)$ is a constant (i.e., $\frac{w'(\zeta)}{|w'(\zeta)|} = 1, \exp(\mathrm{i}\theta) = \exp(\mathrm{i}\vartheta)$; see Eq. (2.31)). As a consequence, point A at the tunnel-soil interface (see Fig. 2.1) is mapped onto two different points A^+ and A^- (as shown in Fig. 2.3) using mapping functions $w^{(1)}(\zeta)$ and $w^{(2)}(\zeta)$, respectively. When we apply the continuity conditions at the tunnel-soil interface (see Section 2.6), we need to take this issue into account. Let ϑ^+ and ϑ denote the arguments of the vectors $\overrightarrow{OA^+}$ and $\overrightarrow{OA^-}$ in the image domain, respectively. The relation between these two angles can be derived using $\kappa^{(1)} = \kappa^{(2)}$:

$$-\mathrm{i}G\frac{1+\beta_\mathrm{o}\mathrm{e}^{\mathrm{i}\vartheta^+}}{1-\beta_\mathrm{o}\mathrm{e}^{\mathrm{i}\vartheta^+}} = -\mathrm{i}H + \frac{R_\mathrm{o}}{\beta_\mathrm{o}}\beta_\mathrm{o}\mathrm{e}^{\mathrm{i}\vartheta}, \tag{2.32}$$

and is given as

$$\vartheta^+(\vartheta) = \arg\left[\frac{\mathrm{i}R_\mathrm{o}\mathrm{e}^{\mathrm{i}\vartheta} + H - G}{\mathrm{i}R_\mathrm{o}\mathrm{e}^{\mathrm{i}\vartheta} + H + G}\right]. \tag{2.33}$$

2.6. SOLVING THE UNKNOWN COEFFICIENTS

As shown in Section 2.4, the potentials, displacements and stresses are written in terms of complex variables κ and $\bar{\kappa}$. The derivatives of potentials related to the plane waves with respect to κ and $\bar{\kappa}$ can be obtained by simply applying the chain rule (i.e., first with respect to y and z, and then to κ and $\bar{\kappa}$), and the derivatives of potentials related to cylindrical waves with respect to the complex variables can be derived using both the chain rule and the recurrence relations of Hankel/Bessel functions (see Appendix C).

To solve the problem in the image domain where the boundary surfaces are of the same type, we need to get the expressions for displacements and stresses in terms of the complex variables ζ and $\bar{\zeta}$. Applying the derivatives of potentials with respect to κ and $\bar{\kappa}$

and then replacing the complex variables κ and $\bar{\kappa}$ by the appropriate mapping function (see Eqs. (2.29) and (2.30)) and their conjugates, we can get the potentials, displacements and stresses written in terms of ζ and $\bar{\zeta}$; they are not shown in this chapter for brevity.

Considering the total wave field in the half-space and tunnel (see Eqs. (2.25) and (2.26)), and using the expressions for displacements and stresses in terms of complex variables ζ and $\bar{\zeta}$, we obtain a set of algebraic equations based on the boundary and continuity conditions (see Eq. (2.9)):

$$\sum_{i=1}^{12}\sum_{n=-\infty}^{\infty} k_n^{(j,i)}(\vartheta)x_n^{(i)} = b^{(j)}(\vartheta), \tag{2.34}$$

where $x_n^{(1)} = a_n$, ..., $x_n^{(12)} = l_n$; $i = \{1,...,12\}$ indicates the term related to the corresponding potentials of cylindrical waves; see Eqs. (2.21) and (2.23). $j = \{1,...,12\}$ denotes the specific boundary condition: $j = \{1,2,3\}$ and $j = \{4,5,6\}$ refer to the stress-free boundary conditions at the half-space surface and at the inner surface of the tunnel, respectively; $j = \{7,...,12\}$ refer to the continuity conditions at the tunnel-soil interface; see Eq. (2.9). Not all the entries of $k_n^{(j,i)}$ and $b^{(j)}$ are presented in this thesis, but they are understood as functions of complex variables ζ and $\bar{\zeta}$. For the aim of demonstration, we present the entries of $k_n^{(j,i)}$ and $b^{(j)}$ related to the tenth continuity condition (i.e., $\sigma_{r_1\theta_1}^{(1)} = \sigma_{r_1\theta_1}^{(2)}$) in Appendix D. In addition, for the set of algebraic equations ($j = \{7,...,12\}$) formulated based on the continuity conditions, all the displacements and stresses related to the soil medium, namely, $u_{r_1}^{(1)}$, $u_{\theta_1}^{(1)}$, $u_{x_1}^{(1)}$, $\sigma_{r_1r_1}^{(1)}$, $\sigma_{r_1\theta_1}^{(1)}$ and $\sigma_{r_1x_1}^{(1)}$, are functions of $\vartheta^+(\vartheta)$ while those related to the tunnel are functions of ϑ (see also Section 2.5).

Multiplying Eq. (2.34) by the complex conjugate of the circumferential basis functions $\exp(\mathrm{i}\,n\vartheta)$, which appears in the expression for the potentials of the cylindrical waves, integrating over the interval $[0,2\pi]$ and applying the orthogonality relation wherever possible, we get

$$\sum_{i=1}^{12}\sum_{n=-\infty}^{\infty} k_{n,s}^{(j,i)}x_n^{(i)} = b_s^{(j)}, \tag{2.35}$$

where $s = \{0,\pm1,\pm2,...\}$ and

$$k_{n,s}^{(j,i)} = \frac{1}{2\pi}\int_0^{2\pi} k_n^{(j,i)}(\vartheta)\exp(-\mathrm{i}\,s\vartheta)\,\mathrm{d}\vartheta, \tag{2.36}$$

$$b_s^{(j)} = \frac{1}{2\pi}\int_0^{2\pi} b^{(j)}(\vartheta)\exp(-\mathrm{i}\,s\vartheta)\,\mathrm{d}\vartheta. \tag{2.37}$$

For the potentials related to the directly scattered waves in the half-space ($\phi_{\mathrm{s},1}^{(1)}, \psi_{\mathrm{s},1}^{(1)}, \chi_{\mathrm{s},1}^{(1)}$ in Eq. (2.21)) and for the potentials related to the refracted waves in the tunnel (Eq. (2.23)), orthogonality of the exponential functions can be employed (i.e., $k_{n,s}^{(j,i)} = 0$ for $s \neq n$, and $i = \{1,2,3,7,...,12\}$). The maximum values of n and s need to be finite in order to be able to evaluate the unknown coefficients, which means that the sum over circumferential modes needs to be truncated. The amount of modes for refracted waves in the tunnel is $2N+1$ when we consider n from $-N$ to N. If we use the same amount of modes $2N+1$ for both the directly scattered waves ($\phi_{\mathrm{s},1}^{(1)}$, $\psi_{\mathrm{s},1}^{(1)}$, $\chi_{\mathrm{s},1}^{(1)}$) and secondary scattered waves ($\phi_{\mathrm{s},2}^{(1)}$, $\psi_{\mathrm{s},2}^{(1)}$, $\chi_{\mathrm{s},2}^{(1)}$), we use the following multiplication function:

$$\exp(-\mathrm{i}\,s\vartheta),\ j = \{1,...,12\}; s = \{0,\pm1,\pm2,...,\pm N\}. \tag{2.38}$$

The matrix equation that is formulated based on Eq. (2.35) becomes

$$[\mathbf{K}]_{12(2N+1)\times 12(2N+1)}\,[\mathbf{x}]_{12(2N+1)\times 1} = \left[\mathbf{b}\right]_{12(2N+1)\times 1}. \tag{2.39}$$

If we use $2N+1$ modes for the directly scattered waves and $2M+1$ ($M \neq N$) modes for the secondary scattered waves, in order to still formulate a square matrix, different rows in Eq. (2.34) are multiplied by different multiplication functions, respectively, as follows:

$$\begin{aligned}&\exp(-\mathrm{i}\, s_{\mathrm{D}}\vartheta),\ j=\{1,\dots,3\};\, s_{\mathrm{D}}=\{0,\pm1,\pm2,\dots,\pm M\},\\ &\exp(-\mathrm{i}\, s\vartheta),\ \ j=\{4,\dots,12\};\, s=\{0,\pm1,\pm2,\dots,\pm N\},\end{aligned} \tag{2.40}$$

and the matrix equation obtained from Eq. (2.35) reads

$$\begin{aligned}&[\mathbf{K}]_{(9(2N+1)+3(2M+1))\times(9(2N+1)+3(2M+1))}\,[\mathbf{x}]_{(9(2N+1)+3(2M+1))\times 1}\\ &=\left[\mathbf{b}\right]_{(9(2N+1)+3(2M+1))\times 1}.\end{aligned} \tag{2.41}$$

By using different numbers of modes for the directly and secondary scattered waves, we acknowledge their contributions to the final response in the system. It can be shown that, for converged results at the tunnel, more circumferential modes of the directly scattered waves are needed than of the secondary scattered waves (i.e., $N > M$), while for converged results at the ground surface, more circumferential modes of the secondary scattered waves are needed. This is because, due to geometrical attenuation, the potentials have larger contributions to the response in the near field than in the far field. An advantage of using a different number of circumferential modes is that the size and condition of the matrix **K** can be smaller, and the computation time can be reduced.

Matlab is used to solve for the unknown coefficients. The calculation is performed on a laptop with CPU of Intel Core i7 5600U/2.6 GHz. For example, the computation time varies from 15 seconds to 2 minutes depending on the value of N (and M, if different) from 3 to 10, respectively, for a tunnel embedded in a half-space (3D case) using the first set of parameters in Table 2.1. Since the computation is very efficient even when using large values of N and M, the same number of circumferential modes for both wave fields will be used in the following analysis (i.e., we use the multiplication function in Eq. (3.36) instead of the one in Eq. (2.40)).

From the analysis using the proposed method, we find that matrix **K** may have a relatively high condition number. That happens particularly when Hankel functions have small arguments (i.e., when one of the cylindrical wavenumbers $k_{\mathrm{a}}^{(1)}$, $k_{\mathrm{b}}^{(1)}$, $k_{\mathrm{a}}^{(2)}$ and $k_{\mathrm{b}}^{(2)}$ is relatively small, see Eqs. (2.21) and (2.23)), see explanation in Section 2.7.2.

2.7. CONVERGENCE TESTS AND VALIDATIONS

This section presents convergence tests and validations of the present method by comparing with results obtained by other methods. Three categories of comparisons are discussed: 2D anti-plane shear (SH waves), 2D plane-strain (P and SV waves) and 3D cases. Table 2.1 presents the five parameter sets comprising parameters of the soil and tunnel, the geometries of the system and the frequencies of the incident harmonic waves.

In Table 2.1, $\tilde{E}^{(1)}$ and $\tilde{E}^{(2)}$ are the Young's moduli of the soil and tunnel, respectively, $\nu^{(1,2)}$ are the Poisson's ratios, and h is the thickness of the tunnel. $\eta = \tilde{\omega}\tilde{R}_{\mathrm{o}}/\left(\pi\tilde{c}_{\mathrm{S}}^{(1)}\right)$ is the dimensionless frequency used in the literature [de Barros and Luco, 1994], which is different from the dimensionless frequency ω introduced in this chapter (see Eq. (2.7)).

Table 2.1: Five sets of parameters of the system

Parameter sets	Soil parameters	Tunnel parameters	Geometries and frequencies
① Liu et al. Liu *et al.* [1991]	$\tilde{E}^{(1)} = 7.567$ GPa $\nu^{(1)} = 0.333$ $\tilde{\rho}^{(1)} = 2664\ \mathrm{kg/m^3}$	$\tilde{E}^{(2)} = 16$ GPa $\nu^{(2)} = 0.2$ $\tilde{\rho}^{(2)} = 2240\ \mathrm{kg/m^3}$	$H = 5R_\mathrm{i}$ $h = 0.1R_\mathrm{i}$ $\eta = 0.105$
② Lee et al. Lee and Trifunac [1979]	$\tilde{E}^{(1)} = 0.29593$ GPa $\nu^{(1)} = 0.333$ $\tilde{\rho}^{(1)} = 1640\ \mathrm{kg/m^3}$	$\tilde{E}^{(2)} = 0.7992$ GPa $\nu^{(2)} = 0.2$ $\tilde{\rho}^{(2)} = 3 \times \tilde{\rho}^{(1)}$	$H = 1.5R_\mathrm{o}$ $h = 0.1R_\mathrm{o}$ $\eta = 0.5$
③ Balendra et al. Balendra *et al.* [1984]	$\tilde{\mu}^{(1)} = 0.111$ GPa $\tilde{c}_\mathrm{s}^{(1)} = 260$ m/s $\tilde{\rho}^{(1)} = 1640\ \mathrm{kg/m^3}$	$\tilde{\mu}^{(2)} = 8.4$ GPa $\nu^{(2)} = 0.2$ $\tilde{\rho}^{(2)} = 2410\ \mathrm{kg/m^3}$	$H = 2.5R_\mathrm{o}$ $h = 0.1R_\mathrm{o}$ $\eta = 0.245$
④ Datta et al. Datta *et al.* [1984]	$\tilde{E}^{(1)} = 0.69$ Gpa $\nu^{(1)} = 0.45$ $\tilde{\rho}^{(1)} = 2665\ \mathrm{kg/m^3}$	$\tilde{E}^{(2)} = 16$ GPa $\nu^{(2)} = 0.2$ $\tilde{\rho}^{(2)} = 2240\ \mathrm{kg/m^3}$	$H = 8.33R_\mathrm{i}$ $h = 0.1R_\mathrm{i}$ $\eta = 0.132$
⑤ Wong et al. Wong *et al.* [1986a,b]	$\tilde{E}^{(1)} = 0.69$ GPa $\nu^{(1)} = 0.45$ $\tilde{\rho}^{(1)} = 2665\ \mathrm{kg/m^3}$	$\tilde{E}^{(2)} = 16$ GPa $\nu^{(2)} = 0.2$ $\tilde{\rho}^{(2)} = 2240\ \mathrm{kg/m^3}$	$H = 2R_\mathrm{i}$ $h = 0.1R_\mathrm{i}$ $\eta = 0.132$

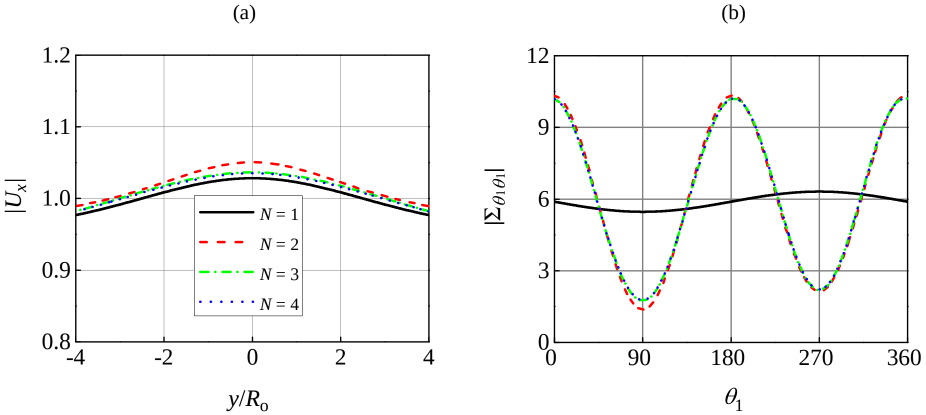

Figure 2.4: Convergence tests: (a) longitudinal displacement U_x at the half-space surface $z = 0$ and (b) hoop stress $\Sigma_{\theta_1\theta_1}$ at $r_1 = R_\mathrm{o}$. The first parameter set in Table 2.1 is used for a 3D problem with an incident P wave, $\theta_\mathrm{v} = 30^\circ$ and $\theta_\mathrm{h} = 0^\circ$.

For results presented in the following, all displacements and stresses are normalised.

The displacement components are normalised by the amplitude of the incident compressional (P) or shear (S) wave:

$$U = u/U_{\{\mathrm{P,S}\}}, \tag{2.42}$$

where u denotes an arbitrary (but corresponding to U) displacement component, and U_P and U_S are the amplitudes of the corresponding incident P and S waves, respectively, which can be derived using Eq. (2.10):

$$\begin{aligned} U_\mathrm{P} &= \mathrm{i}\, k_\mathrm{P}^{(1)} \phi_0, \\ U_\mathrm{S} &= \mathrm{i}\, k_\mathrm{b}^{(1)} \psi_0 \text{ or } U_\mathrm{S} = k_\mathrm{b}^{(1)} \chi_0. \end{aligned} \tag{2.43}$$

The normalised stress is given as

$$\Sigma = \sigma \Big/ \left[\omega \rho^{(1)} c_\mathrm{S}^{(1)} U_{\{\mathrm{P,S}\}}\right], \tag{2.44}$$

where σ denotes an arbitrary (but corresponding to Σ) stress component.

For a 3D problem, a convergence test using the first parameter set in Table 2.1 is shown in Fig. 2.4. The system is subject to an incident P wave ($\eta = 0.105$, $\tilde{f} = 10.84$ Hz). The vertical and horizontal incident angles are $\theta_\mathrm{v} = 30^\circ$ and $\theta_\mathrm{h} = 0^\circ$. It is shown that both the normalised displacement U_x at the half-space surface $z = 0$ and the normalised hoop stress $\Sigma_{\theta_1\theta_1}$ at $r_1 = R_\mathrm{o}$ converge very quickly. It can be verified that for relatively high frequencies, $N = 5$ appears sufficient. All the results in this chapter are obtained using $N = 5$ and employing the representations of cylindrical waves in the tunnel in terms of Bessel functions (see Eq. (2.23)) unless specified otherwise. The remainder of this section is devoted to validations.

2.7.1. 2D ANTI-PLANE SHEAR CASES

This subsection presents the following three comparisons. We consider a problem of a tunnel embedded in a half-space subjected to incident SH waves (i.e., $\chi_\mathrm{inc}^{(1)}$) using the parameter sets in Table 2.1. In the following Figs. 2.5-2.11, the black solid line indicates the present results while the red dashed line indicates the results taken from the literature [1].

The first comparison is made with the results obtained by Lee and Trifunac [1979] for a vertically incident SH wave ($\theta_\mathrm{v} = 0^\circ$ and $\theta_\mathrm{h} = 90^\circ$). The second parameter set in Table 2.1 is used. The longitudinal displacement U_x at the half-space surface $z = 0$, the longitudinal displacement U_{x1} and shear stress $\Sigma_{r_1x_1}$ at the tunnel-soil interface $r_1 = R_\mathrm{o}$, and the shear stress $\Sigma_{\theta_1x_1}$ at the inner surface of the tunnel $r_1 = R_\mathrm{i}$ are shown in Fig. 2.5. An excellent agreement between the present results and those from Lee and Trifunac [1979] is observed.

The responses in Fig. 2.5 are symmetric with respect to 90° and 270° as expected based on the excitation. In Fig. 2.5(a), we observe the screening effect of the tunnel, as the longitudinal displacement is smaller in the range of $y/R_\mathrm{o} = [-2, 2]$ above the tunnel. Comparing Fig. 2.5(c) and (d), we observe that the magnitude of $\Sigma_{\theta_1x_1}$ is much larger than that of $\Sigma_{r_1x_1}$.

---

[1] Note that all the data used in this thesis in comparison with literature findings were extracted from graphs using an online tool called PlotDigitizer.

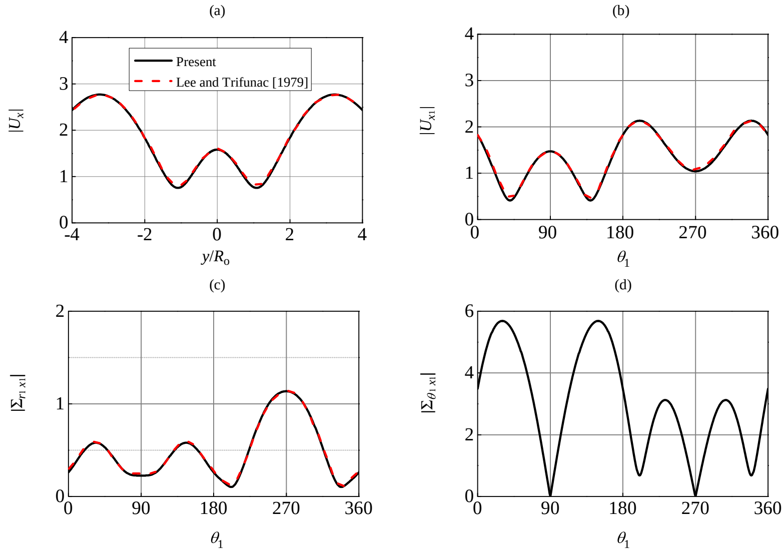

Figure 2.5: The first comparison example for the 2D SH wave case ($\chi^{(1)}_{\mathrm{inc}}$): (a) U_x at $z = 0$, (b) U_{x_1} at $r_1 = R_\mathrm{o}$, (c) $\Sigma_{r_1 x_1}$ at $r_1 = R_\mathrm{o}$ and (d) $\Sigma_{\theta_1 x_1}$ at $r_1 = R_\mathrm{i}$. The excitation is a vertically incident SH wave ($\theta_\mathrm{v} = 0^\circ$ and $\theta_\mathrm{h} = 90^\circ$), and the second parameter set in Table 2.1 is used. Note that for panel (d) no result from literature is available.

The second comparison is made between the present results and those obtained by Balendra *et al.* [1984] for a non-vertically incident SH wave ($\theta_\mathrm{v} = 30^\circ$ and $\theta_\mathrm{h} = 90^\circ$). The same quantities as in the previous example are shown in Fig. 2.6, but the shear stress is normalized differently for consistency with the literature result as follows: $\Sigma_{\theta_1 x_1} = \left|2\sigma_{\theta_1 x_1} / [(1-\nu^{(2)})\omega\rho^{(1)} c_\mathrm{S}^{(1)} U_\mathrm{S}]\right|$. A very good agreement is observed. For this obliquely incident SH wave ($\theta_\mathrm{v} = 30^\circ$), the response loses symmetry (compare Figs. 2.5 and 2.6). In Fig. 2.6(a), we observe that the response is smaller to the right of the tunnel due to the screening effect. Fig. 2.6(d) shows that the shear stress $\Sigma_{\theta_1 x_1}$ is amplified much more than $\Sigma_{r_1 x_1}$ (this is also the case when the original normalization is used), which is the same as in the first example.

For the third comparison, we consider the first parameter set in Table 2.1 and validate the current results with the results obtained by Liu *et al.* [1991], and by de Barros and Luco [1994]. The system is subjected to a vertically incident wave ($\theta_\mathrm{v} = 0^\circ$ and $\theta_\mathrm{h} = 90^\circ$). We observe an excellent agreement; see Fig. 2.7. The normalisation factor for $\Sigma_{\theta_1 x_1}$ is taken the same as in the previous example. It is interesting to note that the screening effect is not observed in the third example, and the maximum displacement occurs above the tunnel. The reason is that the frequency is lower and the tunnel is embedded deeper in the third example ($\eta = 0.105$, $H = 5R_\mathrm{i} = 4.545R_\mathrm{o}$) than in the first example ($\eta = 0.5$, $H = 1.5R_\mathrm{o}$). We can see that the screening effect is also not observed for another example, which uses the fourth parameter set ($\eta = 0.132$, $H = 8.33R_\mathrm{i}$) in Table 2.1; see Fig. 2.8(c) and (f).

By comparing the first and third examples in this subsection, we see that the distri-

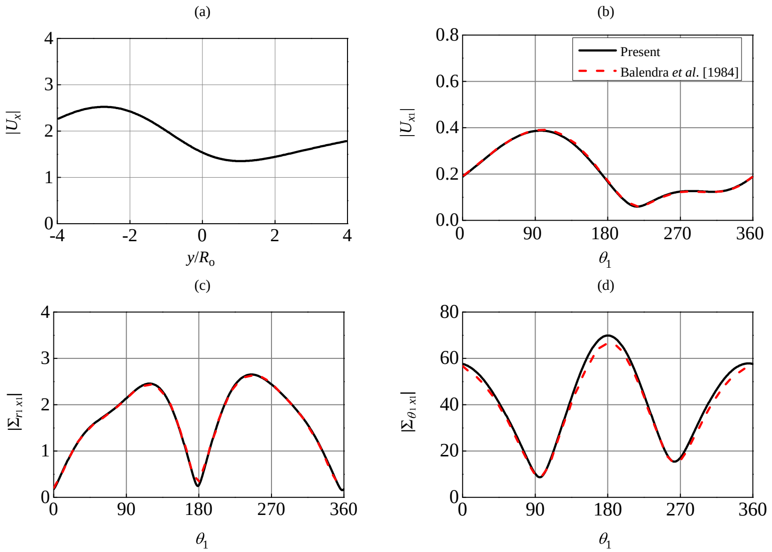

Figure 2.6: The second comparison example for the 2D SH wave case ($\chi_{\text{inc}}^{(1)}$): (a) U_x at $z = 0$, (b) U_{x_1} at $r_1 = R_\text{o}$, (c) $\Sigma_{r_1 x_1}$ at $r_1 = R_\text{o}$ and (d) $\Sigma_{\theta_1 x_1}$ at $r_1 = R_\text{i}$. The excitation is a non-vertically incident SH wave ($\theta_\text{v} = 30^\circ$ and $\theta_\text{h} = 90^\circ$), and the third parameter set in Table 2.1 is used. Note that for panel (a) no result from literature is available.

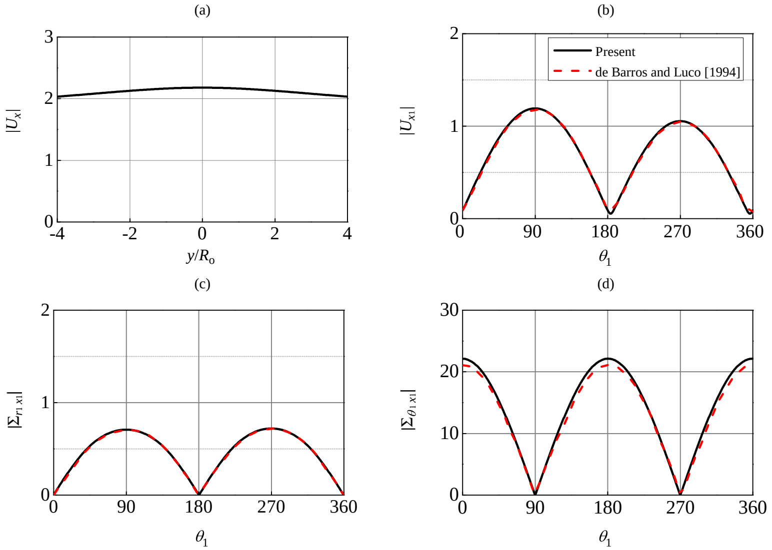

Figure 2.7: The third comparison example for the 2D SH wave case ($\chi_{\text{inc}}^{(1)}$): (a) U_x at $z = 0$, (b) U_{x_1} at $r_1 = R_\text{o}$, (c) $\Sigma_{r_1 x_1}$ at $r_1 = R_\text{o}$ and (d) $\Sigma_{\theta_1 x_1}$ at $r_1 = R_\text{i}$. The excitation is a vertically incident SH wave ($\theta_\text{v} = 0^\circ$ and $\theta_\text{h} = 90^\circ$), and the first parameter set in Table 2.1 is used. Note that for panel (a) no result from literature is available.

butions and amplitudes of the responses are quite different in these two examples even though they are both subject to vertically incident SH waves. That is because the system parameters (i.e., the dimensionless frequency, the stiffness ratio of the tunnel to soil, and the embedded depth of the tunnel) are different. We will discuss the effect of these and other two parameters (the vertical incident angle and the thickness of the tunnel) on the response of the system in Section 2.8.

2.7.2. 2D PLANE-STRAIN CASES

The comparison studies for the two-dimensional plane-strain cases consider the problem of a tunnel embedded in an elastic half-space subjected to incident P and SV waves (i.e., $\phi_{\mathrm{inc}}^{(1)}$ and $\psi_{\mathrm{inc}}^{(1)}$, respectively). We discuss three examples. First, we consider a case of vertically incident P and SV waves ($\theta_{\mathrm{v}} = 0^{\circ}$ and $\theta_{\mathrm{h}} = 90^{\circ}$) using the fourth parameter set in Table 2.1 and compare our results with the results obtained by Datta *et al.* [1984]. Fig. 2.8(a) and (b) show the radial displacement U_{r_1} at the tunnel-soil interface $r_1 = R_{\mathrm{o}}$ and the hoop stresses $\Sigma_{\theta_1\theta_1}$ at the centre-line of the tunnel $r_1 = R_{\mathrm{c}}$ for the incident P wave, while Fig. 2.8(d) and (e) show these quantities for the incident SV waves. It is clear that the results obtained by the present method are in good agreement with those in the literature.

For comparison, in Fig. 2.8(e), we added the results obtained by the present method using Hankel functions to represent the cylindrical waves in the tunnel (see Section 2.3.2), and small differences are observed compared with the literature results. Furthermore, we can verify that the results obtained using Hankel functions are not completely smooth; this is because the cylindrical wavenumbers in the tunnel are small (the combination of frequency and tunnel stiffness leads to $k_{\mathrm{b}}^{(2)}$ ($= k_{\mathrm{S}}^{(2)}$) being small), which makes that the corresponding Hankel functions become large. In this situation, the Hankel functions render the columns of matrix **K** (see Eq. (2.39)) linearly dependent given the limitation of the computer precision, which leads to an ill-conditioned system of equations and **K** having a large condition number (the results can be improved to some extent when quadruple precision is used (not standard in Matlab) in solving the system of equations). We see a similar non-smooth curve in the second 2D plane-strain example, Fig. 2.9(d), for which the cylindrical wavenumbers are even smaller. It can be verified that the non-smooth feature does not disappear even when large amounts of hysteretic damping are added in the system (results not shown). From Figs. 2.8(e) and 2.9(d), we observe that when Bessel functions are used instead of Hankel functions to represent the cylindrical waves in the tunnel, the method gives smooth and accurate results. The reason is that Bessel functions do not render the columns of matrix **K** linearly dependent, and therefore the problem of limited precision is less severe with Bessel functions than with Hankel functions. As a result, the condition number of matrix **K** is effectively reduced when Bessel functions are used. We also found that the boundary conditions at the inner surface of the tunnel and the continuity conditions at the tunnel-soil interface are then satisfied much better.

In order to demonstrate that the literature result in Fig. 2.8 (as well as the present result) is correct, we also included the hoop stress (Fig. 2.8(e)) obtained by the indirect boundary element method (indirect BEM). Clearly, a perfect match with the literature result is observed. More details regarding our implementation of the indirect BEM can be found in Section 2.8.

We also present the displacements at the ground surface for the first example. Fig. 2.8(c) and (f) show that under the vertically incident P wave, the vertical displacement U_z is approximately equal to 2 (i.e., amplification factor is 2), while the horizontal displacement U_y is approximately equal to 0. On the contrary, for the vertically incident SV wave, the horizontal displacement $U_y \approx 2$ and $U_z \approx 0$. Therefore, the vertical and horizontal displacement components are the dominant displacement components for the incident P ($\phi^{(1)}_{\text{inc}}$) and SV ($\psi^{(1)}_{\text{inc}}$) waves, respectively. It can be verified that for a 3D problem the vertical, horizontal and longitudinal displacements (i.e., U_z, U_y and U_x) are the dominant displacement components for $\phi^{(1)}_{\text{inc}}$, $\psi^{(1)}_{\text{inc}}$ and $\chi^{(1)}_{\text{inc}}$, respectively. In Section 2.8, we study the effect of system parameters on the dominant displacement components at the ground surface for the three different incident wave types.

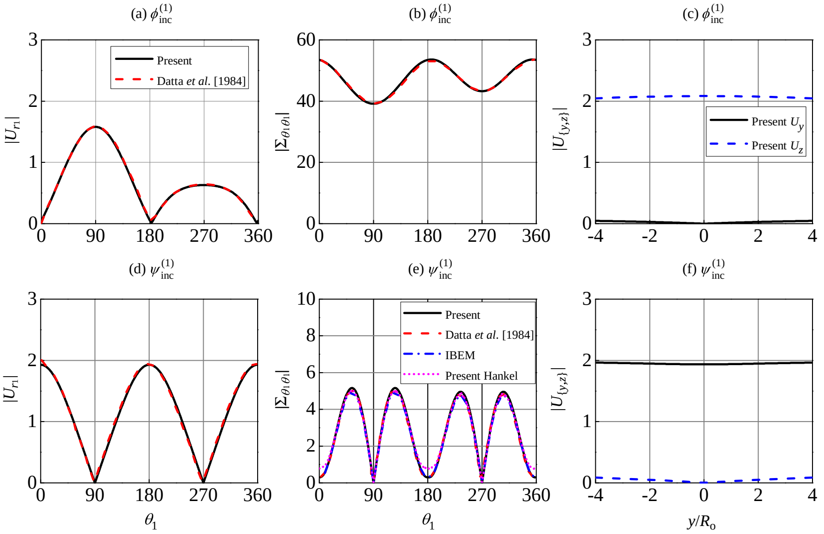

Figure 2.8: The first comparison example for the 2D P-SV wave case ($\phi^{(1)}_{\text{inc}}$ and $\psi^{(1)}_{\text{inc}}$): (a), (d): U_{r_1} at $r_1 = R_o$; (b), (e): $\Sigma_{\theta_1\theta_1}$ at $r_1 = R_c$; and (c), (f): $U_{\{y,z\}}$ at $z = 0$. The excitations are vertically incident P and SV waves ($\theta_v = 0^\circ$ and $\theta_h = 90^\circ$), respectively. The fourth parameter set in Table 2.1 is used. Note that for panels (c) and (f) no result from literature is available.

In the second example, the fifth parameter set in Table 2.1 is used. The ratio of the tunnel depth to its inner radius ($H/R_i = 2.0$) is smaller than that in the first example ($H/R_i = 8.33$), and we consider a non-vertically incident wave case ($\theta_v = 10^\circ$ and $\theta_h = 90^\circ$). Fig. 2.9 shows the response under the incident P and SV waves. We observe that the agreement with results from Wong *et al.* [1986b] is very good but $\Sigma_{\theta_1\theta_1}$ is not smooth when Hankel functions are used to represent the waves in the tunnel, which is again related to the cylindrical wavenumbers in the tunnel being small. Clearly, the non-smoothness is more severe for the incident S wave case. Therefore, one may infer that the present method works better for the incident P wave case than the S wave case; see also Section 2.8.1. However, that is not necessarily true, as shown in Section 2.8.2, where the influence of the stiffness contrast is investigated in more detail. In addition, the non-smoothness of the response curves is more severe in the shallow tunnel case (see Fig. 2.9(d)) than the deep tunnel case (see Fig. 2.8(e)). This is confirmed by the analysis in Section 2.8.3.

It is shown in Fig. 2.9 that the distributions of the hoop stress $\Sigma_{\theta_1\theta_1}$ and axial stress $\Sigma_{x_1x_1}$ are very similar, though the amplification of the hoop stress is much higher than that of the axial stress. Fig. 2.9(c) and (f) show that the extremes of the radial and tangential displacements U_{r_1} and U_{θ_1} are both around 2, which is different from what we observed at the free surface, where there is one dominant displacement component (dependent on incident wave type). However, we do see that the radial displacement U_{r_1} has maxima where the tangential displacement U_{θ_1} has minima, and vice versa.

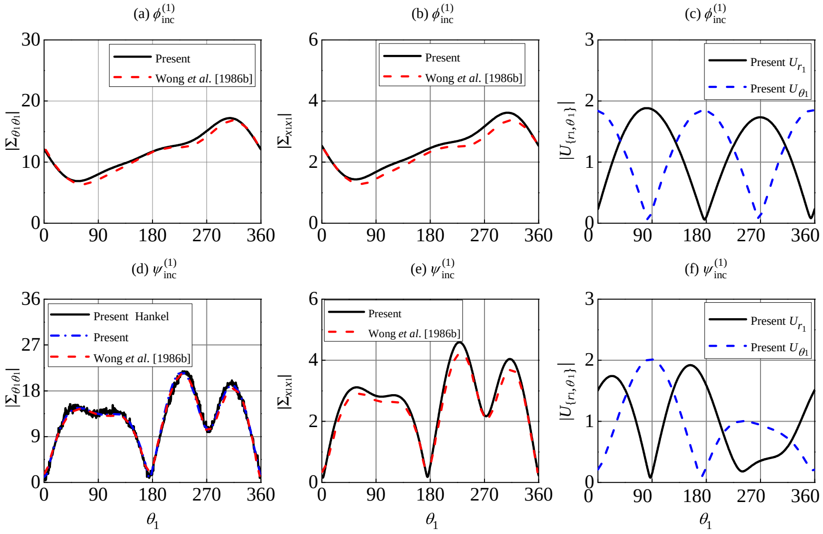

Figure 2.9: The second comparison example for the 2D P-SV wave case ($\phi^{(1)}_{\text{inc}}$ and $\psi^{(1)}_{\text{inc}}$): (a), (d): $\Sigma_{\theta_1\theta_1}$ at $r_1 = R_{\text{c}}$; (b), (e): $\Sigma_{x_1x_1}$ at $r_1 = R_{\text{c}}$; and (c), (f): $U_{\{r_1,\theta_1\}}$ at $r_1 = R_{\text{o}}$. The excitations are non-vertically incident P and SV waves ($\theta_{\text{v}} = 10^{\circ}$ and $\theta_{\text{h}} = 90^{\circ}$), respectively. The fifth parameter set in Table 2.1 is used. Note that for panels (c) and (f) no result from literature is available.

In the third example, we consider a vertically incident wave case ($\theta_{\text{v}} = 0^{\circ}$ and $\theta_{\text{h}} = 90^{\circ}$), and use the first parameter set. The obtained results are shown in Fig. 2.10, where we observe a perfect match between the present results and those obtained by Liu *et al.* [1991]. In this example, the stiffness ratio of the tunnel to soil is small, and the tunnel is embedded at relatively large depth. Therefore, as opposed to the first two examples considered in this section, the results obtained when Hankel functions are used also match perfectly the literature results, but they are not shown in Fig. 2.10 for brevity. Fig. 2.10(c) and (f) show the normal radial stress $\Sigma_{r_1r_1}$ and shear stress $\Sigma_{r_1\theta_1}$ for the vertically incident P and SV waves, respectively. We see that the distributions of $\Sigma_{r_1r_1}$ and $\Sigma_{\theta_1\theta_1}$ are the same, and the amplitude of $\Sigma_{r_1r_1}$ does not exceed 1. Furthermore, we observe that the bending in the circumferential direction is more severe for the incident SV wave case

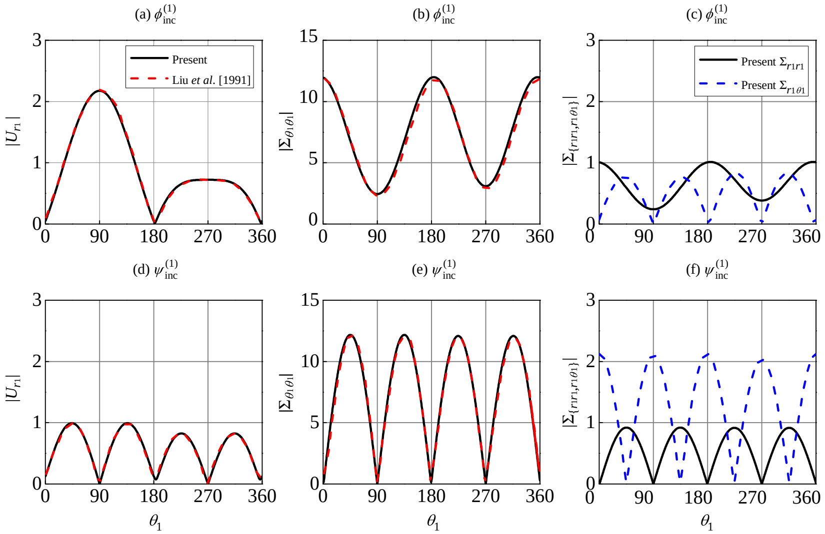

Figure 2.10: The third comparison example for the 2D P-SV wave case ($\phi^{(1)}_{\text{inc}}$ and $\psi^{(1)}_{\text{inc}}$): (a), (d): U_{r_1} at $r_1 = R_{\text{o}}$; (b), (e): $\Sigma_{\theta_1\theta_1}$ at $r_1 = R_{\text{c}}$; and (c), (f): $\Sigma_{\{r_1r_1, r_1\theta_1\}}$ at $r_1 = R_{\text{o}}$. The excitations are vertically incident P and SV waves ($\theta_{\text{v}} = 0^{\circ}$ and $\theta_{\text{h}} = 90^{\circ}$), respectively. The first parameter set in Table 2.1 is used. Note that for panels (c) and (f) no result from literature is available.

than for the incident P wave case.

2.7.3. 3D CASE

One example of a 3D problem with incident P and S waves (i.e., $\phi^{(1)}_{\text{inc}}$ and $\chi^{(1)}_{\text{inc}}$, respectively) is given in this subsection. The first parameter set is used with obliquely incident P and S waves under incident angles $\theta_{\text{v}} = 30^{\circ}$ and $\theta_{\text{h}} = 0^{\circ}$. The obtained results are shown in Fig. 2.11, where we observe excellent agreement between the present results and those obtained by Liu *et al.* [1991]. Note that the results obtained using the indirect BEM are also included for this validation case, and good agreement is observed as well.

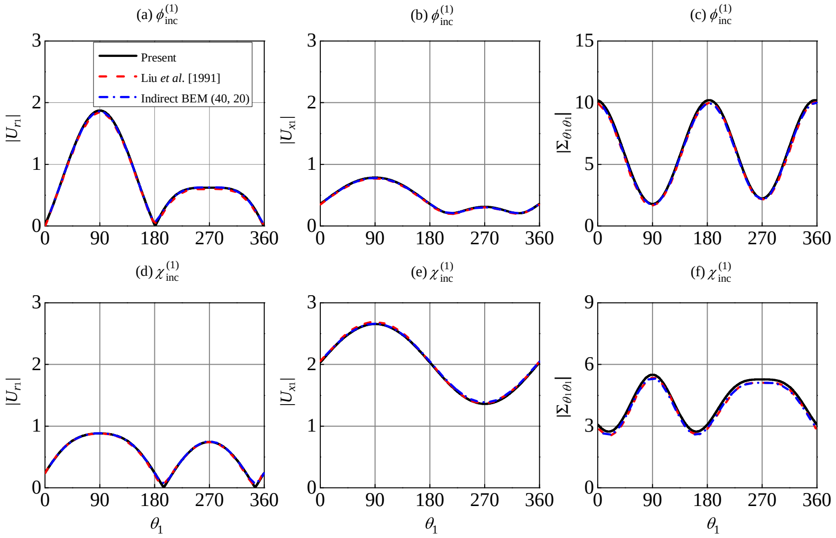

Figure 2.11: An example for the 3D case ($\phi_{\text{inc}}^{(1)}$ and $\chi_{\text{inc}}^{(1)}$): (a), (d): U_{r_1} at $r_1 = R_\text{o}$; (b), (e): U_{x_1} at $r_1 = R_\text{o}$; and (c), (f): $\Sigma_{\theta_1\theta_1}$ at $r_1 = R_\text{c}$. The excitations are non-vertically incident P and S waves ($\theta_\text{v} = 30^\circ$ and $\theta_\text{h} = 0^\circ$), respectively. The first parameter set in Table 2.1 is used.

2.8. ACCURACY OF THE PRESENT METHOD AND PARAMETRIC STUDIES

As shown in Section 2.7, the present method works very well when Bessel functions are used for the wave field in the tunnel. This is not necessarily the case when Hankel functions are used instead (i.e., when there is high stiffness contrast between the tunnel and soil, or when the tunnel is shallow; see Figs. 2.8 and 2.9). To gain more insight into the accuracy of the present method, we evaluate in this section the influence of five different parameters in the system: the dimensionless frequency, the stiffness ratio of the tunnel to soil, the embedded depth of the tunnel, the vertical incident wave angle and the thickness of the tunnel. Note that for the analysis in Sections 2.8.1, 2.8.3, 2.8.4 and 2.8.5, the results obtained when Hankel functions are used for the wave field in the tunnel are the same as the ones obtained using Bessel functions, but the former results are not shown for brevity.

To evaluate the accuracy of the present method, we also implemented the indirect BEM. The formulation of the indirect BEM for the current seismic wave problem is similar to the formulation for the moving-load problem (Chapter 4), only the external force is different. The implementation of the indirect BEM for the seismic wave problem has been validated for each case, but only two cases are shown in this chapter; see Figs. 2.8 and 2.11. To check the convergence of the indirect BEM, we considered different numbers of receiver and source points: $(N_\text{r}, N_\text{s}) = (40, 20)$ and $(N_\text{r}, N_\text{s}) = (80, 40)$. Figs. 2.12-2.16 show that $(N_\text{r}, N_\text{s}) = (40, 20)$ is sufficient for all the calculations in this chapter. Note that we considered a very small amount of hysteretic material damping (i.e., material damping ratio being 0.001) in the implementation of the indirect BEM.

Throughout this section, we display the hoop stress at the centre-line of the tunnel and displacements at the ground surface. The hoop stress is chosen as it is the most important response component for the tunnel. For the ground vibrations, we choose the vertical, horizontal and longitudinal displacements U_z, U_y and U_x for $\phi^{(1)}_{\mathrm{inc}}$, $\psi^{(1)}_{\mathrm{inc}}$ and $\chi^{(1)}_{\mathrm{inc}}$, respectively, as they are the dominant displacement components; see Section 2.7.2. The first parameter set in Table 2.1, and $\theta_{\mathrm{v}} = 30^{\circ}$ and $\theta_{\mathrm{h}} = 0^{\circ}$ are used as the base case in the following analysis. We display the maximum of the absolute value of hoop stresses around the tunnel, and the maximum of the absolute value of ground vibrations in the range of $y/R_{\mathrm{o}} = [-4,4]$. Furthermore, the effects of the five different parameters on the response of the system are briefly discussed as well.

2.8.1. DIMENSIONLESS FREQUENCY

As seismic waves typically have low frequencies, we consider the dimensionless frequency in the range of 0.002 – 1.5 ($\tilde{f} = 0.2 - 154.8$ Hz). Fig. 2.12(a)-(c) show that the present method works well in terms of the hoop stress. Fig. 2.12(d)-(f) show that the present method also works well in terms of the ground vibrations for dimensionless frequencies up to 0.7, 0.69 and 0.46 ($\tilde{f} = 72.3, 71.2$ and 47.5 Hz) under $\phi^{(1)}_{\mathrm{inc}}$ and $\psi^{(1)}_{\mathrm{inc}}$, and $\chi^{(1)}_{\mathrm{inc}}$, respectively. Clearly, the method performs well for the frequency band of seismic waves. We included the higher frequencies in view of the applicability of the method for other, higher-frequency loadings.

For high dimensionless frequencies, the condition number of the formulated matrix **K** is very large, and the matrix equation Eq. (2.39) cannot be solved accurately. From the numerical analysis, we found that the boundary conditions at the inner surface of the tunnel and continuity conditions at the interface are still satisfied well for high frequencies, but the boundary conditions at the ground surface are not. Results are thus only accurate at the tunnel surfaces, not at the ground surface. The reason for the inaccuracy lies in the fact that the secondary scattered waves in the soil are represented by cylindrical waves and not plane waves, while the latter are most likely more suitable to represent the response at the flat ground surface at high frequencies. Using more circumferential modes does not help increasing accuracy; on the contrary, we can verify that the condition number gets larger, so the results obtained using more modes can be even worse. In fact, it is difficult to get converged results using the present method for high-frequency cases.

We observe that the present method generally works better for the incident P wave case ($\phi^{(1)}_{\mathrm{inc}}$) than the incident S wave case ($\psi^{(1)}_{\mathrm{inc}}$ and $\chi^{(1)}_{\mathrm{inc}}$); see also Fig. 2.9. The reason is that, for the incident S wave case, the longitudinal wavenumber $k^{(1)}_{x}$ is larger than that for the case of the incident P wave under the same frequency, as the speed of the S wave is smaller than that of the P wave. Thus, $k^{(1)}_{\mathrm{a}}$ is smaller, which eventually results in a higher condition number of matrix **K** and less accurate responses; see explanation in Section 2.7.2, although the inaccuracy in this case originates from the Hankel functions in the soil, which cannot be replaced by Bessel functions as there are only outgoing waves.

Fig. 2.12 shows that for different incident wave types, the hoop stress has a dominant peak value at low frequencies, oscillates as frequency increases, and has a decreasing trend. The first two dimensionless resonance frequencies under $\phi_{\mathrm{inc}}^{(1)}$ are 0.15 and 0.74, respectively, under $\psi_{\mathrm{inc}}^{(1)}$ 0.11 and 0.33, and under $\chi_{\mathrm{inc}}^{(1)}$ 0.24 and 0.59. We also see that the curve for the incident S wave case oscillates more. In addition, as opposed to the decreasing trend for the hoop stress, the curves for ground vibrations exhibit a slightly increasing trend.

To conclude, the advantage of the proposed semi-analytical method is that it is very efficient regarding computational time. However, the condition number increases as frequency increases, which may lead to an increase in computational time (still efficient compared with indirect BEM) and, at some point, to inaccurate results. Thus, for seismic wave excitations, the semi-analytical method is beneficial, but its accuracy is lost for high-frequency loadings.

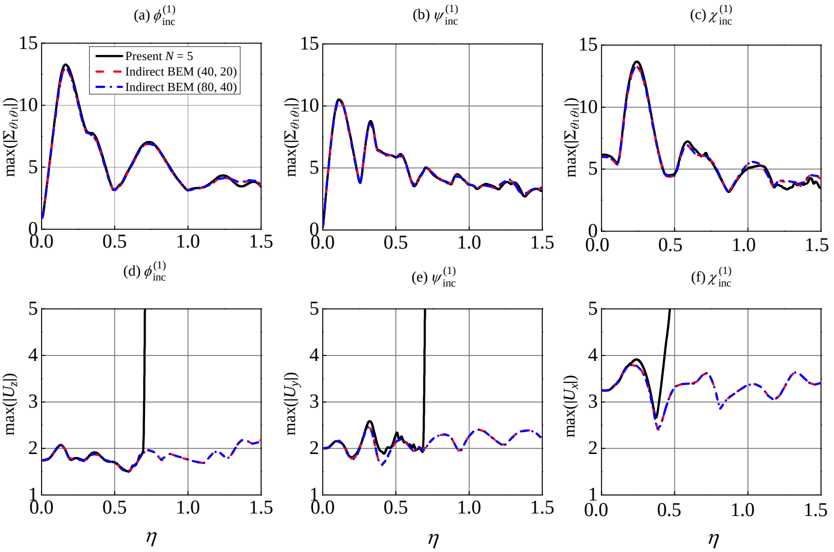

Figure 2.12: Evaluation of the present method for the dimensionless frequency η: (a)-(c) hoop stress $\Sigma_{\theta_1\theta_1}$ at $r_1 = R_{\mathrm{c}}$; (d)-(f) vertical displacement U_z, horizontal displacement U_y and longitudinal displacement U_x at $z = 0$ subject to $\phi_{\mathrm{inc}}^{(1)}$, $\psi_{\mathrm{inc}}^{(1)}$ and $\chi_{\mathrm{inc}}^{(1)}$, respectively.

2.8.2. STIFFNESS RATIO OF THE TUNNEL TO SOIL

As mentioned in Section 2.7.2, the large stiffness contrast ($E^{(2)}/E^{(1)} = 23$) between the tunnel and soil may induce inaccuracies in the results obtained by the present method when using Hankel functions to represent the cylindrical waves in the tunnel. Therefore, we evaluate it for varying stiffness ratio: $E^{(2)}/E^{(1)} = [0.5-25]$. The corresponding range for shear wave velocity in the soil is $C_{\mathrm{S}}^{(1)} = [2123\ \mathrm{m/s} - 300\ \mathrm{m/s}]$ based on the shear velocity $C_{\mathrm{S}}^{(2)} = 1725\ \mathrm{m/s}$. In this section, we show the results obtained by the present method using both Bessel and Hankel functions in Fig. 2.13. It is shown that the present method using Bessel functions works well for both the incident P and S waves in the complete considered range. However, regarding the hoop stress, the present method using Hankel functions does not give accurate results in the stiffness ratio range of 10 – 15 for the incident P wave case. This improvement was already touched upon in Section 2.7.2.

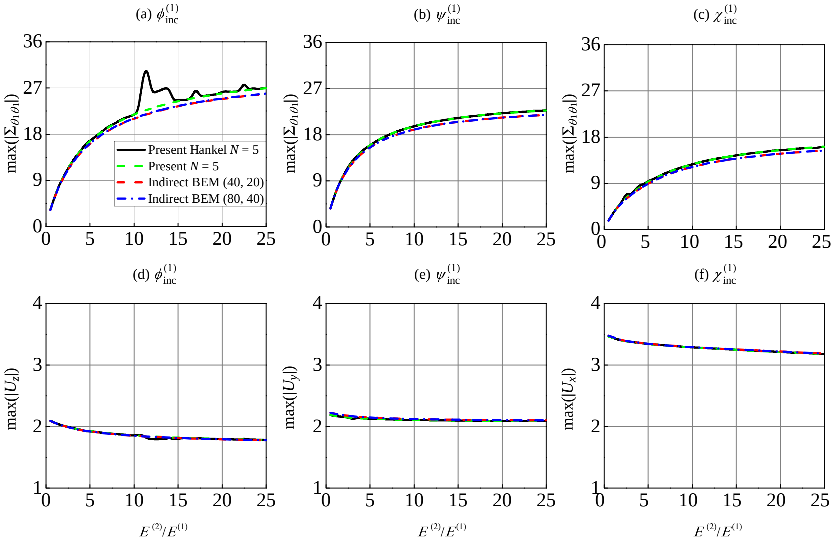

Figure 2.13: Evaluation of the present method for the stiffness ratio of the tunnel to soil $E^{(2)}/E^{(1)}$: (a)-(c) hoop stress $\Sigma_{\theta_1\theta_1}$ at $r_1 = R_{\mathrm{c}}$; (d)-(f) vertical displacement U_z, horizontal displacement U_y and longitudinal displacement U_x at $z = 0$ subject to $\phi^{(1)}_{\mathrm{inc}}$, $\psi^{(1)}_{\mathrm{inc}}$ and $\chi^{(1)}_{\mathrm{inc}}$, respectively.

The large stiffness contrast causes only a small inaccuracy in the results (i.e., the small difference in trend as the stiffness ratio increases); they are still satisfactory. Therefore, a large stiffness ratio does not necessarily lead to inaccurate results. It is surprising to see that the results are actually least accurate for a moderate stiffness contrast (range 10 – 15), and for the incident P wave case. This is different from what we observed in Sections 2.8.1 (and in Sections 2.8.3-2.8.5), where the present method seemed to perform better for the incident P than the incident S wave case.

To understand the inaccuracy in the range of 10 – 15 for the incident P wave case, we consider the wavenumbers of refracted waves in the tunnel. One can verify that $k^{(2)}_{\mathrm{b}}$ (see Eq. (2.24)) becomes imaginary when $E^{(2)}/E^{(1)} = 12.5$, which implies that the refracted shear wave becomes evanescent; $|k^{(2)}_{\mathrm{b}}|$ is small in the interval of $E^{(2)}/E^{(1)} = [10 - 15]$, and $|k^{(2)}_{\mathrm{b}}|$ is the smallest when $E^{(2)}/E^{(1)} = 12$. As explained in Section 2.7.2, the small argument of a Hankel function results in inaccurate responses (it can be verified that the inaccuracy does not completely disappear when large amounts of hysteretic damping are added in the system). That is the reason why the responses are inaccurate for $E^{(2)}/E^{(1)} = [10 - 15]$, and why the largest discrepancy occurs when $E^{(2)}/E^{(1)} = 12$. Similarly, the (small) inaccuracy observed for the incident S wave case (see Fig. 2.13(c) and (e)) when $E^{(2)}/E^{(1)} = 3$ is again caused by the refracted S wave becoming evanescent, and $k^{(2)}_{\mathrm{b}}$ being the smallest for this stiffness contrast. Fortunately, when Bessel functions are used, the condition number of matrix $\mathbf{K}$ is effectively reduced and accurate results can be obtained for the small wavenumbers.

Fig. 2.13 shows that the hoop stress increases dramatically as the stiffness ratio increases, which indicates that the hoop stress in the tunnel can be reduced effectively by replacing the surrounding soft soil by stiff soil (i.e., by means of ground improvement). The hoop stress under $\phi_{\mathrm{inc}}^{(1)}$ is the largest, and the one under $\chi_{\mathrm{inc}}^{(1)}$ is the smallest. It is also shown that the ground vibrations decrease only slightly as the stiffness ratio increases.

2.8.3. EMBEDDED DEPTH OF THE TUNNEL

In this section, we evaluate the present method for the embedded depth of the tunnel, and the considered range of embedded depth ratio is that $H/R_{\mathrm{o}} = [1.5-20]$. The results are shown in Fig. 2.14. We observe that the present method works very well in general for both the P and S wave cases, despite some small differences between the current results and those obtained using the indirect BEM. The reason why the present method works less good for shallow tunnels with $H/R_{\mathrm{o}} = [1.5-2]$ (see Fig. 2.14(e) and (f)) is that the wavenumbers are small in this range.

Fig. 2.14(d)-(f) show that the ground vibrations at the ground surface have a decreasing trend. The ground vibrations are amplified more for shallow tunnels due to 'trapped' waves between the top of the tunnel and the ground surface [Alielahi *et al.*, 2015, 2016]. We observe in Fig. 2.14(a)-(c) that the embedded depth has a large effect on the hoop stress, for all three incident wave types. Both the distributions and magnitudes of the hoop stress are different, and the peak values occur at different depth ratios. In addition, we see that the response (both the hoop stress and ground vibration) for the incident P wave is not always larger than that for the incident S wave, which is different from what is claimed in Alielahi *et al.* [2015] that generally greater amplifications are observed for P waves than for SV waves. For example, the hoop stress under $\phi_{\mathrm{inc}}^{(1)}$ is the largest when $H/R_{\mathrm{o}} = [5-9.25]$; the hoop stress under $\psi_{\mathrm{inc}}^{(1)}$ is the largest when $H/R_{\mathrm{o}} = [2-5, 14.5-20]$; the hoop stress under $\chi_{\mathrm{inc}}^{(1)}$ is the largest when $H/R_{\mathrm{o}} = [9.25-14.5]$. Therefore, a larger embedded depth does not necessarily make the tunnel safer. In fact, we can verify that the hoop stress shows a decreasing trend with increasing embedded depth, but the decrease is not monotonic as quasi-periodic patterns appear. The ground displacements (Fig. 2.14(d)-(f)) show similar patterns, although the oscillation is less strong.

2.8.4. VERTICAL INCIDENT ANGLE

Here, we evaluate the present method for the vertical incident angle θ_{v}, while we consider $\theta_{\mathrm{h}} = 0^{\circ}$. Note that for the considered soil parameter set with $\nu^{(1)} = 0.333$, $\theta_{\mathrm{v}}^{\mathrm{crit}} = \arcsin\left(\sqrt{\left(1-2\nu^{(1)}\right)/\left(2-2\nu^{(1)}\right)}\right) \approx 30^{\circ}$ for the incident S wave case (see Eq. (2.19)). Fig. 2.15 shows that the results obtained by the present method are accurate for both the incident P and S wave cases. Note that the scattered compressional waves in the soil become evanescent (i.e., $k_{\mathrm{a}}^{(1)}$ becomes imaginary) when $\theta_{\mathrm{v}} \approx 30^{\circ}$ (see Eqs. (2.15), (2.19) and (2.22); as we consider $\theta_{\mathrm{h}} = 0^{\circ}$, $k_{y}^{(1)} = 0$ and $k_{\mathrm{a}}^{(1)} = k_{z,\mathrm{P}}^{(1)}$). As explained in Section 2.8.2, we expect inaccuracy at the transition to evanescent waves. One can verify that the obtained results are indeed less accurate around $\theta_{\mathrm{v}} = 30^{\circ}$ especially when using $N = 10$; however, the obtained results using $N = 5$ are satisfactory. Therefore, the inaccuracy issue regarding the angle (i.e., scattered compressional waves becoming evanescent) is

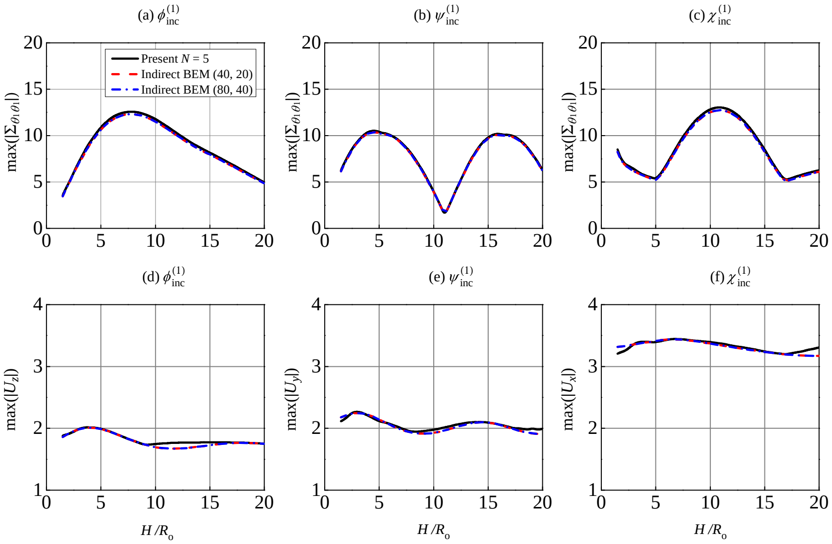

Figure 2.14: Evaluation of the present method for the depth ratio $H/R_{\rm o}$: (a)-(c) hoop stress $\Sigma_{\theta_1\theta_1}$ at $r_1 = R_{\rm c}$; (d)-(f) vertical displacement U_z, horizontal displacement U_y and longitudinal displacement U_x at $z = 0$ subject to $\phi^{(1)}_{\rm inc}$, $\psi^{(1)}_{\rm inc}$ and $\chi^{(1)}_{\rm inc}$, respectively.

less severe than in the case of unfavorable stiffness ratio (i.e., refracted shear waves becoming evanescent). In addition, this suggests that it is not recommendable to use more than necessary circumferential modes in the computations.

Fig. 2.15(a) and (b) show that the hoop stress decreases significantly as $\theta_{\rm v}$ increases for the cases of $\phi^{(1)}_{\rm inc}$ and $\psi^{(1)}_{\rm inc}$; however, the hoop stress first increases and then decreases for the case of $\chi^{(1)}_{\rm inc}$. We observe two small peaks at $\theta_{\rm v} = 24.5^\circ$ and $\theta_{\rm v} = \theta^{\rm crit}_{\rm v} \approx 30^\circ$, and a pronounced peak at $\theta_{\rm v} = 39^\circ$. Similar to the trend of the hoop stress, the dominant displacement U_z decreases under $\phi^{(1)}_{\rm inc}$. However, the influence of $\theta_{\rm v}$ on the dominant displacement U_y is very small. The dominant longitudinal displacement under $\chi^{(1)}_{\rm inc}$ varies more as $\theta_{\rm v}$ increases, and there is a pronounced peak at $\theta_{\rm v} = \theta^{\rm crit}_{\rm v} \approx 30^\circ$ and a second small peak at $\theta_{\rm v} = 64^\circ$. We can conclude that $\theta^{\rm crit}_{\rm v}$ has a large effect on the response of the system, especially under $\chi^{(1)}_{\rm inc}$.

2.8.5. THICKNESS OF THE TUNNEL

The evaluation of the present method for changing thickness ratio $h/R_{\rm o}$ is presented in this section. We consider a range of 0.05 – 0.5. Fig. 2.16 shows that the present method works well for both the incident P and S wave cases. The reason why the (small) difference between the results obtained using the present method and those using the indirect BEM increases as the thickness ratio increases, is that the tunnel is modelled by the Flügge shell theory in the indirect BEM, while the tunnel is modelled as an elastic continuum in the current method.

Fig. 2.16(a)-(c) show that the hoop stress decreases significantly as the thickness of

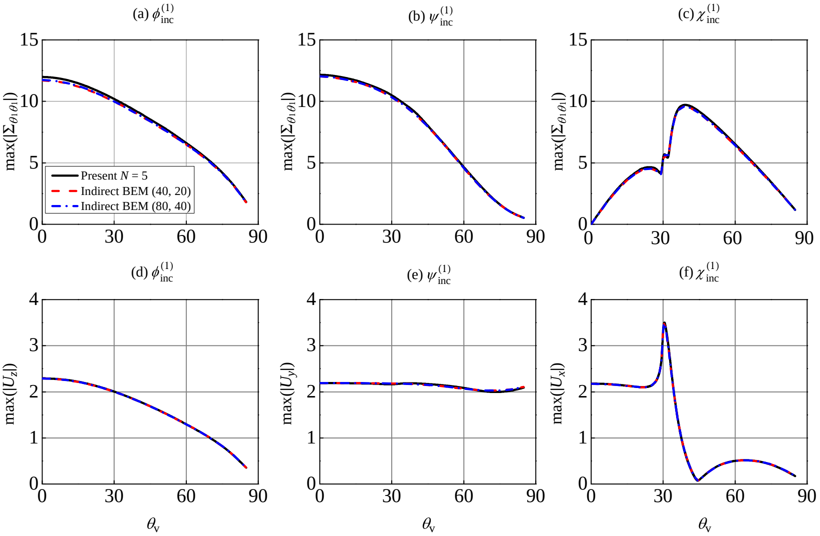

Figure 2.15: Evaluation of the present method for the vertical incident angle θ_{v}: (a)-(c) hoop stress $\Sigma_{\theta_1\theta_1}$ at $r_1 = R_{\text{c}}$; (d)-(f) vertical displacement U_z, horizontal displacement U_y and longitudinal displacement U_x at $z = 0$ subject to $\phi^{(1)}_{\text{inc}}$, $\psi^{(1)}_{\text{inc}}$ and $\chi^{(1)}_{\text{inc}}$, respectively.

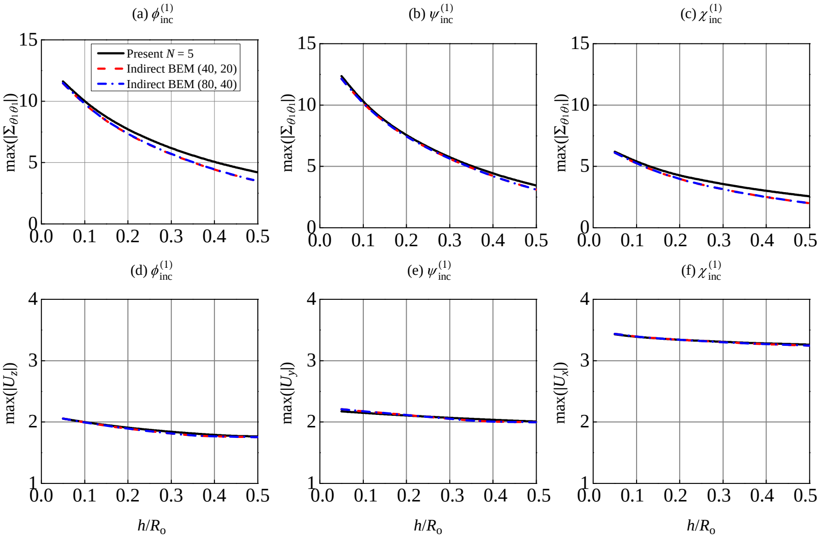

Figure 2.16: Evaluation of the present method for the thickness ratio of the tunnel h/R_{o}: (a)-(c) hoop stress $\Sigma_{\theta_1\theta_1}$ at $r_1 = R_{\text{c}}$; (d)-(f) vertical displacement U_z, horizontal displacement U_y and longitudinal displacement U_x at $z = 0$ subject to $\phi^{(1)}_{\text{inc}}$, $\psi^{(1)}_{\text{inc}}$ and $\chi^{(1)}_{\text{inc}}$, respectively.

the tunnel increases. This suggest that a thicker tunnel is indeed safer. Furthermore, the hoop stress under $\phi^{(1)}_{\text{inc}}$ and $\psi^{(1)}_{\text{inc}}$ is much larger than that under $\chi^{(1)}_{\text{inc}}$. Fig. 2.16(d)-(f) show that all the dominant displacement components decrease slightly as the thickness of the tunnel increases. Different from what we observed for the hoop stress, the dominant displacement under $\chi^{(1)}_{\text{inc}}$ is much larger than that under $\phi^{(1)}_{\text{inc}}$ and $\psi^{(1)}_{\text{inc}}$.

2.9. CONCLUSIONS

A semi-analytical solution for the 3D response of a tunnel embedded in an elastic half-space subject to seismic waves has been presented in this chapter. An existing method has been extended successfully from 2D to 3D. Both the tunnel and soil were modelled as an elastic continuum. The method of conformal mapping (which employs the complex-variable theory) was used to map the original physical domain with boundary surfaces of two different types onto an image domain with boundary surfaces of the same type. The total wave field in the soil consists of incident and reflected plane waves, and directly and secondary scattered cylindrical waves, while the total wave field in the tunnel only consists of refracted cylindrical waves. The secondary scattered waves are generated when the cylindrical waves directly scattered from the tunnel meet the half-space surface. They were represented by cylindrical waves that originate from a source of a priori unknown intensity located at the centre of the image of the tunnel, which is positioned symmetrically with respect to the half-space surface.

The unknown coefficients of the potentials related to the cylindrical waves were determined by the boundary and continuity conditions of the tunnel-soil system. The boundary value problem was solved in the image domain from a system of algebraic equations obtained by projecting the boundary and continuity conditions onto the set of the circumferential basis functions/modes. Convergence tests were conducted regarding the number of circumferential modes (N), and it was shown that $N = 5$ appears sufficient for the considered scenarios in this chapter. The results obtained by the present method were validated for 2D anti-plane, 2D plane-strain and 3D cases by literature results. Excellent agreement was observed.

The performance of the present solution method has been systematically evaluated and the effect of five important parameters on the response of the system has been addressed briefly as well. The main findings are as follows:

- The present method performs well for the frequency band of seismic waves. For high dimensionless frequencies, the condition number of the formulated matrix obtained from the boundary and continuity conditions is very high, which causes inaccurate results. The proposed method generally works better for the incident P wave case than the incident S wave case. The reason is that the wavenumbers in the arguments of the Hankel functions (representing the cylindrical waves in the soil) are small, implying that the Hankel functions render the columns of matrix **K** linearly dependent for the S wave case, which eventually results in ill-conditioned system of equations and less accurate responses.

  The hoop stress decreases as frequency increases in a global sense, while the dominant displacement component increases as frequency increases. Furthermore, the results reveal pronounced resonances which should be avoided in the design of tunnels.

- In the considered range of the stiffness ratio of the tunnel to soil, the proposed method works well in general when Bessel functions are used to represent the cylindrical waves in the tunnel. In contrast, when Hankel functions are used to represent waves in the tunnel, the hoop stress becomes inaccurate for a stiffness ratio in the range of 10 – 15. The reason is that the wavenumbers in the Hankel functions (representing the cylindrical waves in tunnel) are small in this moderate stiffness contrast range, which is due to refracted shear waves (in the tunnel) becoming evanescent (in the 3D case). These inaccuracies can be perfectly overcome by representing the cylindrical waves in the tunnel by Bessel functions.

  The hoop stress increases dramatically as the stiffness ratio of the tunnel to soil increases, which indicates that the hoop stress in the tunnel can be reduced effectively by replacing the surrounding soft soil by stiff soil, while the ground vibrations decrease slightly as the soil stiffness decreases.

- The present method generally works well in the considered range of the embedded depth of the tunnel.

  It is shown that the hoop stress has a peak value at different embedded depths for three different incident waves (P wave and two differently polarized S waves), and the ground vibrations are amplified more for shallow tunnels. A larger embedded depth does not necessarily make the tunnel safer. The hoop stress shows a decreasing trend with increasing embedded depth, but the decrease is not monotonic as quasi-periodic patterns appear. The ground displacements show similar patterns, although the oscillation is less strong.

- The present method generally works well in the considered range of the vertical incident angle.

  The vertical incident angle has a large effect on the response of the system. The hoop stress decreases significantly as the vertical incident angle increases for $\phi_{\text{inc}}^{(1)}$ (P wave) and $\psi_{\text{inc}}^{(1)}$ (S wave), while the hoop stress for $\chi_{\text{inc}}^{(1)}$ (different S wave) first increases and then decreases, with a pronounced peak value where the vertical incident angle is slightly larger than the critical vertical incident angle. The dominant ground vibration decreases as the vertical incident angle increases for $\phi_{\text{inc}}^{(1)}$; the dominant ground vibration does not change much for $\psi_{\text{inc}}^{(1)}$, while there is a pronounced peak at the critical vertical incident angle for $\chi_{\text{inc}}^{(1)}$.

- The present method generally works well in the considered thickness range of the tunnel.

  The hoop stress decreases significantly as the thickness of the tunnel increases, while the dominant ground vibrations decrease only slightly. This suggest that a thicker tunnel is indeed safer, and it is also somewhat beneficial for structures on the ground surface.

Finally, we can conclude that the proposed method is in general a fast, elegant and accurate method for solving the seismic wave scattering problem, and can be used for preliminary design.

3

RESPONSE OF AN ELASTIC HALF-SPACE WITH AN EMBEDDED CYLINDRICAL CAVITY SUBJECT TO A HARMONIC ANTI-PLANE SHEAR WAVE: A COMPARISON OF METHODS

In this chapter, we investigate the two-dimensional response of a cavity embedded in an elastic half-space subjected to a harmonic plane SH wave. Main focus is the comparison of three methods: the method of images, the method of conformal mapping and the indirect boundary element method (indirect BEM). For the considered model, closed-form solutions can be obtained using the method of images, which serve as benchmark solutions for the other two methods. Regarding the first two methods, the total wave field in the half-space comprises harmonic incident and reflected plane waves, as well as directly and secondary scattered cylindrical waves. The secondary scattered waves arise when the cylindrical waves directly scattered from the cavity encounter the free surface of the half-space. In the method of conformal mapping, the secondary scattered waves are represented by cylindrical waves originating from a source with an a priori unknown intensity located at the image of the cavity. Conversely, in the method of images, the intensity is known and is the same as that of the directly scattered wave. In both methods, orthogonality relations are applied to the boundary value problem, resulting in a set of algebraic equations. To obtain numerical results, the sum over the circumferential modes in the potentials related to the cylindrical waves needs to be truncated. Convergence tests and validation examples are provided to assess the accuracy and reliability of the methods. The results demonstrate that both the method of images and the method of conformal mapping converge with a small number of circumferential modes, while the indirect BEM converges with a small number of source and receiver points. Moreover, the results obtained using the proposed

methods align perfectly with those reported in the literature. In comparative studies, we observe that both the method of conformal mapping and the method of images require a similar number of circumferential modes to achieve converged results. In terms of computational efficiency, the method of images outperforms the method of conformal mapping, whereas the indirect BEM is the least efficient one among the three methods due to its highest computational cost. Through a systematic evaluation, we confirm that both the method of conformal mapping and the indirect BEM accurately work within the complete considered ranges of the dimensionless frequency, the embedded cavity depth and the vertical incident angle. This study therefore verifies the accuracy of the specific application of the method of conformal mapping (in which the waves scattered from the half-space surface are represented by cylindrical waves that originate from an image source of a priori unknown intensity) and of the indirect BEM. Thus, all the three methods can be applied in the preliminary design of an embedded cavity to assess stress distributions at the cavity and ground vibrations. Furthermore, parametric studies reveal significant effects of the system parameters on the responses. The system's response curves display nearly equally spaced resonances, which is in line with those of the one-dimensional shear layer subject to bedrock motion, while similar response curves for the three-dimensional case do not have this feature. In practical engineering, careful consideration should be given to the choice of the embedded cavity depth and the vertical incident angle to avoid pronounced resonances in the system response.

3.1. INTRODUCTION

The dynamic response of a half-space with an underground structure subject to seismic waves has been an important research topic. This is due to the potential for substantial amplifications of ground motion and dynamic stress concentrations. However, resolving the associated difficulty in solving the dynamic problem arising from the distinct types of boundary surfaces presents a challenge. Specifically, the flat surface of the half-space and the surface of the underground structure differ in nature. To tackle this problem, researchers have employed conformal mapping functions, which enables the mapping of surfaces of different types in the physical domain to surfaces of the same type in an image domain. The method of conformal mapping has been widely applied in addressing two-dimensional (2D) problems of wave scattering by inclusions embedded in an elastic half-space. Notably, this approach offers computational efficiency and yields accurate results, making it a promising and viable solution. Building upon these foundations, an initial endeavor was undertaken to extend the method of conformal mapping to address the three-dimensional (3D) wave scattering problem, as detailed in Chapter 2.

However, it was observed that inaccurate results may arise, particularly in high frequency scenarios. As pointed out in Chapter 2, the reason for the inaccuracy probably lies in the fact that the secondary scattered waves in the soil are represented by cylindrical waves and not by plane waves, while the latter are most likely more suitable to represent the responses at the flat ground surface at high frequencies. This observation motivates the study in this chapter, where we aim to verify the accuracy of the specific application of the method of conformal mapping (used throughout the thesis) in which the waves scattered from the half-space surface are represented by cylindrical waves that originate from an image source of a priori unknown intensity. To this end, a simple 2D problem of a circular cavity embedded in an elastic half-space subject to a harmonic anti-plane shear wave is considered. The performance of the indirect BEM is evaluated too for this model in view of the choice of the appropriate solution method for the second type of dynamic problem considered in this thesis (Chapter 4). In this chapter, we actually conduct a comparative analysis involving three methods: the method of images, the method of conformal mapping and the indirect BEM. As the considered model is two dimensional, the geometry is regular, and the excitation is an anti-plane shear wave, closed-form solutions can be obtained using the method of images. These closed-form solutions serve as benchmark results for evaluating the outcomes obtained by the other two methods. Our study aims to validate the accuracy of the specific application of the method of conformal mapping and of the indirect BEM, not only for specific parameters but also through a systematic evaluation encompassing a large range of system parameters. Such a comprehensive systematic evaluation of the method of conformal mapping and the indirect BEM for the 2D anti-plane shear wave case has not been undertaken previously.

This chapter is organised as follows. Section 3.2 provides a statement of the problem under consideration. The method of images, the method of conformal mapping, and the indirect BEM are presented in Sections 3.3, 3.4 and 3.5, respectively. In Section 3.6, we conduct convergence tests and validations. Section 3.7 presents comprehensive comparisons of the three methods, along with parametric studies and an evaluation of their accuracy. Specifically, we analyse the accuracy with respect to varying dimensionless frequency, the embedded depth of the cavity and the vertical incident angle. Additionally, we briefly discuss the effects of these three important factors on the system response. Finally, Section 3.8 summarises the conclusions of the study in this chapter.

3.2. PROBLEM STATEMENT

3.2.1. MODEL DESCRIPTION

In this chapter, we consider a two-dimensional (2D) problem of a cylindrical cavity embedded in an elastic half-space subject to a harmonic plane SH wave; as illustrated in Fig. 3.1. The half-space is modelled by an elastic continuum, which is assumed to be linear, elastic, homogeneous and isotropic. The soil domain is denoted as region Ω in Fig. 3.1. To facilitate the analysis, we employ six coordinate systems: global Cartesian (y, z) and polar (r, θ) coordinates with the origin at the free surface of the half-space, local Cartesian (y_1, z_1) and polar (r_1, θ_1) coordinates with the origin at the centre of the cavity, and local Cartesian (y_2, z_2) and polar (r_2, θ_2) coordinates originated at the centre of the image of the cavity. The image of the cavity is symmetrically positioned with respect to the free surface. The centre of the cavity, denoted as o_1, is located beneath the free surface at a depth of H, and its radius is represented by R. We define the vertical incident angle, θ_v, as the angle between the wave propagation direction and the positive vertical z axis.

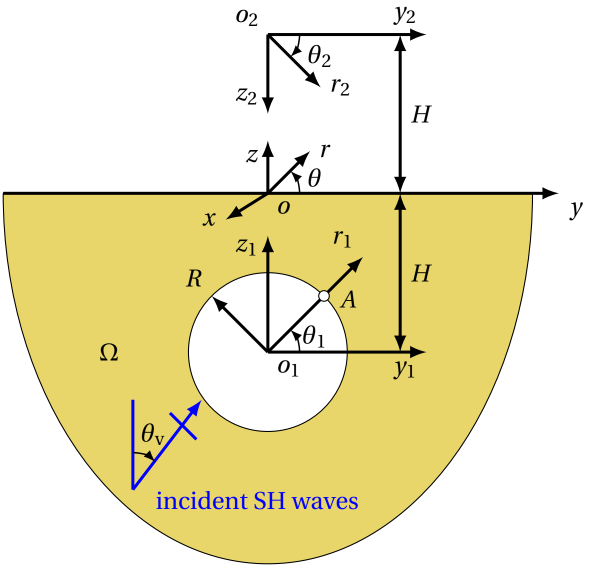

Figure 3.1: Model of a cylindrical cavity embedded in an elastic half-space subjected to a harmonic anti-plane shear wave including employed coordinate systems.

3.2.2. GOVERNING EQUATION AND BOUNDARY CONDITIONS

Considering our focus on the steady-state solution to the 2D anti-plane problem, we assume that both the excitations and responses of the system are harmonic and proportional to $e^{+i\omega t}$; i denotes the imaginary unit, t represents time, $\omega = 2\pi f$ is the angular frequency, and f is the frequency in Hz. For brevity, we omit the factor $e^{+i\omega t}$ in all subsequent expressions. The governing equation of motion of the soil medium in the frequency domain, in the absence of external forces, reads [Achenbach, 1973; Aki and Richards, 2002]

$$\mu\nabla^2 u = -\omega^2\rho_1 u, \tag{3.1}$$

where the symbols μ and ρ_1 signify the shear modulus and density of the soil, respectively; the operator ∇^2 denotes the 2D Laplace operator. As an example, in Cartesian coordinates, the Laplace operator can be expressed as $\nabla^2 = \partial_y^2 + \partial_z^2$. The variable u denotes the anti-plane displacement in the x direction.

The system is excited by seismic wave originating from beneath the cavity. Consequently, stress-free boundary conditions are imposed at both the free surface of the half-space and the cavity surface. These boundary conditions are written as follows:

$$\sigma_{zx} = 0, \qquad z = 0, \tag{3.2}$$

$$\sigma_{r_1 x_1} = 0, \qquad r_1 = R. \tag{3.3}$$

3.3. METHOD OF IMAGES

3.3.1. SOLUTION IN TERMS OF REAL VARIABLES

In the absence of the cavity, the wave field in the homogenous elastic half-space comprises incident and reflected plane waves. By considering the governing equation (see Eq. (3.1)) with the Laplace operator in Cartesian coordinates, we can determine the solution. The expressions for the incident and reflected plane waves are written as

$$u_{\text{inc}} = u_0 \exp\left(-i k_y y - i k_z z\right) = u_0 \exp\left(-i k_y r_1 \cos(\theta_1) - i k_z (r_1 \sin(\theta_1) - H)\right), \tag{3.4}$$

$$u_{\text{ref}} = u_0 \exp\left(-i k_y y + i k_z z\right) = u_0 \exp\left(-i k_y r_1 \cos(\theta_1) + i k_z (r_1 \sin(\theta_1) - H)\right), \tag{3.5}$$

where subscripts "inc" and "ref" indicate the incident and reflected plane waves; the wavenumbers in the horizontal and vertical directions are represented as $k_y = k_S \sin(\theta_v)$ and $k_z = k_S \cos(\theta_v)$, respectively; $k_S = \omega / c_S$ denotes the wavenumber of the SH wave, and $c_S = \sqrt{\mu/\rho_1}$ is the velocity of the shear wave; u_0 is the amplitude of the incident SH wave, and the amplitude of the reflected wave is equal to that of the incident wave (which can be proven easily using the method of images). Note that in Eqs. (3.4) - (3.8) the expressions given in terms of the global Cartesian coordinates will be used to compute responses at the half-space surface, while the expressions in terms of local polar coordinates will be used to compute responses at the cavity surface.

The presence of the cavity induces the scattering of elastic waves, resulting in the generation of scattered cylindrical waves denoted as $u_{s,1}$. The subscript "s, 1" signifies these waves as the 'directly scattered' waves propagating away from the cavity in the half-space. Upon interaction with the free surface of the half-space, these directly scattered waves give rise to secondary scattered waves referred to as $u_{s,2}$. The subscript "s, 2" designates these waves as the 'secondary scattered' waves. Employing the method of images, these secondary scattered waves are considered to originate from an image source, and its intensity is assumed identical to that of the directly scattered waves. The image source is located at the centre of the image of the cavity, positioned symmetrically with respect to the free surface.

To describe the waves propagating away from the cavity and its image, the method of separation of variables is employed to solve the wave equation shown in Eq. (3.1). We assume a harmonic variation in the azimuth, taking the form of $\exp(\mathrm{i}n\theta)$ [Graff, 1975; Kausel, 2006]. In order to satisfy the continuity condition at $\theta = 0$ and $\theta = 2\pi$, the parameter n is required to be an integer. Notably, for a fixed value of n, the radial behaviour is described by a Hankel function. Consequently, the general solution is constructed as an infinite series, commonly known as a wave-function expansion, which represents the entire scattered wave field. The scattered wave fields in the half-space are given as follows:

$$u_{\mathrm{s},1} = \sum_{n=-\infty}^{\infty} a_n H_n^{(2)}\left(k_{\mathrm{S}} r_1\right) \exp\left(\mathrm{i}n\theta_1\right), \tag{3.6}$$

$$u_{\mathrm{s},2} = \sum_{n=-\infty}^{\infty} a_n H_n^{(2)}\left(k_{\mathrm{S}} r_2\right) \exp\left(\mathrm{i}n\theta_2\right), \tag{3.7}$$

where

$$\begin{aligned} r_1 &= \sqrt{y^2 + \left(z+H\right)^2},\ \theta_1 = \arctan\left(\frac{z+H}{y}\right), \\ r_2 &= \sqrt{y^2 + \left(-z+H\right)^2} = \sqrt{r_1^2 + 4H^2 - 4Hr_1 \sin\left(\theta_1\right)}, \\ \theta_2 &= \arctan\left(\frac{-z+H}{y}\right) = \arctan\left(\frac{-r_1\sin\left(\theta_1\right) + 2H}{r_1\cos\left(\theta_1\right)}\right), \end{aligned} \tag{3.8}$$

and a_n denotes the unknown coefficients which will be determined from the boundary conditions; $H_n^{(2)}(..)$ denotes the Hankel function of the second kind and of order n. It represents for outgoing waves (propagating away from the cavity) accounting for the time-dependent factor $\mathrm{e}^{+\mathrm{i}\omega t}$. The coefficients for the secondary scattered cylindrical waves are identical to those of the directly scattered cylindrical waves, as determined using the method of images. It can be verified that the stress-free boundary condition at the ground surface as shown in Eq. (3.2), is satisfied exactly for both the pair of plane waves (i.e., u_{inc} and u_{ref}) and the pair of scattered cylindrical waves (i.e., $u_{\mathrm{s},1}$ and $u_{\mathrm{s},2}$). This verification confirms the correctness of applying the method of images. The total wave field is composed of the sum of the incident and reflected plane waves, as well as the directly and secondary scattered cylindrical waves:

$$u_{\mathrm{tot}} = u_{\mathrm{inc}} + u_{\mathrm{ref}} + u_{\mathrm{s},1} + u_{\mathrm{s},2}. \tag{3.9}$$

The expressions for stresses $\sigma_{r_1 x_1}$ and $\sigma_{\theta_1 x_1}$ (the latter is given in view of the results presented in Sections 3.6 and 3.7) are given as follows:

$$\begin{aligned}
\sigma_{r_1x_1} &= \mu\frac{\partial u_{\text{tot}}}{\partial r_1}\\
&= \mu\Big(-\mathrm{i}\,k_y\cos\left(\theta_1\right)-\mathrm{i}\,k_z\sin\left(\theta_1\right)\Big)\,u_{\text{inc}}+\mu\Big(-\mathrm{i}\,k_y\cos\left(\theta_1\right)+\mathrm{i}\,k_z\sin\left(\theta_1\right)\Big)\,u_{\text{ref}}\\
&+\mu\sum_{n=-\infty}^{\infty}a_n\left[-k_{\text{S}}H_{n+1}^{(2)}\left(k_{\text{S}}r_1\right)+\frac{n}{r_1}H_n^{(2)}\left(k_{\text{S}}r_1\right)\right]\exp\left(\mathrm{i}\,n\theta_1\right)\\
&+\mu\sum_{n=-\infty}^{\infty}a_n\left[\frac{r_1-2H\sin\left(\theta_1\right)}{r_2}\left[-k_{\text{S}}H_{n+1}^{(2)}\left(k_{\text{S}}r_2\right)+\frac{n}{r_2}H_n^{(2)}\left(k_{\text{S}}r_2\right)\right]\right]\exp\left(\mathrm{i}\,n\theta_2\right)\\
&+\mu\sum_{n=-\infty}^{\infty}a_n\left[\frac{2\,\mathrm{i}\,nH\cos\left(\theta_1\right)}{4Hr_1\sin\left(\theta_1\right)-4H^2-r_1^2}H_n^{(2)}\left(k_{\text{S}}r_2\right)\right]\exp\left(\mathrm{i}\,n\theta_2\right),
\end{aligned}\tag{3.10}$$

$$\begin{aligned}
\sigma_{\theta_1x_1} &= \mu\frac{1}{r_1}\frac{\partial u_{\text{tot}}}{\partial\theta_1}\\
&= \mu\Big(\mathrm{i}\,k_y\sin\left(\theta_1\right)-\mathrm{i}\,k_z\cos\left(\theta_1\right)\Big)\,u_{\text{inc}}+\mu\Big(\mathrm{i}\,k_y\sin\left(\theta_1\right)+\mathrm{i}\,k_z\cos\left(\theta_1\right)\Big)\,u_{\text{ref}}\\
&+\mu\sum_{n=-\infty}^{\infty}a_n\left[\frac{\mathrm{i}\,n}{r_1}H_n^{(2)}\left(k_{\text{S}}r_1\right)\right]\exp\left(\mathrm{i}\,n\theta_1\right)\\
&+\mu\sum_{n=-\infty}^{\infty}a_n\left[\frac{-2H\cos\left(\theta_1\right)}{r_2}\left[-k_{\text{S}}H_{n+1}^{(2)}\left(k_{\text{S}}r_2\right)+\frac{n}{r_2}H_n^{(2)}\left(k_{\text{S}}r_2\right)\right]\right]\exp\left(\mathrm{i}\,n\theta_2\right)\\
&+\mu\sum_{n=-\infty}^{\infty}a_n\left[\frac{\mathrm{i}\,n\Big(r_1-2H\sin\left(\theta_1\right)\Big)}{4Hr_1\sin\left(\theta_1\right)-4H^2-r_1^2}H_n^{(2)}\left(k_{\text{S}}r_2\right)\right]\exp\left(\mathrm{i}\,n\theta_2\right),
\end{aligned}\tag{3.11}$$

where u_{inc} and u_{ref} are the incident and reflected wave fields as shown in Eqs. (3.4) and (3.5), respectively.

3.3.2. SOLVING THE UNKNOWN COEFFICIENTS

As explained in Section 3.3.1, the boundary condition at the free surface is already satisfied by virtue of the method of images (and thus choosing the magnitudes of the scattered wave fields equal). Now, the unknown coefficients of the scattered cylindrical waves, as presented in Eqs. (3.6) and (3.7), are determined by enforcing the stress-free boundary condition at the cavity surface as given by Eq. (3.3). Based on this boundary condition, we obtain one algebraic equation with infinitely many unknowns:

$$\sum_{n=-\infty}^{\infty}k_nx_n=b,\tag{3.12}$$

where $x_n = a_n$ are the coefficients of the scattered cylindrical waves. Entries of k_n and b are functions of real variable θ_1. Their expressions can be easily derived but are not shown in this chapter for brevity (see Eqs. (3.8) and (3.10)).

By multiplying Eq. (3.12) with the complex conjugate of the circumferential basis functions $\exp(\mathrm{i}\,n\theta_1)$, integrating over the interval $[0,2\pi]$ and utilizing the orthogonality property wherever applicable, a set of algebraic equations is created:

$$\sum_{n=-\infty}^{\infty} k_{n,s} x_n = b_s, \tag{3.13}$$

where $s = \{0, \pm 1, \pm 2, ...\}$ and

$$k_{n,s} = \frac{1}{2\pi} \int_0^{2\pi} k_n(\theta_1) \exp(-\mathrm{i}\, s\theta_1)\, \mathrm{d}\theta_1, \tag{3.14}$$

$$b_s = \frac{1}{2\pi} \int_0^{2\pi} b(\theta_1) \exp(-\mathrm{i}\, s\theta_1)\, \mathrm{d}\theta_1. \tag{3.15}$$

For the wave field related to the directly scattered waves in the half-space (i.e., $u_{\mathrm{s},1}$ in Eq. (3.6)), orthogonality of the exponential functions can be employed (i.e., $k_{n,s} = 0$ for $s \neq n$). It is essential to account for finite maximum values of n and s to enable numerical evaluation of the unknown coefficients, necessitating the truncation of the sum over circumferential modes. If we use the same number of modes $2N+1$ for both the waves directly scattered by the cavity (i.e, $u_{\mathrm{s},1}$) and the secondary scattered waves (i.e, $u_{\mathrm{s},2}$), we use the following multiplication function:

$$\exp(-\mathrm{i}\, s\theta_1), \; s = \{0, \pm 1, \pm 2, ..., \pm N\}, \tag{3.16}$$

and the matrix equation that is formulated based on Eq. (3.12) becomes

$$[\mathbf{K}]_{(2N+1)\times(2N+1)} \, [\mathbf{x}]_{(2N+1)\times 1} = \left[\mathbf{b}\right]_{(2N+1)\times 1}. \tag{3.17}$$

3.4. METHOD OF CONFORMAL MAPPING

3.4.1. SOLUTION IN TERMS OF COMPLEX VARIABLES

The solution (see Eqs. (3.4)-(3.7)) to the governing equation is presented in terms of real variables in Section 3.3. However, to be able to apply the method of conformal mapping, we express the solution in terms of complex variables through the application of complex-variable theory. In this regard, we introduce a complex variable, denoted as $\kappa = y + \mathrm{i}\, z = r\mathrm{e}^{\mathrm{i}\theta}$, along with its conjugate, $\bar{\kappa} = y - \mathrm{i}\, z = r\mathrm{e}^{-\mathrm{i}\theta}$. By employing these complex variables, the lengths in the local coordinate systems r_1 and r_2 can be expressed in terms of κ and $\bar{\kappa}$, which are related to the global coordinate system through the following coordinate transformation:

$$\begin{aligned} r_1 &= |y_1 + \mathrm{i}\, z_1| = |y + \mathrm{i}(z + H)| = |\kappa + \mathrm{i}\, H|, \\ r_2 &= |y_2 + \mathrm{i}\, z_2| = |y + \mathrm{i}(-z + H)| = |\bar{\kappa} + \mathrm{i}\, H|. \end{aligned} \tag{3.18}$$

The arguments θ_1 and θ_2 of the local coordinates, present in Eqs. (3.6) and (3.7), can alternatively be written in terms of the complex variables κ and $\bar{\kappa}$ as

$$\mathrm{e}^{\mathrm{i}\theta_1} = \frac{y_1 + \mathrm{i}\, z_1}{r_1} = \frac{\kappa + \mathrm{i}\, H}{|\kappa + \mathrm{i}\, H|}, \; \mathrm{e}^{\mathrm{i}\theta_2} = \frac{y_2 + \mathrm{i}\, z_2}{r_2} = \frac{\bar{\kappa} + \mathrm{i}\, H}{|\bar{\kappa} + \mathrm{i}\, H|}. \tag{3.19}$$

As explained before, the secondary scattered waves, denoted as $u_{\mathrm{s},2}$, arise when the directly scattered waves encounter the free surface of the half-space. By employing the method of conformal mapping and following the principle of the method of images, we again represent these secondary scattered waves as cylindrical waves originating from a source located at the image of the cavity. However, the intensity of this source, denoted as b_n, is now assumed unknown and may in essence differ from that of the directly scattered wave (i.e., a_n). In the traditional application of the method of images (Section 3.3), b_n was set equal to a_n. It is important to note that while the method of images can be applied to the 2D anti-plane shear problem under consideration, it is not applicable to more complex problems such as 2D plane-strain and three-dimensional (3D) cases. In our previous work, we combined the method of conformal mapping and the spirit of the method of images to address these more complex problems, and choosing the coefficients of the primary and secondary scattered fields differently was a necessity. For that reason, a_n and b_n are not chosen the same a priori in the current analysis either. It will enable us to check the accuracy of the conformal mapping method for this simple problem; for the more complex problem, inaccuracies were observed at high frequency [Liu *et al.*, 2013; Zhao *et al.*, 2023].

The expressions of the incident and reflected plane waves and scattered cylindrical waves can be reformulated in terms of complex variables κ and $\bar{\kappa}$ as follows:

$$u_{\text{inc}} = u_0 \exp\left(C_{11}\kappa + C_{12}\bar{\kappa}\right), \tag{3.20}$$

$$u_{\text{ref}} = u_0 \exp\left(C_{21}\kappa + C_{22}\bar{\kappa}\right), \tag{3.21}$$

$$u_{\text{s},1} = \sum_{n=-\infty}^{\infty} a_n H_n^{(2)}\left(k_{\text{S}}\left|\kappa + \mathrm{i}H\right|\right)\left(\frac{\kappa + \mathrm{i}H}{\left|\kappa + \mathrm{i}H\right|}\right)^n, \tag{3.22}$$

$$u_{\text{s},2} = \sum_{n=-\infty}^{\infty} b_n H_n^{(2)}\left(k_{\text{S}}\left|\bar{\kappa} + \mathrm{i}H\right|\right)\left(\frac{\bar{\kappa} + \mathrm{i}H}{\left|\bar{\kappa} + \mathrm{i}H\right|}\right)^n, \tag{3.23}$$

where $C_{11} = C_{22} = -\left(\mathrm{i}k_y + k_z\right)/2$ and $C_{12} = C_{21} = -\left(\mathrm{i}k_y - k_z\right)/2$. To get the expressions for stresses associated with the plane waves in terms of κ and $\bar{\kappa}$, the chain rule is applied by first taking derivatives of the corresponding displacements with respect to y and z, and then with respect to κ and $\bar{\kappa}$. For stresses associated with the cylindrical waves, the expressions are derived using both the chain rule and the recurrence relations of Hankel functions (see Appendix C). The resulting expressions for stresses in terms of complex variables are as follows:

$$\begin{aligned}
\sigma_{zx} = \mu\frac{\partial u_{\mathrm{tot}}}{\partial z} &= \mathrm{i}\mu\left(\frac{\partial u_{\mathrm{tot}}}{\partial \kappa} - \frac{\partial u_{\mathrm{tot}}}{\partial \bar{\kappa}}\right) \\
&= \mathrm{i}\mu\left(C_{11} - C_{12}\right) u_{\mathrm{inc}} + \mathrm{i}\mu\left(C_{21} - C_{22}\right) u_{\mathrm{ref}} \\
&+ \mathrm{i}\mu\frac{k_{\mathrm{S}}}{2}\sum_{n=-\infty}^{\infty} a_n\left[H^{(2)}_{n-1}\left(k_{\mathrm{S}}\left|\kappa + \mathrm{i}H\right|\right)\left(\frac{\kappa + \mathrm{i}H}{\left|\kappa + \mathrm{i}H\right|}\right)^{n-1}\right] \\
&+ \mathrm{i}\mu\frac{k_{\mathrm{S}}}{2}\sum_{n=-\infty}^{\infty} a_n\left[H^{(2)}_{n+1}\left(k_{\mathrm{S}}\left|\kappa + \mathrm{i}H\right|\right)\left(\frac{\kappa + \mathrm{i}H}{\left|\kappa + \mathrm{i}H\right|}\right)^{n+1}\right] \\
&+ \mathrm{i}\mu\frac{k_{\mathrm{S}}}{2}\sum_{n=-\infty}^{\infty} b_n\left[-H^{(2)}_{n+1}\left(k_{\mathrm{S}}\left|\bar{\kappa} + \mathrm{i}H\right|\right)\left(\frac{\bar{\kappa} + \mathrm{i}H}{\left|\bar{\kappa} + \mathrm{i}H\right|}\right)^{n+1}\right] \\
&+ \mathrm{i}\mu\frac{k_{\mathrm{S}}}{2}\sum_{n=-\infty}^{\infty} b_n\left[-H^{(2)}_{n-1}\left(k_{\mathrm{S}}\left|\bar{\kappa} + \mathrm{i}H\right|\right)\left(\frac{\bar{\kappa} + \mathrm{i}H}{\left|\bar{\kappa} + \mathrm{i}H\right|}\right)^{n-1}\right],
\end{aligned} \tag{3.24}$$

$$\begin{aligned}
\sigma_{rx} = \mu\frac{\partial u_{\mathrm{tot}}}{\partial r} &= \mu\left(\mathrm{e}^{\mathrm{i}\theta}\frac{\partial u_{\mathrm{tot}}}{\partial \kappa} + \mathrm{e}^{-\mathrm{i}\theta}\frac{\partial u_{\mathrm{tot}}}{\partial \bar{\kappa}}\right) \\
&= \mu\left(\mathrm{e}^{\mathrm{i}\theta}C_{11} + \mathrm{e}^{-\mathrm{i}\theta}C_{12}\right) u_{\mathrm{inc}} + \mu\left(\mathrm{e}^{\mathrm{i}\theta}C_{21} + \mathrm{e}^{-\mathrm{i}\theta}C_{22}\right) u_{\mathrm{ref}} \\
&+ \mu\frac{k_{\mathrm{S}}}{2}\sum_{n=-\infty}^{\infty} a_n\left[\mathrm{e}^{\mathrm{i}\theta}H^{(2)}_{n-1}\left(k_{\mathrm{S}}\left|\kappa + \mathrm{i}H\right|\right)\left(\frac{\kappa + \mathrm{i}H}{\left|\kappa + \mathrm{i}H\right|}\right)^{n-1}\right] \\
&+ \mu\frac{k_{\mathrm{S}}}{2}\sum_{n=-\infty}^{\infty} a_n\left[-\mathrm{e}^{-\mathrm{i}\theta}H^{(2)}_{n+1}\left(k_{\mathrm{S}}\left|\kappa + \mathrm{i}H\right|\right)\left(\frac{\kappa + \mathrm{i}H}{\left|\kappa + \mathrm{i}H\right|}\right)^{n+1}\right] \\
&+ \mu\frac{k_{\mathrm{S}}}{2}\sum_{n=-\infty}^{\infty} b_n\left[-\mathrm{e}^{\mathrm{i}\theta}H^{(2)}_{n+1}\left(k_{\mathrm{S}}\left|\bar{\kappa} + \mathrm{i}H\right|\right)\left(\frac{\bar{\kappa} + \mathrm{i}H}{\left|\bar{\kappa} + \mathrm{i}H\right|}\right)^{n+1}\right] \\
&+ \mu\frac{k_{\mathrm{S}}}{2}\sum_{n=-\infty}^{\infty} b_n\left[\mathrm{e}^{-\mathrm{i}\theta}H^{(2)}_{n-1}\left(k_{\mathrm{S}}\left|\bar{\kappa} + \mathrm{i}H\right|\right)\left(\frac{\bar{\kappa} + \mathrm{i}H}{\left|\bar{\kappa} + \mathrm{i}H\right|}\right)^{n-1}\right],
\end{aligned} \tag{3.25}$$

$$
\begin{aligned}
\sigma_{\theta x} = \mu \frac{1}{r}\frac{\partial u_{\text{tot}}}{\partial \theta} &= \mathrm{i}\mu\left(\mathrm{e}^{\mathrm{i}\theta}\frac{\partial u_{\text{tot}}}{\partial \kappa} - \mathrm{e}^{-\mathrm{i}\theta}\frac{\partial u_{\text{tot}}}{\partial \bar{\kappa}}\right) \\
&= \mathrm{i}\mu\left(\mathrm{e}^{\mathrm{i}\theta}C_{11} - \mathrm{e}^{-\mathrm{i}\theta}C_{12}\right)u_{\text{inc}} + \mathrm{i}\mu\left(\mathrm{e}^{\mathrm{i}\theta}C_{21} - \mathrm{e}^{-\mathrm{i}\theta}C_{22}\right)u_{\text{ref}} \\
&+ \mathrm{i}\mu\frac{k_{\text{S}}}{2}\sum_{n=-\infty}^{\infty} a_n\left[\mathrm{e}^{\mathrm{i}\theta}H^{(2)}_{n-1}\left(k_{\text{S}}\left|\kappa+\mathrm{i}H\right|\right)\left(\frac{\kappa+\mathrm{i}H}{\left|\kappa+\mathrm{i}H\right|}\right)^{n-1}\right] \\
&+ \mathrm{i}\mu\frac{k_{\text{S}}}{2}\sum_{n=-\infty}^{\infty} a_n\left[\mathrm{e}^{-\mathrm{i}\theta}H^{(2)}_{n+1}\left(k_{\text{S}}\left|\kappa+\mathrm{i}H\right|\right)\left(\frac{\kappa+\mathrm{i}H}{\left|\kappa+\mathrm{i}H\right|}\right)^{n+1}\right] \\
&+ \mathrm{i}\mu\frac{k_{\text{S}}}{2}\sum_{n=-\infty}^{\infty} b_n\left[-\mathrm{e}^{\mathrm{i}\theta}H^{(2)}_{n+1}\left(k_{\text{S}}\left|\bar{\kappa}+\mathrm{i}H\right|\right)\left(\frac{\bar{\kappa}+\mathrm{i}H}{\left|\bar{\kappa}+\mathrm{i}H\right|}\right)^{n+1}\right] \\
&+ \mathrm{i}\mu\frac{k_{\text{S}}}{2}\sum_{n=-\infty}^{\infty} b_n\left[-\mathrm{e}^{-\mathrm{i}\theta}H^{(2)}_{n-1}\left(k_{\text{S}}\left|\bar{\kappa}+\mathrm{i}H\right|\right)\left(\frac{\bar{\kappa}+\mathrm{i}H}{\left|\bar{\kappa}+\mathrm{i}H\right|}\right)^{n-1}\right].
\end{aligned}
\tag{3.26}
$$

The stresses σ_{rx} and $\sigma_{\theta x}$ are represented in terms of the global coordinates, as shown in Eqs. (3.25)-(3.26). To validate the appropriateness of using these expressions for stresses at the cavity surface, we also provide the expressions of stresses at the cavity surface in the local coordinates (note that the boundary condition in Eq. (3.3) contains the stress in the local coordinate system). The complex variables κ and $\bar{\kappa}$ can be expressed as functions of the local coordinates, yielding the following formulations:

$$
\begin{aligned}
\kappa &= y + \mathrm{i}z = y_1 + \mathrm{i}(z_1 - H) = r_1\mathrm{e}^{\mathrm{i}\theta_1} - \mathrm{i}H, \\
\bar{\kappa} &= y - \mathrm{i}z = y_1 - \mathrm{i}(z_1 - H) = r_1\mathrm{e}^{-\mathrm{i}\theta_1} + \mathrm{i}H.
\end{aligned}
\tag{3.27}
$$

The expressions of stresses at the cavity surface in terms of the local coordinates are presented below:

$$
\sigma_{r_1 x_1} = \mu\frac{\partial u_{\text{tot}}}{\partial r_1} = \mu\left(\mathrm{e}^{\mathrm{i}\theta_1}\frac{\partial u_{\text{tot}}}{\partial \kappa} + \mathrm{e}^{-\mathrm{i}\theta_1}\frac{\partial u_{\text{tot}}}{\partial \bar{\kappa}}\right), \tag{3.28}
$$

$$
\sigma_{\theta_1 x_1} = \mu\frac{1}{r_1}\frac{\partial u_{\text{tot}}}{\partial \theta_1} = \mathrm{i}\mu\left(\mathrm{e}^{\mathrm{i}\theta_1}\frac{\partial u_{\text{tot}}}{\partial \kappa} - \mathrm{e}^{-\mathrm{i}\theta_1}\frac{\partial u_{\text{tot}}}{\partial \bar{\kappa}}\right). \tag{3.29}
$$

Upon examining Eqs. (3.25), (3.26), (3.28) and (3.29), we observe that the difference between the stress expressions in the global and local coordinates lies solely in the exponential terms. The former employ $\mathrm{e}^{\mathrm{i}\theta}$ and $\mathrm{e}^{-\mathrm{i}\theta}$, while the latter employ $\mathrm{e}^{\mathrm{i}\theta_1}$ and $\mathrm{e}^{-\mathrm{i}\theta_1}$. The exponential terms $\mathrm{e}^{\mathrm{i}\theta_1}$ and $\mathrm{e}^{\mathrm{i}\theta}$ are given in Eqs. (3.19) and (3.31), respectively. The exponential terms $\mathrm{e}^{-\mathrm{i}\theta}$ and $\mathrm{e}^{-\mathrm{i}\theta_1}$ are not explicitly provided in this chapter, but they can be derived straightforwardly. Strictly speaking, the expressions for the stress components in the boundary condition at the cavity surface should be formulated in terms of local coordinates. However, it can be verified that the numerical outcomes obtained using the expressions in terms of the global coordinates coincide with those acquired using expressions in terms of the local coordinates. The explanation is that the stresses at the cavity surface (a local position) can be correctly calculated by considering $\zeta = \beta e^{i\theta}$ when the expressions in terms of the global coordinates are used. The definition of ζ is given in Section 3.4.2, and $|\zeta| = \beta$ corresponds to the the cavity surface. Consequently, we conclude that utilising stress expressions in the global coordinates (for example, σ_{rx} and $\sigma_{\theta x}$) to evaluate the responses in the local coordinate system (for example, $\sigma_{r_1 x_1}$ and $\sigma_{\theta_1 x_1}$ at the cavity surface) is valid when employing the method of conformal mapping, as long as the radius in the image domain is chosen appropriately. Here, $|\zeta| = 1$ and $|\zeta| = \beta$ refer to the flat surface and cavity surface, respectively; see Section 3.4.2.

3.4.2. CONFORMAL MAPPING

Fig. 3.1 illustrates the presence of two distinct boundary surfaces in the model, namely, a flat free surface and a circular surface representing the cavity. The existence of these dissimilar boundary types typically poses a challenge when solving the corresponding boundary value problem. To overcome this challenge, the method of conformal mapping is employed, enabling the mapping of the original domain with its boundary surfaces of different types onto an image domain with boundary surfaces of the same type. The utilisation of conformal mapping function is demonstrated in this section.

In Section 3.4.1, we introduced the complex variable κ and its conjugate $\bar{\kappa}$ in the original physical domain. Now, we introduce a new complex variable $\zeta = \xi + i\eta = \rho e^{i\vartheta}$ and its conjugate $\bar{\zeta} = \xi - i\eta = \rho e^{-i\vartheta}$, both defined in the image domain. To establish the relationship between the two complex variables κ and ζ in the original and image domains, we employ a conformal mapping function denoted as $w(\zeta)$, which is expressed as follows:

$$\kappa = w(\zeta) = -iG\frac{1+\zeta}{1-\zeta}, \tag{3.30}$$

where $G = H\left(1-\beta^2\right)/\left(1+\beta^2\right)$, $\beta = H/R - \sqrt{\left(H/R\right)^2 - 1}$. Accordingly, the region Ω (as depicted in Fig. 3.1) is mapped onto region Γ in the image domain (as shown in Fig. 3.2). The free surface of the half-space $z = 0$ and the cavity surface $r_1 = R$ correspond to surfaces defined by circles $|\zeta| = 1$ and $|\zeta| = \beta$, respectively. Notably, the boundary surfaces in the image domain are of the the same type as they are concentric.

The mapping of the region Ω in the physical domain onto the region Γ in the image domain is conformal and reversible. It can be easily proven that the mapping function $w(\zeta)$ is analytic (except at a single point ($\rho = 1, \vartheta = 0$) that corresponds to points at infinity in the physical domain). Additionally, the derivatives of $w(\zeta)$ with respect to the complex variable ζ, denoted as $w'(\zeta)$, is not zero.

In general, mapping functions introduce a phase shift between the complex variables in the two domains. For a given conformal mapping function $\kappa = w(\zeta)$, the relationship between the coordinate θ in the physical domain and the coordinate ϑ in the image domain is defined as [Muskhelishvili, 1966]:

$$e^{i\theta} = \frac{\zeta}{\rho}\frac{w'(\zeta)}{|w'(\zeta)|} = e^{i\vartheta}\frac{w'(\zeta)}{|w'(\zeta)|}. \tag{3.31}$$

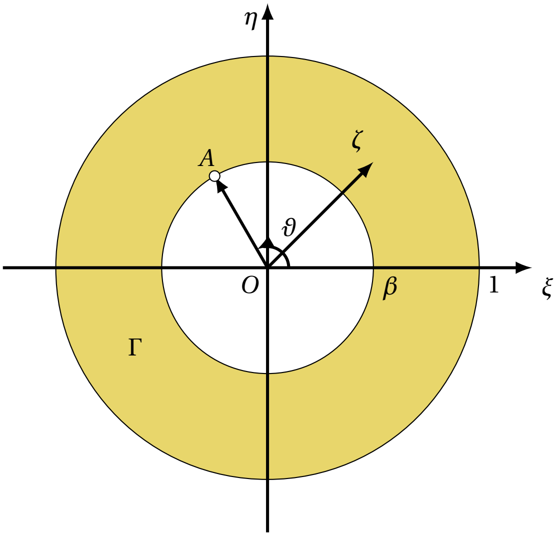

Figure 3.2: Image domain.

3.4.3. SOLVING THE UNKNOWNS COEFFICIENTS

As shown in Section 3.4.1, the displacement and stresses are formulated in terms of complex variables κ and $\bar{\kappa}$. However, to address the problem in the image domain, it is necessary to express the displacement and stresses in terms of the complex variables ζ and $\bar{\zeta}$. This can be achieved by taking the derivatives of the displacement with respect to κ and $\bar{\kappa}$ (see Eqs. (C.3)-(C.6)), and subsequently replacing the complex variables κ and $\bar{\kappa}$ by the mapping function (see Eq. (3.30)) and its conjugate. For the sake of brevity, the expressions for the displacements and stresses in terms of ζ and $\bar{\zeta}$ are not presented in this thesis. By utilising the expressions for stresses σ_{zx} and σ_{rx} in terms of complex variables ζ and $\bar{\zeta}$, we establish a system of algebraic equations based on the boundary conditions (Eq. (3.2) and (3.3)):

$$\sum_{i=1}^{2}\sum_{n=-\infty}^{\infty} k_n^{(j,i)}(\vartheta)\, x_n^{(i)} = b^{(j)}(\vartheta), \tag{3.32}$$

where $x_n^{(1)} = a_n$ and $x_n^{(2)} = b_n$; $i = \{1,2\}$ indicate the terms related to the corresponding cylindrical waves; see Eqs. (3.22) and (3.23). Additionally, $j = \{1,2\}$ denote the stress-free boundary conditions at the flat surface and at the cavity surface, respectively. Entries of $k_n^{(j,i)}$ and $b^{(j)}$ are functions dependent on complex variables ζ and $\bar{\zeta}$, and their detailed formulations can be found in Appendix E.

By multiplying Eq. (3.32) with the complex conjugate of the circumferential basis functions $\exp(\mathrm{i}\, n\vartheta)$, which appears in the expression for the potentials of the cylindrical waves, integrating over the interval $[0, 2\pi]$ and applying the orthogonality property wherever applicable, we obtain

$$\sum_{i=1}^{2}\sum_{n=-\infty}^{\infty} k_{n,s}^{(j,i)}\, x_n^{(i)} = b_s^{(j)}, \tag{3.33}$$

where $s = \{0, \pm 1, \pm 2, ...\}$ and

$$k_{n,s}^{(j,i)} = \frac{1}{2\pi} \int_0^{2\pi} k_n^{(j,i)}(\vartheta) \exp(-\mathrm{i}\, s\vartheta) \,\mathrm{d}\vartheta, \tag{3.34}$$

$$b_s^{(j)} = \frac{1}{2\pi} \int_0^{2\pi} b^{(j)}(\vartheta) \exp(-\mathrm{i}\, s\vartheta) \,\mathrm{d}\vartheta. \tag{3.35}$$

For the potentials associated with the directly scattered waves in the half-space (Eq. (3.22)), we can employ the orthogonality of the exponential functions (i.e., $k_{n,s}^{(ji)} = 0$ for $s \neq n$, and $i = \{1,2\}$). To evaluate the unknown coefficients, the maximum values of n and s need to be finite, requiring the truncation of the sum over circumferential modes. We utilise the same number of modes $2N+1$ for both the waves directly scattered by the cavity ($u_{\mathrm{s},1}$) and the secondary scattered waves ($u_{\mathrm{s},2}$). In this regard, we employ the following multiplication function:

$$\exp(-\mathrm{i}\, s\vartheta),\; j = \{1,2\};\; s = \{0, \pm 1, \pm 2, ..., \pm N\}. \tag{3.36}$$

The matrix equation that is formulated based on Eq. (3.33) reads

$$[\mathbf{K}]_{2(2N+1)\times 2(2N+1)}\, [\mathbf{x}]_{2(2N+1)\times 1} = \left[\mathbf{b}\right]_{2(2N+1)\times 1}. \tag{3.37}$$

In this analysis, the unknown coefficients are determined using Matlab. Through numerical analysis, it can be verified that b_n is nearly exactly the same as a_n when applying the method of conformal mapping. This observation serves as evidence for the validity and accuracy of the method of conformal mapping as well as its implementation, as this should be the case in order to respect the boundary condition at the half-space surface, as argued in Section 3.3.1.

3.5. INDIRECT BOUNDARY ELEMENT METHOD

Next, we utilise the indirect BEM to calculate the response of the system. To achieve this, the Green's functions of the soil are required; note that the indirect BEM relies on the Green's functions of the soil in the absence of a cavity (i.e., half-space configuration). Section 3.5.1 presents these Green's functions. The formulation of the indirect BEM is then outlined in Section 3.5.2.

3.5.1. GREEN'S FUNCTIONS OF THE SOIL

In our work, we use the 2D Green's functions based on the so-called two-and-a-half dimensional Green's functions of an elastodynamic full-space [Tadeu and Kausel, 2000] and a half-space [Tadeu *et al.*, 2001]. The 2D case can be recovered by setting $k_x = 0$; k_x is the wavenumber in the longitudinal direction. These Green's functions are employed in conjunction with a specific source configuration described in the reference papers. For the 2D SH case, the source is characterised by a harmonic line load $f_x(y,z) = F_x \delta(y - y_{\mathrm{s}})\delta(z - z_{\mathrm{s}}) \exp(\mathrm{i}(\omega t))$. Here, f_x denotes the load in x direction, F_x represents source amplitude, the subscript “s" denotes the coordinates of the source point, and ω is the excitation angular frequency. It is noted that the Green's functions can be obtained by setting F_x to 1.

The Green's function of the half-space is composed of a source term which is identical to that of the full-space, and a surface term that is required to satisfy the boundary condition at the stress-free half-space surface [Tadeu *et al.*, 2001]. However, we observed that the Green's function presented in Tadeu *et al.* [2001] fails to satisfy the stress-free condition, while it is satisfied when the source term is replaced by the one presented in Tadeu and Kausel [2000]. As a result, the Green's functions of the half-space employed in this study consist of the source term from Tadeu and Kausel [2000] and the surface term from Tadeu *et al.* [2001].

Because the reference frames in Tadeu *et al.* [2001] are different from that in the current chapter, the displacement and stresses given in Tadeu *et al.* [2001] are transformed through the following relations: $u = u_{\text{ref}}$, $\sigma_{r_1 x_1} = \sigma_{r_1 x_1,\text{ref}}$ and $\sigma_{\theta_1 x_1} = -\sigma_{\theta_1 x_1,\text{ref}}$. The subscript "ref" denotes the responses defined in the coordinate system of the reference paper.

3.5.2. FORMULATION OF THE INDIRECT BOUNDARY ELEMENT METHOD

This section presents the formulation of the indirect BEM used in this study. Following the principles of the indirect BEM, the displacement and stress vectors in the soil are determined as described by Luco and de Barros [Luco and de Barros, 1994b; Zhao *et al.*, 2021]

$$\mathbf{U}(\mathbf{x}_\text{r}) = \int_{L_\text{s}} \mathbf{G}_u\left(\mathbf{x}_\text{r},\mathbf{x}_\text{s}\right)\mathbf{F}\left(\mathbf{x}_\text{s}\right)\,\mathrm{d}l\left(\mathbf{x}_\text{s}\right), \tag{3.38}$$

$$\Sigma(\mathbf{x}_\text{r}) = \int_{L_\text{s}} \mathbf{G}_\sigma(\mathbf{x}_\text{r},\mathbf{x}_\text{s})\mathbf{F}\left(\mathbf{x}_\text{s}\right)\,\mathrm{d}l\left(\mathbf{x}_s\right), \tag{3.39}$$

where $\mathbf{F}\left(\mathbf{x}_\text{s}\right)$ represents the vector of the unknown source amplitudes placed within the fictitious cavity, which is commonly used in the indirect BEM (see Fig. 3.3). Vectors $\mathbf{x}_\text{s} = [y_\text{s}, z_\text{s}]$ and $\mathbf{x}_\text{r} = [y_\text{r}, z_\text{r}]$ denote the coordinates of the source and receiver points, respectively. The surface L_s corresponds to the location of the source points, with its radius defined as $R_\text{s} = R_\text{o} - 3(2\pi R_\text{o}/N_\text{r})$. Here, N_r represents the number of the receiver points, and it is recommended to have $N_\text{r} \geqslant 20$ as suggested in Luco and de Barros [1994b]. The receiver points are situated on the surface L_r at $r_1 = R$, which corresponds to the cavity surface. $\mathbf{G}_u$ and $\mathbf{G}_\sigma$ are matrices containing the Green's functions for displacement and stress $\sigma_{r_1 x_1}$ of the soil without tunnel/cavity (i.e., of the half-space), respectively, and they are matrices with dimensions of $(N_\text{r} \times N_\text{s})$. N_s represents the number of the source points.

By considering the stress-free boundary condition at the cavity surface (see Eq. (3.3)), we proceed to derive the boundary integral equation expressed in relation to the vector of the unknown source amplitudes:

$$\int_{L_\text{s}} \mathbf{K}\left(\mathbf{x}_\text{r},\mathbf{x}_\text{s}\right)\mathbf{F}\left(\mathbf{x}_\text{s}\right)\,\mathrm{d}l\left(\mathbf{x}_\text{s}\right) = \mathbf{R}\left(\mathbf{x}_\text{r}\right), \tag{3.40}$$

where

$$\begin{aligned}
&\mathbf{K}\left(\mathbf{x}_\text{r},\mathbf{x}_\text{s}\right) = \mathbf{G}_\sigma(\mathbf{x}_\text{r},\mathbf{x}_\text{s}),\\
&\mathbf{R}\left(\mathbf{x}_\text{r}\right) = -\mu\left(-\mathrm{i}\,k_y\cos\left(\theta_1\right) - \mathrm{i}\,k_z\sin\left(\theta_1\right)\right)u_{\text{inc}} - \mu\left(-\mathrm{i}\,k_y\cos\left(\theta_1\right) + \mathrm{i}\,k_z\sin\left(\theta_1\right)\right)u_{\text{ref}}.
\end{aligned} \tag{3.41}$$

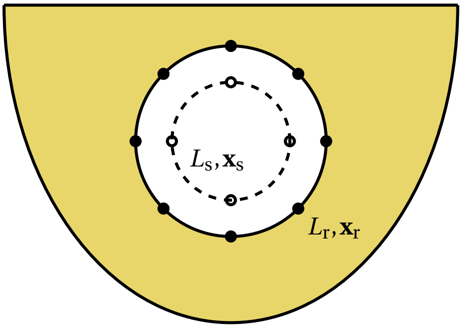

Figure 3.3: The elastic half-space with a fictitious cavity. The source (open circles) and receiver (filled circles) points are located at surfaces L_s (dashed line) and L_r (solid line), respectively.

It should be noted that the matrix associated with **K** has dimensions of $(N_r \times N_s)$. Consequently, this matrix is relatively small, and the inversion process is not time-consuming. The most computationally intensive aspect (even throughout the entire seismic wave analysis procedure) is the evaluation of integrals over the horizontal wavenumber k_y in the Green's function of the half-space, for which we employ the "quadv" routine in Matlab. Note that after solving Eq. (3.40), one can compute the shear stress $\sigma_{\theta_1 x_1}$ at the cavity surface using Eq. (3.39) provided that the corresponding Green's function matrix for stress $\sigma_{\theta_1 x_1}$ of the half-space is used.

3.6. VALIDATIONS

Before conducting the analysis, it is essential to perform convergence tests for the three methods: the method of images, the method of conformal mapping and the indirect BEM. In the subsequent presentation of results, the anti-plane displacement and shear stress are normalised. Specifically, the displacement is normalised as follows:

$$U = u/u_0, \tag{3.42}$$

where u denotes the anti-plane displacement, and u_0 is the amplitude of the displacement associated with the incident SH wave. The normalised stress is given as

$$\Sigma_{\theta_1 x_1} = \sigma_{\theta_1 x_1} / \left[\omega \rho_1 c_S u_0\right]. \tag{3.43}$$

To assess the convergence of the methods, we examine the displacement U at the surface of the half-space and the shear stress $\Sigma_{\theta_1 x_1}$ at the cavity. The parameters of the soil medium are as follows: $E = 3.26 \times 10^7$ Pa and $\rho_1 = 1932$ kg/m^3. The geometry of the cavity is as follows: $R = 5$ m and $H/R = 1.5$. The system is subjected to a vertically $(\theta_V = 0^{\circ})$ incident SH wave and $\eta = 0.5$, where η is the dimensionless frequency and is defined as $\eta = \omega R / (\pi c_S)$. Fig. 3.4 illustrates the results of the convergence tests. For the method of images and the method of conformal mapping, convergence is observed at $N = 3$ and $N = 5$, respectively. In the case of the indirect BEM, converged results are obtained with $(N_s, N_r) = (20, 40)$. Note that the convergence tests indicate that different

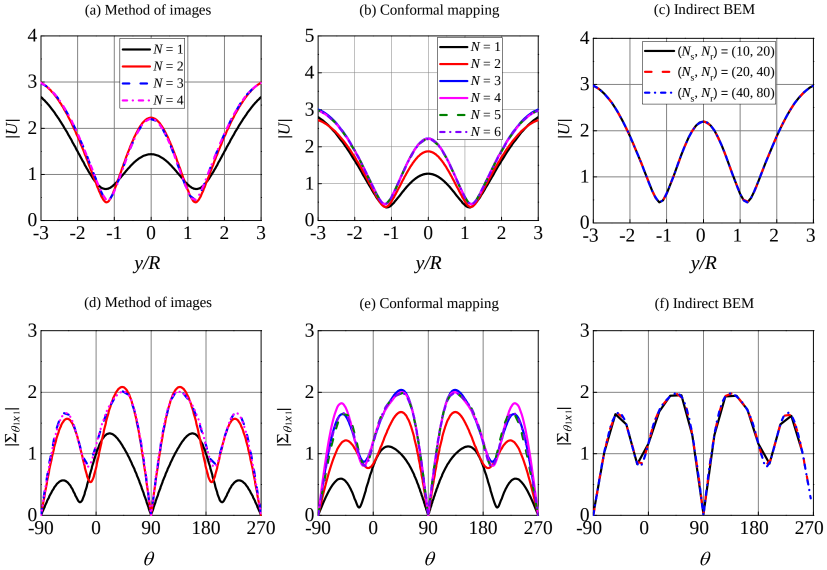

Figure 3.4: Convergence tests for three methods: (a) (b) (c) anti-plane displacement U at the half-space surface $z = 0$ and (d) (e) (f) shear stress $\Sigma_{\theta_1 x_1}$ at $r_1 = R$. The system parameters considered in these tests are $\eta = 0.5$, $H/R = 1.5$ and $\theta_\mathrm{v} = 0^\circ$.

methods may need a different number of circumferential modes to converge (also see Section 3.7.1).

To assess the accuracy of the three methods, we present two validation examples. In the first example, we consider a medium frequency case with $\eta = 0.5$ (the corresponding dimensional frequency is 6.49 Hz) as depicted in Fig. 3.5. The results obtained using the three methods align well with the results in the literature [Luco and de Barros, 1994b] for both shallow and deep embedded cavities.

Fig. 3.6 presents the second validation example, which corresponds to a high frequency case with $\eta = 1.0$ (the corresponding dimensional frequency is 12.99 Hz). The results obtained using the three methods exhibit a perfect agreement, thereby affirming the accuracy of these methods. Furthermore, Figs. 3.5 and 3.6 demonstrate that the excitation frequency and the embedded depth of the cavity have a significant influence on the distribution and amplitude of the responses at both the half-space surface and the cavity surface. In Section 3.7, we will thoroughly investigate the effect of these two parameters, as well as the vertical incident angle, on the response of the system.

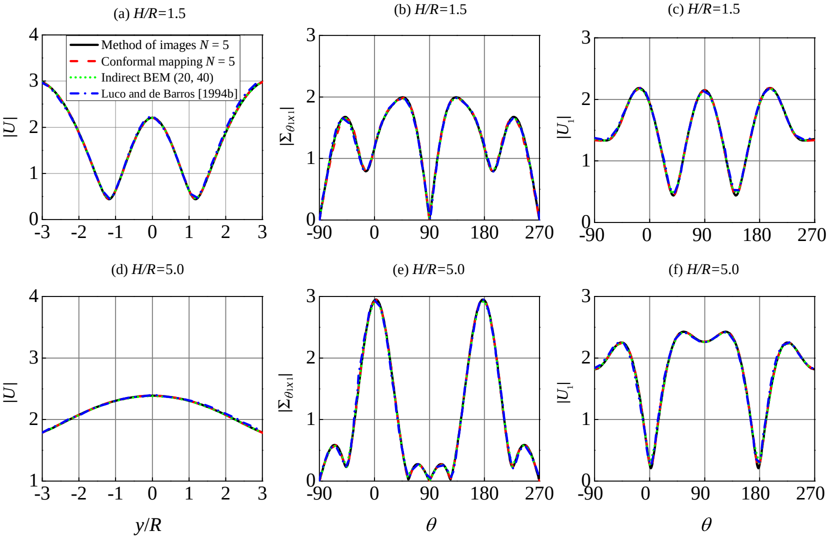

Figure 3.5: The first validation example with $\eta = 0.5$: (a) (d) anti-plane displacement at the ground surface U at $z = 0$, (b) (e) shear stress $\Sigma_{\theta_1 x_1}$ at $r_1 = R$, and (c) (f) anti-plane displacement U_1 at $r_1 = R$ for a shallow $(H/R = 1.5)$ and deep $(H/R = 5)$ embedded cavity, respectively. $\theta_\mathrm{v} = 0^\circ$.

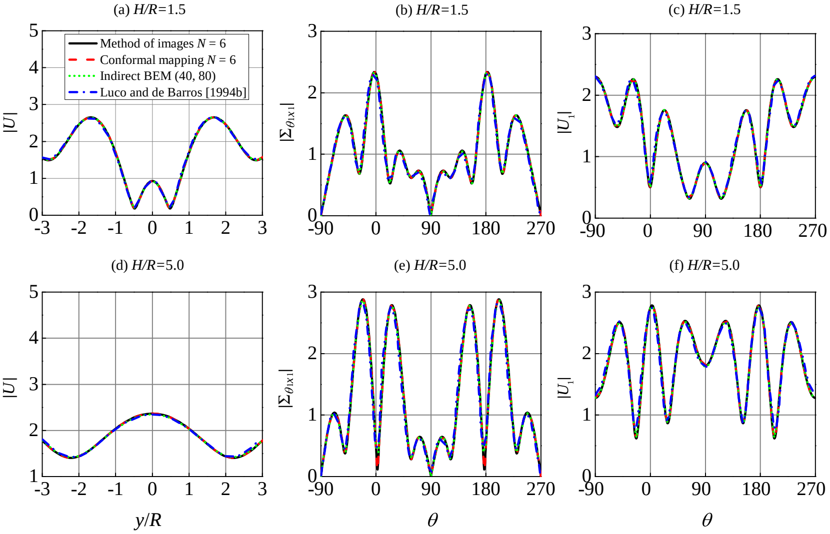

Figure 3.6: The second validation example with $\eta = 1.0$: (a) (d) anti-plane displacement at the ground surface U at $z = 0$, (b) (e) shear stress $\Sigma_{\theta_1 x_1}$ at $r_1 = R$, and (c) (f) anti-plane displacement U_1 at $r_1 = R$ for a shallow $(H/R = 1.5)$ and deep $(H/R = 5)$ embedded cavity, respectively. $\theta_\mathrm{v} = 0^\circ$.

3.7. COMPARISONS AND PARAMETRIC STUDIES

3.7.1. COMPARISONS

In this section, we present a comparative analysis of the three methods. The considered parameters are $H/R = 5.0$ and $\theta_{\mathrm{v}} = 0^{\circ}$. Table 3.1 provides a summary of the comparisons focusing on the number of circumferential modes required for convergence in the method of images and the method of conformal mapping, and the numbers of the source and receiver points needed for convergence in the indirect BEM. We observe that both the method of images and the method of conformal mapping achieve convergence with a small number of circumferential modes. Furthermore, these two methods require the same number of circumferential modes to obtain converged results at dimensionless frequencies of 1.0 and 2.0. However, at a dimensionless frequencies of 0.5 and 3.0, the method of conformal mapping requires two and one additional circumferential modes compared to the method of images, respectively. This indicates that the method of images may converge faster than the method of conformal mapping, see also Fig. 3.4. The reason is that the accuracy of the method of images is higher. The computed a_n and b_n turn out to be very close but not exactly the same in the method of conformal mapping, which is a result of small inaccuracies in the corresponding matrix inversion.

In this analysis, the unknown coefficients were solved using Matlab. The calculations were performed on a laptop equipped with Intel Core i7-12800H/2.4 GHz CPU. Table 3.2 presents the computational time required for the three methods. The results demonstrate that the method of images exhibits higher efficiency compared to the method of conformal mapping. On the other hand, the indirect BEM necessitates significantly more computational time, making it the least efficient among the three methods.

Table 3.1: The required number of circumferential modes N or the number of source and receiver points $(N_{\mathrm{s}}, N_{\mathrm{r}})$ to achieve converged results for different methods and different dimensionless frequencies.

Methods	$\eta = 0.5$	$\eta = 1.0$	$\eta = 2.0$	$\eta = 3.0$
Method of images	$N = 3$	$N = 6$	$N = 10$	$N = 12$
Method of conformal mapping	$N = 5$	$N = 6$	$N = 10$	$N = 13$
Indirect BEM	$(N_{\mathrm{s}}, N_{\mathrm{r}}) = (20, 40)$	$(N_{\mathrm{s}}, N_{\mathrm{r}}) = (40, 80)$	$(N_{\mathrm{s}}, N_{\mathrm{r}}) = (60, 120)$	$(N_{\mathrm{s}}, N_{\mathrm{r}}) = (60, 120)$

Table 3.2: The computational time required for different methods and different dimensionless frequencies.

Methods	$\eta = 0.5$	$\eta = 1.0$	$\eta = 2.0$	$\eta = 3.0$
Method of images	$t = 0.15$ (s)	$t = 0.18$ (s)	$t = 0.46$ (s)	$t = 0.73$ (s)
Method of conformal mapping	$t = 5.06$ (s)	$t = 5.83$ (s)	$t = 16.46$ (s)	$t = 39.38$ (s)
Indirect BEM	$t = 48.46$ (s)	$t = 99.81$ (s)	$t = 241.53$ (s)	$t = 269.03$ (s)

3.7.2. DIMENSIONLESS FREQUENCY

As discussed in Sections 3.6 and 3.7.1, all three methods demonstrate accurate performance for the individual frequencies considered. However, for the 3D wave scattering problem (Chapter 2), it has been shown that accurate results cannot be obtained at high frequencies using the method of conformal mapping while the indirect BEM can provide accurate results. In this section, we further investigate the accuracy of the specific application of the method of conformal mapping (in which the waves scattered from the half-space surface are represented by cylindrical waves that originate from an image source of a priori unknown intensity) and the indirect BEM within specified ranges of the dimensionless frequency, the embedded depth of the cavity and the vertical incident angle. The solutions obtained by the method of images are taken as the benchmark solutions. Moreover, we examine the effects of the three system parameters on the system response. The parameters of the soil medium are as follows: $E = 3.26 \times 10^7$ Pa and $\rho_1 = 1932$ kg/m^3. The geometry of the cavity is that: $R = 5$ m. The base-case parameters are set as $\eta = 0.5$, $H/R = 5.0$ and $\theta_{\mathrm{v}} = 0^{\circ}$. In the following analysis, we present the maximum absolute value of the displacement U at the ground surface within the range $y/R = [-4, 4]$, as well as the maximum absolute values of the shear stress $\Sigma_{\theta_1 x_1}$ and the displacement U_1 at the cavity surface.

The considered dimensionless frequencies are in the range of $\eta = 0.002 - 3.0$, corresponding to $f = 0.16 - 244.85$ Hz. While the low-frequency range is typically of interest for seismic wave problems, we also investigate high frequencies to evaluate the applicability of the methods for other, high-frequency loadings. Fig. 3.7 illustrates that the results obtained by the three methods coincide, indicating accurate performance of the method of conformal mapping and the indirect BEM across the entire range of the dimensionless frequency. In contrast to the 3D case (Chapter 2), the method of conformal mapping demonstrates accurate behavior at high frequencies for the 2D SH problem under consideration. Notably, the method of conformal mapping exhibits superior performance in the simpler 2D SH case than in the the more complex 3D case. The discrepancy can be attributed to the fact that the secondary scattered waves in the soil are represented by cylindrical waves originating from the image source, and not by plane waves, while the latter are most likely more suitable to represent the response (in the 3D case) at the flat ground surface at high frequencies; the relatively poor representation leads to a larger condition number of the matrix that needs to be inverted, which in turns leads to inaccurate results. In any case, we can ascertain the accuracy of the method of conformal mapping and the indirect BEM for the current problem, as the obtained the results align with the closed-form solutions.

The frequency-response curves are shown in Fig. 3.7. The displacement at the ground surface shows an increasing trend with increasing dimensionless frequency, while the displacement and shear stress at the cavity surface exhibit a decreasing trend. The response curves display many resonances, some of which are a bit more pronounced than others. Fig. 3.7 (a) illustrates that the first two peak values (though not the most pronounced ones) occur at $\eta = 0.09$ and $\eta = 0.27$ for the ground surface displacement U. Fig. 3.7 (b) demonstrates two prominent peaks at the same frequencies for the shear stress $\Sigma_{\theta_1 x_1}$. Fig. 3.7 (c) reveals a trough at $\eta = 0.09$, a small peak at $\eta = 0.14$, and a pronounced peak at $\eta = 0.28$ for the displacement U_1 at the cavity surface. Furthermore, we observe that the resonances are nearly equally spaced, which is very similar to the result for the well-known one-dimensional (1D) shear layer subject to bedrock motion shown in the book by Kramer [1996]. The resonances in the 1D model are predicted by $\cos(k_S L) = 0$, where L is the thickness of the soil layer; this leads to the expression for the resonance frequencies $\omega_n = (\pi/2 + n\pi)c_S/L$. Note that for the considered scenario, the thickness of the soil layer above the cavity is $L = H - R = 4R$. The corresponding dimensionless resonance frequencies can be easily derived, and their spacing turns out to be 0.25 ($\Delta\omega = \pi c_S/L$, so that $\Delta\eta = \Delta\omega R/(\pi c_S) = R/L = 1/4$). This is in line with what we observe in Fig. 7; see for example the distance between the peaks in the range of $\eta = (1-2)$ in Fig. 3.7 (b) and (c).

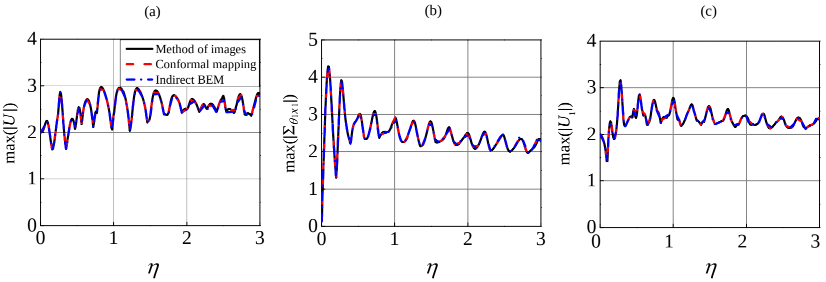
(a)
(b)
(c)

Figure 3.7: Evaluation of the methods for the dimensionless frequency η: (a) anti-plane displacement at the ground surface U at $z = 0$, (b) shear stress $\Sigma_{\theta_1 x_1}$ at $r_1 = R$, and (c) anti-plane displacement U_1 at $r_1 = R$. The parameters considered are $H/R = 5$ and $\theta_V = 0^{\circ}$.

3.7.3. EMBEDDED DEPTH OF THE CAVITY

This section presents an evaluation of the methods for the embedded depth of the cavity. We consider a range of embedded depth ratios from 1.5 to 20. Fig. 3.8 demonstrates that the three methods yield consistent results, indicating that the method of conformal mapping and the indirect BEM work accurately for the considered embedded depths of the cavity.

Fig. 3.8 demonstrates that both the responses at the ground surface and at the cavity surface oscillate as the embedded depth increases. Furthermore, the amplitude of the ground vibrations exhibits a decreasing trend. The amplitude of the displacement at the cavity surface decreases slightly as depth increases. However, the amplitude of the shear stress at the cavity surface remains relatively constant with increasing embedment depth. In any case, different nearly equally spaced resonances can be observed, which is in line with the results in Fig. 3.7. The spacing between resonances is approximately equal to 2. To investigate the resonances at different frequencies, we examine the responses of the system at frequencies of 0.25 and 0.5 as well; see Fig. 3.9. The results highlight the significant influence of frequency on the system response, which is to be expected (based on the 1D model of the shear layer). For $\eta = 0.25$, the resonance spacing increases to 4, whereas for $\eta = 1.0$, the resonance spacing reduces to 1. In general, the spacing is approximately equal to $1/\eta$. Note that for the 1D model, the expression of the resonance thickness of the soil layer is the following: $L_n = (\pi/2 + n\pi)c_S/\omega$. The dimen-

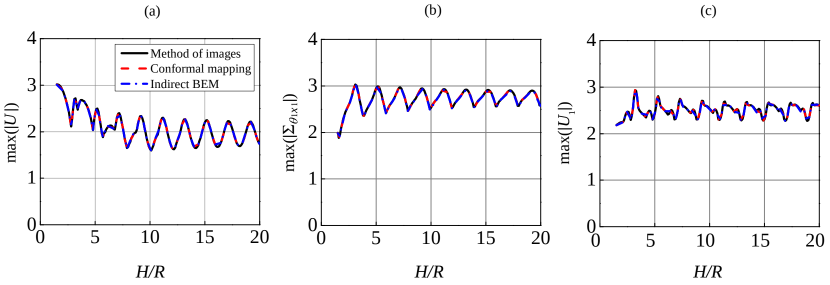

Figure 3.8: Evaluation of the methods for the depth ratio H/R: (a) anti-plane displacement at the ground surface U at $z = 0$, (b) shear stress $\Sigma_{\theta_1 x_1}$ at $r_1 = R$, and (c) anti-plane displacement U_1 at $r_1 = R$. The parameters considered are $\eta = 0.5$ and $\theta_\mathrm{v} = 0^\circ$.

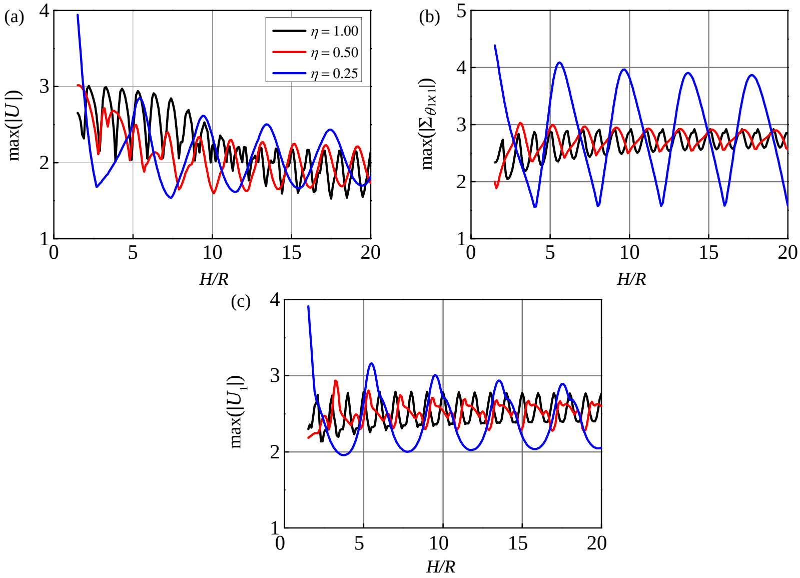

Figure 3.9: Evaluation of the methods for the depth ratio H/R and for different frequencies: (a) anti-plane displacement at the ground surface U at $z = 0$, (b) shear stress $\Sigma_{\theta_1 x_1}$ at $r_1 = R$, and (c) anti-plane displacement U_1 at $r_1 = R$. The parameter considered is $\theta_\mathrm{v} = 0^\circ$.

sionless resonance thicknesses of the soil layer can be easily derived, and their spacing turns out to be exactly $1/\eta$ (i.e., $\Delta L/R = \pi c_\mathrm{S}/(\omega R) = 1/\eta$).

3.7.4. VERTICAL INCIDENT ANGLE

In this section, we evaluate the methods for the variation of the vertical incident angle and investigate its effect on the system response. The vertical incident angle considered in this study ranges from 0° to 90°. The results, depicted in Fig. 3.10, demonstrate a good agreement of the three methods across the entire range. This agreement validates the accuracy and reliability of the method of conformal mapping and of the indirect BEM.

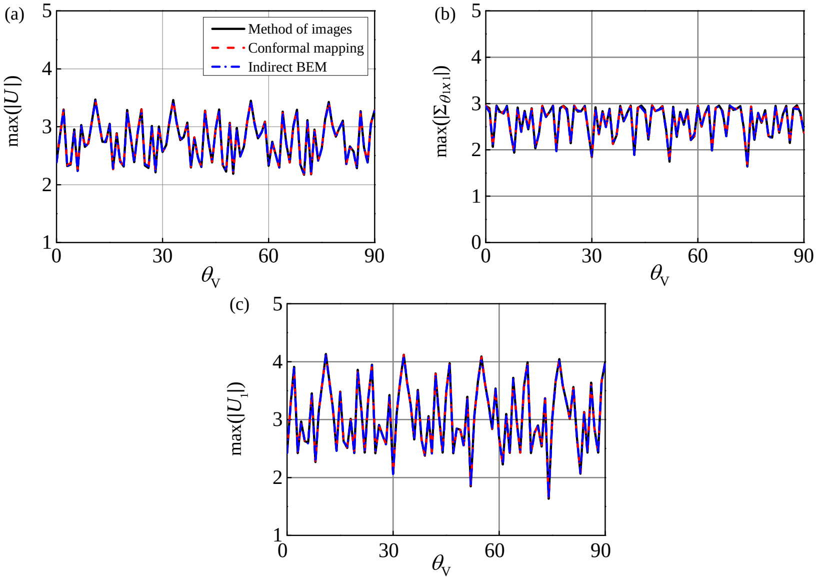

Figure 3.10: Evaluation of the methods for the vertical incident angle θ_{V}: (a) anti-plane displacement at the ground surface U at $z = 0$, (b) shear stress $\Sigma_{\theta_1 x_1}$ at $r_1 = R$, and (c) anti-plane displacement U_1 at $r_1 = R$. The parameters considered are $\eta = 0.5$ and $H/R = 5.0$.

Fig. 3.10 illustrates the presence of resonances in both the responses at the ground surface and at the cavity surface. There are many peaks. Pronounced peaks are observed at angles of $\theta_{\mathrm{V}} = 11^{\circ}, 33^{\circ}, 55^{\circ}$ and 77° for the displacements at both surfaces; see Fig. 3.10 (a) and (c). However, these pronounced peaks are not evident in the shear stress at the cavity surface; see Fig. 3.10 (b). To further investigate this difference, we consider a lower frequency case of $\eta = 0.25$ and a shallower depth case of $H/R = 1.5$ and specifically consider the shear stress. Remarkably, pronounced peaks are now observed at the aforementioned angles; see Fig. 3.11. It is worth noting that similar pronounced peaks are also observed for the displacements at those angles for the lower frequency and smaller depth cases, but these results are not included in this chapter for brevity. Additionally, the results indicate that the spacing between the pronounced resonances is $\theta_{\mathrm{V}} = 22^{\circ}$, and the amplitudes of these pronounced resonances exhibit minimal variation.

In contrast to the findings for the 3D case (Chapter 2), the response curves obtained in the 2D SH case exhibit the distinct characteristic of nearly equally spaced resonances for varying dimensionless frequency, embedded depth ratio and vertical incident angle. In addition, the resonances are more closely spaced in the 2D case.

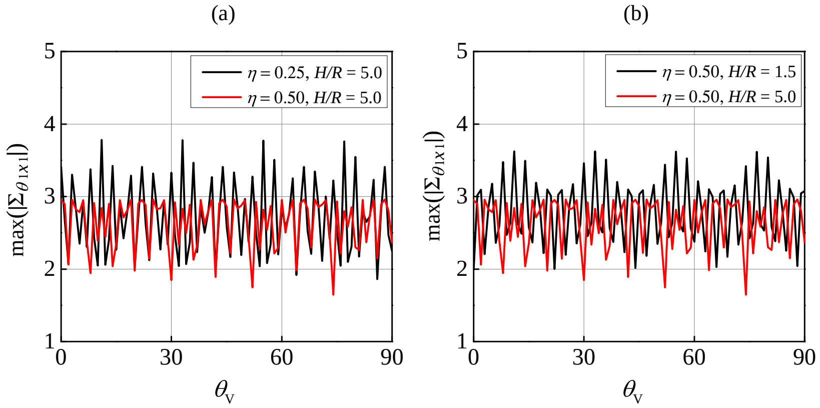

Figure 3.11: Shear stress $\Sigma_{\theta_1 x_1}$ at $r_1 = R$ for the vertical incident angle θ_V for : (a) different dimensionless frequencies $\eta = 0.25$ and $\eta = 0.50$, and (b) different depth ratios $H/R = 1.5$ and $H/R = 5.0$.

3.8. CONCLUSIONS

The response of a cavity embedded in an elastic half-space subject to a harmonic plane SH wave has been examined in this study. We employed three methods: the method of images, the method of conformal mapping (utilising complex-variable theory) and the indirect boundary element method (indirect BEM). By conducting comparisons of the three methods for the considered simple model, we have successfully verified the accuracy of the specific application of the method of conformal mapping (in which the waves scattered from the half-space surface are represented by cylindrical waves that originate from an image source of a priori unknown intensity) and of the indirect BEM.

In the first two methods employed, the total wave field in the half-space comprises incident and reflected plane waves, as well as directly and secondary scattered cylindrical waves. The secondary scattered waves arise when the cylindrical waves directly scattered from the cavity encounter the free surface of the half-space. In the method of conformal mapping, these waves were represented by cylindrical waves originating from an image source with an unknown intensity. Conversely, in the method of images, the intensity is assumed identical to that of the directly scattered wave. The unknown coefficients associated with the potentials of the cylindrical waves were determined from the boundary conditions. More specifically, to obtain numerical results, the unknown coefficients were solved from a system of algebraic equations obtained by projecting the boundary conditions onto the set of circumferential basis functions/modes. The numerical calculations require truncating the sum over circumferential modes.

Convergence tests demonstrated that both the method of images and the method of conformal mapping converge with a small number of circumferential modes; the indirect BEM converges with a small number of source and receiver points. To validate the three methods, medium and high frequency examples were examined. We observed perfect agreement between the results obtained by the presented methods and those in the literature.

The three methods were compared regarding two aspects: the required number of circumferential modes for the first two methods (or the number of source and receiver points for the indirect BEM) to achieve converged results, and the computational time. The method of images and the method of conformal mapping exhibit similar convergence behavior, requiring almost the same number of circumferential modes. However, the method of images is proven to be more efficient than the method of conformal mapping in terms of computational time. On the other hand, the indirect BEM exhibits significantly longer computational time, making it the least efficient method among the three.

Next, in a parametric study, the results obtained by the method of images were considered as benchmark solutions against which the outcomes of the other two methods were evaluated. It was observed that both the method of conformal mapping and the indirect BEM perform accurately across the entire ranges of the dimensionless frequency, the embedded depth of the cavity and the vertical incident angle. This is in contrast to the three-dimensional case (Chapter 2), where converged results could not be obtained at high frequencies for the method of conformal mapping. The findings suggest that representing the waves scattered from the free surface by cylindrical waves (originating from an image source of a priori unknown intensity) in the method of conformal mapping (Chapter 2) is indeed the cause of the inaccuracies at high frequency in the 3D problem. As no inaccuracies are observed for the current 2D anti-plane shear problem, the inaccuracy for the 3D problem is likely due to the use of cylindrical waves (instead of plane waves) that are apparently not fully able to capture all wave conversions taking place at the free surface. Further parametric studies revealed the substantial influence of the dimensionless frequency, the embedded depth of the cavity and the vertical incident angle on the responses at both the ground surface and the cavity surface. Several key findings can be summarized as follows:

- The system's response curves display nearly equally spaced resonances, which is in line with the resonances observed for the well-known one-dimensional shear layer subject to bedrock mention [Kramer, 1996]. The system's response curves for the three-dimensional case (Chapter 2) do not display equally spaced resonances.

- Regarding the frequency-response curves, the resonance spacing (in the considered frequency range) turns out to be the ratio of the cavity radius to the thickness of the soil layer above the cavity. The displacement at the ground surface demonstrates a slightly increasing trend as the dimensionless frequency (denoted as η) increases, whereas the displacement and shear stress at the cavity surface display a decreasing trend.

- Regarding the response curves for the varying depth ratio, the resonance spacing is approximately equal to $1/\eta$. As the embedded depth increases, the amplitude of ground vibrations decreases. The amplitude of the displacement at the cavity surface decreases slightly as depth increases, while the amplitude of the shear stress remains relatively consistent.

- Regarding the response curves for the varying vertical incident angle, the spacing between the pronounced resonances is 22°. The amplitude of these pronounced resonances does not vary significantly from one to another.

In conclusion, all three methods presented in this study can be effectively utilised in the preliminary design of a cavity embedded in a half-space to evaluate stress distributions at the cavity and the level of ground vibrations. From an engineering standpoint, it is advisable to give careful consideration to the embedded depth and vertical incident angle (if it can be controlled) to avoid pronounced resonances in the system response.

4

INSTABILITY OF VIBRATIONS OF AN OSCILLATOR MOVING AT HIGH SPEED THROUGH A TUNNEL EMBEDDED IN SOFT SOIL

This chapter investigates the stability of vertical vibrations of an object moving uniformly through a tunnel embedded in soft soil. Using the indirect Boundary Element Method in the frequency domain, the equivalent dynamic stiffness of the tunnel-soil system at the point of contact with the moving object, modelled as a mass-spring system or as the limiting case of a single mass, is computed numerically. Using the equivalent stiffness, the original 2.5D model is reduced to an equivalent discrete model, whose parameters depend on the vibration frequency and the object's velocity. The critical velocity beyond which the instability of the object vibration may occur is found, and it is the same for both the oscillator and the single mass. This critical velocity turns out to be much larger than the operational velocity of high-speed trains and ultra-high-speed transportation vehicles. This means that the model adopted in this chapter does not predict the vibrations of Maglev and Hyperloop vehicles to become unstable. Furthermore, the critical velocity for resonance of the system is found to be slightly smaller than the velocity of Rayleigh waves, which is very similar to that for the model of a half-space with a regular track placed on top (with damping). However, for that model, the critical velocity for instability is only slightly larger than the critical velocity for resonance (of the undamped system), while for the current model the critical velocity for instability is much larger than the critical velocity for resonance due to the large stiffness of the tunnel and the radiation damping of the waves excited in the tunnel. A parametric study shows that the thickness and material

---

This chapter has been published as a journal paper in *Journal of Sound and Vibration* **494**, 115776 (2021) [Zhao *et al.*, 2021]. Minor changes have been made.

damping ratio of the tunnel, the stiffness of the soil and the burial depth have a stabilising effect, while the damping of the soil may have a slightly destabilising effect (i.e., lower critical velocity for instability). In order to investigate the stability of the moving object for velocities larger than the identified critical velocity for instability, we employ the D-decomposition method and find instability domains in the space of system parameters. In addition, the dependency of the critical mass and stiffness on the velocity is found. We conclude that the higher the velocity, the smaller the mass of the object should be to ensure stability (single mass case); moreover, the higher the velocity, the larger the stiffness of the spring should be when a spring is added (oscillator case). Finally, in view of the stability assessment of Maglev and Hyperloop vehicles, the approach presented in this chapter can be applied to more advanced models with more points of contact between the moving object and the tunnel, which resembles reality even better.

4.1. INTRODUCTION

This thesis encompasses two distinct types of dynamic problems. The first type focuses on wave scattering by underground cavity/tunnel, which has been addressed in Chapters 2 and 3 utilising the method of conformal mapping. Through these investigations, it has been demonstrated that the method offers both accuracy and efficiency within the frequency range of seismic waves. However, it should be noted that inaccurate results may arise when dealing with high-frequency loadings in the three-dimensional (3D) problem. The second type of dynamic problem considered in this thesis entails a moving-load problem, and it is discussed in this chapter. In this context, the method of conformal mapping is not the best suited given the said potential inaccuracies. Consequently, an alternative approach is pursued, namely, the indirect Boundary Element Method (indirect BEM). The objective is to investigate the stability of vibrations of an oscillator moving at high speed through an underground tunnel.

Many researchers have used a one-dimensional (1D) or two-dimensional model (2D) of the railway track [Denisov *et al.*, 1985; Bogacz *et al.*, 1986; Metrikine and Dieterman, 1997; Mazilu *et al.*, 2012; Kononov and De Borst, 2002; Zheng *et al.*, 2000; Zheng and Fan, 2002; Metrikine and Verichev, 2001; Verichev and Metrikine, 2002; Mazilu, 2013; Stojanović *et al.*, 2017; Dimitrovová, 2019], which may be less accurate than 3D models [Metrikine and Popp, 1999; Metrikine *et al.*, 2005] to predict the instability of moving trains. However, they all convey the very important message that, in the presence of damping, the instability of moving trains may happen at speeds that exceed the critical velocity for resonance of the undamped system (which is equal to the minimum phase velocity of waves in the structure); that is, the critical velocity for instability is larger than the critical velocity for resonance. The few existing works related to stability analysis employing 3D models of the railway track consider trains moving on a track founded on the ground surface [Metrikine and Popp, 1999; Metrikine *et al.*, 2005]. It has been shown that the critical velocity for instability of the moving object is close to the Rayleigh wave speed in the soil. Stability of trains moving through an underground tunnel has not been analysed yet. In this chapter, we therefore aim to conduct the stability analyses for an oscillator and the limiting case of a single mass moving through a tunnel embedded in soft soil. We will investigate whether the critical velocity for instability of the moving object is also close to the Rayleigh wave speed in the soil, for both a shallow and a deep tunnel. The results are of practical relevance especially for contemporary high-speed railway tracks as well as upcoming ultra-high-speed transportation systems such as Maglev and Hyperloop, respectively [Rote and Cai, 2002; Abdelrahman *et al.*, 2017; Janzen, 2017].

The chapter is organised as follows. The model and a framework to conduct the stability analysis are presented in Section 4.2. Section 4.3 discusses the 2.5D Green's functions of a full-space and a half-space [Tadeu and Kausel, 2000; Tadeu *et al.*, 2001], presents the Green's functions of the shell that is used to model the tunnel and the formulation indirect BEM. Validations of the proposed indirect BEM are given in Section 4.4. In Section 4.5, the stability analysis of the single mass and the mass-spring oscillator is conducted. To this end, the equivalent dynamic stiffness is studied to find the critical mass and stiffness. In Section 4.6, the effect of the tunnel thickness, the material damping ratios in the tunnel-soil system, the Lamé parameters of the soil and the burial depth of the tunnel on the critical velocity for instability are analysed. Moreover, the dependency of the critical mass and stiffness on the velocity is investigated. Conclusions are given in Section 4.7.

4.2. MODEL AND SOLUTION OF THE PROBLEM

4.2.1. MODEL DESCRIPTION

In this chapter, we study the vibrations of an object moving through a tunnel embedded in soft soil using a so-called 2.5D model. The soil is modelled as an elastic continuum, whereas the tunnel is modelled by the Flügge shell theory [Leissa, 1973]. Both the soil and tunnel are assumed to be linear, elastic, homogeneous and isotropic. The soil is characterised by density ρ_1, Poisson's ratio ν_1, and complex Lamé parameters $\lambda_1^* = \lambda_1\left(1+2\mathrm{i}\,\mathrm{sgn}(\omega)\xi_1\right)$ and $\mu_1^* = \mu_1\left(1+2\mathrm{i}\,\mathrm{sgn}(\omega)\xi_1\right)$, where i is the imaginary unit, ω is the frequency and ξ_1 the material damping ratio of the soil related to the adopted hysteretic damping model. The parameters of the tunnel are density ρ_2, Poisson's ratio ν_2, and complex Lamé parameters $\lambda_2^* = \lambda_2\left(1+2\mathrm{i}\,\mathrm{sgn}(\omega)\xi_2\right)$ and $\mu_2^* = \mu_2\left(1+2\mathrm{i}\,\mathrm{sgn}(\omega)\xi_2\right)$, with ξ_2 being the hysteretic material damping ratio of the tunnel. The burial depth of the tunnel is H, and its inner and outer radii are R_i and R_o. The object is modelled by a mass-spring oscillator (see Fig. 4.1), which is characterised by its mass M and spring stiffness K, and moves through the tunnel with a constant velocity V. Note that there is no vertical external force acting on the mass because the presence of such a force is irrelevant for the dynamic-stability analysis.

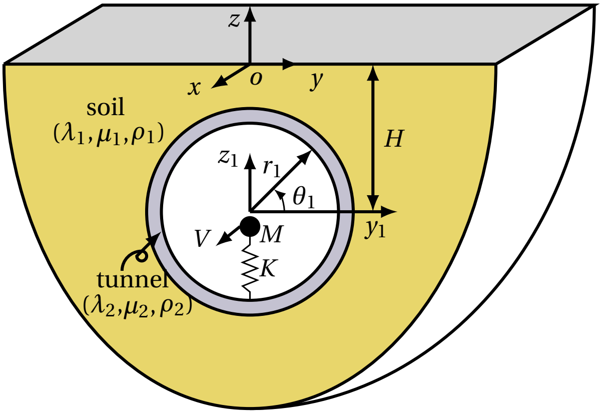

Figure 4.1: A 2.5D model of an oscillator (i.e., mass-spring system) moving through a tunnel embedded in an elastic half-space and the associated coordinate systems.

Shallow and deep embedded tunnels are considered in this chapter. For the shallow tunnel, the soil medium is modelled as a half-space, while for the deep tunnel, the soil is modelled as a full-space. Fig. 4.1 only shows the configuration of the shallow tunnel. If $H \to \infty$, it essentially becomes a deep tunnel.

The governing equations of the shell are presented later, in Section 4.3. The current section only presents the framework to conduct stability analysis.

4.2.2. METHOD OF SOLUTION

To analyse stability of vibrations of the moving object, the concept of the equivalent stiffness (also referred to as dynamic stiffness) is employed [Dieterman and Metrikine, 1996; Lu *et al.*, 2020]. The procedure is illustrated in Fig. 4.2 and goes as follows. First, we compute the steady-state response of the system shown in Fig. 4.2 (a) which is subject to a uniformly moving oscillatory point load applied at the tunnel invert ($r_1 = R_\mathrm{i}, \theta_1 = -\frac{\pi}{2}, x = Vt$). The oscillatory load has the form of $P(t) = P_0 \exp(\mathrm{i}\Omega t)$, in which P_0 is the amplitude, $\Omega = 2\pi f_0$ is the angular frequency; f_0 is the load frequency in Hz. $P(t)$ essentially represents a harmonic interaction force between the moving object and the tunnel-soil system. The steady-state radial displacement at the loading point can be expressed as $U_{r_1}(r_1 = R_\mathrm{i}, \theta_1 = -\frac{\pi}{2}, x = Vt) = U_0(\Omega, V)\exp(\mathrm{i}\Omega t)$, where $U_0(\Omega, V)$ is the complex amplitude of this harmonic vibration. The indirect Boundary Element Method is employed to compute the response of the system, which is presented in detail in Section 4.3. From the result, we obtain the equivalent stiffness of the tunnel-soil system at the loading point using the following relation:

$$K_\mathrm{eq}(\Omega, V) = \frac{P_0}{U_0(\Omega, V)}. \tag{4.1}$$

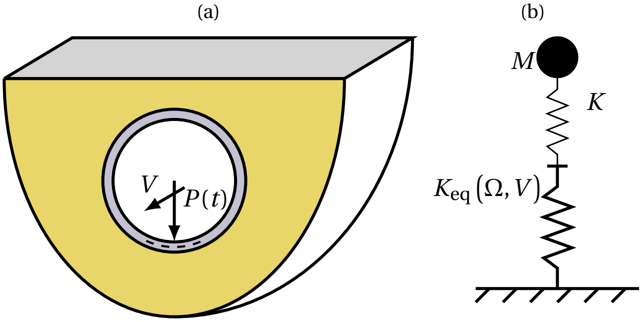

Figure 4.2: (a) A tunnel embedded in an elastic half-space subject to a uniformly moving oscillatory point load $P(t) = P_0 \exp(\mathrm{i}\Omega t)$, (b) an equivalent discrete model consisting of a mass-spring oscillator resting on an equivalent spring $K_\mathrm{eq}(\Omega, V)$; Ω is the angular frequency of vibrations and V the velocity of the oscillator.

By doing so, the original 2.5D model can be reduced to an equivalent discrete model, shown in Fig. 4.2 (b), consisting of a mass-spring system resting on an equivalent spring with a complex-valued stiffness $K_\mathrm{eq}(\Omega, V)$, which depends on the frequency and velocity of the oscillator.

To study the stability of a moving oscillator, we apply, in accordance with previous dynamic-stability studies [Metrikine and Dieterman, 1997; Dimitrovová, 2019], the Laplace integral transform with respect to time t (s denotes the Laplace parameter)

$$W(s) = \int_0^\infty w(t) \exp(-st)\,\mathrm{d}t \tag{4.2}$$

to the well-known governing equation of the vertical motion of the oscillator. Assuming zero initial conditions (which can be done as they do not influence the stability

[Metrikine and Dieterman, 1997; Dimitrovová, 2019]), the following characteristic equation for the free vibration of the oscillator is obtained:

$$Ms^2 + \frac{KK_{\mathrm{eq}}(s,V)}{K + K_{\mathrm{eq}}(s,V)} = 0. \tag{4.3}$$

The roots of Eq. (4.3) determine the (complex) eigenfrequencies, $\Omega = -\mathrm{i}\,s$, of the vertical motion of the oscillator as it interacts with the tunnel-soil system. If one of the roots s of the characteristic equation has a positive real part, the response will grow exponentially, which implies that the vertical vibration of the oscillator is unstable [Metrikine and Dieterman, 1997; Metrikine and Verichev, 2001; Metrikine and Popp, 1999; Metrikine *et al.*, 2005; Wolfert *et al.*, 1998]. Obviously, the equivalent stiffness must be single-valued for all Ω in order for Eq. (4.3) to be meaningful; see also Section 4.2.3.

It has been shown in Metrikine and Dieterman [1997] that the instability of a moving object may occur if and only if the imaginary part of the equivalent stiffness K_{eq} is negative in a frequency band. In [Metrikine and Dieterman, 1997], a single moving mass is considered, the motion of which is even necessarily unstable as soon as $\mathrm{Im}(K_{\mathrm{eq}}) < 0$. The imaginary part of the equivalent stiffness can be considered to be the damping coefficient of the dashpot in the equivalent mass-spring system. A negative imaginary part of the equivalent stiffness indicates a negative damping, which makes the vibration of the moving mass unstable.

It would be very laborious to determine all the roots of the characteristic equation and check whether one of these roots has a positive real part. Alternatively, we follow a convenient method of root analysis, namely the D-decomposition method, to determine the number of 'unstable roots'. This method has been used in several papers [Metrikine and Dieterman, 1997; Metrikine and Verichev, 2001; Metrikine and Popp, 1999; Metrikine *et al.*, 2005; Wolfert *et al.*, 1998]. The idea of this method is to map the imaginary axis of the complex s plane (i.e., the border between stability and instability) onto the plane of a system parameter, M or K, which is allowed to be complex. The mapped line divides the M or K plane into domains with different numbers of unstable roots. It is noted that the imaginary part of the complex system parameter has no physical meaning. Only the positive real part of the system parameter is physical, and the crucial question is whether one of the so-called instability domains overlay the positive real axis.

The procedure is as follows. Consider $s = \mathrm{i}\Omega$, where Ω serves as the parameter of the mapping, is real valued and has the meaning of frequency (same as introduced above), and has to be varied from minus to plus infinity. We discuss the following two cases in this chapter. The first one is the limit case of a single mass moving through the tunnel, thus assuming $K \to \infty$. The characteristic equation for a single mass is reduced from Eq. (4.3) to

$$Ms^2 + K_{\mathrm{eq}}(s,V) = 0. \tag{4.4}$$

Substituting $s = \mathrm{i}\Omega$ into Eq. (4.4) gives the following rule for the mapping:

$$M = \frac{K_{\mathrm{eq}}(\Omega,V)}{\Omega^2}. \tag{4.5}$$

The second case we consider is the more general one of the moving oscillator, taking into account both the mass and the spring of the oscillator. In this case, the stiffness K

will be used as the parameter for the D-decomposition assuming M to be constant because it is of practical relevance. Taking the limit case of the moving mass as the starting point, it is interesting to know what the added stiffness of the spring should be to render the oscillator vibration unstable (see also Section 4.5.2). Substituting $s = \mathrm{i}\Omega$ into Eq. (4.3), we get the following mapping rule for the complex K plane:

$$K = M\Omega^2 \frac{K_{\mathrm{eq}}(\Omega, V)}{K_{\mathrm{eq}}(\Omega, V) - M\Omega^2}. \tag{4.6}$$

By replacing s by $\mathrm{i}\Omega$ in $K_{\mathrm{eq}}(s, V)$, which essentially entails considering the limit case of $s \to \mathrm{i}\Omega$, one can use the equivalent stiffness (Eq. (4.1)) which is determined based on the steady-state response to the harmonic loading. Employing Eq. (4.5) or (4.6) as the mapping rule, one can plot the D-decomposition curve, for example, $\mathrm{Im}(M)$ versus $\mathrm{Re}(M)$ (as shown in Fig. 4.11, for example), where Ω is the running parameter along this curve. One side of the D-decomposition curve is shaded, and this side is related to the right-hand side of the imaginary axis in the s plane. Crossing the curve in the direction of the shading once indicates that there is an additional unstable root. Thus, one can find information on the relative number of unstable roots in domains of the complex M or K planes. The number of unstable roots in all the domains can be determined if the absolute number of those is known for any arbitrary value of the considered system parameter. By doing so, the instability domains can be found in the M or K plane, which generally allows to identify the critical velocity for instability (defined as the velocity at which an instability domain first overlays the positive real axis when increasing the velocity). The stability analysis is conducted in Section 4.5.

4.2.3. RESPONSE TO A MOVING OSCILLATORY POINT LOAD AND DERIVATION OF EQUIVALENT STIFFNESS

As shown in Section 4.2.2, it is customary to employ the equivalent stiffness K_{eq} to conduct the stability analysis. In the current section, we aim to derive the expression for the equivalent stiffness. To this end, we first derive the steady-state response to a moving oscillatory point load at the loading point. Additionally, the response at a fixed observation point is derived, which is needed for validating the indirect BEM in Section 4.4. All the responses can be computed using the indirect BEM presented in Section 4.3. Here we summarise the important steps and outcome in view of the specified aim.

The shear stresses $\sigma_{r_1\theta_1}$ and $\sigma_{x_1\theta_1}$ at the inner surface of the tunnel wall induced by the moving oscillatory point load (see Fig. 4.2 (a)) are zero. The non-zero normal stress $\sigma_{r_1r_1}(R_{\mathrm{i}},\theta_1,x,t)$ can be expressed as

$$\sigma_{r_1r_1}\left(R_{\mathrm{i}},\theta_1,x,t\right) = \frac{P_0}{R_{\mathrm{i}}}\delta\left(\theta_1 + \frac{\pi}{2}\right)\delta\left(x - Vt\right)\exp\left(\mathrm{i}\Omega t\right), \tag{4.7}$$

where $\delta(.)$ is the Dirac delta function.

As the considered problem is linear, we apply the Fourier Transform to derive the response of the system subject to the uniformly moving oscillatory point load in the wavenumber-frequency (k_x, ω) domain. The Fourier Transform applied with respect to time t and spatial coordinate x is defined in the following form (for an arbitrary function

$g\left(r_1,\theta_1,x,t\right)$):

$$\tilde{\tilde{g}}\left(r_1,\theta_1,k_x,\omega\right)=\int_{-\infty}^{\infty}\int_{-\infty}^{\infty} g\left(r_1,\theta_1,x,t\right)\exp\Big(-\mathrm{i}\left(\omega t-k_x x\right)\Big)\ \mathrm{d}x\mathrm{d}t \tag{4.8}$$

with the inverse Fourier Transform given by

$$g\left(r_1,\theta_1,x,t\right)=\frac{1}{4\pi^2}\int_{-\infty}^{\infty}\int_{-\infty}^{\infty} \tilde{\tilde{g}}\left(r_1,\theta_1,k_x,\omega\right)\exp\Big(+\mathrm{i}\left(\omega t-k_x x\right)\Big)\ \mathrm{d}k_x\mathrm{d}\omega. \tag{4.9}$$

The Fourier series, which is used to derive the response in the $(k_x,\ \omega)$ domain, of a general response quantity $f(\theta_1)$ reads

$$f\left(\theta_1\right)=\sum_{n=-\infty}^{n=\infty} f_n\exp\left(\mathrm{i}n\theta_1\right),\quad f_n=\frac{1}{2\pi}\int_0^{2\pi} f\left(\theta_1\right)\exp\left(-\mathrm{i}n\theta_1\right)\ \mathrm{d}\theta_1. \tag{4.10}$$

Expanding the term $\delta\left(\theta_1+\pi/2\right)$ in Eq. (4.7) into a Fourier series, the normal stress can be rewritten as

$$\sigma_{r_1r_1}\left(R_\mathrm{i},\theta_1,x,t\right)=\sum_{n=-\infty}^{n=\infty}\frac{P_0}{2\pi R_\mathrm{i}}\exp\left(\mathrm{i}n\left(\theta_1+\frac{\pi}{2}\right)\right)\delta\left(x-Vt\right)\exp\left(\mathrm{i}\Omega t\right). \tag{4.11}$$

Applying the Fourier Transform defined by Eq. (4.8) to Eq. (4.11), the normal stress in the wavenumber-frequency domain is obtained as:

$$\begin{aligned}\tilde{\tilde{\sigma}}_{r_1r_1}\left(R_\mathrm{i},\theta_1,k_x,\omega\right)&=\sum_{n=-\infty}^{n=\infty}\frac{P_0}{2\pi R_\mathrm{i}}\exp\left(\mathrm{i}n\left(\theta_1+\frac{\pi}{2}\right)\right)2\pi\delta\left(\omega-\Omega-k_xV\right)\\&=\tilde{\tilde{\sigma}}_\mathrm{aux}\left(R_\mathrm{i},\theta_1,k_x,\omega\right)2\pi P_0\delta\left(\omega-\Omega-k_xV\right).\end{aligned} \tag{4.12}$$

The response induced by the auxiliary stress $\tilde{\tilde{\sigma}}_\mathrm{aux}\left(R_\mathrm{i},\theta_1,k_x,\omega\right)$, which relates to a radial stress in the form of $\delta\left(\theta_1+\frac{\pi}{2}\right)\cdot\delta(x)\delta(t)$, can be computed using the indirect BEM (Section 4.3) and is denoted as $\tilde{\tilde{\mathbf{U}}}_{1,\mathrm{aux}}\left(r_1,\theta_1,k_x,\omega\right)$. Thereafter, we get the expression of the actual displacement vector excited by the stress $\tilde{\tilde{\sigma}}_{r_1r_1}\left(R_\mathrm{i},\theta_1,k_x,\omega\right)$ shown in Eq. (4.12):

$$\tilde{\tilde{\mathbf{U}}}_1\left(r_1,\theta_1,k_x,\omega\right)=\tilde{\tilde{\mathbf{U}}}_{1,\mathrm{aux}}\left(r_1,\theta_1,k_x,\omega\right)2\pi P_0\delta\left(\omega-\Omega-k_xV\right). \tag{4.13}$$

We obtain the space-time domain response by applying the inverse Fourier Transform over wavenumber k_x and frequency ω to Eq. (4.13):

$$\begin{aligned}\mathbf{U}_1(r_1,\theta_1,x,t)&=\frac{1}{4\pi^2}\int_{-\infty}^{\infty}\int_{-\infty}^{\infty}\tilde{\tilde{\mathbf{U}}}_1\left(r_1,\theta_1,k_x,\omega\right)\exp\Big(+\mathrm{i}\left(\omega t-k_xx\right)\Big)\ \mathrm{d}k_x\mathrm{d}\omega\\&=\frac{P_0}{2\pi}\int_{-\infty}^{\infty}\int_{-\infty}^{\infty}\tilde{\tilde{\mathbf{U}}}_{1,\mathrm{aux}}\left(r_1,\theta_1,k_x,\omega\right)\delta\left(\omega-\Omega-k_xV\right)\exp\Big(+\mathrm{i}\left(\omega t-k_xx\right)\Big)\ \mathrm{d}k_x\mathrm{d}\omega\\&=\frac{P_0}{2\pi}\int_{-\infty}^{\infty}\frac{1}{V}\tilde{\tilde{\mathbf{U}}}_{1,\mathrm{aux}}\left(r_1,\theta_1,\frac{\omega-\Omega}{V},\omega\right)\exp\left(-\mathrm{i}\frac{\omega-\Omega}{V}x\right)\exp(\mathrm{i}\omega t)\ \mathrm{d}\omega.\end{aligned} \tag{4.14}$$

In Eq. (4.14), the inverse Fourier Transform over wavenumber k_x has been evaluated analytically, whereas the inverse Fourier Transform over frequency ω needs to be evaluated numerically.

The radial displacement component of the steady-state response at the loading point can be obtained by substituting $x = Vt$ into Eq. (4.14):

$$U_{r_1}\left(R_\mathrm{i}, -\frac{\pi}{2}, Vt, t\right) = \frac{P_0 \exp\left(\mathrm{i}\Omega t\right)}{2\pi} \int_{-\infty}^{\infty} \frac{1}{V} \tilde{\tilde{U}}_{r_1,\mathrm{aux}}\left(R_\mathrm{i}, -\frac{\pi}{2}, \frac{\omega - \Omega}{V}, \omega\right) \mathrm{d}\omega. \tag{4.15}$$

In accordance with Eq. (4.15), the complex amplitude of this harmonic response, which is relevant for the computation of the equivalent stiffness, is given as

$$U_0(\Omega, V) = \frac{P_0}{2\pi} \int_{-\infty}^{\infty} \frac{1}{V} \tilde{\tilde{U}}_{r_1,\mathrm{aux}}\left(R_\mathrm{i}, -\frac{\pi}{2}, \frac{\omega - \Omega}{V}, \omega\right) \mathrm{d}\omega. \tag{4.16}$$

Using Eq. (4.16), the equivalent stiffness K_eq defined in Eq. (4.1) is obtained:

$$K_\mathrm{eq} = \frac{1}{\frac{1}{2\pi} \int_{-\infty}^{\infty} \frac{1}{V} \tilde{\tilde{U}}_{r_1,\mathrm{aux}}\left(R_\mathrm{i}, -\frac{\pi}{2}, \frac{\omega - \Omega}{V}, \omega\right) \mathrm{d}\omega}. \tag{4.17}$$

We note that this result is single-valued for all Ω as the Green's functions (see Section 4.3) used in the indirect BEM computations are uniquely defined.

We also consider the steady-state response at a fixed observation point $x = 0$, which is needed for the validation of the indirect BEM. Substituting $x = 0$ into Eq. (4.14) gives the corresponding displacement vector:

$$\mathbf{U}_1(r_1, \theta_1, 0, t) = \frac{P_0}{2\pi} \int_{-\infty}^{\infty} \frac{1}{V} \tilde{\tilde{\mathbf{U}}}_{1,\mathrm{aux}}\left(r_1, \theta_1, \frac{\omega - \Omega}{V}, \omega\right) \exp(\mathrm{i}\omega t)\, \mathrm{d}\omega. \tag{4.18}$$

Eq. (4.18) contains the responses observed at $x = 0$; for an observation point at the tunnel invert, $t < 0$ indicates that $x = 0 > Vt$, which means that the moving load has not reached the observation point yet; $t = 0$ indicates that the moving load is at the observation point; $t > 0$ indicates that $x = 0 < Vt$, which means that the moving load has passed the observation point.

For the case of a stationary (i.e., non-moving) harmonic point load, which is also used in Section 4.4 for validation, an expression for the induced displacements is given in Appendix F.

4.3. INDIRECT BOUNDARY ELEMENT METHOD

In this chapter, the indirect BEM is employed to compute the response of the tunnel-soil system in the wavenumber-frequency $(r_1, \theta_1, k_x, \omega)$ domain. To this end, the Green's functions of the soil and tunnel are needed; note that the indirect BEM uses the Green's functions of the soil without cavity (full-space or half-space). In Sections 4.3.1 and 4.3.2, the Green's functions of the soil and tunnel are presented. The indirect BEM is formulated in Section 4.3.3.

4.3.1. GREEN'S FUNCTIONS OF THE SOIL

The so-called two-and-a-half dimensional Green's functions of an elastodynamic full-space [Tadeu and Kausel, 2000] and a half-space [Tadeu *et al.*, 2001] are used in our work. The source considered in the mentioned papers is a spatially varying line load in the longitudinal direction, having the form of $f_j(y,z,x,t) = F_j\delta(y-y_\mathrm{s})\delta(z-z_\mathrm{s})\exp(\mathrm{i}\left(\omega t - k_x x\right))$, where $j = y,z,x$ indicates the direction of the load, subscript “s" indicates the coordinates of the source point, and F_j is the amplitude of the source (Green's functions can be obtained by setting $F_j = 1$).

The Green's functions of the half-space consist of source terms which are the same as those of the full-space, and of surface terms which are necessary to satisfy the stress-free boundary conditions at the surface of the half-space [Tadeu *et al.*, 2001]. However, we found that the stress-free conditions are not satisfied using the Green's functions presented in Tadeu *et al.* [2001], while they are satisfied when the source terms are replaced by the ones presented in Tadeu and Kausel [2000] that contains the full-space Green's functions. Therefore, the Green's functions of the half-space used in the current chapter consist of the source terms presented in Tadeu and Kausel [2000] and of the surface terms presented in Tadeu *et al.* [2001].

Because the reference frames in Tadeu *et al.* [2001] are different from that in the current chapter, we have to transform the Green's functions for displacements and stresses given in Tadeu *et al.* [2001] through the following relations $\tilde{\tilde{\mathbf{G}}}_{u,1} = \mathbf{T}_1\tilde{\tilde{\mathbf{G}}}_{u,\mathrm{ref}}\mathbf{T}_1^\mathrm{T}$ and $\tilde{\tilde{\mathbf{G}}}_{\sigma,1} = [\mathbf{T}_1]\tilde{\tilde{\mathbf{G}}}_{\sigma,\mathrm{ref}}\mathbf{T}_1^\mathrm{T}$, where subscripts “1" and “ref" denote the responses defined in the coordinate systems of the current chapter and the reference paper, respectively. The transformation matrix reads:

$$\mathbf{T}_1 = \begin{pmatrix} 1 & 0 & 0 \\ 0 & -1 & 0 \\ 0 & 0 & 1 \end{pmatrix}. \tag{4.19}$$

$\tilde{\tilde{\mathbf{G}}}_{u,1}$ and $\tilde{\tilde{\mathbf{G}}}_{\sigma,1}$ are the Green's functions for displacements and stresses of the soil without tunnel/cavity (i.e., of the full-space or half-space), and are 3×3 matrices. In matrix $\tilde{\tilde{\mathbf{G}}}_{u,1}$, the first, second and third rows represent the displacement components $\tilde{\tilde{u}}_{r_1}$, $\tilde{\tilde{u}}_{\theta_1}$ and $\tilde{\tilde{u}}_x$, while the first, second and third columns correspond to the spatially varying unit line loads acting in y, z and x directions, respectively. In matrix $\tilde{\tilde{\mathbf{G}}}_{\sigma,1}$, the first, second and third rows represent the stress components $\tilde{\tilde{\sigma}}_{r_1r_1}$, $\tilde{\tilde{\sigma}}_{r_1\theta_1}$ and $\tilde{\tilde{\sigma}}_{r_1x}$, while the columns also correspond to the loads in different directions.

4.3.2. GREEN'S FUNCTIONS AND RESPONSE OF A CYLINDRICAL SHELL

The tunnel is modelled by an infinitely long cylindrical Flügge shell. The associated coordinate system is shown in Fig. 4.3. The equations of motion of the shell read [Leissa, 1973]:

$$\begin{aligned}&-\rho_2 R\frac{\left(1-\nu_2^2\right)}{E_2}\frac{\partial^2\bar{u}}{\partial t^2}-\nu_2\frac{\partial\bar{w}}{\partial x_2}-\frac{1}{R}\frac{\partial\bar{v}}{\partial\theta_2}-\frac{1}{R}\bar{u}-\frac{h^2}{12}\left[R\frac{\partial^4\bar{u}}{\partial x_2^4}+\frac{2}{R}\frac{\partial^4\bar{u}}{\partial x_2^2\partial\theta_2^2}+\frac{1}{R^3}\frac{\partial^4\bar{u}}{\partial\theta_2^4}\right]+R\frac{\left(1-\nu_2^2\right)}{E_2 h}q_{r_2}\\&+\frac{h^2}{12}\left[\frac{\partial^3\bar{w}}{\partial x_2^3}-\frac{\left(1-\nu_2\right)}{2R^2}\frac{\partial^3\bar{w}}{\partial x_2\partial\theta_2^2}+\frac{\left(3-\nu_2\right)}{2R}\frac{\partial^3\bar{v}}{\partial x_2^2\partial\theta_2}-\frac{1}{R^3}\bar{u}-\frac{2}{R^3}\frac{\partial^2\bar{u}}{\partial\theta_2^2}\right]=0,\end{aligned}\tag{4.20}$$

$$\begin{aligned}&-\rho_2 R\frac{\left(1-\nu_2^2\right)}{E}\frac{\partial^2\bar{v}}{\partial t^2}+\frac{\left(1+\nu_2\right)}{2}\frac{\partial^2\bar{w}}{\partial x_2\partial\theta_2}+R\frac{\left(1-\nu_2\right)}{2}\frac{\partial^2\bar{v}}{\partial x_2^2}+\frac{1}{R}\frac{\partial^2\bar{v}}{\partial\theta_2^2}+\frac{1}{R}\frac{\partial\bar{u}}{\partial\theta_2}\\&+R\frac{\left(1-\nu_2^2\right)}{E_2 h}q_{\theta_2}+\frac{h^2}{12}\left[\frac{3\left(1-\nu_2\right)}{2R}\frac{\partial^2\bar{v}}{\partial x_2^2}-\frac{\left(3-\nu_2\right)}{2R}\frac{\partial^3\bar{u}}{\partial x_2^2\partial\theta_2}\right]=0,\end{aligned}\tag{4.21}$$

$$\begin{aligned}&-\rho_2 R\frac{\left(1-\nu_2^2\right)}{E_2}\frac{\partial^2\bar{w}}{\partial t^2}+R\frac{\partial^2\bar{w}}{\partial x_2^2}+\frac{\left(1-\nu_2\right)}{2R}\frac{\partial^2\bar{w}}{\partial\theta_2^2}+\frac{\left(1+\nu_2\right)}{2}\frac{\partial^2\bar{v}}{\partial x_2\partial\theta_2}+\nu_2\frac{\partial\bar{u}}{\partial x_2}\\&+R\frac{\left(1-\nu_2^2\right)}{E_2 h}q_{x_2}+\frac{h^2}{12}\left[\frac{\left(1-\nu_2\right)}{2R^3}\frac{\partial^2\bar{w}}{\partial\theta_2^2}-\frac{\partial^3\bar{u}}{\partial x_2^3}+\frac{\left(1-\nu_2\right)}{2R^2}\frac{\partial^3\bar{u}}{\partial x_2\partial\theta_2^2}\right]=0,\end{aligned}\tag{4.22}$$

where $\bar{u}$, $\bar{v}$ and $\bar{w}$ are the mid-surface displacements in directions r_2, θ_2 and x_2, respectively. E_2 is the Young's modulus of the shell and h its thickness. The radii of the inner and outer surface of the shell can be expressed as $R_\mathrm{i} = R - \frac{h}{2}$ and $R_\mathrm{o} = R + \frac{h}{2}$, respectively. q_{r_2}, q_{θ_2} and q_{x_2} are the net external stresses acting on the shell, namely the difference between the stresses acting at the inner and outer surfaces.

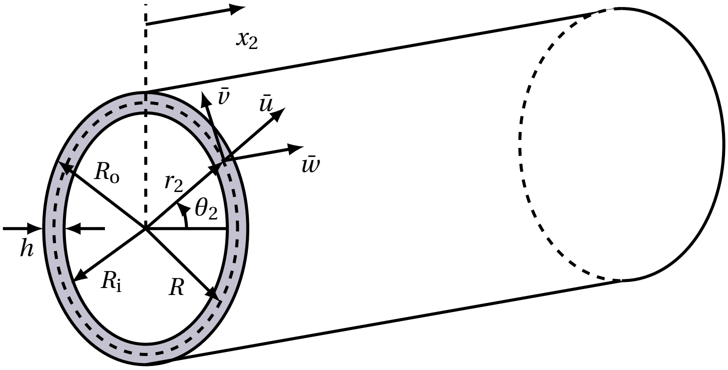

Figure 4.3: A cylindrical shell, the associated coordinate system and displacement components of the shell.

The governing equations of the shell can be rewritten into matrix form as

$$\mathbf{A}\bar{\mathbf{u}}_2 = \bar{\mathbf{q}}_2,\tag{4.23}$$

where $\bar{\mathbf{u}}_2 = (\bar{u}, \bar{v}, \bar{w})$ is the displacement vector, $\bar{\mathbf{q}}_2 = (\bar{q}_{r_2}, \bar{q}_{\theta_2}, \bar{q}_{x_2})$ is the net stress vector corresponding to the mid-surface of the shell, and $\mathbf{A}$ is an operator matrix given in Appendix G.

The stress vector $\bar{\mathbf{q}}_2$ is related to the stress vectors $\mathbf{q}_2^{\mathrm{o}}$ and $\mathbf{q}_2^{\mathrm{i}}$ corresponding to the outer and inner surfaces of the shell, respectively, through the following relations [Luco and de Barros, 1994a]:

$$\bar{\mathbf{q}}_2 = \begin{pmatrix} 1 & \frac{h}{2R}\frac{\partial}{\partial\theta_2} & \frac{h}{2}\frac{\partial}{\partial x_2} \\ 0 & 1+\frac{h}{2R} & 0 \\ 0 & 0 & 1 \end{pmatrix} \mathbf{q}_2^{\mathrm{o}} = \mathbf{B}^{\mathrm{o}}\mathbf{q}_2^{\mathrm{o}}, \quad \bar{\mathbf{q}}_2 = \begin{pmatrix} 1 & \frac{-h}{2R}\frac{\partial}{\partial\theta_2} & \frac{-h}{2}\frac{\partial}{\partial x_2} \\ 0 & 1+\frac{-h}{2R} & 0 \\ 0 & 0 & 1 \end{pmatrix} \mathbf{q}_2^{\mathrm{i}} = \mathbf{B}^{\mathrm{i}}\mathbf{q}_2^{\mathrm{i}}. \tag{4.24}$$

According to Love's simplification in the shell theory [Soedel, 2004], the longitudinal and tangential displacements vary linearly across the shell's thickness, whereas the radial displacement is independent of radial coordinate. Therefore, the mid-surface displacement vector $\bar{\mathbf{u}}_2$ is related to the displacement vector $\mathbf{u}_2^{\mathrm{o}}$ corresponding to the outer surface of the shell through the following relation

$$\mathbf{u}_2^{\mathrm{o}} = \begin{pmatrix} 1 & 0 & 0 \\ -\frac{h}{2R}\frac{\partial}{\partial\theta_2} & 1+\frac{h}{2R} & 0 \\ -\frac{h}{2}\frac{\partial}{\partial x_2} & 0 & 1 \end{pmatrix} \bar{\mathbf{u}}_2 = \mathbf{D}\bar{\mathbf{u}}_2. \tag{4.25}$$

After applying the Fourier Transform over time t and spatial coordinate x_2 to Eq. (4.23), computing the Fourier coefficients of the circumferential harmonics (i.e., the second relation in Eq. (4.10)), and considering Eqs. (4.24) and (4.25), the governing equations of the shell can be written as

$$\tilde{\tilde{\mathbf{A}}}_n \tilde{\tilde{\mathbf{D}}}_n^{-1} \tilde{\tilde{\mathbf{u}}}_{2,n}^{\mathrm{o}} = \tilde{\tilde{\mathbf{B}}}_n^{\mathrm{o}} \tilde{\tilde{\mathbf{q}}}_{2,n}^{\mathrm{o}} + \tilde{\tilde{\mathbf{B}}}_n^{\mathrm{i}} \tilde{\tilde{\mathbf{q}}}_{2,n}^{\mathrm{i}}, \tag{4.26}$$

which is essentially a set of algebraic equations; n denotes the number of the circumferential harmonic, and matrices $\tilde{\tilde{\mathbf{A}}}_n$, $\tilde{\tilde{\mathbf{B}}}_n^{\mathrm{o}}$, $\tilde{\tilde{\mathbf{B}}}_n^{\mathrm{i}}$ and $\tilde{\tilde{\mathbf{D}}}_n$ are given in Appendix G; $\tilde{\tilde{\mathbf{u}}}_{2,n}^{\mathrm{o}}$ and $\tilde{\tilde{\mathbf{q}}}_{2,n}^{\{\mathrm{o,i}\}}$ contain the Fourier coefficients of $\tilde{\tilde{\mathbf{u}}}_2^{\mathrm{o}}$ and $\tilde{\tilde{\mathbf{q}}}_2^{\{\mathrm{o,i}\}}$, respectively. If $\mathbf{q}_2^{\{\mathrm{o,i}\}}$ are taken as $\mathbf{q}_2^{\{\mathrm{o,i}\}} = \left[\delta(\theta_2), \delta(\theta_2), \delta(\theta_2)\right]^{\mathrm{T}} \delta(x_2)\delta(t)$, then $\tilde{\tilde{\mathbf{q}}}_{2,n}^{\{\mathrm{o,i}\}} = \left[\frac{1}{2\pi}, \frac{1}{2\pi}, \frac{1}{2\pi}\right]^{\mathrm{T}}$. The associated Green's functions of the shell can be derived by solving Eq. (4.26) for each of the load components, and subsequently adding the solutions for all components in the Fourier series (see Eq. (4.10)):

$$\begin{aligned} \tilde{\tilde{\mathbf{g}}}^{\mathrm{o}}(\theta_2, k_{x2}, \omega) &= \sum_{n=-\infty}^{n=\infty} \tilde{\tilde{\mathbf{g}}}_n^{\mathrm{o}} \exp\left(\mathrm{i}\, n\theta_2\right) = \sum_{n=-\infty}^{n=\infty} \frac{1}{2\pi} \tilde{\tilde{\mathbf{D}}}_n \tilde{\tilde{\mathbf{A}}}_n^{-1} \tilde{\tilde{\mathbf{B}}}_n^{\mathrm{o}} \exp\left(\mathrm{i}\, n\theta_2\right), \\ \tilde{\tilde{\mathbf{g}}}^{\mathrm{i}}(\theta_2, k_{x2}, \omega) &= \sum_{n=-\infty}^{n=\infty} \tilde{\tilde{\mathbf{g}}}_n^{\mathrm{i}} \exp\left(\mathrm{i}\, n\theta_2\right) = \sum_{n=-\infty}^{n=\infty} \frac{1}{2\pi} \tilde{\tilde{\mathbf{D}}}_n \tilde{\tilde{\mathbf{A}}}_n^{-1} \tilde{\tilde{\mathbf{B}}}_n^{\mathrm{i}} \exp\left(\mathrm{i}\, n\theta_2\right), \end{aligned} \tag{4.27}$$

where $\tilde{\tilde{\mathbf{g}}}_n^{\mathrm{o}}$ interrelates $\tilde{\tilde{\mathbf{u}}}_{2,n}^{\mathrm{o}}$ and $\tilde{\tilde{\mathbf{q}}}_{2,n}^{\mathrm{o}}$, $\tilde{\tilde{\mathbf{g}}}_n^{\mathrm{i}}$ interrelates $\tilde{\tilde{\mathbf{u}}}_{2,n}^{\mathrm{o}}$ and $\tilde{\tilde{\mathbf{q}}}_{2,n}^{\mathrm{i}}$, and $\tilde{\tilde{\mathbf{g}}}^{\mathrm{o}}$, $\tilde{\tilde{\mathbf{g}}}^{\mathrm{i}}$, $\tilde{\tilde{\mathbf{g}}}_n^{\mathrm{o}}$ and $\tilde{\tilde{\mathbf{g}}}_n^{\mathrm{i}}$ are 3 × 3 matrices. The positive directions of the longitudinal axes in the global coordinate system (see Fig. 4.1) and the local coordinate system for the shell (see Fig. 4.3) are opposite to each other (i.e., $x_2 = -x$). Therefore, the relation between the longitudinal wavenumbers k_{x2} and k_x (which, for the moving oscillatory point load considered in Section 4.2.3, is defined as $\frac{\omega-\Omega}{V}$) is as follows: $k_{x2} = -k_x$; this relation is used below.

Using the convolution rule, the displacement vector of the shell under an arbitrary load can be obtained as

$$\begin{aligned}\tilde{\tilde{\mathbf{u}}}_2^{\mathrm{o}}(\theta_2, k_{x2}, \omega) = R_{\mathrm{o}} \int_0^{2\pi} \sum_{n=-\infty}^{n=\infty} \frac{1}{2\pi R_{\mathrm{o}}} \tilde{\tilde{\mathbf{D}}}_n \tilde{\tilde{\mathbf{A}}}_n^{-1} \tilde{\tilde{\mathbf{B}}}_n^{\mathrm{o}} \exp\left(\mathrm{i}\, n \left(\theta_2 - \theta_2'\right)\right) \tilde{\tilde{\mathbf{q}}}_2^{\mathrm{o}}(\theta_2', k_{x2}, \omega)\, \mathrm{d}\theta_2' \\ + R_{\mathrm{i}} \int_0^{2\pi} \sum_{n=-\infty}^{n=\infty} \frac{1}{2\pi R_{\mathrm{i}}} \tilde{\tilde{\mathbf{D}}}_n \tilde{\tilde{\mathbf{A}}}_n^{-1} \tilde{\tilde{\mathbf{B}}}_n^{\mathrm{i}} \exp\left(\mathrm{i}\, n \left(\theta_2 - \theta_2'\right)\right) \tilde{\tilde{\mathbf{q}}}_2^{\mathrm{i}}(\theta_2', k_{x2}, \omega)\, \mathrm{d}\theta_2'.\end{aligned} \tag{4.28}$$

The displacements in Eq. (4.28) are defined in the local coordinate system of the shell (r_2, θ_2, x_2, see Fig. 4.3). To satisfy the continuity of displacements and stresses at the shell-soil interface, the displacement and stress vectors $\tilde{\tilde{\mathbf{u}}}_2^{\mathrm{o}}$, $\tilde{\tilde{\mathbf{q}}}_2^{\mathrm{o}}$ and $\tilde{\tilde{\mathbf{q}}}_2^{\mathrm{i}}$ defined in the local coordinate system of the shell have to be transformed to $\tilde{\tilde{\mathbf{U}}}_2^{\mathrm{o}}$, $\tilde{\tilde{\mathbf{Q}}}_2^{\mathrm{o}}$ and $\tilde{\tilde{\mathbf{Q}}}_2^{\mathrm{i}}$, respectively, defined in the global cylindrical coordinate system of the soil (r_1, θ_1, x), which has origin at the center of the tunnel (see Fig. 4.1), through relations

$$\begin{aligned}&\tilde{\tilde{\mathbf{U}}}_2^{\mathrm{o}}(\theta_1, k_x, \omega) = \mathbf{T}_2 \tilde{\tilde{\mathbf{u}}}_2^{\mathrm{o}}(\theta_2, -k_x, \omega), \\ &\tilde{\tilde{\mathbf{q}}}_2^{\mathrm{o}}(\theta_2, -k_x, \omega) = \mathbf{T}_2^{\mathrm{T}} \tilde{\tilde{\mathbf{Q}}}_2^{\mathrm{o}}(\theta_1, k_x, \omega), \quad \tilde{\tilde{\mathbf{q}}}_2^{\mathrm{i}}(\theta_2, -k_x, \omega) = \mathbf{T}_2^{\mathrm{T}} \tilde{\tilde{\mathbf{Q}}}_2^{\mathrm{i}}(\theta_1, k_x, \omega),\end{aligned} \tag{4.29}$$

in which $\theta_1 = \theta_2$ and

$$\mathbf{T}_2 = \begin{pmatrix} 1 & 0 & 0 \\ 0 & 1 & 0 \\ 0 & 0 & -1 \end{pmatrix}. \tag{4.30}$$

Substituting Eq. (4.29) into Eq. (4.28), we obtain the displacements of the shell in the global cylindrical coordinate system:

$$\begin{aligned}\tilde{\tilde{\mathbf{U}}}_2^{\mathrm{o}}(\theta_1, k_x, \omega) = R_{\mathrm{o}} \int_0^{2\pi} \sum_{n=-\infty}^{n=\infty} \frac{1}{2\pi R_{\mathrm{o}}} \mathbf{T}_2 \tilde{\tilde{\mathbf{D}}}_n \tilde{\tilde{\mathbf{A}}}_n^{-1} \tilde{\tilde{\mathbf{B}}}_n^{\mathrm{o}} \mathbf{T}_2^{\mathrm{T}} \exp\left(\mathrm{i}\, n \left(\theta_1 - \theta_2'\right)\right) \tilde{\tilde{\mathbf{Q}}}_2^{\mathrm{o}}(\theta_2', k_x, \omega)\, \mathrm{d}\theta_2' \\ + R_{\mathrm{i}} \int_0^{2\pi} \sum_{n=-\infty}^{n=\infty} \frac{1}{2\pi R_{\mathrm{i}}} \mathbf{T}_2 \tilde{\tilde{\mathbf{D}}}_n \tilde{\tilde{\mathbf{A}}}_n^{-1} \tilde{\tilde{\mathbf{B}}}_n^{\mathrm{i}} \mathbf{T}_2^{\mathrm{T}} \exp\left(\mathrm{i}\, n \left(\theta_1 - \theta_2'\right)\right) \tilde{\tilde{\mathbf{Q}}}_2^{\mathrm{i}}(\theta_2', k_x, \omega)\, \mathrm{d}\theta_2'.\end{aligned} \tag{4.31}$$

4.3.3. Formulation of the indirect Boundary Element Method

In this section, the formulation of the employed indirect BEM is presented. The excitation stress vectors are $[\tilde{\tilde{\sigma}}_{\mathrm{aux}}, 0, 0]$ and $[\tilde{\sigma}_{\mathrm{aux}}, 0, 0]$ for the moving and stationary point load cases, respectively, which come into play through $\tilde{\tilde{\mathbf{Q}}}_2^{\mathrm{i}}$ (as shown below). The expressions for $\tilde{\tilde{\sigma}}_{\mathrm{aux}}$ and $\tilde{\sigma}_{\mathrm{aux}}$ are given in Eq. (4.12) and Eq. (F.3), respectively. For the considered problem, we assume perfect bonding between the soil and tunnel, implying continuous displacements and stresses at the tunnel-soil interface L_{r}:

$$\tilde{\tilde{\mathbf{U}}}_1(R_{\mathrm{o}}, \theta_1, k_x, \omega) = \tilde{\tilde{\mathbf{U}}}_2^{\mathrm{o}}(\theta_1, k_x, \omega), \tag{4.32}$$

$$\tilde{\tilde{\Sigma}}_1(R_{\mathrm{o}}, \theta_1, k_x, \omega) = \tilde{\tilde{\Sigma}}_2^{\mathrm{o}}(\theta_1, k_x, \omega), \tag{4.33}$$

where $\tilde{\tilde{\mathbf{U}}}_1$ and $\tilde{\tilde{\mathbf{U}}}_2$ are the displacement vectors of the soil and tunnel, respectively, and $\tilde{\tilde{\Sigma}}_1$ and $\tilde{\tilde{\Sigma}}_2$ their stress vectors. The displacement and stress vectors of the soil and shell at the soil-tunnel interface are expressed as $\tilde{\tilde{\mathbf{U}}}_1 = [\tilde{\tilde{U}}_{r_1}, \tilde{\tilde{U}}_{\theta_1}, \tilde{\tilde{U}}_x]^{\mathrm{T}}$, $\tilde{\tilde{\Sigma}}_1 = [\tilde{\tilde{\sigma}}_{r_1 r_1}, \tilde{\tilde{\sigma}}_{r_1\theta_1}, \tilde{\tilde{\sigma}}_{r_1 x}]^{\mathrm{T}}$, $\tilde{\tilde{\mathbf{U}}}_2^{\mathrm{o}} = [\tilde{\tilde{U}}^{\mathrm{o}}_{r_2}, \tilde{\tilde{U}}^{\mathrm{o}}_{\theta_2}, \tilde{\tilde{U}}^{\mathrm{o}}_{x_2}]^{\mathrm{T}}$ and $\tilde{\tilde{\Sigma}}_2^{\mathrm{o}} = [\tilde{\tilde{\sigma}}^{\mathrm{o}}_{r_2 r_2}, \tilde{\tilde{\sigma}}^{\mathrm{o}}_{r_2\theta_2}, \tilde{\tilde{\sigma}}^{\mathrm{o}}_{r_2 x_2}]^{\mathrm{T}}$. Note that all these displacements and stresses are defined in the global cylindrical coordinate system (r_1, θ_1, x).

According to the indirect BEM, the displacement and stress vectors in the soil are given as [Luco and de Barros, 1994a]

$$\tilde{\tilde{\mathbf{U}}}_1(\mathbf{x}_{\mathrm{r}}, k_x, \omega) = \int_{L_{\mathrm{s}}} \tilde{\tilde{\mathbf{G}}}_{u,1}\left(\mathbf{x}_{\mathrm{r}}, \mathbf{x}_{\mathrm{s}}, k_x, \omega\right) \mathbf{F}\left(\mathbf{x}_{\mathrm{s}}\right) \, \mathrm{d}l\left(\mathbf{x}_{\mathrm{s}}\right), \tag{4.34}$$

$$\tilde{\tilde{\Sigma}}_1(\mathbf{x}_{\mathrm{r}}, k_x, \omega) = \int_{L_{\mathrm{s}}} \tilde{\tilde{\mathbf{G}}}_{\sigma,1}(\mathbf{x}_{\mathrm{r}}, \mathbf{x}_{\mathrm{s}}, k_x, \omega) \mathbf{F}\left(\mathbf{x}_{\mathrm{s}}\right) \, \mathrm{d}l\left(\mathbf{x}_{s}\right), \tag{4.35}$$

where $\mathbf{F}\left(\mathbf{x}_{\mathrm{s}}\right)$ is the yet unknown vector of the source amplitudes placed inside the fictitious cavity which is commonly used for the indirect BEM (see Fig. 4.4). Vectors $\mathbf{x}_{\mathrm{r}} = [x_{\mathrm{r}}, y_{\mathrm{r}}, z_{\mathrm{r}}]$ and $\mathbf{x}_{\mathrm{s}} = [x_{\mathrm{s}}, y_{\mathrm{s}}, z_{\mathrm{s}}]$ are coordinates of the receiver and source points, respectively. L_{s} is the surface at which the source points are located, and the radius of the surface L_{s} is taken as $R_{\mathrm{s}} = R_{\mathrm{o}} - 3(2\pi R_{\mathrm{o}}/N_{\mathrm{r}})$, where N_{r} denotes the number of receiver points, and $N_{\mathrm{r}} \geqslant 20$ as suggested in Luco and de Barros [1994a]. The surface L_{r} at which the receiver points are located lies at $r_1 = R_{\mathrm{o}}$, which is the outer surface of the actual tunnel.

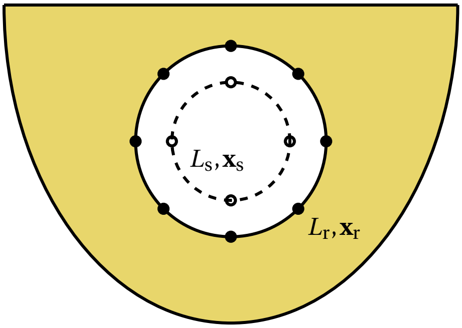

Figure 4.4: The elastic half-space with the fictitious cavity. L_{r} (solid line) and L_{s} (dashed line) are surfaces at which the receiver (filled circles) and source (open circles) points are located, respectively.

An expression for the displacement vector of the shell has been obtained in Eq. (4.31), and can be rewritten as

$$\begin{aligned}\tilde{\tilde{\mathbf{U}}}_2^{\mathrm{o}}(\mathbf{x}_{\mathrm{r}}, k_x, \omega) = &\int_{L_{\mathrm{r}}} \tilde{\tilde{\mathbf{G}}}^{\mathrm{o}}_{u,2}\left(\mathbf{x}_{\mathrm{r}}, \mathbf{x}'_{\mathrm{r}}, k_x, \omega\right) \tilde{\tilde{\mathbf{Q}}}_2^{\mathrm{o}}\left(\mathbf{x}'_{\mathrm{r}}, k_x, \omega\right) \, \mathrm{d}l(\mathbf{x}'_{\mathrm{r}}) \\ &+ \int_{L} \tilde{\tilde{\mathbf{G}}}^{\mathrm{i}}_{u,2}\left(\mathbf{x}_{\mathrm{r}}, \mathbf{x}', k_x, \omega\right) \tilde{\tilde{\mathbf{Q}}}_2^{\mathrm{i}}\left(\mathbf{x}', k_x, \omega\right) \, \mathrm{d}l(\mathbf{x}'),\end{aligned} \tag{4.36}$$

where $\tilde{\tilde{\mathbf{G}}}^{\{\mathrm{o,i}\}}_{u,2}$ contain the Green's functions for the displacements of the shell defined in the global cylindrical reference frame. The integration surfaces in Eq. (4.36) are L_{r} and L (i.e., source points located at $r_1 = R_{\mathrm{o}}$ and $r_1 = R_{\mathrm{i}}$, respectively) corresponding to the

Green's functions of the shell related to the forces acting at its outer and inner surfaces. The stress vectors acting at the outer and inner surfaces of the shell, respectively, for the current problem read, employing Eq. (4.33)

$$\tilde{\tilde{\mathbf{Q}}}_2^{\mathrm{o}}\left(\mathbf{x}_{\mathrm{r}}', k_x, \omega\right) = \tilde{\tilde{\Sigma}}_2\left(\mathbf{x}_{\mathrm{r}}', k_x, \omega\right) = \tilde{\tilde{\Sigma}}_1\left(\mathbf{x}_{\mathrm{r}}', k_x, \omega\right), \quad \tilde{\tilde{\mathbf{Q}}}_2^{\mathrm{i}}\left(\mathbf{x}', k_x, \omega\right) = \tilde{\tilde{\mathbf{P}}}\left(\mathbf{x}', k_x, \omega\right), \tag{4.37}$$

where $\tilde{\tilde{\mathbf{P}}}$ is the excitation stress vector (i.e., $[\tilde{\tilde{\sigma}}_{\mathrm{aux}}, 0, 0]^{\mathrm{T}}$ or $[\tilde{\sigma}_{\mathrm{aux}}, 0, 0]^{\mathrm{T}}$) induced by the external point load (see Fig. 4.2 (a)).

Substituting Eqs. (4.34) and (4.36) into Eq. (4.32), and considering Eqs. (4.35) and (4.37), we derive the boundary integral equation in terms of the unknown source amplitude vector:

$$\int_{L_{\mathrm{s}}} \tilde{\tilde{\mathbf{K}}}\left(\mathbf{x}_{\mathrm{r}}, \mathbf{x}_{\mathrm{s}}, k_x, \omega\right) \mathbf{F}\left(\mathbf{x}_{\mathrm{s}}\right)\, \mathrm{d}l\left(\mathbf{x}_{\mathrm{s}}\right) = \tilde{\tilde{\mathbf{R}}}\left(\mathbf{x}_{\mathrm{r}}, k_x, \omega\right), \tag{4.38}$$

where

$$\begin{aligned} \tilde{\tilde{\mathbf{K}}}\left(\mathbf{x}_{\mathrm{r}}, \mathbf{x}_{\mathrm{s}}, k_x, \omega\right) &= \tilde{\tilde{\mathbf{G}}}_{u,1}\left(\mathbf{x}_{\mathrm{r}}, \mathbf{x}_{\mathrm{s}}, k_x, \omega\right) - \int_{L_{\mathrm{r}}} \tilde{\tilde{\mathbf{G}}}_{u,2}^{\mathrm{o}}\left(\mathbf{x}_{\mathrm{r}}, \mathbf{x}_{\mathrm{r}}', k_x, \omega\right) \tilde{\tilde{\mathbf{G}}}_{\sigma,1}(\mathbf{x}_{\mathrm{r}}', \mathbf{x}_{\mathrm{s}}, k_x, \omega)\, \mathrm{d}l(\mathbf{x}_{\mathrm{r}}'), \\ \tilde{\tilde{\mathbf{R}}}\left(\mathbf{x}_{\mathrm{r}}, k_x, \omega\right) &= \int_{L} \tilde{\tilde{\mathbf{G}}}_{u,2}^{\mathrm{i}}\left(\mathbf{x}_{\mathrm{r}}, \mathbf{x}', k_x, \omega\right)\, \tilde{\tilde{\mathbf{P}}}\left(\mathbf{x}', k_x, \omega\right)\, \mathrm{d}l(\mathbf{x}'). \end{aligned} \tag{4.39}$$

In order to compute the source vector for every k_x and ω combination, Eq. (4.38) is discretised (i.e., surfaces L_{r}, L and L_{s}), as indicated above. Note that the size of the matrix related to $\tilde{\tilde{\mathbf{K}}}$ is $(3N_{\mathrm{r}} \times 3N_{\mathrm{s}})$, where N_{s} denotes the number of source points; this implies that it is a small matrix, and the inversion of the matrix does not take much time. The most time consuming part (even in the entire procedure of stability analysis) is the evaluation of integrals over the horizontal wavenumber k_y in the Green's functions of the half-space, for which we use the “quadv" routine in Matlab.

4.4. VALIDATIONS

To validate the accuracy of the presented indirect BEM, we compare the results obtained by the proposed method with those calculated by Yuan *et al.* [2017]. The first validation is performed for the case of a tunnel embedded in an elastic full-space subject to a stationary harmonic point load at the tunnel invert. The excitation for the indirect BEM computation in this case is $\tilde{\sigma}_{\mathrm{aux}}$ (Eq. (F.3)), with $P_0 = 1$ N, and the steady-state response is given in Eq. (F.5). The elastic full-space is characterised by its longitudinal wave speed $C_{\mathrm{P},1} = 944$ m/s, shear wave speed $C_{\mathrm{S},1} = 309$ m/s, density $\rho_1 = 2000$ kg/m^3 and material damping ratio $\xi_1 = 0.03$. The elastic parameters for the tunnel are the Young's modulus $E_2 = 50$ GPa, Poisson's ratio $\nu_2 = 0.3$, density $\rho_2 = 2500$ kg/m^3 and material damping ratio $\xi_2 = 0$. The inner and outer radii of the tunnel are $R_{\mathrm{i}} = 2.75$ m and $R_{\mathrm{o}} = 3$ m.

Before showing the results, we first present a convergence test for the proposed method for the considered loading case. As shown in Eq. (F.5), the inverse Fourier Transform over longitudinal wavenumber k_x has to be evaluated to get the harmonic response in the space-time domain. The integral was computed numerically using an inverse fast Fourier Transform algorithm in Matlab. The convergence was tested regarding the discretisation of k_x (i.e., Δk_x and $k_x^{\max}$), the maximum number of circumferential modes of the shell $N_{\mathrm{shell}}^{\max}$ in Eq. (4.31) and the maximum number of Fourier components $N_{\mathrm{load}}^{\max}$

in Eq. (F.3), and the number of source and receiver points (N_s, N_r). We found that it is sufficient to use $k_x^{\max} = 2\pi$, $\Delta k_x = \frac{2\pi}{1023}$, $N_\mathrm{shell}^{\max} = 20$ and $N_\mathrm{load}^{\max} = 20$. The convergence test for the number of source and receiver points (N_s, N_o) at different locations (r_1, θ_1, x) is given in Table 4.1. Responses at the tunnel invert, tunnel apex (R_o, $\frac{\pi}{2}$, 0), tunnel side (R_o, π, 0) and at a point far from the load (20 m, π, 20 m) are presented; the load is characterised by $P_0 = 1$ N and $f_0 = \frac{\Omega}{2\pi} = 10$ Hz. It is clear that converged results can indeed be obtained using (N_s, N_r) = (20, 40).

Fig. 4.5 shows the converged vertical displacements at the tunnel invert, tunnel apex and tunnel side as a function of frequency for the first validation case. A good agreement can be observed between the results obtained by different methods, which validates the proposed method and its implementation.

Table 4.1: Displacement components ($20\log_{10}|U_i|$) at different locations (r_1, θ_1, x) for a tunnel embedded in an elastic full-space subjected to a stationary harmonic point load with excitation frequency $f_0 = 10$ Hz obtained using different numbers of source and receiver points ($N_\mathrm{s}, N_\mathrm{r}$). In each row, the displacements are normalised by the corresponding response obtained using ($N_\mathrm{s}, N_\mathrm{r}$) = (20, 40).

Displacements	($N_\mathrm{s}, N_\mathrm{r}$) = (20, 40)	($N_\mathrm{s}, N_\mathrm{r}$) = (30, 60)	($N_\mathrm{s}, N_\mathrm{r}$) = (40, 80)	($N_\mathrm{s}, N_\mathrm{r}$) = (60, 60)
U_{r_1} ($R_\mathrm{o}, -\frac{\pi}{2}, 0$)	1.0000	1.0002	1.0002	1.0002
U_{r_1} ($R_\mathrm{o}, \frac{\pi}{2}, 0$)	1.0000	1.0008	1.0008	1.0008
U_{r_1} ($R_\mathrm{o}, \pi, 0$)	1.0000	1.0000	1.0000	1.0000
U_{y_1} (20 m, π, 20 m)	1.0000	1.0000	1.0000	1.0000
U_{z_1} (20 m, π, 20 m)	1.0000	1.0000	1.0000	1.0000
U_x (20 m, π, 20 m)	1.0000	1.0000	1.0000	1.0000

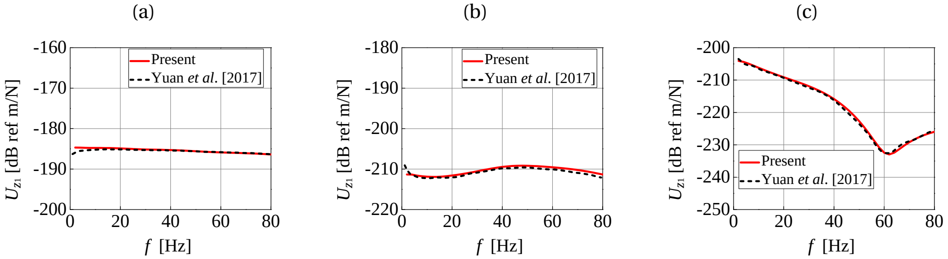

Figure 4.5: Vertical displacements ($20 \cdot \log_{10}|U_{z_1}|$) at locations of (a) tunnel invert ($r_1 = R_\mathrm{o}, \theta_1 = -\frac{\pi}{2}, x = 0$), (b) tunnel apex ($r_1 = R_\mathrm{o}, \theta_1 = \frac{\pi}{2}, x = 0$) and (c) tunnel side ($r_1 = R_\mathrm{o}, \theta_1 = \pi, x = 0$) for the case of a tunnel embedded in an elastic full-space subject to a stationary harmonic point load.

The second validation case is that of a shallow tunnel embedded in an elastic half-space subject to a stationary harmonic load. The soil is characterised by its longitudinal wave speed $C_{\mathrm{P},1} = 400$ m/s, shear wave speed $C_{\mathrm{S},1} = 200$ m/s, density $\rho_1 = 1800$ kg/m^3 and material damping ratio $\xi_1 = 0.02$. The parameters of the tunnel are the same as in the previous case, except that $\xi_2 = 0.015$, and the burial depth of the tunnel is $H = 5$ m. It is noted that in the reference paper yuan2017, the mentioned material damping ratio should be the loss factor (there is a difference of a factor 2), which is indicated in paper [Hussein *et al.*, 2014]. This also holds for the next validation case. The displacement components (again obtained using Eq. (F.5)) at a point on the ground surface ($y = -20$ m, $z = 0$, $x = 20$ m) are presented in Fig. 4.6, where again a good match between the results is observed. The minor differences can be attributed to the use of a continuum to model the tunnel in Yuan *et al.* [2017], instead of a shell.

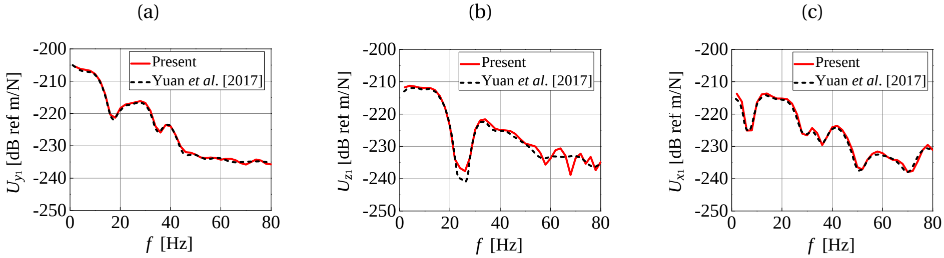

Figure 4.6: Displacement components ($20 \cdot \log_{10}|U_i|$) at a point on the ground surface ($y = -20$ m, $z = 0$, $x = 20$ m) for the case of a tunnel embedded in an elastic half-space ($H = 5$ m) subject to a stationary harmonic point load acting at the tunnel invert: (a) horizontal displacement, (b) vertical displacement and (c) longitudinal displacement.

The third validation comprises the case of a tunnel embedded in an elastic half-space subject to a uniformly moving constant point load. The excitation for the indirect BEM computation in this case is $\tilde{\tilde{\sigma}}_{\mathrm{aux}}$ (Eq. (4.12)) and the steady-state response is given in Eq. (4.14). The parameters for the soil and tunnel are as follows: $\mu_1 = 1.154 \times 10^7$ N/m^2, $\lambda_1 = 1.731 \times 10^7$ N/m^2, $\rho_1 = 1900$ kg/m^3, $\xi_1 = 0.025$, $\mu_2 = 1.042 \times 10^{10}$ N/m^2, $\lambda_2 = 6.944 \times 10^9$ N/m^2, $\rho_2 = 2400$ kg/m^3, $\xi_2 = 0.01$, $R_{\mathrm{i}} = 2.75$ m, $R_{\mathrm{o}} = 3$ m, $H = 15$ m. The moving load is characterised by velocity $V = 75$ m/s, excitation frequency $f_0 = 0$ and $P_0 = 1$ N. The inverse Fourier Transform over frequencies needs to be evaluated to get the space-time domain response (see Eq. (4.14)). The convergence for the moving point load case was tested regarding the discretisation of ω (i.e., $\Delta\omega$ and $\omega^{\max}$), $N_{\mathrm{shell}}^{\max}$ in Eq. (4.31) and $N_{\mathrm{load}}^{\max}$ in Eq. (4.12), and the number of source and receiver points (N_{s}, N_{r}). Numerical results related to two points on the ground surface and one at the tunnel invert are presented in Table 4.2 for the considered case of the moving load using different number of source and receiver points (N_{s}, N_{r}). We found that converged results can be obtained using $f^{\max} = \frac{\omega^{\max}}{2\pi} = 15$ Hz, $\Delta f = \frac{\Delta\omega}{2\pi} = 0.05$ Hz, $N_{\mathrm{shell}}^{\max} = 20$, $N_{\mathrm{load}}^{\max} = 20$ and (N_{s}, N_{r}) = (20, 40). This is clear from Table 4.2 which presents the responses observed at $x = 0$ for varying time moments: $t = 0$ means that the load is right below the observation point, whereas $t = 1$ s indicates that the load has passed that point. Fig. 4.7 presents the comparison between the results obtained by the proposed method and those shown in the literature.

The good agreement gives confidence about the accuracy of the proposed method.

The convergence requirements for the computation of the equivalent dynamic stiffness for different velocities are presented in Appendix H.

Table 4.2: Velocities ($V_i(y,z,x)$) and displacement ($U_{r_1}(r_1,\theta_1,x)$) at different locations for a tunnel embedded in an elastic half-space subject to a uniformly moving point load ($V = 75$ m/s, $f_0 = 0$) using different numbers of source and receiver points ($N_\mathrm{s}, N_\mathrm{r}$). In each row, the responses are normalised by the corresponding response obtained using ($N_\mathrm{s}, N_\mathrm{r}$) = (20, 40).

Responses	Time (s)	$(N_\mathrm{s}, N_\mathrm{r}) = (20,40)$	$(N_\mathrm{s}, N_\mathrm{r}) = (30,60)$	$(N_\mathrm{s}, N_\mathrm{r}) = (40,80)$	$(N_\mathrm{s}, N_\mathrm{r}) = (60,60)$
V_z	$t = 0$	1.0000	1.0000	1.0000	1.0000
(0, 0, 0)	$t = 1$	1.0000	1.0000	1.0000	1.0000
V_x	$t = 0$	1.0000	1.0000	1.0000	1.0000
(0, 0, 0)	$t = 1$	1.0000	1.0000	1.0000	1.0000
V_z	$t = 0$	1.0000	1.0000	1.0000	1.0000
(−20 m, 0, 0)	$t = 1$	1.0000	1.0000	1.0000	1.0000
V_x	$t = 0$	1.0000	1.0000	1.0000	1.0000
(−20 m, 0, 0)	$t = 1$	1.0000	1.0000	1.0000	1.0000
U_{r_1}	$t = 0$	1.0000	0.9998	0.9998	0.9998
$(R_\mathrm{o}, -\frac{\pi}{2}, 0)$	$t = 1$	1.0000	1.0000	1.0000	1.0000

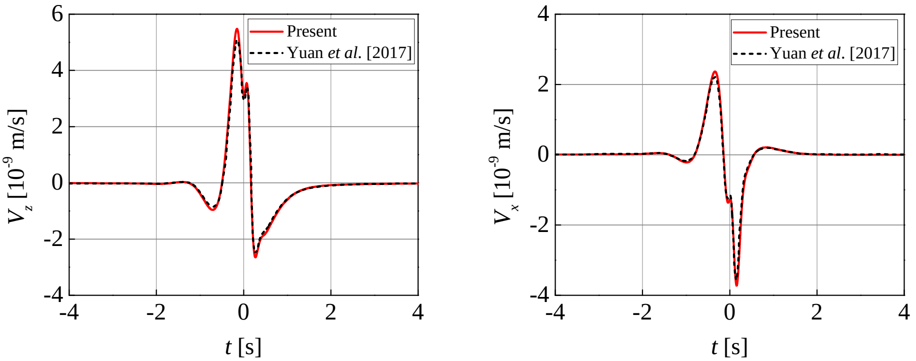

Figure 4.7: Velocities (V_i) at the origin ($y = 0$, $z = 0$, $x = 0$) on the ground surface for the case of a tunnel embedded in an elastic half-space ($H = 15$ m) subject to a uniformly moving point load ($V = 75$ m/s, $f_0 = 0$): (a) vertical velocity and (b) longitudinal velocity.

4.5. INSTABILITY OF VIBRATIONS

The main framework to conduct stability analysis has been given in Section 4.2.2. In the current section, we present the results for both the full-space and half-space. The base-case parameters of the tunnel-soil system are listed in Table 4.3; it is noted that the base case assumes that the burial depth $H \to \infty$. The parameters presented in Table 4.3 represent a soft soil and a concrete tunnel.

We chose the full-space case as the base case simply because the results for the half-space are pretty similar, and the computation of the two-and-a-half dimensional Green's functions of the full-space [Tadeu and Kausel, 2000] is less expensive than that of the half-space Green's functions [Tadeu *et al.*, 2001]. The Green's functions of the full-space are available analytically and can be evaluated very fast; however, the surface-terms part of the Green's functions of the half-space (see Section 4.3.1) are not available analytically, and integrals over the horizontal wavenumber k_y need to be evaluated numerically.

Table 4.3: Base-case parameters of the tunnel-soil system

Soil	Tunnel
$\mu_1 = 1.154 \times 10^7$ N/m^2	$\mu_2 = 1.042 \times 10^{10}$ N/m^2
$\lambda_1 = 1.731 \times 10^7$ N/m^2	$\lambda_2 = 6.944 \times 10^9$ N/m^2
$\rho_1 = 1900$ kg/m^3	$\rho_2 = 2400$ kg/m^3
$\xi_1 = 0.05$	$\xi_2 = 0.02$
$C_{\mathrm{S},1} = 77.94$ m/s	$C_{\mathrm{S},2} = 2083.7$ m/s
$C_{\mathrm{P},1} = 145.80$ m/s	$C_{\mathrm{P},2} = 3402.5$ m/s
$C_{\mathrm{R},1} = 72.29$ m/s	$R_\mathrm{i} = 2.75$ m, $R_\mathrm{o} = 3$ m, $h = 0.25$ m, $H \to \infty$

4.5.1. CRITICAL VELOCITY FOR INSTABILITY OF THE MOVING OBJECT

As has been discussed in Section 4.2.2, the imaginary part of the equivalent stiffness being negative indicates that the vibration of the object (i.e., moving mass or oscillator) can become unstable. Therefore, we first study the equivalent stiffness to find the critical velocity for instability of the moving object (here defined as the velocity at which $\mathrm{Im}(K_{\mathrm{eq}}) < 0$ first takes places). Note that the critical velocity for instability generally differs from the classical critical velocity at which the steady-state response induced by a moving load is extreme (i.e., resonance). In the general case, where the oscillator has dissipative components, the critical velocity for instability should be identified from the D-decomposition curve in the complex M or K planes (see Sections 4.2.2 and 4.5.2), not from the analysis of $\mathrm{Im}(K_{\mathrm{eq}})$ alone [Metrikine and Verichev, 2001; Metrikine *et al.*, 2005]. $\mathrm{Im}(K_{\mathrm{eq}}) < 0$ is only a necessary condition for instability. As the moving oscillator and moving mass considered in this chapter do not have intrinsic dissipative components, their critical velocities for instability are the same.

In previous studies [Metrikine and Dieterman, 1997; Metrikine and Verichev, 2001] where beam on elastic foundation models (without damping) are considered, it is shown that the critical velocity for instability $V_{\mathrm{cr}}^{\mathrm{inst}}$ of the moving object is equal to the critical velocity for resonance (of the undamped system), which in turn is equal to the minimum phase velocity $V_{\mathrm{ph}}^{\mathrm{min}}$ of waves in the system. For a half-space model with a regular track on top [Metrikine and Popp, 1999; Metrikine *et al.*, 2005], the critical velocity for instability in the presence of damping is slightly larger than $V_{\mathrm{ph}}^{\mathrm{min}}$. Additionally, $V_{\mathrm{ph}}^{\mathrm{min}}$, which is close to and smaller than the velocity of Rayleigh waves, is easily found from the dispersion relation of the system [Metrikine, 1994; Metrikine and Vrouwenvelder, 2000]. However, for the tunnel-soil system considered in this chapter, it is very difficult to get the

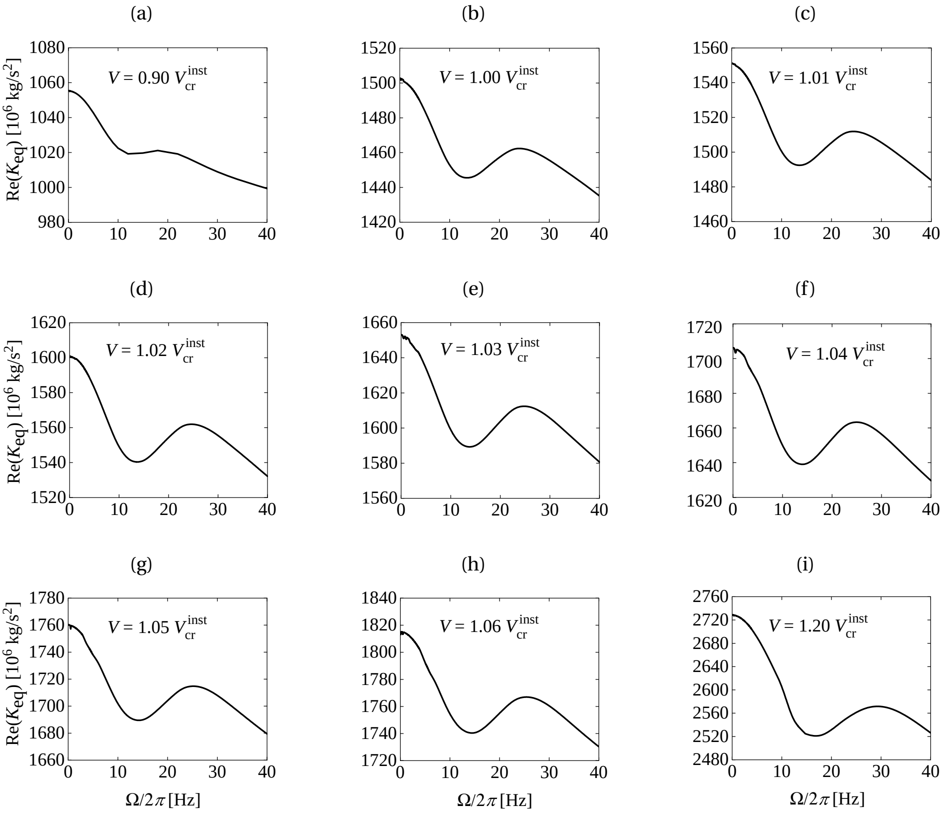

Figure 4.8: The real part of the equivalent stiffness for different velocities: (a) $V = 0.90V_{\mathrm{cr}}^{\mathrm{inst}}$, (b) $V = 1.00V_{\mathrm{cr}}^{\mathrm{inst}}$, (c) $V = 1.01V_{\mathrm{cr}}^{\mathrm{inst}}$, (d) $V = 1.02V_{\mathrm{cr}}^{\mathrm{inst}}$, (e) $V = 1.03V_{\mathrm{cr}}^{\mathrm{inst}}$, (f) $V = 1.04V_{\mathrm{cr}}^{\mathrm{inst}}$, (g) $V = 1.05V_{\mathrm{cr}}^{\mathrm{inst}}$, (h) $V = 1.06V_{\mathrm{cr}}^{\mathrm{inst}}$ and (i) $V = 1.20V_{\mathrm{cr}}^{\mathrm{inst}}$. These results are related to the base case presented in Table 4.3, and $V_{\mathrm{cr}}^{\mathrm{inst}} = 942$ m/s.

dispersion curves, as the dispersion characteristics of the system are considerably more complicated. Therefore, the minimum phase velocity cannot be easily computed. We can, however, compute the steady-state response of the tunnel-soil system subject to a uniformly moving non-oscillatory load and check the features of responses for different velocities to determine the critical velocity for resonance (for the system with damping, strictly speaking, but the influence of the damping on $V_{\mathrm{cr}}^{\mathrm{res}}$ is small). This analysis is presented in Appendix H, and it shows that $V_{\mathrm{cr}}^{\mathrm{res}} \approx 70$ m/s for the current tunnel-soil system, which is also close to and smaller than the velocity of Rayleigh waves, like for the above-mentioned half-space model.

For the system with the base-case parameters, we find that the imaginary part of the equivalent stiffness starts having a negative sign for at least a small frequency range at a velocity of $V_{\mathrm{cr}}^{\mathrm{inst}} = 942$ m/s. Based on this critical velocity for instability, we study the behavior of $K_{\mathrm{eq}}(\Omega, V)$ for different velocities in the range of $(0.9 - 1.2)\,V_{\mathrm{cr}}^{\mathrm{inst}}$. The real and imaginary parts are shown in Figs. 4.8 and 4.9, respectively. Nine different velocities were

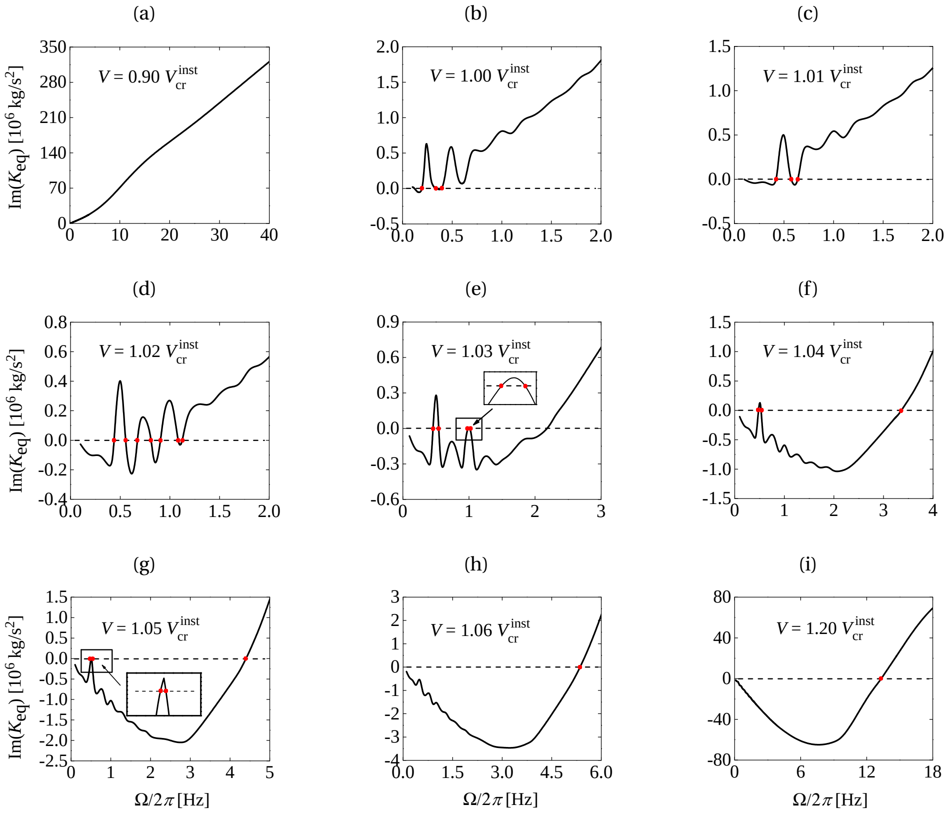

Figure 4.9: The imaginary part of the equivalent stiffness for different velocities: (a) $V = 0.90V_{\text{cr}}^{\text{inst}}$, (b) $V = 1.00V_{\text{cr}}^{\text{inst}}$, (c) $V = 1.01V_{\text{cr}}^{\text{inst}}$, (d) $V = 1.02V_{\text{cr}}^{\text{inst}}$, (e) $V = 1.03V_{\text{cr}}^{\text{inst}}$, (f) $V = 1.04V_{\text{cr}}^{\text{inst}}$, (g) $V = 1.05V_{\text{cr}}^{\text{inst}}$, (h) $V = 1.06V_{\text{cr}}^{\text{inst}}$ and (i) $V = 1.20V_{\text{cr}}^{\text{inst}}$. These results are related to the base case presented in Table 4.3, and $V_{\text{cr}}^{\text{inst}} = 942$ m/s. The read dots indicate the crossings.

chosen to show the features of $\text{Re}(K_{\text{eq}})$ and $\text{Im}(K_{\text{eq}})$ as a function of the load frequency Ω. Note that, if its mass is relatively small, the vibration of the object can still be stable when it moves faster than $V_{\text{cr}}^{\text{inst}}$, as will be demonstrated in the next section (see also Fig. 4.11).

In Fig. 4.8, we observe that the real part of the equivalent stiffness is positive, and the decaying trend of $\text{Re}(K_{\text{eq}})$ with frequency Ω is similar for each velocity. The decaying trend may be related to the effect of inertia. The trough can probably be interpreted as a quasi-resonance which takes place at low frequencies and is related to the wave resonance which occurs if the velocity of the moving load is the same as the group velocity of a wave excited by the load [Metrikine and Popp, 1999].

The imaginary part of the equivalent stiffness is shown in Fig. 4.9 for each of the chosen velocities. For the ‘sub-critical’ ($V < V_{\text{cr}}^{\text{inst}}$) case shown in Fig. 4.9 (a), $V = 0.9V_{\text{cr}}^{\text{inst}}$, $\text{Im}(K_{\text{eq}})$ is positive for all the frequencies Ω, which indicates that the damping coefficient of the equivalent mass-spring system is positive, and thus, the system is always stable (see Section 4.2.2). The frequency band considered in this study of the dynamic stiffness is limited to $(0-40)$ Hz, because instability is determined by the behaviour at low frequencies [Metrikine and Popp, 1999; Metrikine *et al.*, 2005]; see also the explanation given at the end of this section. For the 'critical' and 'super-critical' ($V \geq V_{\mathrm{cr}}^{\mathrm{inst}}$) cases, shown in Figs. 4.9 (b) - (i), the imaginary part of the equivalent stiffness is negative at low frequencies and becomes positive at higher frequencies. We can verify that the curves of $\mathrm{Im}(K_{\mathrm{eq}})$ in the high-frequency band have the same trend as that in the sub-critical case; they are not shown here since we focus on features of $\mathrm{Im}(K_{\mathrm{eq}})$ in the low-frequency band. There are peaks and troughs in the curves of $\mathrm{Im}(K_{\mathrm{eq}})$, and these are suppressed or enlarged as the velocity increases. We observe that the $\mathrm{Im}(K_{\mathrm{eq}})$ curve crosses the real axis 0, 4, 3, 7, 5, 3, 3, 1 and 1 times for $V = (0.9, 1.00, 1.01, 1.02, 1.03, 1.04, 1.05, 1.06, 1.20)\,V_{\mathrm{cr}}^{\mathrm{inst}}$, respectively. We can verify that for velocities $V = (1.06-1.20)\,V_{\mathrm{cr}}^{\mathrm{inst}}$, similar features of $\mathrm{Im}(K_{\mathrm{eq}})$ are observed (i.e., the $\mathrm{Im}(K_{\mathrm{eq}})$ curve crosses the real axis only once), the only difference is that the crossing occurs at higher frequency Ω as the velocity increases (see Figs. 4.9 (h) and (i)). The different features of $\mathrm{Im}(K_{\mathrm{eq}})$ observed in the entire considered velocity range imply that in the complex M or K plane different amounts of separated domains, each having a specific number of 'unstable roots/eigenvalues', are expected for different velocities (see Section 4.5.2). At this point, it is concluded that the equivalent dynamic stiffness, especially its imaginary part, strongly depends on V.

In order to trace similarities and differences, let us now compare two different stability problems: the above mentioned model of an object moving on a track placed on the ground surface [Metrikine and Popp, 1999; Metrikine *et al.*, 2005], and the current model of an object moving through a tunnel embedded in a half-space. The critical velocity for instability for the current model with all parameters in accordance with the base case, except the burial depth H which is taken as 15 m, is found to be 891 m/s (see also Section 4.6.4). Clearly, $V_{\mathrm{cr}}^{\mathrm{inst}}$ is much larger than the critical velocity for resonance ($V_{\mathrm{cr}}^{\mathrm{res}} \approx 70$ m/s) in the model with an embedded tunnel, while $V_{\mathrm{cr}}^{\mathrm{inst}}$ is just slightly larger than $V_{\mathrm{cr}}^{\mathrm{res}}$ in the model with a track directly placed on the ground [Metrikine and Popp, 1999; Metrikine *et al.*, 2005] ($V_{\mathrm{cr}}^{\mathrm{res}}$ is related to the undamped system in these studies, but the influence of the damping on $V_{\mathrm{cr}}^{\mathrm{res}}$ is small). The difference is due to the large stiffness of the tunnel and the radiation damping/leaky character of the waves excited in the tunnel. However, there are similarities regarding ground vibrations in these two models. In the regime of $V < V_{\mathrm{cr}}^{\mathrm{res}}$ ($\approx V_{\mathrm{ph}}^{\mathrm{min}}$), for both models mostly the medium in the vicinity of the load is disturbed by the eigenfield excited by the moving non-oscillating object, while in the regime of $V > V_{\mathrm{cr}}^{\mathrm{res}}$, both the vicinity of the moving source and the field far from the source are disturbed because waves are generated (see Appendix H). As mentioned above, the critical velocity for resonance of the current tunnel-soil system is close to and smaller than the velocity of Rayleigh waves, like that of the other model. Therefore, from the ambient-vibration point of view, there is a clear similarity between both problems. However, instability happens only far beyond the critical velocity for resonance for the model with the tunnel, which is clearly different from the finding for the half-space with a track placed on top.

As shown in Metrikine [1994], an external source has to supply a vibrating object with energy in order to maintain its uniform motion. In the case of unstable vibrations, the work done by the source is partially transferred to vibration energy of the object by the so-called anomalous Doppler waves [Ginzburg, 1979], which are waves of negative frequency. Typical dispersion curves of the current tunnel-soil system, which are similar to the ones of the beam on elastic foundation model [Wolfert *et al.*, 1998], are shown in Fig. 4.10 and can be used to explain why the instability only happens in the low-frequency band, as stated above. Fig. 4.10 also shows the so-called kinematic invariant $\omega = k_x V + \Omega$, which is essentially found in the argument of the Dirac function in the response to a moving oscillatory load (see Eq. (4.14)). The kinematic invariant is a straight line indicating the relation between the load frequency Ω, and the frequency ω and wavenumber k_x of the waves that are potentially excited by the moving object; different realizations (i.e., Ω being zero and nonzero, together with two different velocities) are shown in the Fig. 4.10. Intersections of the kinematic invariant with the dispersion curves represent the excited waves. We observe that intersections with negative frequency ω (i.e., anomalous Doppler waves) are only possible when the load frequency Ω is relatively small. If the load frequency Ω is large, the kinematic invariant will practically never intersect the dispersion curves at negative frequency, which explains why the vibration of the moving object is always stable in the high-frequency band (i.e., $\mathrm{Im}(K_{\mathrm{eq}}) > 0$, see Fig. 4.9); this also justifies that we restricted the analysis of K_{eq} to the low-frequency band in Figs. 4.8 and 4.9.

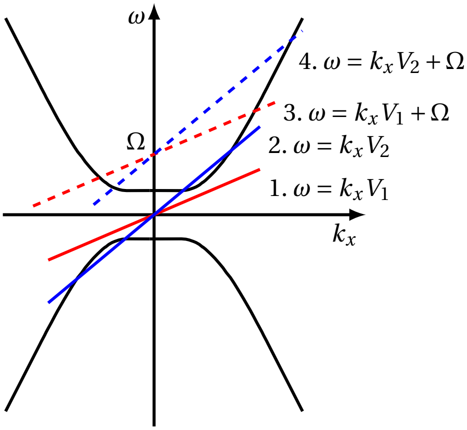

Figure 4.10: Typical dispersion curves of the current system, which are similiar to the ones for an Euler-Bernoulli beam resting on an elastic foundation. Four different realizations of the kinematic invariant (i.e., Ω being zero and nonzero, together with two different velocities V_1 and V_2) are considered. Ω is the load frequency, ω and k_x are the frequency and wavenumber of the waves excited by the load.

4.5.2. D-DECOMPOSITION: COMPLEX M AND K PLANES

In order to investigate the stability of the object vibrations for velocities larger than the corresponding critical velocity for instability identified in the previous section, we apply the D-decomposition method. We first investigate the limit case of the single mass moving through the tunnel. Considering the base case, the D-decomposition curve can be plotted in the complex M plane (i.e., $\mathrm{Im}(M)$ versus $\mathrm{Re}(M)$) using the mapping rule shown in Eq. (4.5) and is presented in Fig. 4.11. For most of the considered velocities, the D-decomposition curve crosses the positive real axis, that is, one or more crossing points M^* are obtained. It can be verified that the frequency at which the curve crosses the real axis corresponds to the frequency at which the imaginary part of the dynamic stiffness changes sign (see Fig. 4.9). A crossing point lying on the positive real axis can be explained by the fact that $\mathrm{Re}(K_{\mathrm{eq}})$ is positive when the $\mathrm{Im}(K_{\mathrm{eq}})$ changes its sign (see Fig. 4.8).

As it is clearly shown in Fig. 4.11, the crucial difference between the D-decomposition curves in the super-critical and sub-critical cases - compare Figs. 4.12 (b) and (a), for example - is that there are crossing points M_1^*, M_2^*, M_3^* and M_4^* on the positive axis of $\mathrm{Re}(M)$ for the super-critical case. The existence of such crossing points means that the number N of unstable roots (roots with a positive real part) is different in the domains of $M < M_1^*$, $M_2^* < M < M_3^*$ and $M > M_4^*$ from that in domains of $M_1^* < M < M_2^*$ and $M_3^* < M < M_4^*$.

The procedure to determine N is as follows. The relative number of unstable roots in domains of the complex M plane can be calculated by counting the number of times that one crosses the D-decomposition curve in the direction of the shading, which has been explained in Section 4.2.2. To get the absolute number in all domains, the number of unstable roots for $M = 0$ has to be determined. $M = 0$ means that there is essentially no moving mass, which implies that the vibration of the mass cannot be unstable (i.e., the number of unstable roots $N = 0$). Thereafter, the absolute number of unstable roots in each domain can be determined and the result is shown in Fig. 4.11. The number of unstable roots has also been validated using the Argument Principle, but this is not shown in the chapter.

In Fig. 4.11, we observe that the vibration of the moving mass is stable for all values of M for $V = 0.9V_{\mathrm{cr}}^{\mathrm{inst}}$; for $V = 1.00V_{\mathrm{cr}}^{\mathrm{inst}}$, the vibration of the moving mass is unstable when $M_1^* < M < M_2^*$ and $M_3^* < M < M_4^*$ $(N = 2)$; for $V = 1.01V_{\mathrm{cr}}^{\mathrm{inst}}$, when $M_1^* < M < M_2^*$ and $M > M_3^*$, etc. Note that the vibration of a mass which moves faster then the critical velocity is not necessarily unstable. For relatively small values of the mass, for example, the vibration is stable even for super-critical velocities (as illustrated in Section 4.6).

The question of practical relevance when studying the stability of the moving mass is whether adding flexibility (by creating a spring between the mass and the tunnel) may destabilize the system. For the mass-spring oscillator with the mass being constant, the D-decomposition curve can be plotted in the complex K plane (i.e., $\mathrm{Im}(K)$ versus $\mathrm{Re}(K)$) using the mapping rule shown in Eq. (4.6) and is presented in Fig. 4.12. The mass of the moving oscillator is taken as $M = 2 \times 10^4$ kg, which is a realistic value for a train wagon. In order to get the absolute number of unstable roots in the complex K plane with this mass, we have to connect the stability analysis of the moving oscillator to that of the single moving mass shown in Fig. 4.11. From that figure, we find that $N = 0$ for $M = 2 \times 10^4$ kg, which implies that the system is stable for this value of the mass for all the considered velocity cases. The single mass case corresponds to the oscillator case with $K \to \infty$. Therefore, knowing that the number of unstable roots at $K \to \infty$ is zero and following the direction of the shading, the absolute number of unstable roots in domains of the complex K plane can be determined.

The following can be observed from the D-decomposition curve in the complex K

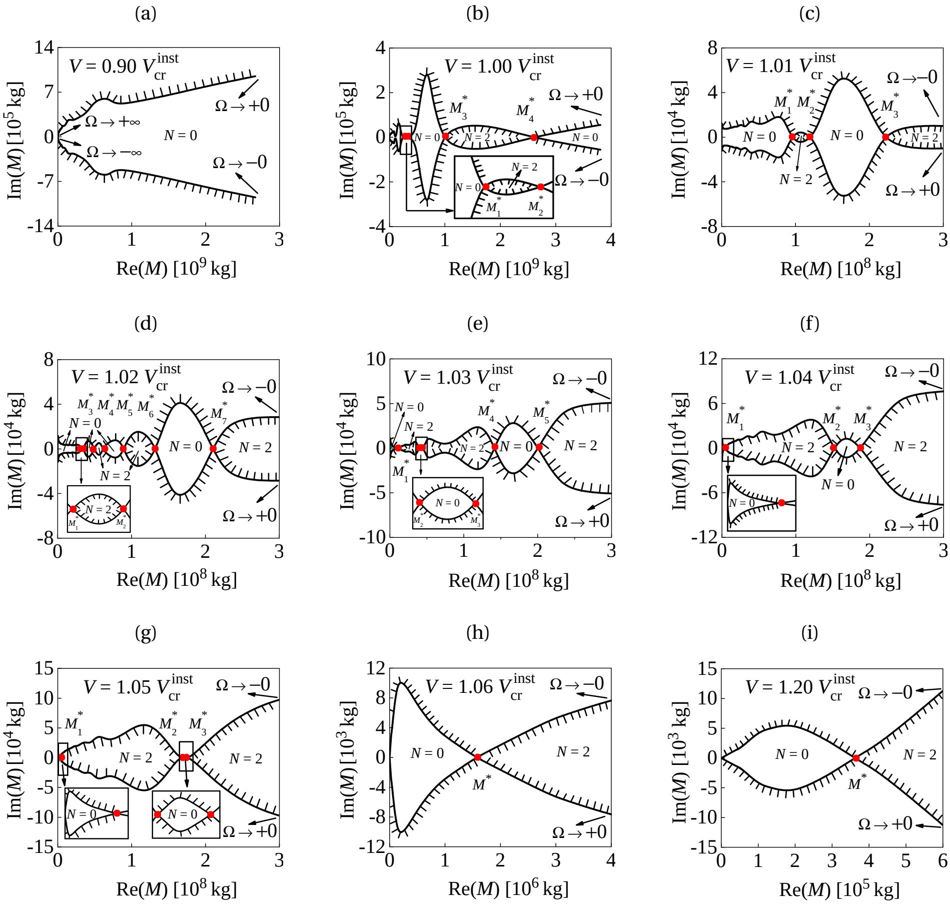

Figure 4.11: Separation of the complex M plane into domains with different number N of unstable roots: (a) $V = 0.90V_{\text{cr}}^{\text{inst}}$, (b) $V = 1.00V_{\text{cr}}^{\text{inst}}$, (c) $V = 1.01V_{\text{cr}}^{\text{inst}}$, (d) $V = 1.02V_{\text{cr}}^{\text{inst}}$, (e) $V = 1.03V_{\text{cr}}^{\text{inst}}$, (f) $V = 1.04V_{\text{cr}}^{\text{inst}}$, (g) $V = 1.05V_{\text{cr}}^{\text{inst}}$, (h) $V = 1.06V_{\text{cr}}^{\text{inst}}$ and (i) $V = 1.20V_{\text{cr}}^{\text{inst}}$. These results are related to the base case presented in Table 4.3, and $V_{\text{cr}}^{\text{inst}} = 942$ m/s. The red dots indicate the crossings (i.e., the critical masses M^*), and N in each separated domain is shown. Points $\Omega \to \pm 0$ are indicated in (a)-(i), while points $\Omega \to \pm\infty$ are only indicated in (a) for visibility reasons.

plane shown in Fig. 4.12. For $V = 0.9V_{\text{cr}}^{\text{inst}}$, the vibration of the moving oscillator is stable for all values of the stiffness; for $V = 1.00V_{\text{cr}}^{\text{inst}}$, the vibration of the moving oscillator is destabilized by the added spring when $K_1^* < K < K_2^*$ and $K_3^* < K < K_4^*$ ($N = 2$); for $V = 1.01V_{\text{cr}}^{\text{inst}}$, that happens when $K < K_1^*$ and $K_2^* < K < K_3^*$, etc. Using these findings, it can be readily concluded that for the sub-critical case, the vibration of the oscillator is stable independently of the oscillator's stiffness, while for the super-critical cases, the stability of the oscillator depends on the stiffness of the added spring.

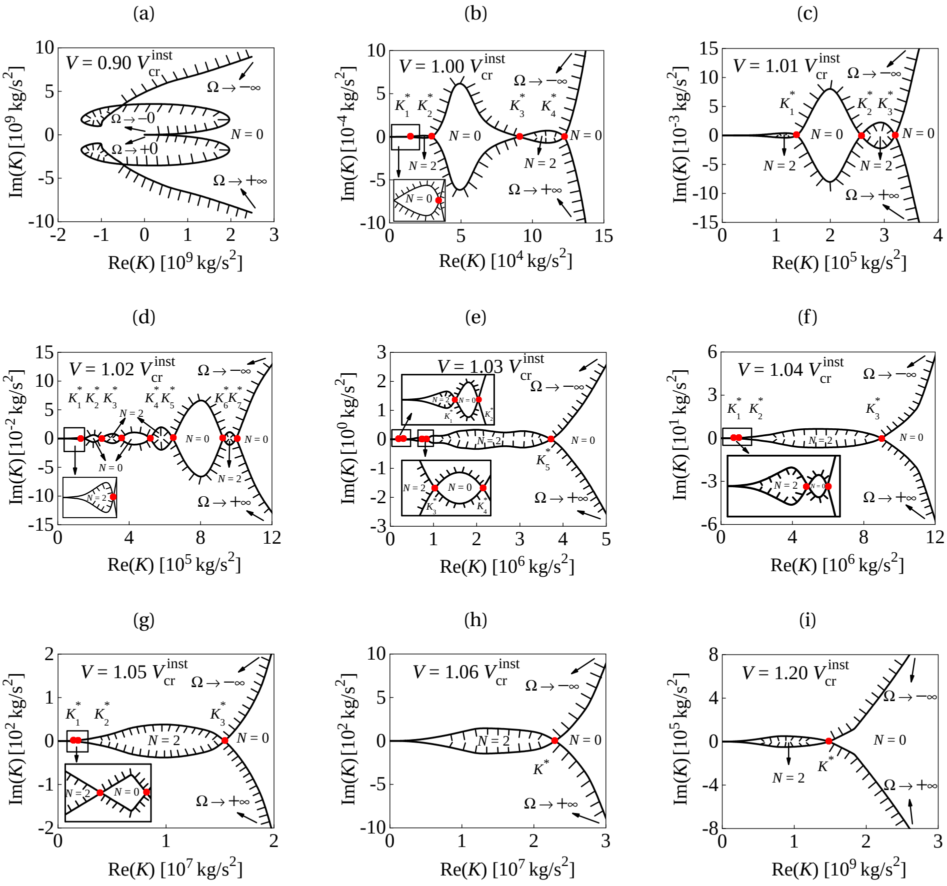

Figure 4.12: Separation of the complex K plane into domains with different number N of unstable roots: (a) $V = 0.90V_{\text{cr}}^{\text{inst}}$, (b) $V = 1.00V_{\text{cr}}^{\text{inst}}$, (c) $V = 1.01V_{\text{cr}}^{\text{inst}}$, (d) $V = 1.02V_{\text{cr}}^{\text{inst}}$, (e) $V = 1.03V_{\text{cr}}^{\text{inst}}$, (f) $V = 1.04V_{\text{cr}}^{\text{inst}}$, (g) $V = 1.05V_{\text{cr}}^{\text{inst}}$, (h) $V = 1.06V_{\text{cr}}^{\text{inst}}$ and (i) $V = 1.20V_{\text{cr}}^{\text{inst}}$. These results are related to the base case presented in Table 4.3, and $V_{\text{cr}}^{\text{inst}} = 942$ m/s. The red dots indicate the crossings (i.e., the critical masses K^*), and N in each separated domain is shown. Points $\Omega \to \pm\infty$ are indicated in (a)-(i), while points $\Omega \to \pm 0$ are only indicated in (a) for visibility reasons.

4.6. PARAMETRIC STUDY

In Section 4.5.1, we found the critical velocity beyond which instability of the moving object may occur. As the critical velocity for instability is the most important outcome of the stability analysis, the effects of the tunnel thickness, the material damping ratios in the tunnel-soil system, the Lamé parameters of the soil and the burial depth of the tunnel on the critical velocity are studied here. In addition, the dependency of the critical mass and stiffness (identified in Section 4.5.2) of the corresponding moving mass and moving oscillator on velocity is considered; this is only done for full-space cases because of the computational demand of the calculations for the half-space.

4.6.1. EFFECT OF THE THICKNESS OF THE TUNNEL

Four different thicknesses of the tunnel are considered, and the corresponding critical velocities for instability are shown in Table 4.4, where the subscript “B" (also shown in Tables 4.5–4.8) indicates the parameters of the base case shown in Table 4.3. Table 4.4 shows that the critical velocity for instability decreases as the tunnel thickness decreases. The reason of this reduction is the reduction of the stiffness of the tunnel. Moreover, we observe that even for the thinnest tunnel with thickness $h = 0.05$ m, the critical velocity for instability is still much higher than the (envisaged) operational velocity of Maglev trains ($V \approx 125$ m/s) and Hyperloop pods ($V \approx 277$ m/s).

Table 4.4: Critical velocities for instability for different thicknesses of the tunnel

Thickness of the tunnel (m)	$h = h_\mathrm{B} = 0.25$	$h = 0.20$	$h = 0.10$	$h = 0.05$
Critical velocity for instability (m/s)	$V_\mathrm{cr}^\mathrm{inst} = 942$	$V_\mathrm{cr}^\mathrm{inst} = 934$	$V_\mathrm{cr}^\mathrm{inst} = 887$	$V_\mathrm{cr}^\mathrm{inst} = 617$

4.6.2. EFFECT OF THE MATERIAL DAMPING RATIOS IN THE TUNNEL-SOIL SYSTEM

We consider four different combinations of the material damping ratios of the soil and tunnel as shown in Table 4.5. It demonstrates that the critical velocity for instability increases as the damping ratio of the tunnel increases and that of soil decreases. Therefore, we can conclude that the material damping of the tunnel stabilises the vibration of the moving object, while the material damping ratio of the soil may have a destabilising effect, which is similar to the finding in Metrikine *et al.* [2005].

Table 4.5: Critical velocities for instability for different material damping ratios of the soil and tunnel

Damping ratios of the soil and tunnel	$\xi_1 = \xi_{1,\mathrm{B}} = 0.05$ $\xi_2 = \xi_{2,\mathrm{B}} = 0.02$	$\xi_1 = \xi_{1,\mathrm{B}}$ $\xi_2 = \xi_{2,\mathrm{B}} \times 2.0$	$\xi_1 = \xi_{1,\mathrm{B}} \times 0.6$ $\xi_2 = \xi_{2,\mathrm{B}}$	$\xi_1 = \xi_{1,\mathrm{B}} \times 0.6$ $\xi_2 = \xi_{2,\mathrm{B}} \times 2.0$
Critical velocity for instability (m/s)	$V_\mathrm{cr}^\mathrm{inst} = 942$	$V_\mathrm{cr}^\mathrm{inst} = 967$	$V_\mathrm{cr}^\mathrm{inst} = 956$	$V_\mathrm{cr}^\mathrm{inst} = 979$

4.6.3. EFFECT OF THE LAMÉ PARAMETERS OF THE SOIL

Three sets of the Lamé parameters of the soil are considered, see Table 4.6. It shows that the critical velocity for instability of the moving object increases as the Lamé parameters of the soil increase. Thus, the stiffness of the soil has a stabilising effect on the vibration of the moving object, which is in line with the literature finding [Metrikine *et al.*, 2005].

Table 4.6: Critical velocities for instability for different Lamé parameters of the soil

Lamé parameters of the soil (N/m^2)	$\lambda_1 = \lambda_{1,\mathrm{B}} = 1.731 \times 10^7$ $\mu_1 = \mu_{1,\mathrm{B}} = 1.154 \times 10^7$	$\lambda_1 = \lambda_{1,\mathrm{B}} \times 2.0$ $\mu_1 = \lambda_{1,\mathrm{B}} \times 2.0$	$\lambda_1 = \lambda_{1,\mathrm{B}} \times 3.0$ $\mu_1 = \lambda_{1,\mathrm{B}} \times 3.0$
Critical velocity for instability (m/s)	$V_\mathrm{cr}^\mathrm{inst} = 942$	$V_\mathrm{cr}^\mathrm{inst} = 1000$	$V_\mathrm{cr}^\mathrm{inst} = 1027$

4.6.4. EFFECT OF THE BURIAL DEPTH OF THE TUNNEL

It is interesting to compare the critical velocity for instability for the full-space and half-space cases. Table 4.7 shows that V_{cr} decreases as the depth of embedded tunnel decreases. This reduction is probably mostly because the Rayleigh wave, which is slower than the body waves in the soil, also starts to play a role, although its influence is not very large.

Table 4.7: Critical velocities for instability for different burial depths of the tunnel

Burial depth of the tunnel H(m)	$H = H_{\mathrm{B}} \to \infty$	$H = 15$
Critical velocity for instability (m/s)	$V_{\mathrm{cr}}^{\mathrm{inst}} = 942$	$V_{\mathrm{cr}}^{\mathrm{inst}} = 891$

4.6.5. DEPENDENCY OF THE CRITICAL MASS AND STIFFNESS ON VELOCITY

In this section, three cases (see Table 4.8) are considered to investigate the dependency of the critical mass and stiffness of the moving mass and moving oscillator, respectively, on the velocity in the range of $V = (1.00 - 1.20)\,V_{\mathrm{cr}}^{\mathrm{inst}}$. We chose three full-space cases to investigate the dependency relationship. As observed in Figs. 4.11 and 4.12, there are many critical masses and stiffnesses for some velocities. For these velocities, we only consider the smallest critical mass M_1^* and the largest critical stiffness $K_{\max}^*$ because we are interested to find the regions where the vibration of the moving oscillator is stable (even though $V > V_{\mathrm{cr}}^{\mathrm{inst}}$). The results are shown in Figs. 4.13 and 4.14. The smallest critical mass and largest critical stiffness correspond to the zero crossing of $\mathrm{Im}(K_{\mathrm{eq}})$ (Fig. 4.9) with largest frequency Ω.

Table 4.8: Three cases considered in the study of the dependency of the critical mass and stiffness on velocity

Cases	Thickness of the tunnel	Lamé parameters of the soil	Damping ratios of the soil and tunnel	Burial depth of the tunnel
Case I ($V_{\mathrm{cr}}^{\mathrm{inst}} =$ 942 m/s)	$h = h_{\mathrm{B}}$	$\lambda_1 = \lambda_{1,\mathrm{B}}$ $\mu_1 = \mu_{1,\mathrm{B}}$	$\xi_1 = \xi_{1,\mathrm{B}}$ $\xi_2 = \xi_{2,\mathrm{B}}$	$H = H_{\mathrm{B}}$
Case II ($V_{\mathrm{cr}}^{\mathrm{inst}} =$ 967 m/s)	$h = h_{\mathrm{B}}$	$\lambda_1 = \lambda_{1,\mathrm{B}}$ $\mu_1 = \mu_{1,\mathrm{B}}$	$\xi_1 = \xi_{1,\mathrm{B}}$ $\xi_2 = \xi_{2,\mathrm{B}} \times 2.0$	$H = H_{\mathrm{B}}$
Case III ($V_{\mathrm{cr}}^{\mathrm{inst}} =$ 1000 m/s)	$h = h_{\mathrm{B}}$	$\lambda_1 = \lambda_{1,\mathrm{B}} \times 2.0$ $\mu_1 = \mu_{1,\mathrm{B}} \times 2.0$	$\xi_1 = \xi_{1,\mathrm{B}}$ $\xi_2 = \xi_{2,\mathrm{B}}$	$H = H_{\mathrm{B}}$

In Figs. 4.13 and 4.14, the interval of $V = (1.00 - 1.20)\,V_{\mathrm{cr}}^{\mathrm{inst}}$ is divided into three sub-intervals: $V = (1.00 - 1.02)\,V_{\mathrm{cr}}^{\mathrm{inst}}$, $V = (1.02 - 1.04)\,V_{\mathrm{cr}}^{\mathrm{inst}}$ and $V = (1.04 - 1.20)\,V_{\mathrm{cr}}^{\mathrm{inst}}$. The reason is that the critical mass and stiffness can decrease and increase dramatically as the velocity increases, and by distinguishing the three sub-intervals, we clearly show the trend in each interval. In Fig. 4.13, we observe that the critical mass in all three cases decreases as the velocity increases, which is in line with Metrikine and Dieterman [1997]. Fig. 4.13 also shows that the critical mass of the moving object (single-mass case) in case III is the largest and the one in case I is the smallest when $V = V_{\mathrm{cr}}^{\mathrm{inst}}$, and that the difference between the three critical masses is very large. However, the critical mass in case III becomes the smallest and the one in case I the largest when $V = 1.20V_{\text{cr}}^{\text{inst}}$, and the difference between the three critical masses becomes much smaller. Fig. 4.14 shows that the critical stiffness of the oscillator in the three cases increases as the velocity increases, which is again in line with the literature finding in Metrikine and Popp [1999]. Another similarity between our result and the literature is that the instability of the moving oscillator occurs when its stiffness is in the order of 10^6 (kg/s^2), which is approximately the same as the value of the stiffness of springs used for conventional trains. However, the critical stiffness increases dramatically up to the order of 10^8 (kg/s^2) for our model while K^* stays in the same magnitude as the velocity increases for the model considered in the literature [Metrikine and Popp, 1999]. Fig. 4.14 also shows that the critical stiffness in case III is the smallest and the one in case I is the largest when $V = V_{\text{cr}}^{\text{inst}}$, and that the difference between the three critical stiffnesses is very small. However, when $V = 1.20V_{\text{cr}}^{\text{inst}}$, the critical stiffness in case III becomes the largest and the one in case I the smallest, and the difference between the three critical stiffnesses becomes much larger. Finally, Figs. 4.13 and 4.14 show that the dependency of the critical mass and stiffness on the velocity is similar in the considered velocity range for the three cases; however, as is clear from the comparison of cases II and III, the Lamé parameters of the soil have a larger effect on the curves compared to the damping ratio of the tunnel.

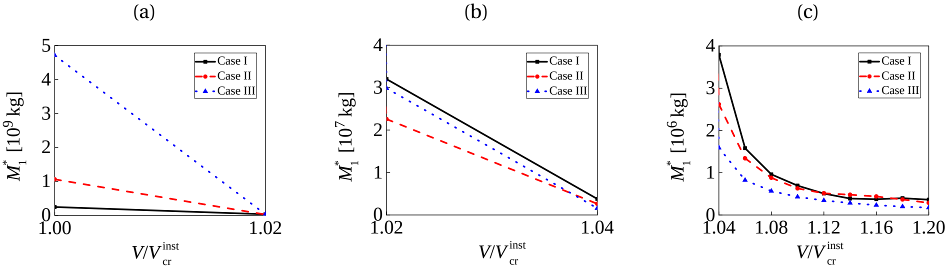

Figure 4.13: Dependency of the critical mass on velocity: (a) $V/V_{\text{cr}}^{\text{inst}} = (1.00-1.02)$, (b) $V/V_{\text{cr}}^{\text{inst}} = (1.02-1.04)$ and (c) $V/V_{\text{cr}}^{\text{inst}} = (1.04-1.20)$. The three cases are defined in Table 4.8, and three small intervals are considered to clearly show the trend in each interval. The region below the line relates to stable vibrations of the single mass.

In Fig. 4.13 (4.14), the region below (above) the line relates to stable vibrations of the object. In the region above (below) the line, the object vibration can be either purely unstable, or alternately either stable or unstable, which is the case when $\text{Im}(K_{\text{eq}})$ has many zero crossings (see Figs. 4.11 and 4.12). In case I, for velocities $V = (1.06-1.20)V_{\text{cr}}^{\text{inst}}$, the vibration of the moving mass in the region above the line shown in Fig. 4.13 is always unstable. It can be verified, however, that for velocities $V = (1.00-1.05)V_{\text{cr}}^{\text{inst}}$, both stable and unstable sub-regions exist above the lines. For example, for $V = V_{\text{cr}}^{\text{inst}}$, the vibration of the moving mass is unstable in sub-regions of $M_1^* < M < M_2^*$ and $M_3^* < M < M_4^*$, but stable in the sub-regions $M_2^* < M < M_3^*$ and $M > M_4^*$. Related to that, the vibration of the moving oscillator can be verified to be unstable for $V = V_{\text{cr}}^{\text{inst}}$ in the sub-regions of $K_1^* < K < K_2^*$ and $K_3^* < K < K_4^*$, but stable in the sub-regions $K_2^* < K < K_3^*$ and $K < K_1^*$. In case II, for velocities $V = 1.00V_{\text{cr}}^{\text{inst}}$ and $V = 1.02V_{\text{cr}}^{\text{inst}}$, the number of

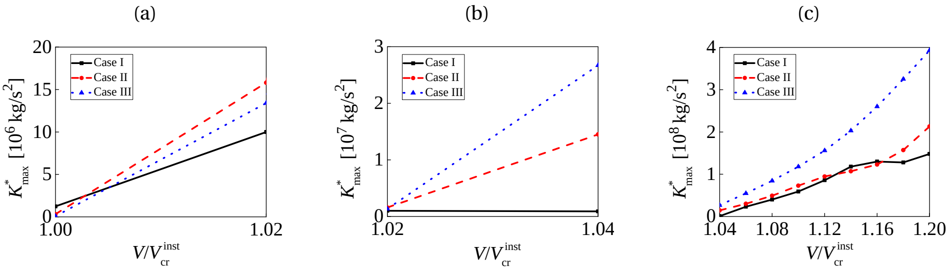

Figure 4.14: Dependency of the critical stiffness on velocity: (a) $V/V^{\text{inst}}_{\text{cr}} = (1.00-1.02)$, (b) $V/V^{\text{inst}}_{\text{cr}} = (1.02-1.04)$ and (c) $V/V^{\text{inst}}_{\text{cr}} = (1.04-1.20)$. The three cases are defined in Table 4.8, and three small intervals are considered to clearly show the trend in each interval. The region above the line relates to stable vibrations of the oscillator.

the critical masses and stiffnesses can be verified to be 2 and 9, respectively; for velocities $V = (1.04-1.20)V^{\text{inst}}_{\text{cr}}$, however, the number is 1. In case III, in the velocity range of $V = (1.00-1.08)V^{\text{inst}}_{\text{cr}}$, the number of the critical masses and stiffnesses varies significantly and jumps from 1 to 11 and then back to 3; for velocities $V = (1.10-1.20)V^{\text{inst}}_{\text{cr}}$, the number is again 1. Clearly, the precise number of sub-regions highly depends on the stiffness of the soil, and on the damping ratios of soil and shell.

4.7. CONCLUSIONS

In this chapter, stability of the vibration of an object moving through a tunnel embedded in soft soil has been studied. We employed the concept of the equivalent dynamic stiffness, which reduces the original 2.5D model to an equivalent discrete model, whose parameters depend on the vibration frequency and the object's velocity. The frequency-domain indirect Boundary Element Method was used to obtain the equivalent stiffness of the tunnel-soil system at the point of contact with the moving object (i.e., the mass-spring system and the limit case of a single mass). Prior to that, the indirect BEM was validated for specific problems: the response of the system to a stationary harmonic point load and to a moving non-oscillatory load acting at the invert of a tunnel. Using the equivalent stiffness, the critical velocity beyond which the instability of the object may occur was found (it is the same for both the moving mass and the moving oscillator). The critical velocity for instability is the most important result of the stability analysis. We found that the critical velocity for instability turns out to be much larger than the operational velocity of high-speed trains and ultra-high-speed Hyperloop pods, which implies that the model adopted in this chapter predicts the vibrations of these objects moving through a tunnel embedded in soft soil to be stable.

For the model of a track founded on top of the elastic half-space, considered for comparison, the critical velocity for instability in the presence of damping is just slightly larger than the critical velocity for resonance of the undamped system (which is equal to the minimum phase velocity of the system). However, for the current model, the critical velocity for instability is much larger than the critical velocity for resonance (of the damped system, strictly speaking, but the influence of the damping on the resonant velocity is small). For both models, the critical velocity for resonance is slightly smaller than the velocity of Rayleigh waves, and the fact that the critical velocity for instability is so much larger in the model with the embedded tunnel is due to the large stiffness of the tunnel and the radiation damping of the waves excited in the tunnel. Other parameters affect the instability as well. A parametric study shows that the thickness of the tunnel, the material damping ratio of the tunnel, the stiffness of the soil and the burial depth have a stabilising effect, while the damping of the soil may have a slightly destabilizing effect.

In order to investigate the stability of the moving object in case the velocity exceeds the identified critical velocity for instability, we employed the D-decomposition method and found the instability domains in the space of system parameters. For a deep tunnel, the dependency of the critical mass and stiffness on the velocity was investigated. We conclude that the higher the velocity, the smaller the mass of the object (single mass case) should be to ensure its stability. Furthermore, the higher the velocity, the larger the stiffness of the spring should be when the spring is added (oscillator case). Our findings regarding the velocity dependency of the critical mass and stiffness are aligned with the conclusions obtained by Metrikine *et al.* [Metrikine and Dieterman, 1997; Metrikine and Popp, 1999] for other models.

The fact that the critical velocity for instability for the current model is much higher than the operational velocity of contemporary and future vehicles is promising for the Maglev and Hyperloop transportation systems. Furthermore, the approach presented in this chapter can be applied to more advanced models with more points of contact between the moving object and the tunnel, which would resemble reality even better. Finally, as the dynamic stiffness is very important for the stability analysis for the tunnel-soil system, a refined model of the tunnel, which can potentially increase the accuracy of the response at its interior, can be considered in future work.

5

CONCLUSIONS AND RECOMMENDATIONS

5.1. CONCLUSIONS

Underground tunnels are important infrastructures due to their diverse applications in civil engineering. The dynamics of underground tunnels subjected to seismic waves or the passage of high-speed moving trains have been important research topics in recent decades. Amplifications of displacements and stress concentrations may take place due to wave scattering and wave interference occurring between the ground surface and surfaces of embedded inclusions. The environmental vibrations induced by moving trains and the vibration stability of moving trains themselves are the main concerns for engineers to assess vibration hindrance of residents and passengers, and to ensure their safety.

The dynamic response of an elastic half-space with an embedded tunnel subject to seismic waves is not a new problem. Numerous researchers have dedicated their work to providing analytical or numerical solutions for this type of problem. The challenges are as follows: (1) The half-space domain is infinite, and it is often computationally expensive and challenging to satisfy the radiation condition when applying numerical methods; (2) The boundary surfaces are of two different types, which is difficult to deal with especially when applying the analytical methods; (3) It can be very difficult to get accurate results due to ill-conditioned matrices.

Regarding the problem of stability of moving trains, the majority of research studies have employed one-dimensional (1D) or two-dimensional (2D) models of the railway track. Only a limited number of existing works analysed the stability using three-dimensional (3D) models of the railway track, but the focus was limited to trains moving on a track situated on the ground surface [Metrikine and Popp, 1999; Metrikine *et al.*, 2005]. The stability of trains moving through an underground tunnel using a 3D model has not been analysed yet.

The method of conformal mapping, which utilises complex-variable theory, seemed to be a promising analytical method to be used throughout the thesis due to its computational efficiency and accuracy [Liu and Wang, 2012; Liu *et al.*, 2013]. As the first objective of this thesis, the method of conformal mapping has been extended to the 3D case, and a systematic evaluation of its accuracy has been conducted (Chapter 2). It has been shown that inaccurate results maybe obtained, particularly at high frequencies. This observation motivated the second objective of this thesis to verify the accuracy of the specific application of the method of conformal mapping (used throughout the thesis) in which the waves scattered from the half-space surface are represented by cylindrical waves that originate from an image source of a priori unknown intensity (Chapter 3). To this end, a simpler 2D model was considered, involving a cylindrical cavity embedded in an elastic half-space subject to a harmonic anti-plane shear wave. The performance of the indirect BEM was evaluated too for this model in view of the choice of the appropriate solution method for the second type of dynamic problem considered in this thesis. For this second type of dynamic problem, due to the identified inaccuracies at high frequencies for the 3D problem, the indirect BEM has been utilised to investigate the stability of vibrations of an oscillator moving at high speeds through a tunnel embedded in soft soil, which is the third objective of this thesis (Chapter 4).

As stated above, in Chapter 2, the semi-analytical solution employing the conformal mapping method for the 3D response of a tunnel embedded in an elastic half-space subject to seismic waves has been presented. Both the tunnel and soil were modelled as an elastic continuum. The original physical domain with boundary surfaces of two different types was mapped onto an image domain with boundary surfaces of the same type employing two conformal mapping functions. The total wave field in the soil consists of incident and reflected plane waves, and directly and secondary scattered cylindrical waves, while the total wave field in the tunnel only consists of refracted cylindrical waves. The unknown coefficients of the potentials related to the cylindrical waves were determined from a system of algebraic equations obtained by projecting the boundary and continuity conditions onto the set of the circumferential basis functions/modes. The main findings of the study in Chapter 2 are as follows:

- Excellent agreement between the results obtained by the proposed method and existing literature results was observed for the validation examples of 2D anti-plane, 2D plane-strain and 3D cases.

- The systematic evaluation of the method shows that the present method performs well for the frequency band of seismic waves, as well as across the complete considered ranges of the stiffness ratio of the tunnel to soil, the embedded depth of the tunnel, the vertical incident angle and the thickness of the tunnel.

- For high dimensionless frequencies, the condition number of the formulated coefficient matrix $\mathbf{K}$ (related to the mentioned algebraic equations) is very high, leading to inaccurate results. The reason for the inaccuracy probably lies in the fact that the secondary scattered waves in the soil are represented by cylindrical waves and not by plane waves, while the latter are most likely more suitable to represent the responses at the flat ground surface at high frequencies (see conclusions related to Chapter 3).

- The proposed method generally works better for the incident P wave case than the incident S wave case. The reason is that the wavenumbers in the arguments of the Hankel functions (representing the cylindrical waves in the soil) are small, implying that the Hankel functions render the columns of matrix **K** linearly dependent for the S wave case, which eventually results in an ill-conditioned system of equations and less accurate responses.
- When Hankel functions are used to represent the cylindrical waves in the tunnel, the hoop stress may become inaccurate for a moderate tunnel-soil stiffness contrast. The reason is that the wavenumbers in the Hankel functions are small in these cases, which is due to refracted shear waves in the tunnel becoming evanescent in the 3D scenario. These inaccuracies can be perfectly overcome by representing the cylindrical waves in the tunnel by Bessel functions.
- When varying the incident-wave frequency, the embedded depth of the tunnel and the incident angle, the results exhibit notable resonances that should be carefully considered and avoided during tunnel design.
- In view of engineering practice, the tunnel is safer when the surrounding soil is stiffer (i.e., a smaller stiffness ratio between tunnel and soil), the tunnel is thicker and the vertical incident angle is larger.

As stated above, in Chapter 3, the response of an elastic half-space with an embedded cylindrical cavity subject to a plane harmonic SH wave has been examined. Three methods have been employed: the method of images, the method of conformal mapping and the indirect BEM. By conducting a comparisons of the three methods for the considered simple model, we have successfully verified the accuracy of the specific application of the method of conformal mapping and of the indirect BEM. In the method of conformal mapping, the secondary scattered waves were represented by cylindrical waves originating from an image source with an unknown intensity, like in Chapter 2. Conversely, in the method of images, the intensity is assumed identical to that of the directly scattered wave. The unknown coefficients associated with the potentials of the cylindrical waves were determined from the boundary conditions. In parametric studies, the results obtained by the method of images were considered as benchmark solutions against which the outcomes of the other two methods were evaluated. The main findings of numerical studies in this chapter are as follows:

- Convergence tests demonstrate that both the method of images and the method of conformal mapping converge with a small number of circumferential modes; the indirect BEM converges with a small number of source and receiver points.
- Perfect agreement between the results obtained by the presented methods and those in the literature was observed.
- The comparison of the three methods shows that the method of images and the method of conformal mapping exhibit similar convergence behavior, necessitating almost the same number of circumferential modes. However, the method of images is proven to be more efficient than the method of conformal mapping in

terms of computational time. On the other hand, the indirect BEM needs significantly longer computational time, making it the least efficient method among the three.

- The systematic evaluation of the methods shows that both the method of conformal mapping and the indirect BEM perform accurately across the entire ranges of the dimensionless frequency, the embedded depth of the cavity and the vertical incident angle. This is in contrast to the 3D case (see Chapter 2), where converged results could not be obtained at high frequencies for the method of conformal mapping. The findings suggest that representing the waves scattered from the free surface by cylindrical waves (originating from an image source of a priori unknown intensity) in the method of conformal mapping is indeed the cause of the inaccuracies at high frequency in the 3D problem (Chapter 2). As no inaccuracies are observed for the current 2D anti-plane shear problem, the inaccuracy for the 3D problem is likely due to the use of cylindrical waves (instead of plane waves) that are apparently not fully able to capture all wave conversions taking place at the free surface.

- Further parametric studies reveal the substantial influence of the dimensionless frequency, the embedded depth of the cavity and the vertical incident angle on the responses at both the ground surface and the cavity surface. It has been shown that the system response curves display nearly equally spaced resonances, which is in line with the resonances observed for the well-known 1D shear layer subject to bedrock motion [Kramer, 1996]. The system response curves for the 3D case do not display equally spaced resonances.

- All three methods presented in this study can be effectively utilised in the preliminary design of a cavity embedded in a half-space to evaluate stress distributions at the cavity and the level of ground vibrations.

As stated above, in Chapter 4, the stability of vibrations of an object moving through a tunnel embedded in soft soil has been investigated. The soil was modeled as an elastic continuum, while the tunnel was modelled by the Flügge shell. The moving object was modeled as the mass-spring system and the limit case of a single mass. The concept of the equivalent dynamic stiffness was employed to reduce the original 2.5D model to an equivalent discrete model, whose parameters depend on the vibration frequency and the velocity of the object. The indirect BEM was validated for two illustrative examples and was used to obtain the equivalent stiffness of the tunnel-soil system at the point of contact with the moving object. The critical velocity for instability is the most important result of the stability analysis. By employing the equivalent stiffness, this critical velocity beyond which the instability of the object may occur was found. The D-decomposition method was employed to identify the instability domains in the space of system parameters when the velocity of the moving object exceeds the identified critical velocity for instability. The main findings of numerical studies in this chapter are as follows:

- The critical velocity for instability is the same for both the moving mass and the moving oscillator, and it turns out to be much larger than the operational velocity of high-speed trains and ultra-high-speed Hyperloop pods. This observation implies that the model adopted in this chapter predicts the vibrations experienced by these objects, while moving through a tunnel embedded in soft soil, to be stable.

- The critical velocity for instability was found to be much larger than the critical velocity for resonance, contrary to the literature finding for the model of a railway track founded on top of the elastic half-space. For both models (i.e., tunnel embedded in the half-space, and track on top of the half-space), the critical velocity for resonance is slightly smaller than the velocity of Rayleigh waves, and the fact that the critical velocity for instability is so much larger in the current model is due to the large stiffness of the tunnel and the radiation damping of the waves excited in the tunnel.

- A parametric study demonstrates that the thickness of the tunnel, the material damping ratio of the tunnel, the stiffness of the soil and the burial depth have a stabilising effect, while the damping of the soil may have a slightly destabilizing effect.

- For a deep tunnel, the results reveal that as the velocity increases, the mass of the object (single mass case) needs to be smaller to maintain stability. Similarly, the stiffness of the added spring (oscillator case) should be larger as the velocity increases.

5.2. RECOMMENDATIONS

Regarding the application of the method of conformal mapping to solve the first type of dynamic problem (i.e., dynamic response of an underground tunnel subject to seismic waves) considered in this thesis, the following recommendations are given for future work:

- The method of conformal mapping should also be applied to solve 3D wave scattering problems for inclusions embedded in poroelastic medium, layered soil and a functionally graded half-space.

- It is also recommended to study inclusions of other shapes (e.g., oval, rectangular or arbitrary) in these media, as the method of conformal mapping is not limited to cylindrical inclusions.

- To overcome the accuracy problems that originate from waves in the tunnel transitioning from propagating to evanescent, shell modelling of the tunnel can be helpful. As an alternative, the tunnel can still be considered as a continuum when it is modeled by FEM (Finite Element Modeling). This way, a structure inside the tunnel can also be easily incorporated.

- A challenge that should be taken by future research is to improve the representation of the wave field scattered from the free surface in order to obtain accurate results at high frequencies.

Regarding the second type of dynamic problem considered in this thesis (i.e., vibration stability of high-speed trains moving through a tunnel embedded in soft soil), the following recommendations are given for future work:

- The approach presented in this chapter can be extended to more advanced models with more points of contact between the moving object and the tunnel (i.e., more advanced models of the moving trains), which would resemble reality even better.
- Another important aspect is to include a detailed track structure placed between the moving trains and the tunnel. This track could be modeled using FEM.
- Moreover, as the dynamic stiffness is very important for the stability analysis for the tunnel-soil system, a refined model of the tunnel, which can potentially increase the accuracy of the response at its interior, should be considered in future work.
- Finally, it is key to include the effect of electromagnetic suspension/levitation on the vibration stability, which is very relevant for the overall stability behaviour of Maglev and Hyperloop vehicles and the associated vibration-control strategies.

A

AMPLITUDE RATIOS OF POTENTIALS OF REFLECTED TO INCIDENT PLANE WAVES

Amplitude ratios of potentials of reflected waves to incident plane waves in a homogeneous half-space without embedded structures can be determined based on the stress-free boundary conditions at the half-space surface. The result is presented in this appendix, which is related to Chapter 2.

Case 1: Incident compressional wave ($\phi_{\mathrm{inc}}^{(1)}$). The amplitude ratios ($R_{\phi,\phi}$, $R_{\psi,\phi}$ and $R_{\chi,\phi}$) of the reflected waves ($\phi_{\mathrm{ref}}^{(1)}$, $\psi_{\mathrm{ref}}^{(1)}$ and $\chi_{\mathrm{ref}}^{(1)}$) to incident wave ($\phi_{\mathrm{inc}}^{(1)}$) are given as follows:

$$\begin{aligned}
R_{\phi,\phi} &= \frac{4k_{z,\mathrm{P}}k_{z,\mathrm{S}}k^2 - \left(2k^2 - k_{\mathrm{S}}^2\right)^2}{4k_{z,\mathrm{P}}k_{z,\mathrm{S}}k^2 + \left(2k^2 - k_{\mathrm{S}}^2\right)^2}, \quad R_{\psi,\phi} = \frac{4k_{z,\mathrm{P}}k_y\left(2k^2 - k_{\mathrm{S}}^2\right)\left(k_{\mathrm{S}}/k_{\mathrm{b}}\right)^2}{4k_{z,\mathrm{P}}k_{z,\mathrm{S}}k^2 + \left(2k^2 - k_{\mathrm{S}}^2\right)^2}, \\
R_{\chi,\phi} &= \frac{4\,\mathrm{i}\,k_{z,\mathrm{P}}k_{z,\mathrm{S}}k_x k_{\mathrm{S}}\left(2k^2 - k_{\mathrm{S}}^2\right)/k_{\mathrm{b}}^2}{4k_{z,\mathrm{P}}k_{z,\mathrm{S}}k^2 + \left(2k^2 - k_{\mathrm{S}}^2\right)^2},
\end{aligned} \tag{A.1}$$

where the first and second subscripts indicate the potentials of the reflected and incident waves, respectively. It is understood that all the wavenumbers shown in this section are associated with the soil medium and should have the superscript “(1)". However, this superscript is omitted for brevity. For example, $k = k^{(1)}$, as defined in Eq. (2.16).

Note that when the axial wavenumber k_x equals to zero, a 2D problem is recovered. Consequently, we have $k = k_y$, $k_{\mathrm{S}} = k_{\mathrm{b}}$, and the amplitude ratios shown in Eq. (A.1) are reduced to the following expressions:

$$R_{\phi,\phi} = \frac{4k_{z,\mathrm{P}}k_{z,\mathrm{S}}k^2 - \left(2k^2 - k_\mathrm{S}^2\right)^2}{4k_{z,\mathrm{P}}k_{z,\mathrm{S}}k^2 + \left(2k^2 - k_\mathrm{S}^2\right)^2},\ R_{\psi,\phi} = \frac{4k_{z,\mathrm{P}}k_y\left(2k^2 - k_\mathrm{S}^2\right)}{4k_{z,\mathrm{P}}k_{z,\mathrm{S}}k^2 + \left(2k^2 - k_\mathrm{S}^2\right)^2},\ R_{\chi,\phi} = 0. \tag{A.2}$$

Case 2: Incident shear wave ($\psi^{(1)}_{\mathrm{inc}}$). The amplitude ratios ($R_{\phi,\psi}$, $R_{\psi,\psi}$ and $R_{\chi,\psi}$) of the reflected waves ($\phi^{(1)}_{\mathrm{ref}}$, $\psi^{(1)}_{\mathrm{ref}}$ and $\chi^{(1)}_{\mathrm{ref}}$) to incident wave ($\psi^{(1)}_{\mathrm{inc}}$) are given as follows:

$$\begin{aligned}
R_{\phi,\psi} &= \frac{-4k_{z,\mathrm{S}}k_y\left(2k^2 - k_\mathrm{S}^2\right)}{4k_{z,\mathrm{P}}k_{z,\mathrm{S}}k^2 + \left(2k^2 - k_\mathrm{S}^2\right)^2},\\
R_{\psi,\psi} &= \frac{8k_{z,\mathrm{P}}k_{z,\mathrm{S}}k_y^2k_\mathrm{S}^2/k_\mathrm{b}^2 - \left[4k_{z,\mathrm{P}}k_{z,\mathrm{S}}k^2 + \left(2k^2 - k_\mathrm{S}^2\right)^2\right]}{4k_{z,\mathrm{P}}k_{z,\mathrm{S}}k^2 + \left(2k^2 - k_\mathrm{S}^2\right)^2},\\
R_{\chi,\psi} &= \frac{8\,\mathrm{i}\,k_{z,\mathrm{P}}k_{z,\mathrm{S}}^2k_\mathrm{S}k_yk_x/k_\mathrm{b}^2}{4k_{z,\mathrm{P}}k_{z,\mathrm{S}}k^2 + \left(2k^2 - k_\mathrm{S}^2\right)^2}.
\end{aligned} \tag{A.3}$$

For $k_x = 0$, we obtain the amplitude ratios for the 2D problem (P-SV or plane-strain problem):

$$R_{\phi,\psi} = \frac{-4k_{z,\mathrm{S}}k_y\left(2k^2 - k_\mathrm{S}^2\right)}{4k_{z,\mathrm{P}}k_{z,\mathrm{S}}k^2 + \left(2k^2 - k_\mathrm{S}^2\right)^2},\ R_{\psi,\psi} = \frac{4k_{z,\mathrm{P}}k_{z,\mathrm{S}}k^2 - \left(2k^2 - k_\mathrm{S}^2\right)^2}{4k_{z,\mathrm{P}}k_{z,\mathrm{S}}k^2 + \left(2k^2 - k_\mathrm{S}^2\right)^2},\ R_{\chi,\psi} = 0. \tag{A.4}$$

Case 3: Incident shear wave ($\chi^{(1)}_{\mathrm{inc}}$). The amplitude ratios ($R_{\phi,\chi}$, $R_{\psi,\chi}$ and $R_{\chi,\chi}$) of the reflected waves ($\phi^{(1)}_{\mathrm{ref}}$, $\psi^{(1)}_{\mathrm{ref}}$ and $\chi^{(1)}_{\mathrm{ref}}$) to incident wave ($\chi^{(1)}_{\mathrm{inc}}$) are given as follows:

$$\begin{aligned}
R_{\phi,\chi} &= \frac{4\,\mathrm{i}\,k_x\left(2k^4 - 3k^2k_\mathrm{S}^2 + k_\mathrm{S}^4\right)/k_\mathrm{S}}{4k_{z,\mathrm{P}}k_{z,\mathrm{S}}k^2 + \left(2k^2 - k_\mathrm{S}^2\right)^2},\ R_{\psi,\chi} = \frac{8\,\mathrm{i}\,k_{z,\mathrm{P}}k_{z,\mathrm{S}}^2k_\mathrm{S}k_yk_x/k_\mathrm{b}^2}{4k_{z,\mathrm{P}}k_{z,\mathrm{S}}k^2 + \left(2k^2 - k_\mathrm{S}^2\right)^2},\\
R_{\chi,\chi} &= \frac{8k_{z,\mathrm{P}}k_{z,\mathrm{S}}k_y^2k_\mathrm{S}^2/k_\mathrm{b}^2 - \left[4k_{z,\mathrm{P}}k_{z,\mathrm{S}}k^2 - \left(2k^2 - k_\mathrm{S}^2\right)^2\right]}{4k_{z,\mathrm{P}}k_{z,\mathrm{S}}k^2 + \left(2k^2 - k_\mathrm{S}^2\right)^2}.
\end{aligned} \tag{A.5}$$

For $k_x = 0$, we obtain the amplitude ratios for the 2D problem (SH or anti-plane shear problem):

$$R_{\phi,\chi} = 0,\ R_{\psi,\chi} = 0,\ R_{\chi,\chi} = 1. \tag{A.6}$$

B

EXPRESSIONS FOR DISPLACEMENTS AND STRESSES IN TERMS OF COMPLEX VARIABLES

The components of the displacements and stresses in Cartesian coordinates (y, z, x) expressed in terms of the complex variables κ and $\bar{\kappa}$, to be used in Chapter 2, are as follows, where the superscript $(i = \{1,2\})$ is omitted for brevity (throughout this appendix):

$$u_y = \left(\frac{\partial \phi}{\partial \kappa} + \frac{\partial \phi}{\partial \bar{\kappa}}\right) + \mathrm{i}\left(\frac{\partial \psi}{\partial \kappa} - \frac{\partial \psi}{\partial \bar{\kappa}}\right) - \frac{\mathrm{i}\,k_x}{k_\mathrm{S}}\left(\frac{\partial \chi}{\partial \kappa} + \frac{\partial \chi}{\partial \bar{\kappa}}\right), \tag{B.1}$$

$$u_z = \mathrm{i}\left(\frac{\partial \phi}{\partial \kappa} - \frac{\partial \phi}{\partial \bar{\kappa}}\right) - \left(\frac{\partial \psi}{\partial \kappa} + \frac{\partial \psi}{\partial \bar{\kappa}}\right) + \frac{k_x}{k_\mathrm{S}}\left(\frac{\partial \chi}{\partial \kappa} - \frac{\partial \chi}{\partial \bar{\kappa}}\right), \tag{B.2}$$

$$u_x = -\mathrm{i}\,k_x \phi + \frac{k_\mathrm{b}^2}{k_\mathrm{S}}\chi, \tag{B.3}$$

and

$$\begin{aligned}\sigma_{yy} = &-\lambda k_x^2 \phi - (\lambda + \mu)\, k_\mathrm{a}^2 \phi + 2\mu\left(\frac{\partial^2 \phi}{\partial \kappa^2} + \frac{\partial^2 \phi}{\partial \bar{\kappa}^2}\right) + 2\mathrm{i}\,\mu\left(\frac{\partial^2 \psi}{\partial \kappa^2} - \frac{\partial^2 \psi}{\partial \bar{\kappa}^2}\right) + \frac{\mathrm{i}\,\mu k_x k_\mathrm{b}^2}{k_\mathrm{S}}\chi \\ &- \frac{2\mathrm{i}\,\mu k_x}{k_\mathrm{S}}\left(\frac{\partial^2 \chi}{\partial \kappa^2} + \frac{\partial^2 \chi}{\partial \bar{\kappa}^2}\right),\end{aligned} \tag{B.4}$$

$$\begin{aligned}\sigma_{zz} = &-\lambda k_x^2 \phi - (\lambda + \mu)\, k_\mathrm{a}^2 \phi - 2\mu\left(\frac{\partial^2 \phi}{\partial \kappa^2} + \frac{\partial^2 \phi}{\partial \bar{\kappa}^2}\right) - 2\mathrm{i}\,\mu\left(\frac{\partial^2 \psi}{\partial \kappa^2} - \frac{\partial^2 \psi}{\partial \bar{\kappa}^2}\right) + \frac{\mathrm{i}\,\mu k_x k_\mathrm{b}^2}{k_\mathrm{S}}\chi \\ &+ \frac{2\mathrm{i}\,\mu k_x}{k_\mathrm{S}}\left(\frac{\partial^2 \chi}{\partial \kappa^2} + \frac{\partial^2 \chi}{\partial \bar{\kappa}^2}\right),\end{aligned} \tag{B.5}$$

$$\sigma_{xx} = -\left(\lambda + 2\mu\right) k_x^2 \phi - \lambda k_{\mathrm{a}}^2 \phi - \frac{2\mathrm{i}\mu k_x k_{\mathrm{b}}^2}{k_{\mathrm{S}}} \chi, \tag{B.6}$$

$$\sigma_{yz} = 2\mathrm{i}\mu \left(\frac{\partial^2 \phi}{\partial \kappa^2} - \frac{\partial^2 \phi}{\partial \bar{\kappa}^2} \right) - 2\mu \left(\frac{\partial^2 \psi}{\partial \kappa^2} + \frac{\partial^2 \psi}{\partial \bar{\kappa}^2} \right) + \frac{2\mu k_x}{k_{\mathrm{S}}} \left(\frac{\partial^2 \chi}{\partial \kappa^2} - \frac{\partial^2 \chi}{\partial \bar{\kappa}^2} \right), \tag{B.7}$$

$$\sigma_{yx} = -2\mathrm{i}\mu k_x \left(\frac{\partial \phi}{\partial \kappa} + \frac{\partial \phi}{\partial \bar{\kappa}} \right) + \mu k_x \left(\frac{\partial \psi}{\partial \kappa} - \frac{\partial \psi}{\partial \bar{\kappa}} \right) + \frac{\mu \left(k_{\mathrm{S}}^2 - 2k_x^2 \right)}{k_{\mathrm{S}}} \left(\frac{\partial \chi}{\partial \kappa} + \frac{\partial \chi}{\partial \bar{\kappa}} \right), \tag{B.8}$$

$$\sigma_{zx} = 2\mu k_x \left(\frac{\partial \phi}{\partial \kappa} - \frac{\partial \phi}{\partial \bar{\kappa}} \right) + \mathrm{i}\mu k_x \left(\frac{\partial \psi}{\partial \kappa} + \frac{\partial \psi}{\partial \bar{\kappa}} \right) + \frac{\mathrm{i}\mu \left(k_{\mathrm{S}}^2 - 2k_x^2 \right)}{k_{\mathrm{S}}} \left(\frac{\partial \chi}{\partial \kappa} - \frac{\partial \chi}{\partial \bar{\kappa}} \right). \tag{B.9}$$

Employing the transformation relations shown in Eqs. (2.11) and (2.12), the expressions for displacements and stresses in the cylindrical coordinate system (r, θ, x) are derived in terms of the complex variables κ and $\bar{\kappa}$:

$$u_r = \left(\mathrm{e}^{\mathrm{i}\theta} \frac{\partial \phi}{\partial \kappa} + \mathrm{e}^{-\mathrm{i}\theta} \frac{\partial \phi}{\partial \bar{\kappa}} \right) + \mathrm{i} \left(\mathrm{e}^{\mathrm{i}\theta} \frac{\partial \psi}{\partial \kappa} - \mathrm{e}^{-\mathrm{i}\theta} \frac{\partial \psi}{\partial \bar{\kappa}} \right) - \frac{\mathrm{i} k_x}{k_{\mathrm{S}}} \left(\mathrm{e}^{\mathrm{i}\theta} \frac{\partial \chi}{\partial \kappa} + \mathrm{e}^{-\mathrm{i}\theta} \frac{\partial \chi}{\partial \bar{\kappa}} \right), \tag{B.10}$$

$$u_\theta = \mathrm{i} \left(\mathrm{e}^{\mathrm{i}\theta} \frac{\partial \phi}{\partial \kappa} - \mathrm{e}^{-\mathrm{i}\theta} \frac{\partial \phi}{\partial \bar{\kappa}} \right) - \left(\mathrm{e}^{\mathrm{i}\theta} \frac{\partial \psi}{\partial \kappa} + \mathrm{e}^{-\mathrm{i}\theta} \frac{\partial \psi}{\partial \bar{\kappa}} \right) + \frac{k_x}{k_{\mathrm{S}}} \left(\mathrm{e}^{\mathrm{i}\theta} \frac{\partial \chi}{\partial \kappa} - \mathrm{e}^{-\mathrm{i}\theta} \frac{\partial \chi}{\partial \bar{\kappa}} \right), \tag{B.11}$$

and

$$\begin{aligned} \sigma_{rr} = & -\lambda k_x^2 \phi - \left(\lambda + \mu\right) k_{\mathrm{a}}^2 \phi + 2\mu \left(\mathrm{e}^{2\mathrm{i}\theta} \frac{\partial^2 \phi}{\partial \kappa^2} + \mathrm{e}^{-2\mathrm{i}\theta} \frac{\partial^2 \phi}{\partial \bar{\kappa}^2} \right) \\ & + 2\mathrm{i}\mu \left(\mathrm{e}^{2\mathrm{i}\theta} \frac{\partial^2 \psi}{\partial \kappa^2} - \mathrm{e}^{-2\mathrm{i}\theta} \frac{\partial^2 \psi}{\partial \bar{\kappa}^2} \right) + \frac{\mathrm{i}\mu k_x k_{\mathrm{b}}^2}{k_{\mathrm{S}}} \chi - \frac{2\mathrm{i}\mu k_x}{k_{\mathrm{S}}} \left(\mathrm{e}^{2\mathrm{i}\theta} \frac{\partial^2 \chi}{\partial \kappa^2} + \mathrm{e}^{-2\mathrm{i}\theta} \frac{\partial^2 \chi}{\partial \bar{\kappa}^2} \right), \end{aligned} \tag{B.12}$$

$$\begin{aligned} \sigma_{\theta\theta} = & -\lambda k_x^2 \phi - \left(\lambda + \mu\right) k_{\mathrm{a}}^2 \phi - 2\mu \left(\mathrm{e}^{2\mathrm{i}\theta} \frac{\partial^2 \phi}{\partial \kappa^2} + \mathrm{e}^{-2\mathrm{i}\theta} \frac{\partial^2 \phi}{\partial \bar{\kappa}^2} \right) \\ & - 2\mathrm{i}\mu \left(\mathrm{e}^{2\mathrm{i}\theta} \frac{\partial^2 \psi}{\partial \kappa^2} - \mathrm{e}^{-2\mathrm{i}\theta} \frac{\partial^2 \psi}{\partial \bar{\kappa}^2} \right) + \frac{\mathrm{i}\mu k_x k_{\mathrm{b}}^2}{k_{\mathrm{S}}} \chi + \frac{2\mathrm{i}\mu k_x}{k_{\mathrm{S}}} \left(\mathrm{e}^{2\mathrm{i}\theta} \frac{\partial^2 \chi}{\partial \kappa^2} + \mathrm{e}^{-2\mathrm{i}\theta} \frac{\partial^2 \chi}{\partial \bar{\kappa}^2} \right), \end{aligned} \tag{B.13}$$

$$\begin{aligned} \sigma_{r\theta} = & 2\mathrm{i}\mu \left(\mathrm{e}^{2\mathrm{i}\theta} \frac{\partial^2 \phi}{\partial \kappa^2} - \mathrm{e}^{-2\mathrm{i}\theta} \frac{\partial^2 \phi}{\partial \bar{\kappa}^2} \right) - 2\mu \left(\mathrm{e}^{2\mathrm{i}\theta} \frac{\partial^2 \psi}{\partial \kappa^2} + \mathrm{e}^{-2\mathrm{i}\theta} \frac{\partial^2 \psi}{\partial \bar{\kappa}^2} \right) \\ & + \frac{2\mu k_x}{k_{\mathrm{S}}} \left(\mathrm{e}^{2\mathrm{i}\theta} \frac{\partial^2 \chi}{\partial \kappa^2} - \mathrm{e}^{-2\mathrm{i}\theta} \frac{\partial^2 \chi}{\partial \bar{\kappa}^2} \right), \end{aligned} \tag{B.14}$$

$$\begin{aligned}\sigma_{rx} =& -2\,\mathrm{i}\,\mu k_x \left(\mathrm{e}^{\mathrm{i}\theta}\frac{\partial\phi}{\partial\kappa} + \mathrm{e}^{-\mathrm{i}\theta}\frac{\partial\phi}{\partial\bar{\kappa}}\right) + \mu k_x \left(\mathrm{e}^{\mathrm{i}\theta}\frac{\partial\psi}{\partial\kappa} - \mathrm{e}^{-\mathrm{i}\theta}\frac{\partial\psi}{\partial\bar{\kappa}}\right)\\ &+ \frac{\mu\left(k_\mathrm{S}^2 - 2k_x^2\right)}{k_\mathrm{S}}\left(\mathrm{e}^{\mathrm{i}\theta}\frac{\partial\chi}{\partial\kappa} + \mathrm{e}^{-\mathrm{i}\theta}\frac{\partial\chi}{\partial\bar{\kappa}}\right),\end{aligned} \tag{B.15}$$

$$\begin{aligned}\sigma_{\theta x} =& 2\mu k_x \left(\mathrm{e}^{\mathrm{i}\theta}\frac{\partial\phi}{\partial\kappa} - \mathrm{e}^{-\mathrm{i}\theta}\frac{\partial\phi}{\partial\bar{\kappa}}\right) + \mathrm{i}\,\mu k_x \left(\mathrm{e}^{\mathrm{i}\theta}\frac{\partial\psi}{\partial\kappa} + \mathrm{e}^{-\mathrm{i}\theta}\frac{\partial\psi}{\partial\bar{\kappa}}\right)\\ &+ \frac{\mathrm{i}\,\mu\left(k_\mathrm{S}^2 - 2k_x^2\right)}{k_\mathrm{S}}\left(\mathrm{e}^{\mathrm{i}\theta}\frac{\partial\chi}{\partial\kappa} - \mathrm{e}^{-\mathrm{i}\theta}\frac{\partial\chi}{\partial\bar{\kappa}}\right).\end{aligned} \tag{B.16}$$

C

DERIVATIVES OF POTENTIALS RELATED TO PLANE AND CYLINDRICAL WAVES

Based on the definition of the complex variable $\kappa = y + \mathrm{i}z$ and its conjugate $\bar{\kappa} = y - \mathrm{i}z$ provided in Chapters 2 and 3, we can calculate the derivative of a function f (which represents a potential associated with plane waves) with respect to the complex variables by utilising the chain rule :

$$\frac{\partial f}{\partial \kappa} = \frac{\partial y}{\partial \kappa}\frac{\partial f}{\partial y} + \frac{\partial z}{\partial \kappa}\frac{\partial f}{\partial z}, \; \frac{\partial f}{\partial \bar{\kappa}} = \frac{\partial y}{\partial \bar{\kappa}}\frac{\partial f}{\partial y} + \frac{\partial z}{\partial \bar{\kappa}}\frac{\partial f}{\partial z}. \tag{C.1}$$

The recurrence relation of a Hankel function, such as $H_n^{(2)}(x)$ with the argument x, is expressed as follows:

$$\frac{2n}{x} H_n^{(2)}(x) = H_{n-1}^{(2)}(x) + H_{n+1}^{(2)}(x). \tag{C.2}$$

The calculation of the derivative of Hankel functions, which are present in the potentials associated with cylindrical waves, with respect to the complex variables (κ and $\bar{\kappa}$) can be obtained through the application of the chain rule (see Eq. (C.1)) and the recurrence relation of Hankel functions (see Eq. (C.2)):

$$\begin{aligned}
&\frac{\partial}{\partial \bar{\kappa}} \left[H_n^{(2)}\left(k_\mathrm{S}\left|\kappa + \mathrm{i}h\right|\right) \left(\frac{\kappa + \mathrm{i}h}{\left|\kappa + \mathrm{i}h\right|}\right)^n \right] \\
&= \frac{-k_\mathrm{S}}{2} H_{n+1}^{(2)}\left(k_\mathrm{S}\left|\kappa + \mathrm{i}h\right|\right) \left(\frac{\kappa + \mathrm{i}h}{\left|\kappa + \mathrm{i}h\right|}\right)^n \frac{\left(\kappa + \mathrm{i}h\right)^2}{\left|\kappa + \mathrm{i}h\right| \left(\kappa + \mathrm{i}h\right)} \\
&= \frac{-k_\mathrm{S}}{2} H_{n+1}^{(2)}\left(k_\mathrm{S}\left|\kappa + \mathrm{i}h\right|\right) \left(\frac{\kappa + \mathrm{i}h}{\left|\kappa + \mathrm{i}h\right|}\right)^{n+1},
\end{aligned} \tag{C.3}$$

$$
\begin{aligned}
&\frac{\partial}{\partial\kappa}\left[H_n^{(2)}\left(k_\mathrm{S}\left|\kappa+\mathrm{i}h\right|\right)\left(\frac{\kappa+\mathrm{i}h}{\left|\kappa+\mathrm{i}h\right|}\right)^n\right]\\
&=\frac{-1}{2}\frac{1}{\left|\kappa+\mathrm{i}h\right|\left(\kappa+\mathrm{i}h\right)}\left(\frac{\kappa+\mathrm{i}h}{\left|\kappa+\mathrm{i}h\right|}\right)^n\times\\
&\quad\left[H_{n+1}^{(2)}\left(k_\mathrm{S}\left|\kappa+\mathrm{i}h\right|\right)k_\mathrm{S}\left(y^2+z^2+h^2+2hz\right)-2H_n^{(2)}\left(k_\mathrm{S}\left|\kappa+\mathrm{i}h\right|\right)n\left|\kappa+\mathrm{i}h\right|\right]\\
&=\frac{-1}{2}\frac{\left(\kappa+\mathrm{i}h\right)^{n-1}}{\left|\kappa+\mathrm{i}h\right|^{n+1}}\left[H_{n+1}^{(2)}\left(k_\mathrm{S}\left|\kappa+\mathrm{i}h\right|\right)k_\mathrm{S}\left|\kappa+\mathrm{i}h\right|^2-2H_n^{(2)}\left(k_\mathrm{S}\left|\kappa+\mathrm{i}h\right|\right)n\left|\kappa+\mathrm{i}h\right|\right]\\
&=\frac{-1}{2}\left(\frac{\kappa+\mathrm{i}h}{\left|\kappa+\mathrm{i}h\right|}\right)^{n-1}\left[H_{n+1}^{(2)}\left(k_\mathrm{S}\left|\kappa+\mathrm{i}h\right|\right)k_\mathrm{S}-\frac{2n}{\left|\kappa+\mathrm{i}h\right|}H_n^{(2)}\left(k_\mathrm{S}\left|\kappa+\mathrm{i}h\right|\right)\right]\\
&=\frac{-1}{2}\left(\frac{\kappa+\mathrm{i}h}{\left|\kappa+\mathrm{i}h\right|}\right)^{n-1}\times\\
&\quad\left[H_{n+1}^{(2)}\left(k_\mathrm{S}\left|\kappa+\mathrm{i}h\right|\right)k_\mathrm{S}-k_\mathrm{S}\left[H_{n-1}^{(2)}\left(k_\mathrm{S}\left|\kappa+\mathrm{i}h\right|\right)+H_{n+1}^{(2)}\left(k_\mathrm{S}\left|\kappa+\mathrm{i}h\right|\right)\right]\right]\\
&=\frac{k_\mathrm{S}}{2}H_{n-1}^{(2)}\left(k_\mathrm{S}\left|\kappa+\mathrm{i}h\right|\right)\left(\frac{\kappa+\mathrm{i}h}{\left|\kappa+\mathrm{i}h\right|}\right)^{n-1},
\end{aligned}
\tag{C.4}
$$

$$
\begin{aligned}
&\frac{\partial}{\partial\bar\kappa}\left[H_n^{(2)}\left(k_\mathrm{S}\left|\bar\kappa+\mathrm{i}h\right|\right)\left(\frac{\bar\kappa+\mathrm{i}h}{\left|\bar\kappa+\mathrm{i}h\right|}\right)^n\right]\\
&=\frac{-1}{2}\frac{1}{\left|\bar\kappa+\mathrm{i}h\right|\left(\bar\kappa+\mathrm{i}h\right)}\left(\frac{\bar\kappa+\mathrm{i}h}{\left|\bar\kappa+\mathrm{i}h\right|}\right)^n\times\\
&\quad\left[H_{n+1}^{(2)}\left(k_\mathrm{S}\left|\bar\kappa+\mathrm{i}h\right|\right)k_\mathrm{S}\left(y^2+z^2+h^2-2hz\right)-2H_n^{(2)}\left(k_\mathrm{S}\left|\bar\kappa+\mathrm{i}h\right|\right)n\left|\bar\kappa+\mathrm{i}h\right|\right]\\
&=\frac{-1}{2}\frac{\left(\bar\kappa+\mathrm{i}h\right)^{n-1}}{\left|\bar\kappa+\mathrm{i}h\right|^{n+1}}\left[H_{n+1}^{(2)}\left(k_\mathrm{S}\left|\bar\kappa+\mathrm{i}h\right|\right)k_\mathrm{S}\left|\bar\kappa+\mathrm{i}h\right|^2-2H_n^{(2)}\left(k_\mathrm{S}\left|\bar\kappa+\mathrm{i}h\right|\right)n\left|\bar\kappa+\mathrm{i}h\right|\right]\\
&=\frac{-1}{2}\left(\frac{\bar\kappa+\mathrm{i}h}{\left|\bar\kappa+\mathrm{i}h\right|}\right)^{n-1}\left[H_{n+1}^{(2)}\left(k_\mathrm{S}\left|\bar\kappa+\mathrm{i}h\right|\right)k_\mathrm{S}-\frac{2n}{\left|\bar\kappa+\mathrm{i}h\right|}H_n^{(2)}\left(k_\mathrm{S}\left|\bar\kappa+\mathrm{i}h\right|\right)\right]\\
&=\frac{-1}{2}\left(\frac{\bar\kappa+\mathrm{i}h}{\left|\bar\kappa+\mathrm{i}h\right|}\right)^{n-1}\times\\
&\quad\left[H_{n+1}^{(2)}\left(k_\mathrm{S}\left|\bar\kappa+\mathrm{i}h\right|\right)k_\mathrm{S}-k_\mathrm{S}\left[H_{n-1}^{(2)}\left(k_\mathrm{S}\left|\bar\kappa+\mathrm{i}h\right|\right)+H_{n+1}^{(2)}\left(k_\mathrm{S}\left|\bar\kappa+\mathrm{i}h\right|\right)\right]\right]\\
&=\frac{k_\mathrm{S}}{2}H_{n-1}^{(2)}\left(k_\mathrm{S}\left|\bar\kappa+\mathrm{i}h\right|\right)\left(\frac{\bar\kappa+\mathrm{i}h}{\left|\bar\kappa+\mathrm{i}h\right|}\right)^{n-1},
\end{aligned}
\tag{C.5}
$$

$$\begin{aligned}&\frac{\partial}{\partial\kappa}\left[H_n^{(2)}\left(k_\mathrm{S}\left|\bar{\kappa}+\mathrm{i}\,h\right|\right)\left(\frac{\bar{\kappa}+\mathrm{i}\,h}{\left|\bar{\kappa}+\mathrm{i}\,h\right|}\right)^n\right]\\&=\frac{-k_\mathrm{S}}{2}H_{n+1}^{(2)}\left(k_\mathrm{S}\left|\bar{\kappa}+\mathrm{i}\,h\right|\right)\left(\frac{\bar{\kappa}+\mathrm{i}\,h}{\left|\bar{\kappa}+\mathrm{i}\,h\right|}\right)^n\frac{\left(\bar{\kappa}+\mathrm{i}\,h\right)^2}{\left|\bar{\kappa}+\mathrm{i}\,h\right|\left(\bar{\kappa}+\mathrm{i}\,h\right)}\\&=\frac{-k_\mathrm{S}}{2}H_{n+1}^{(2)}\left(k_\mathrm{S}\left|\bar{\kappa}+\mathrm{i}\,h\right|\right)\left(\frac{\bar{\kappa}+\mathrm{i}\,h}{\left|\bar{\kappa}+\mathrm{i}\,h\right|}\right)^{n+1}.\end{aligned}\tag{C.6}$$

Note that the second terms in the expressions provided in Eqs. (C.3)-(C.6) were derived using Maple. These derivative relationships are also hold for Bessel functions.

D

ENTRIES OF $k_n^{(ji)}$ AND $b^{(j)}$ IN EQ. (2.34)

This appendix is related to Chapter 2. Based on the boundary and continuity conditions (see Eq. (2.9)), substituting potentials of the total wave fields (see Eqs. (2.25) and (2.26)) into the expressions for displacements and stresses in terms of complex variables κ and $\bar{\kappa}$, evaluating the derivative of potentials using Eqs. (C.1) and (C.3)-(C.6), and then replacing the complex variables κ and $\bar{\kappa}$ in the physical domain by complex variables ζ and $\bar{\zeta}$ in the image domain (through appropriate mapping functions, see Eqs. (2.29) and (2.30), and their conjugates), we finally obtain Eq. (2.34), which is a function of complex variables ζ and $\bar{\zeta}$. For the aim of demonstration, this appendix presents the entries of $k_n^{(j,i)}$ and $b^{(j)}$ related to the tenth continuity condition (i.e., $j = 10$, which relates to $\sigma^{(1)}_{r_1\theta_1} = \sigma^{(2)}_{r_1\theta_1}$). For completeness, we also show two terms related to the seventh continuity condition.

The entries of $k_n^{(i,j)}$ related to the tenth continuity condition are written as follows:

$$
\begin{aligned}
k_n^{(10,1)} = &+\lambda^{(1)}\left(k_x^{(1)}\right)^2+\left(\lambda^{(1)}+\mu^{(1)}\right)\left(k_\mathrm{a}^{(1)}\right)^2 H_n^{(2)}\left(k_\mathrm{a}^{(1)}\left|X_1\right|\right)\left(\frac{X_1}{\left|X_1\right|}\right)^n \\
&-\frac{\mu^{(1)}\left(k_\mathrm{a}^{(1)}\right)^2}{2}\times \\
&\left[\mathrm{e}^{2\mathrm{i}\theta}H_{n-2}^{(2)}\left(k_\mathrm{a}^{(1)}\left|X_1\right|\right)\left(\frac{X_1}{\left|X_1\right|}\right)^{n-2}+\mathrm{e}^{-2\mathrm{i}\theta}H_{n+2}^{(2)}\left(k_\mathrm{a}^{(1)}\left|X_1\right|\right)\left(\frac{X_1}{\left|X_1\right|}\right)^{n+2}\right],
\end{aligned}
\tag{D.1}
$$

$$\begin{aligned} k_n^{(10,2)} = &-\frac{\mathrm{i}\,\mu^{(1)}\left(k_{\mathrm{b}}^{(1)}\right)^2}{2}\times \\ &\left[\mathrm{e}^{2\mathrm{i}\theta}H^{(2)}_{n-2}\left(k_{\mathrm{b}}^{(1)}\left|X_1\right|\right)\left(\frac{X_1}{\left|X_1\right|}\right)^{n-2}-\mathrm{e}^{-2\mathrm{i}\theta}H^{(2)}_{n+2}\left(k_{\mathrm{b}}^{(1)}\left|X_1\right|\right)\left(\frac{X_1}{\left|X_1\right|}\right)^{n+2}\right], \end{aligned} \tag{D.2}$$

$$\begin{aligned} k_n^{(10,3)} = &-\frac{\mathrm{i}\,\mu^{(1)}k_x^{(1)}\left(k_{\mathrm{b}}^{(1)}\right)^2}{k_{\mathrm{S}}^{(1)}}H^{(2)}_{n}\left(k_{\mathrm{b}}^{(1)}\left|X_1\right|\right)\left(\frac{X_1}{\left|X_1\right|}\right)^{n} \\ &+\frac{\mathrm{i}\,\mu^{(1)}k_x^{(1)}\left(k_{\mathrm{b}}^{(1)}\right)^2}{2k_{\mathrm{S}}^{(1)}}\times \\ &\left[\mathrm{e}^{2\mathrm{i}\theta}H^{(2)}_{n-2}\left(k_{\mathrm{b}}^{(1)}\left|X_1\right|\right)\left(\frac{X_1}{\left|X_1\right|}\right)^{n-2}+\mathrm{e}^{-2\mathrm{i}\theta}H^{(2)}_{n+2}\left(k_{\mathrm{b}}^{(1)}\left|X_1\right|\right)\left(\frac{X_1}{\left|X_1\right|}\right)^{n+2}\right], \end{aligned} \tag{D.3}$$

$$\begin{aligned} k_n^{(10,4)} = &+\lambda^{(1)}\left(k_x^{(1)}\right)^2+\left(\lambda^{(1)}+\mu^{(1)}\right)\left(k_{\mathrm{a}}^{(1)}\right)^2H^{(2)}_{n}\left(k_{\mathrm{a}}^{(1)}\left|X_2\right|\right)\left(\frac{X_2}{\left|X_2\right|}\right)^{n} \\ &-\frac{\mu^{(1)}\left(k_{\mathrm{a}}^{(1)}\right)^2}{2}\times \\ &\left[\mathrm{e}^{2\mathrm{i}\theta}H^{(2)}_{n+2}\left(k_{\mathrm{a}}^{(1)}\left|X_2\right|\right)\left(\frac{X_2}{\left|X_2\right|}\right)^{n+2}+\mathrm{e}^{-2\mathrm{i}\theta}H^{(2)}_{n-2}\left(k_{\mathrm{a}}^{(1)}\left|X_2\right|\right)\left(\frac{X_2}{\left|X_2\right|}\right)^{n-2}\right], \end{aligned} \tag{D.4}$$

$$\begin{aligned} k_n^{(10,5)} = &-\frac{\mathrm{i}\,\mu^{(1)}\left(k_{\mathrm{b}}^{(1)}\right)^2}{2}\times \\ &\left[\mathrm{e}^{2\mathrm{i}\theta}H^{(2)}_{n+2}\left(k_{\mathrm{b}}^{(1)}\left|X_2\right|\right)\left(\frac{X_2}{\left|X_2\right|}\right)^{n+2}-\mathrm{e}^{-2\mathrm{i}\theta}H^{(2)}_{n-2}\left(k_{\mathrm{b}}^{(1)}\left|X_2\right|\right)\left(\frac{X_2}{\left|X_2\right|}\right)^{n-2}\right], \end{aligned} \tag{D.5}$$

$$\begin{aligned} k_n^{(10,6)} = &-\frac{\mathrm{i}\,\mu^{(1)}k_x^{(1)}\left(k_{\mathrm{b}}^{(1)}\right)^2}{k_{\mathrm{S}}^{(1)}}H^{(2)}_{n}\left(k_{\mathrm{b}}^{(1)}\left|X_2\right|\right)\left(\frac{X_2}{\left|X_2\right|}\right)^{n} \\ &+\frac{\mathrm{i}\,\mu^{(1)}k_x^{(1)}\left(k_{\mathrm{b}}^{(1)}\right)^2}{2k_{\mathrm{S}}^{(1)}}\times \\ &\left[\mathrm{e}^{2\mathrm{i}\theta}H^{(2)}_{n+2}\left(k_{\mathrm{b}}^{(1)}\left|X_2\right|\right)\left(\frac{X_2}{\left|X_2\right|}\right)^{n+2}+\mathrm{e}^{-2\mathrm{i}\theta}H^{(2)}_{n-2}\left(k_{\mathrm{b}}^{(1)}\left|X_2\right|\right)\left(\frac{X_2}{\left|X_2\right|}\right)^{n-2}\right], \end{aligned} \tag{D.6}$$

$$\begin{aligned} k_n^{(10,7)} = &-\lambda^{(2)}\left(k_x^{(2)}\right)^2-\left(\lambda^{(2)}+\mu^{(2)}\right)\left(k_{\mathrm{a}}^{(2)}\right)^2H^{(2)}_{n}\left(k_{\mathrm{a}}^{(2)}\left|X_3\right|\right)\left(\frac{X_3}{\left|X_3\right|}\right)^{n} \\ &+\frac{\mu^{(2)}\left(k_{\mathrm{a}}^{(2)}\right)^2}{2}\times \\ &\left[\mathrm{e}^{2\mathrm{i}\theta}H^{(2)}_{n-2}\left(k_{\mathrm{a}}^{(2)}\left|X_3\right|\right)\left(\frac{X_3}{\left|X_3\right|}\right)^{n-2}+\mathrm{e}^{-2\mathrm{i}\theta}H^{(2)}_{n+2}\left(k_{\mathrm{a}}^{(2)}\left|X_3\right|\right)\left(\frac{X_3}{\left|X_3\right|}\right)^{n+2}\right], \end{aligned} \tag{D.7}$$

$$\begin{aligned} k_n^{(10,8)} = &+\frac{\mathrm{i}\,\mu^{(2)}\left(k_{\mathrm{b}}^{(2)}\right)^2}{2}\times \\ &\left[\mathrm{e}^{2\mathrm{i}\theta}H_{n-2}^{(2)}\left(k_{\mathrm{b}}^{(2)}\left|X_3\right|\right)\left(\frac{X_3}{\left|X_3\right|}\right)^{n-2}-\mathrm{e}^{-2\mathrm{i}\theta}H_{n+2}^{(2)}\left(k_{\mathrm{b}}^{(2)}\left|X_3\right|\right)\left(\frac{X_3}{\left|X_3\right|}\right)^{n+2}\right], \end{aligned} \tag{D.8}$$

$$\begin{aligned} k_n^{(10,9)} = &+\frac{\mathrm{i}\,\mu^{(2)}k_x^{(2)}\left(k_{\mathrm{b}}^{(2)}\right)^2}{k_{\mathrm{S}}^{(2)}}H_n^{(2)}\left(k_{\mathrm{b}}^{(2)}\left|X_3\right|\right)\left(\frac{X_3}{\left|X_3\right|}\right)^{n} \\ &-\frac{\mathrm{i}\,\mu^{(2)}k_x^{(2)}\left(k_{\mathrm{b}}^{(2)}\right)^2}{2k_{\mathrm{S}}^{(2)}}\times \\ &\left[\mathrm{e}^{2\mathrm{i}\theta}H_{n-2}^{(2)}\left(k_{\mathrm{b}}^{(2)}\left|X_3\right|\right)\left(\frac{X_3}{\left|X_3\right|}\right)^{n-2}+\mathrm{e}^{-2\mathrm{i}\theta}H_{n+2}^{(2)}\left(k_{\mathrm{b}}^{(2)}\left|X_3\right|\right)\left(\frac{X_3}{\left|X_3\right|}\right)^{n+2}\right], \end{aligned} \tag{D.9}$$

$$\begin{aligned} k_n^{(10,10)} = &-\lambda^{(2)}\left(k_x^{(2)}\right)^2-\left(\lambda^{(2)}+\mu^{(2)}\right)\left(k_{\mathrm{a}}^{(2)}\right)^2H_n^{(1)}\left(k_{\mathrm{a}}^{(2)}\left|X_3\right|\right)\left(\frac{X_3}{\left|X_3\right|}\right)^{n} \\ &+\frac{\mu^{(2)}\left(k_{\mathrm{a}}^{(2)}\right)^2}{2}\times \\ &\left[\mathrm{e}^{2\mathrm{i}\theta}H_{n-2}^{(1)}\left(k_{\mathrm{a}}^{(2)}\left|X_3\right|\right)\left(\frac{X_3}{\left|X_3\right|}\right)^{n-2}+\mathrm{e}^{-2\mathrm{i}\theta}H_{n+2}^{(1)}\left(k_{\mathrm{a}}^{(2)}\left|X_3\right|\right)\left(\frac{X_3}{\left|X_3\right|}\right)^{n+2}\right], \end{aligned} \tag{D.10}$$

$$\begin{aligned} k_n^{(10,11)} = &+\frac{\mathrm{i}\,\mu^{(2)}\left(k_{\mathrm{b}}^{(2)}\right)^2}{2}\times \\ &\left[\mathrm{e}^{2\mathrm{i}\theta}H_{n-2}^{(1)}\left(k_{\mathrm{b}}^{(2)}\left|X_3\right|\right)\left(\frac{X_3}{\left|X_3\right|}\right)^{n-2}-\mathrm{e}^{-2\mathrm{i}\theta}H_{n+2}^{(1)}\left(k_{\mathrm{b}}^{(2)}\left|X_3\right|\right)\left(\frac{X_3}{\left|X_3\right|}\right)^{n+2}\right], \end{aligned} \tag{D.11}$$

$$\begin{aligned} k_n^{(10,12)} = &+\frac{\mathrm{i}\,\mu^{(2)}k_x^{(2)}\left(k_{\mathrm{b}}^{(2)}\right)^2}{k_{\mathrm{S}}^{(2)}}H_n^{(1)}\left(k_{\mathrm{b}}^{(2)}\left|X_3\right|\right)\left(\frac{X_3}{\left|X_3\right|}\right)^{n} \\ &-\frac{\mathrm{i}\,\mu^{(2)}k_x^{(2)}\left(k_{\mathrm{b}}^{(2)}\right)^2}{2k_{\mathrm{S}}^{(2)}}\times \\ &\left[\mathrm{e}^{2\mathrm{i}\theta}H_{n-2}^{(1)}\left(k_{\mathrm{b}}^{(2)}\left|X_3\right|\right)\left(\frac{X_3}{\left|X_3\right|}\right)^{n-2}+\mathrm{e}^{-2\mathrm{i}\theta}H_{n+2}^{(1)}\left(k_{\mathrm{b}}^{(2)}\left|X_3\right|\right)\left(\frac{X_3}{\left|X_3\right|}\right)^{n+2}\right], \end{aligned} \tag{D.12}$$

where $X_1 = w^{(1)}\left(\zeta(\beta_{\mathrm{o}},\vartheta^+)\right)+\mathrm{i}H$, $X_2 = \overline{w^{(1)}}\left(\zeta(\beta_{\mathrm{o}},\vartheta^+)\right)+\mathrm{i}H$ and $X_3 = w^{(2)}\left(\zeta(\beta_{\mathrm{o}},\vartheta)\right)+\mathrm{i}H = R_{\mathrm{o}}$ (considering Eq. (2.30)). ϑ^+ is a function of ϑ; see Eq. (2.33). The terms of $\mathrm{e}^{+2\mathrm{i}\theta}$ and $\mathrm{e}^{-2\mathrm{i}\theta}$ in the first six entries (i.e., $k_n^{(10,1)}-k_n^{(10,6)}$) and in the last six entries (i.e., $k_n^{(10,7)}-k_n^{(10,12)}$), respectively are written as functions of variable ϑ in the image domain as follows:

$$e^{2\mathrm{i}\theta}=e^{2\mathrm{i}\vartheta^{+}}\left[\frac{w^{(1)\prime}(\zeta)}{|w^{(1)\prime}(\zeta)|}\right]^{2}=-\left(\frac{e^{\mathrm{i}\vartheta^{+}}-\beta_{\mathrm{o}}}{1-\beta_{\mathrm{o}}e^{\mathrm{i}\vartheta^{+}}}\right)^{2},\ e^{-2\mathrm{i}\theta}=-\left(\frac{1-\beta_{\mathrm{o}}e^{\mathrm{i}\vartheta^{+}}}{e^{\mathrm{i}\vartheta^{+}}-\beta_{\mathrm{o}}}\right)^{2}, \tag{D.13}$$

$$e^{2\mathrm{i}\theta}=e^{2\mathrm{i}\vartheta},\ e^{-2\mathrm{i}\theta}=e^{-2\mathrm{i}\vartheta}. \tag{D.14}$$

Similarly, the terms of $e^{\mathrm{i}\theta}$ and $e^{-\mathrm{i}\theta}$ in the first six entries, for example, in the seventh continuity condition, (i.e., $k_n^{(7,1)}-k_n^{(7,6)}$) and in the last six entries (i.e., $k_n^{(7,7)}-k_n^{(7,12)}$), respectively are written as functions of variable ϑ in the image domain as follows:

$$\begin{aligned}
e^{\mathrm{i}\theta}&=e^{\mathrm{i}\vartheta^{+}}\frac{w^{(1)\prime}(\zeta)}{|w^{(1)\prime}(\zeta)|}=\left|\frac{\left(1-\beta_{\mathrm{o}}e^{\mathrm{i}\vartheta^{+}}\right)^{2}}{2\mathrm{i}G}\right|\frac{-2\mathrm{i}Ge^{\mathrm{i}\vartheta^{+}}}{\left(1-\beta_{\mathrm{o}}e^{\mathrm{i}\vartheta^{+}}\right)^{2}},\\
e^{-\mathrm{i}\theta}&=\left|\frac{\left(1-\beta_{\mathrm{o}}e^{\mathrm{i}\vartheta^{+}}\right)^{2}}{2\mathrm{i}G}\right|\frac{2\mathrm{i}Ge^{\mathrm{i}\vartheta^{+}}}{\left(e^{\mathrm{i}\vartheta^{+}}-\beta_{\mathrm{o}}\right)^{2}},
\end{aligned} \tag{D.15}$$

$$e^{\mathrm{i}\theta}=e^{\mathrm{i}\vartheta},\ e^{-\mathrm{i}\theta}=e^{-\mathrm{i}\vartheta}. \tag{D.16}$$

The entry of $b^{(j)}$ related to the tenth continuity condition, with the incident P wave ($\phi_{\mathrm{inc}}^{(1)}$) taken as an example, reads as follows:

$$\begin{aligned}
b^{(10)}=&-\lambda^{(1)}\left(k_x^{(1)}\right)^{2}-\left(\lambda^{(1)}+\mu^{(1)}\right)\left(\phi_{\mathrm{inc}}^{(1)}+\phi_{\mathrm{ref}}^{(1)}\right)\\
&+2\mathrm{i}\mu^{(1)}\left[e^{2\mathrm{i}\theta}\left(-\frac{\mathrm{i}k_y^{(1)}-k_{z,\mathrm{S}}^{(1)}}{2}\right)^{2}-e^{-2\mathrm{i}\theta}\left(-\frac{\mathrm{i}k_y^{(1)}+k_{z,\mathrm{S}}^{(1)}}{2}\right)^{2}\right]\psi_{\mathrm{ref}}^{(1)}\\
&+2\mu^{(1)}\left[e^{2\mathrm{i}\theta}\left(-\frac{\mathrm{i}k_y^{(1)}+k_{z,\mathrm{P}}^{(1)}}{2}\right)^{2}+e^{-2\mathrm{i}\theta}\left(-\frac{\mathrm{i}k_y^{(1)}-k_{z,\mathrm{P}}^{(1)}}{2}\right)^{2}\right]\phi_{\mathrm{inc}}^{(1)}\\
&+2\mu^{(1)}\left[e^{2\mathrm{i}\theta}\left(-\frac{\mathrm{i}k_y^{(1)}-k_{z,\mathrm{P}}^{(1)}}{2}\right)^{2}+e^{-2\mathrm{i}\theta}\left(-\frac{\mathrm{i}k_y^{(1)}+k_{z,\mathrm{P}}^{(1)}}{2}\right)^{2}\right]\phi_{\mathrm{ref}}^{(1)}\\
&+\frac{\mathrm{i}\mu^{(1)}k_x^{(1)}\left(k_b^{(1)}\right)^{2}}{k_{\mathrm{S}}^{(1)}}\chi_{\mathrm{ref}}^{(1)}\\
&-\frac{2\mathrm{i}\mu^{(1)}k_x^{(1)}\left(k_b^{(1)}\right)^{2}}{k_{\mathrm{S}}^{(1)}}\left[e^{2\mathrm{i}\theta}\left(-\frac{\mathrm{i}k_y^{(1)}-k_{z,\mathrm{S}}^{(1)}}{2}\right)^{2}+e^{-2\mathrm{i}\theta}\left(-\frac{\mathrm{i}k_y^{(1)}+k_{z,\mathrm{S}}^{(1)}}{2}\right)^{2}\right]\chi_{\mathrm{ref}}^{(1)},
\end{aligned} \tag{D.17}$$

where the terms of $\mathrm{e}^{+2\mathrm{i}\theta}$ and $\mathrm{e}^{-2\mathrm{i}\theta}$ have the expressions as shown in Eq. (D.13), and

$$\begin{aligned}\phi_{\mathrm{inc}}^{(1)} =& \phi_0 \exp\left(-\mathrm{i}\, k_x^{(1)} x\right) \times \\ & \exp\left[\left(-\frac{\mathrm{i}\, k_y^{(1)} + k_{z,\mathrm{P}}^{(1)}}{2}\right) w^{(1)}\left(\zeta(\beta_\mathrm{o}, \vartheta^+)\right) + \left(-\frac{\mathrm{i}\, k_y^{(1)} - k_{z,\mathrm{P}}^{(1)}}{2}\right) \overline{w^{(1)}}\left(\zeta(\beta_\mathrm{o}, \vartheta^+)\right)\right],\end{aligned} \tag{D.18}$$

$$\begin{aligned}\phi_{\mathrm{ref}}^{(1)} =& R_{\phi,\phi} \phi_0 \exp\left(-\mathrm{i}\, k_x^{(1)} x\right) \times \\ & \exp\left[\left(-\frac{\mathrm{i}\, k_y^{(1)} - k_{z,\mathrm{P}}^{(1)}}{2}\right) w^{(1)}\left(\zeta(\beta_\mathrm{o}, \vartheta^+)\right) + \left(-\frac{\mathrm{i}\, k_y^{(1)} + k_{z,\mathrm{P}}^{(1)}}{2}\right) \overline{w^{(1)}}\left(\zeta(\beta_\mathrm{o}, \vartheta^+)\right)\right],\end{aligned} \tag{D.19}$$

$$\begin{aligned}\psi_{\mathrm{ref}}^{(1)} =& R_{\psi,\phi} \phi_0 \exp\left(-\mathrm{i}\, k_x^{(1)} x\right) \times \\ & \exp\left[\left(-\frac{\mathrm{i}\, k_y^{(1)} - k_{z,\mathrm{S}}^{(1)}}{2}\right) w^{(1)}\left(\zeta(\beta_\mathrm{o}, \vartheta^+)\right) + \left(-\frac{\mathrm{i}\, k_y^{(1)} + k_{z,\mathrm{S}}^{(1)}}{2}\right) \overline{w^{(1)}}\left(\zeta(\beta_\mathrm{o}, \vartheta^+)\right)\right],\end{aligned} \tag{D.20}$$

$$\begin{aligned}\chi_{\mathrm{ref}}^{(1)} =& R_{\chi,\phi} \phi_0 \exp\left(-\mathrm{i}\, k_x^{(1)} x\right) \times \\ & \exp\left[\left(-\frac{\mathrm{i}\, k_y^{(1)} - k_{z,\mathrm{S}}^{(1)}}{2}\right) w^{(1)}\left(\zeta(\beta_\mathrm{o}, \vartheta^+)\right) + \left(-\frac{\mathrm{i}\, k_y^{(1)} + k_{z,\mathrm{S}}^{(1)}}{2}\right) \overline{w^{(1)}}\left(\zeta(\beta_\mathrm{o}, \vartheta^+)\right)\right].\end{aligned} \tag{D.21}$$

E

ENTRIES OF $k_n^{(j,i)}$ AND $b^{(j)}$ IN EQ. (3.32)

This appendix is related to Chapter 3. By incorporating the boundary conditions (see Eqs. (3.2) and (3.3)), substituting the total wave field potentials (see Eqs. (3.20)-(3.23)) into the expressions for stresses in terms of complex variables κ and $\bar{\kappa}$, evaluating the derivatives of the potentials using Eqs. (C.1) and (C.3)-(C.6), and subsequently substituting the complex variables κ and $\bar{\kappa}$ in the physical domain with complex variables ζ and $\bar{\zeta}$ in the image domain (through the utilisation of the conformal mapping function, see Eq. (3.30), and its conjugate), Eq. (3.32) is ultimately derived as a function of complex variables ζ and $\bar{\zeta}$.

The entries of $k_n^{(i,j)}$ associated with the stress-free boundary conditions at the free surface of the half-space and at the cavity surface are expressed as follows:

$$k_n^{(1,1)} = \mathrm{i}\,\mu\frac{k_{\mathrm{S}}}{2}\left[H_{n-1}^{(2)}\left(k_{\mathrm{S}}\left|X_1\right|\right)\left(\frac{X_1}{\left|X_1\right|}\right)^{n-1} + H_{n+1}^{(2)}\left(k_{\mathrm{S}}\left|X_1\right|\right)\left(\frac{X_1}{\left|X_1\right|}\right)^{n+1}\right], \tag{E.1}$$

$$k_n^{(1,2)} = \mathrm{i}\,\mu\frac{k_{\mathrm{S}}}{2}\left[-H_{n+1}^{(2)}\left(k_{\mathrm{S}}\left|X_2\right|\right)\left(\frac{X_2}{\left|X_2\right|}\right)^{n+1} - H_{n-1}^{(2)}\left(k_{\mathrm{S}}\left|X_2\right|\right)\left(\frac{X_2}{\left|X_2\right|}\right)^{n-1}\right], \tag{E.2}$$

$$k_n^{(2,1)} = \mu\frac{k_{\mathrm{S}}}{2}\left[\mathrm{e}^{\mathrm{i}\theta}H_{n-1}^{(2)}\left(k_{\mathrm{S}}\left|X_1\right|\right)\left(\frac{X_1}{\left|X_1\right|}\right)^{n-1} - \mathrm{e}^{-\mathrm{i}\theta}H_{n+1}^{(2)}\left(k_{\mathrm{S}}\left|X_1\right|\right)\left(\frac{X_1}{\left|X_1\right|}\right)^{n+1}\right], \tag{E.3}$$

$$k_n^{(2,2)} = \mu\frac{k_{\mathrm{S}}}{2}\left[-\mathrm{e}^{\mathrm{i}\theta}H_{n+1}^{(2)}\left(k_{\mathrm{S}}\left|X_2\right|\right)\left(\frac{X_2}{\left|X_2\right|}\right)^{n+1} + \mathrm{e}^{-\mathrm{i}\theta}H_{n-1}^{(2)}\left(k_{\mathrm{S}}\left|X_2\right|\right)\left(\frac{X_2}{\left|X_2\right|}\right)^{n-1}\right], \tag{E.4}$$

where $X_1 = w\left(\zeta(\beta,\vartheta)\right) + \mathrm{i}\,H$ and $X_2 = \overline{w}\left(\zeta(\beta,\vartheta)\right) + \mathrm{i}\,H$.

The entries of $b^{(1)}$ and $b^{(2)}$ are related to the stress-free boundary conditions at the free surface of the half-space and at the cavity surface, respectively. They are given as follows:

$$b^{(1)} = -\mathrm{i}\mu\left(C_{11} - C_{12}\right)u_{\mathrm{inc}} - \mathrm{i}\mu\left(C_{21} - C_{22}\right)u_{\mathrm{ref}}, \tag{E.5}$$

$$b^{(2)} = -\mu\left(\mathrm{e}^{\mathrm{i}\theta}C_{11} + \mathrm{e}^{-\mathrm{i}\theta}C_{12}\right)u_{\mathrm{inc}} - \mu\left(\mathrm{e}^{\mathrm{i}\theta}C_{21} + \mathrm{e}^{-\mathrm{i}\theta}C_{22}\right)u_{\mathrm{ref}}, \tag{E.6}$$

where u_{inc} and u_{ref} represent the displacements associated with the incident and reflected SH waves, respectively; see Eqs. (3.20) and (3.21). The parameters C_{11}, C_{12}, C_{21} and C_{22} are defined below Eq. (3.23).

F

STEADY-STATE RESPONSE OF THE TUNNEL-SOIL SYSTEM SUBJECT TO A STATIONARY HARMONIC POINT LOAD

This appendix is related to Chapter 4. We consider the tunnel-soil system subject to a stationary harmonic point load for the purpose of validation (Section 4.4). The shear stresses $\sigma_{r_1\theta_1}$ and $\sigma_{r_1x_1}$ at the inner surface of the tunnel induced by the stationary harmonic point load are zero. The non-zero normal stress $\sigma_{r_1r_1}(R_\mathrm{i},\theta_1,x,t)$ can be expressed in a complex form as

$$\sigma_{r_1r_1}\left(R_\mathrm{i},\theta_1,x,t\right)=\frac{P_0}{R_\mathrm{i}}\delta\left(\theta_1+\pi/2\right)\delta\left(x\right)\exp\left(\mathrm{i}\Omega t\right), \tag{F.1}$$

where P_0 is the amplitude of the harmonic load, $\Omega=2\pi f_0$ is the angular frequency, f_0 the excitation frequency, and R the radius of the centerline of the tunnel. Expanding the term $\delta\left(\theta_1+\pi/2\right)$ in Eq. (F.1) into a Fourier series (see Eq. (4.10)), the normal stress can be rewritten as

$$\sigma_{r_1r_1}\left(R_\mathrm{i},\theta_1,x,t\right)=\sum_{n=-\infty}^{n=\infty}\frac{P_0}{2\pi R_\mathrm{i}}\exp\left(\mathrm{i}n\left(\theta_1+\pi/2\right)\right)\delta\left(x\right)\exp\left(\mathrm{i}\Omega t\right). \tag{F.2}$$

Applying the Fourier Transform over spatial coordinate x (see Eq. (4.8)) to Eq. (F.2), the normal stress in the wavenumber domain is obtained:

$$\begin{aligned}\tilde{\sigma}_{r_1r_1}\left(R_\mathrm{i},\theta_1,k_x,t\right)&=\sum_{n=-\infty}^{n=\infty}\frac{P_0}{2\pi R_\mathrm{i}}\exp\left(\mathrm{i}n\left(\theta_1+\pi/2\right)\right)\exp\left(\mathrm{i}\Omega t\right)\\&=\tilde{\sigma}_\mathrm{aux}\left(R_\mathrm{i},\theta_1,k_x\right)\exp\left(\mathrm{i}\Omega t\right).\end{aligned} \tag{F.3}$$

The response induced by the auxiliary stress $\tilde{\sigma}_{\text{aux}}\left(R_{\text{i}},\theta_1,k_x\right)$ can be computed using the indirect BEM (Section 4.3) and is denoted as $\tilde{\mathbf{U}}_{1,\text{aux}}\left(r_1,\theta_1,k_x\right)$. Thereafter, we get the expression for the actual displacement vector excited by the actual stress $\tilde{\sigma}_{r_1 r_1}\left(R_{\text{i}},\theta_1,k_x,t\right)$ shown in Eq. (F.3):

$$\tilde{\mathbf{U}}_1\left(r_1,\theta_1,k_x,t\right)=\tilde{\mathbf{U}}_{1,\text{aux}}\left(r_1,\theta_1,k_x\right)\exp\left(\text{i}\Omega t\right). \tag{F.4}$$

We get the space-time domain response by applying the inverse Fourier Transform over wavenumber k_x (Eq. (4.9)):

$$\begin{aligned}\mathbf{U}_1(r_1,\theta_1,x,t)&=\frac{1}{2\pi}\int_{-\infty}^{\infty}\tilde{\mathbf{U}}_1\left(r_1,\theta_1,k_x,t\right)\exp\left(-\text{i}\,k_x x\right)\,\text{d}k_x\\&=\frac{1}{2\pi}\int_{-\infty}^{\infty}\tilde{\mathbf{U}}_{1,\text{aux}}\left(r_1,\theta_1,k_x\right)\exp\left(-\text{i}\,k_x x\right)\,\text{d}k_x\exp\left(\text{i}\Omega t\right),\end{aligned} \tag{F.5}$$

where the integral needs to be evaluated numerically. Note that if we take the real part of the complex-valued excitation in Eq. (F.1), then the corresponding displacement will be the real part of the complex-valued displacement shown in Eq. (F.5).

G

MATRICES USED FOR THE GREEN'S FUNCTIONS OF THE FLÜGGE SHELL

This appendix is related to Chapter 4. The components of matrix **A** in Eq. (4.23) are written as follows:

$$
\begin{aligned}
A_{11} &= \rho h \frac{\partial^2 \bar{u}}{\partial t^2} - K_0 \left[\frac{-h^2}{12} \left(\frac{\partial^4}{\partial x_2^4} + \frac{2}{R^2} \frac{\partial^4}{\partial x_2^2 \partial \theta_2^2} + \frac{1}{R^4} \frac{\partial^4}{\partial \theta_2^4} \right) - \frac{1}{R^2} - \frac{h^2}{12} \left(\frac{1}{R^4} + \frac{2}{R^4} \frac{\partial^2}{\partial \theta_2^2} \right) \right], \\
A_{22} &= \rho h \frac{\partial^2 \bar{v}}{\partial t^2} - K_0 \left[\frac{1-\nu_2}{2} \frac{\partial^2}{\partial x_2^2} + \frac{1}{R^2} \frac{\partial^2}{\partial \theta_2^2} + \frac{h^2}{12} \frac{3\left(1-\nu_2\right)}{2R^2} \frac{\partial^2}{\partial x_2^2} \right], \\
A_{33} &= \rho h \frac{\partial^2 \bar{w}}{\partial t^2} - K_0 \left[\frac{\partial^2}{\partial x_2^2} + \frac{1-\nu_2}{2R^2} \frac{\partial}{\partial \theta_2^2} + \frac{h^2}{12} \frac{1-\nu_2}{2R^4} \frac{\partial^2}{\partial \theta_2^2} \right], \\
A_{12} &= -A_{21} = -K_0 \left[\frac{-1}{R^2} \frac{\partial}{\partial \theta_2} + \frac{h^2}{12} \left(\frac{3-\nu_2}{2R^2} \frac{\partial^3}{\partial x_2^2 \partial \theta_2} \right) \right], \\
A_{13} &= -A_{31} = -K_0 \left[\frac{-\nu_2}{R} \frac{\partial}{\partial x_2} + \frac{h^2}{12} \left(\frac{1}{R} \frac{\partial^3}{\partial x_2^3} - \frac{1-\nu_2}{2R^3} \frac{\partial^3}{\partial x_2 \partial \theta_2^2} \right) \right], \\
A_{23} &= A_{32} = -K_0 \left[\frac{1+\nu_2}{2R} \frac{\partial^2}{\partial x_2 \partial \theta_2} \right],
\end{aligned}
\tag{G.1}
$$

where $K_0 = E_2 h/(1-\nu_2^2)$. The components of the matrix $\tilde{\tilde{\mathbf{A}}}_n$ read:

$$\begin{aligned}
\tilde{\tilde{A}}_{11n} &= -\omega^2\rho h + K_0\left[\frac{h^2}{12}\left(k_x^4+\frac{2}{R^2}k_x^2n^2+\frac{n^4}{R^4}\right)+\frac{1}{R^2}+\frac{h^2}{12}\left(\frac{1}{R^4}-\frac{2n^2}{R^4}\right)\right],\\
\tilde{\tilde{A}}_{22n} &= -\omega^2\rho h + K_0\left[\frac{1-\nu_2}{2}k_x^2+\frac{n^2}{R^2}+\frac{h^2}{12}\frac{3\left(1-\nu_2\right)}{2R^2}k_x^2\right],\\
\tilde{\tilde{A}}_{33n} &= -\omega^2\rho h + K_0\left[k_x^2+\frac{1-\nu_2}{2R^2}n^2+\frac{h^2}{12}\frac{1-\nu_2}{2R^4}n^2\right],\\
\tilde{\tilde{A}}_{12n} &= -\tilde{\tilde{A}}_{21n} = K_0\left[\frac{1}{R^2}\,\mathrm{i}\,n+\frac{h^2}{12}\frac{3-\nu_2}{2R^2}\left(\mathrm{i}\,k_x^2n\right)\right],\\
\tilde{\tilde{A}}_{13n} &= -\tilde{\tilde{A}}_{31n} = -K_0\left[\frac{\nu_2}{R}\left(\mathrm{i}\,k_x\right)+\frac{h^2}{12}\left(\frac{1}{R}\,\mathrm{i}\,k_x^3-\frac{1-\nu_2}{2R^3}k_xn^2\right)\right],\\
\tilde{\tilde{A}}_{23n} &= \tilde{\tilde{A}}_{32n} = -K_0\left[\frac{1+\nu_2}{2R}k_xn\right].
\end{aligned} \tag{G.2}$$

Matrices $\tilde{\tilde{\mathbf{B}}}_n^{\mathrm{o}}$, $\tilde{\tilde{\mathbf{B}}}_n^{\mathrm{i}}$ and $\tilde{\tilde{\mathbf{D}}}_n$ in Eq. (4.26) are given as follows

$$\tilde{\tilde{\mathbf{B}}}_n^{\mathrm{o}} = \begin{pmatrix} 1 & \frac{h}{2R}\,\mathrm{i}\,n & -\frac{h}{2}\,\mathrm{i}\,k_x \\ 0 & 1+\frac{h}{2R} & 0 \\ 0 & 0 & 1 \end{pmatrix}, \quad \tilde{\tilde{\mathbf{B}}}_n^{\mathrm{i}} = \begin{pmatrix} 1 & \frac{-h}{2R}\,\mathrm{i}\,n & \frac{h}{2}\,\mathrm{i}\,k_x \\ 0 & 1+\frac{-h}{2R} & 0 \\ 0 & 0 & 1 \end{pmatrix}, \tag{G.3}$$

$$\tilde{\tilde{\mathbf{D}}}_n = \begin{pmatrix} 1 & 0 & 0 \\ -\frac{h}{2R}\,\mathrm{i}\,n & 1+\frac{h}{2R} & 0 \\ \frac{h}{2}\,\mathrm{i}\,k_x & 0 & 1 \end{pmatrix}. \tag{G.4}$$

H

THE CRITICAL VELOCITY FOR RESONANCE OF THE TUNNEL-SOIL SYSTEM AND CONVERGENCE REQUIREMENTS FOR THE COMPUTATION OF THE EQUIVALENT DYNAMIC STIFFNESS

In this appendix which is related to Chapter 4, our first aim is to find the critical velocity for resonance $V_{\mathrm{cr}}^{\mathrm{res}}$ of the current tunnel-soil system. To this end, we analyse the response of the tunnel-soil system induced by a uniformly moving non-oscillatory ($f_0 = \frac{\Omega}{2\pi} = 0$) point load observed at the tunnel invert at $x = 0$ as derived in Section 4.2.3 (see Eq. (4.18)). We consider three cases of $V = 30$ m/s, $V = 69$ m/s and $V = 70$ m/s in the sub-Rayleigh regime ($V < C_{\mathrm{R},1} = 72.29$ m/s), one case of $V = 75$ m/s ($C_{\mathrm{R},1} < V < C_{\mathrm{S},1} = 77.94$ m/s) in the super-Rayleigh regime, and one case of $V = 150$ m/s in the supersonic regime ($V > C_{\mathrm{P},1} = 145.8$ m/s). A half-space model is considered and the burial depth of the tunnel is $H = 15$ m. All other parameter values are taken in accordance with the base case defined in Table 4.3.

Fig. H.1 (a) shows the amplitude spectra of the radial displacements observed at the tunnel invert, at the observation point $x = 0$, for one sub-Rayleigh, one super-Rayleigh and one supersonic case (the others look similarly). The Fourier transformed displacement, $\tilde{U}_{r_1}(r_1, \theta_1, x, \omega)$, is defined as the integrand of Eq. (4.18) except for the term $\exp(\mathrm{i}\omega t)$. It is shown that the spectra are spread around $f = 0$. The time-domain responses are shown in Fig. H.1 (b). Clearly, for $V = 30$ m/s and $V = 69$ m/s, the disturbance is localized around the moving load, and there is no significant wave radiation in these cases.

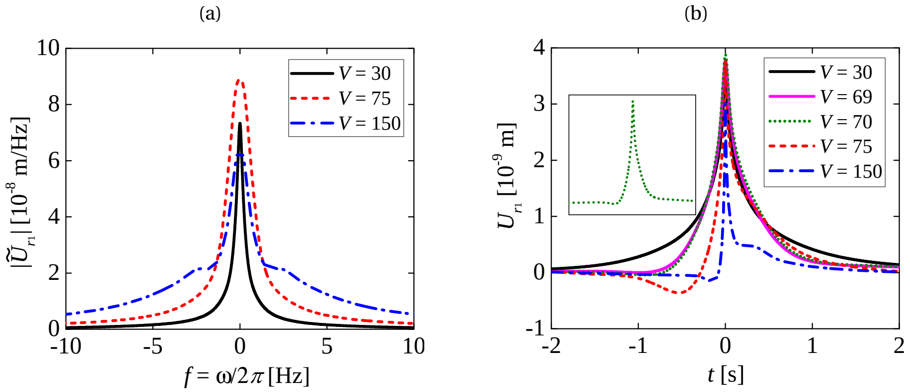

Figure H.1: The radial displacement at the tunnel invert and at the observation point $x = 0$ when the tunnel-soil system is subject to a uniformly moving non-oscillatory ($f_0 = 0$) point load for different velocities [m/s]: (a) amplitude spectra and (b) time-domain responses.

For $V = 70$ m/s, a wave pattern emerges, which comes with significant asymmetry of the profile. For $V = 75$ m/s and $V = 150$ m/s, a more clear wave pattern can be observed; in these two cases, Rayleigh waves, and Rayleigh, shear and compressional waves are generated, respectively. Furthermore, the response is extreme for $V = 70$ m/s, which indicates resonance. Therefore, we conclude that for the current tunnel-soil system, $V_{\mathrm{cr}}^{\mathrm{res}} \approx 70$ m/s. Clearly, a constant load moving faster than this critical speed will radiate waves.

As explained in Subsection 4.2.2, the radial displacement at the loading point, excited by a uniformly moving oscillatory load (i.e., $f_0 \neq 0$), is a key element for the stability analysis (see Eqs. (4.16) and (4.17)). The second aim of this appendix is therefore to find the requirements that need to be met to get converged steady-state responses. Essentially, these requirements need to be defined based on $U_0(\Omega, V)$ in Eq. (4.16), as that quantity is used to obtain the equivalent stiffness (Eq. (4.17)). However, the radial displacement presented in Eq. (4.18), when evaluated at $t = 0$ (i.e., $U_{r_1}(R, -\frac{\pi}{2}, 0, 0)$), is exactly equal to $U_0(\Omega, V)$. Therefore, the convergence requirements can be found based on the spectra and time-domain responses computed using Eq. (4.18).

For illustration purposes, we consider the three cases of $V = 30$ m/s, $V = 75$ m/s and $V = 150$ m/s with a load frequency $f_0 = 5$ Hz shown in Fig. H.2. In this figure, small frequency and time windows are shown in order to present clear features of the spectra and time-domain responses. One observes that the amplitude spectra of displacements become wider compared with the case of $f_0 = 0$ (compare Figs. H.1 (a) and H.2 (a)) and are spread around $f = f_0$. In the time-domain responses, oscillatory patterns are observed even for the sub-critical case due to the oscillation of the load. In addition, the Doppler effect is observed in Fig. H.2 (b) [Denisov *et al.*, 1985; Metrikine and Vrouwenvelder, 2000], which implies that waves are generated at frequencies different from that of the load; these frequencies are usually found from the intersections of the kinematic invariant (e.g., line 3 or 4 in Fig. 4.10) and the dispersion curves.

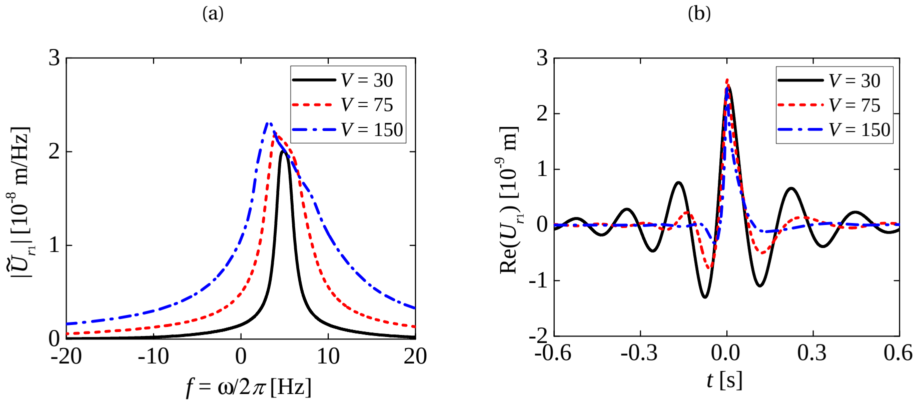

Figure H.2: The radial displacement at the tunnel invert and at the observation point $x = 0$ when the tunnel-soil system is subject to uniformly moving oscillatory ($f_0 = 5$ Hz) point load for different velocities [m/s]: (a) amplitude spectra and (b) real part of the time-domain responses.

Based on the amplitude spectra and time-domain responses for different velocities and loading frequencies, we found the requirements (in terms of Δf, $f^{\max}$ and (N_s, N_r)) to obtain converged results, and they are shown in Table H.1. Note that $N^{\text{shell}} = 20$ and $N^{\text{load}} = 20$ were sufficient for all the computed cases.

Table H.1: Requirements for Δf, $f^{\max}$ and (N_s, N_r) to obtain the converged results for different velocities and loading frequencies.

Velocity (m/s)	Frequency f_0 (Hz)	Δf (Hz)	$f^{\max}$ (Hz)	(N_s, N_r)
$V = 30$	$f_0 = (0-40)$	$\Delta f = 0.05$	$f^{\max} = 100$	$(N_s, N_r) = (20, 40)$
$V = 75$	$f_0 = (0-40)$	$\Delta f = 0.05$	$f^{\max} = 200$	$(N_s, N_r) = (20, 40)$
$V = 150$	$f_0 = (0-40)$	$\Delta f = 0.05$	$f^{\max} = 300$	$(N_s, N_r) = (20, 40)$
$V = 1000$	$f_0 = (0-40)$	$\Delta f = 0.02$	$f^{\max} = 2000$	$(N_s, N_r) = (160, 160)$
$V = 1200$	$f_0 = (0-40)$	$\Delta f = 0.02$	$f^{\max} = 2000$	$(N_s, N_r) = (160, 160)$

REFERENCES

A. G. Muntendam-Bos, G. Hoedeman, K. Polychronopoulou, D. Draganov, C. Weemstra, W. van der Zee, R. R. Bakker, and H. Roest, *An overview of induced seismicity in the netherlands,* Netherlands Journal of Geosciences **101**, e1 (2022).

C. C. Mow and Y. H. Pao, *The diffraction of elastic waves and dynamic stress concentrations* (Crane-Russak, New York, 1971).

J. D. Achenbach, *Wave propagation in elastic solids* (Nord Holland Elsevier, 1973).

K. F. Graff, *Wave motion in elastic solids* (Ohio State University Press, 1975).

K. Aki and P. G. Richards, *Quantitative seismology* (University Science Books, 2002).

T. Ariman and G. E. Muleski, *A review of the response of buried pipelines under seismic excitations,* Earthquake Engineering & Structural Dynamics **9**, 133 (1981).

Y. M. Hashash, J. J. Hook, B. Schmidt, I. John, and C. Yao, *Seismic design and analysis of underground structures,* Tunnelling and Underground Space Technology **16**, 247 (2001).

I. D. Moore and F. Guan, *Three-dimensional dynamic response of lined tunnels due to incident seismic waves,* Earthquake Engineering and Structural Dynamics **25**, 357 (1996).

A. M. Kaynia, C. Madshus, and P. Zackrisson, *Ground vibration from high-speed trains: Prediction and countermeasure,* Journal of Geotechnical and Geoenvironmental Engineering **126**, 531 (2000).

H. Di, S. Zhou, C. He, X. Zhang, and Z. Luo, *Three-dimensional multilayer cylindrical tunnel model for calculating train-induced dynamic stress in saturated soils,* Computers and Geotechnics **80**, 333 (2016).

G. Degrande, D. Clouteau, R. Othman, M. Arnst, H. Chebli, R. Klein, P. Chatterjee, and B. Janssens, *A numerical model for ground-borne vibrations from underground railway traffic based on a periodic finite element–boundary element formulation,* Journal of Sound and Vibration **293**, 645 (2006).

G. G. Denisov, E. K. Kugusheva, and V. V. Novikov, *On the problem of the stability of one-dimensional unbounded elastic systems,* Journal of Applied Mathematics and Mechanics **49**, 533 (1985).

R. Bogacz, S. Nowakowski, and K. Popp, *On the stability of a Timoshenko beam on an elastic foundation under a moving spring-mass system,* Acta Mechanica **61**, 117 (1986).

A. V. Metrikine, *Unstable lateral oscillations of an object moving uniformly along an elastic guide as a result of an anomalous Doppler effect,* Acoustical Physics **40**, 85 (1994).

A. V. Metrikine and H. A. Dieterman, *Instability of vibrations of a mass moving uniformly along an axially compressed beam on a viscoelastic foundation,* Journal of Sound and Vibration **201**, 567 (1997).

T. Mazilu, M. Dumitriu, and C. Tudorache, *Instability of an oscillator moving along a Timoshenko beam on viscoelastic foundation,* Nonlinear Dynamics **67**, 1273 (2012).

V. W. Lee and M. D. Trifunac, *Response of tunnels to incident SH-waves,* Journal of the Engineering Mechanics Division **105**, 643 (1979).

A. A. Stamos and D. E. Beskos, *Dynamic analysis of large 3-D underground structures by the BEM,* Earthquake Engineering and Structural Dynamics **24**, 917 (1995).

J. E. Luco and F. C. P. de Barros, *Seismic response of a cylindrical shell embedded in a layered viscoelastic half-space. I: Formulation,* Earthquake Engineering and Structural Dynamics **23**, 553 (1994a).

G. D. Manolis and D. E. Beskos, *Dynamic response of lined tunnels by an isoparametric boundary element method,* Computer Methods in Applied Mechanics and Engineering **36**, 291 (1983).

J. E. Luco and F. C. P. de Barros, *Dynamic displacements and stresses in the vicinity of a cylindrical cavity embedded in a half-space,* Earthquake Engineering and Structural Dynamics **23**, 321 (1994b).

F. C. P. de Barros and J. E. Luco, *Diffraction of obliquely incident waves by a cylindrical cavity embedded in a layered viscoelastic half-space,* Soil Dynamics and Earthquake Engineering **12**, 159 (1993).

J. E. Luco and F. C. P. de Barros, *On the three-dimensional seismic response of a class of cylindrical inclusions embedded in layered media,* in *International conference on Soil Dynamics and Earthquake Engineering* (1993) pp. 565–580.

F. C. P. de Barros and J. E. Luco, *Seismic response of a cylindrical shell embedded in a layered viscoelastic half-space. II: Validation and numerical results,* Earthquake Engineering and Structural Dynamics **23**, 569 (1994).

M. Dravinski and T. K. Mossessian, *Scattering of plane harmonic P, SV, and Rayleigh waves by dipping layers of arbitrary shape,* Bulletin of the Seismological Society of America **77**, 212 (1987).

A. A. Stamos and D. E. Beskos, *3-D seismic response analysis of long lined tunnels in half-space,* Soil Dynamics and Earthquake Engineering **15**, 111 (1996).

S. W. Liu, S. K. Datta, K. R. Khair, and A. H. Shah, *Three dimensional dynamics of pipelines buried in backfilled trenches due to oblique incidence of body waves,* Soil Dynamics and Earthquake Engineering **10**, 182 (1991).

A. S. M. Israil and P. K. Banerjee, *Two-dimensional transient wave-propagation problems by time-domain BEM,* International Journal of Solids and Structures **26**, 851 (1990).

G. D. Hatzigeorgiou and D. E. Beskos, *Soil–structure interaction effects on seismic inelastic analysis of 3-D tunnels,* Soil Dynamics and Earthquake Engineering **30**, 851 (2010).

H. Alielahi, M. Kamalian, and M. Adampira, *Seismic ground amplification by unlined tunnels subjected to vertically propagating SV and P waves using BEM,* Soil Dynamics and Earthquake Engineering **71**, 63 (2015).

H. Alielahi, M. Kamalian, and M. Adampira, *A BEM investigation on the influence of underground cavities on the seismic response of canyons,* Acta Geotechnica **11**, 391 (2016).

M. Panji and B. Ansari, *Transient SH-wave scattering by the lined tunnels embedded in an elastic half-plane,* Engineering Analysis with Boundary Elements **84**, 220 (2017).

C. Zimmerman and M. Stern, *Boundary element solution of 3-D wave scatter problems in a poroelastic medium,* Engineering Analysis with Boundary Elements **12**, 223 (1993).

Z. Liu, X. Ju, C. Wu, and J. Liang, *Scattering of plane P1 waves and dynamic stress concentration by a lined tunnel in a fluid-saturated poroelastic half-space,* Tunnelling and Underground Space Technology **67**, 71 (2017).

T. Balendra, D. P. Thambiratnam, C. G. Koh, and S.-L. Lee, *Dynamic response of twin circular tunnels due to incident SH-waves,* Earthquake Engineering and Structural Dynamics **12**, 181 (1984).

S. K. Datta and N. El-Akily, *Diffraction of elastic waves by cylindrical cavity in a half-space,* The Journal of the Acoustical Society of America **64**, 1692 (1978).

N. El-Akily and S. K. Datta, *Response of a circular cylindrical shell to disturbances in a half-space,* Earthquake Engineering and Structural Dynamics **8**, 469 (1980).

N. El-Akily and S. K. Datta, *Response of a circular cylindrical shell to disturbances in a half-space - numerical results,* Earthquake Engineering and Structural Dynamics **9**, 477 (1981).

S. K. Datta and A. H. Shah, *Scattering of SH waves by embedded cavities,* Wave Motion **4**, 265 (1982).

V. W. Lee and G. Zhu, *A note on three-dimensional scattering and diffraction by a hemispherical canyon–I: Vertically incident plane P-wave,* Soil Dynamics and Earthquake Engineering **61-62**, 197 (2014).

K. C. Wong, S. K. Datta, and A. H. Shah, *Three-dimensional motion of buried pipeline. I: Analysis,* Journal of Engineering Mechanics **112**, 1319 (1986a).

K. C. Wong, A. H. Shah, and S. K. Datta, *Three-dimensional motion of buried pipeline. II: Numerical results,* Journal of Engineering Mechanics **112**, 1338 (1986b).

H. Cao and V. W. Lee, *Scattering and diffraction of plane P waves by circular cylindrical canyons with variable depth-to-width ratio,* Soil Dynamics and Earthquake Engineering **9**, 141 (1990).

V. W. Lee and J. Karl, *Diffraction of SV waves by underground, circular, cylindrical cavities,* Soil Dynamics and Earthquake Engineering **11**, 445 (1992).

N. Muskhelishvili, *Some basic problems of the mathematical theory of elasticity* (Nauka, Moscow, 1966).

D. Liu, B. Gai, and G. Tao, *Applications of the method of complex functions to dynamic stress concentrations,* Wave motion **4**, 293 (1982).

A. Verruijt, *Deformations of an elastic half plane with a circular cavity,* International Journal of Solids and Structures **35**, 2795 (1998).

Q. Liu and R. Wang, *Dynamic response of twin closely-spaced circular tunnels to harmonic plane waves in a full space,* Tunnelling and Underground Space Technology **32**, 212 (2012).

Q. Liu, M. Zhao, and L. Wang, *Scattering of plane P, SV or Rayleigh waves by a shallow lined tunnel in an elastic half space,* Soil Dynamics and Earthquake Engineering **49**, 52 (2013).

A. R. Kargar, R. Rahmannejad, and M. A. Hajabasi, *A semi-analytical elastic solution for stress field of lined non-circular tunnels at great depth using complex variable method,* International Journal of Solids and structures **51**, 1475 (2014).

X. Zhang, Y. Jiang, and S. Sugimoto, *Anti-plane dynamic response of a non-circular tunnel with imperfect interface in anisotropic rock mass,* Tunnelling and Underground Space Technology **87**, 134 (2019).

J.-H. Wang, J.-F. Lu, and X.-L. Zhou, *Complex variable function method for the scattering of plane waves by an arbitrary hole in a porous medium,* European Journal of Mechanics - A/Solids **28**, 582 (2009).

X.-Q. Fang and H.-X. Jin, *Dynamic response of a non-circular lined tunnel with viscoelastic imperfect interface in the saturated poroelastic medium,* Computers and Geotechnics **83**, 98 (2017).

Q. Liu, C. Yue, and M. Zhao, *Scattering of harmonic P1 and SV waves by a shallow lined circular tunnel in a poroelastic half-plane,* Soil Dynamics and Earthquake Engineering **158**, 107306 (2022).

C. Yue and Q. Liu, *Complex function method for the scattering of harmonic plane waves by an arbitrary-shaped cavity in an unsaturated medium,* Soil Dynamics and Earthquake Engineering **173**, 108139 (2023a).

C. Yue and Q. Liu, *Dynamic response of a shallow lined circular tunnel by incident P1 and SV waves in an unsaturated half-plane,* Tunnelling and Underground Space Technology **141**, 105364 (2023b).

K. Popp, H. Kruse, and I. Kaiser, *Vehicle-track dynamics in the mid-frequency range,* Vehicle System Dynamics **31**, 423 (1999).

J. Varandas, A. Paixão, and E. Fortunato, *A study on the dynamic train-track interaction over cut-fill transitions on buried culverts,* Computers & Structures **189**, 49 (2017).

A. B. Fărăgău, A. V. Metrikine, and K. N. van Dalen, *Transition radiation in a piecewise-linear and infinite one-dimensional structure–a Laplace transform method,* Nonlinear Dynamics **98**, 2435 (2019).

H. Ouyang, *Moving-load dynamic problems: A tutorial (with a brief overview),* Mechanical Systems and Signal Processing **25**, 2039 (2011).

Z. Dimitrovová, *Critical velocity of a uniformly moving load on a beam supported by a finite depth foundation,* Journal of Sound and Vibration **366**, 325 (2016).

Z. Dimitrovová, *Analysis of the critical velocity of a load moving on a beam supported by a finite depth foundation,* International Journal of Solids and Structures **122**, 128 (2017).

V. L. Ginzburg, *Theoretical physics and astrophysics* (Oxford: Pergamon Press, 1979).

A. V. Kononov and R. De Borst, *Instability analysis of vibrations of a uniformly moving mass in one and two-dimensional elastic systems,* European Journal of Mechanics A/Solids **21**, 151 (2002).

D. Y. Zheng, F. T. K. Au, and Y. K. Cheung, *Vibration of vehicle on compressed rail on viscoelastic foundation,* Journal of Engineering Mechanics **126**, 1141 (2000).

D. Y. Zheng and S. C. Fan, *Instability of vibration of a moving-train-and-rail coupling system,* Journal of Sound and Vibration **255**, 243 (2002).

A. V. Metrikine and S. N. Verichev, *Instability of vibrations of a moving two-mass oscillator on a flexibly supported Timoshenko beam,* Archive of Applied Mechanics **71**, 613 (2001).

S. N. Verichev and A. V. Metrikine, *Instability of a bogie moving on a flexibly supported Timoshenko beam,* Journal of Sound and Vibration **253**, 653 (2002).

T. Mazilu, *Instability of a train of oscillators moving along a beam on a viscoelastic foundation,* Journal of Sound and Vibration **332**, 4597 (2013).

V. Stojanović, P. Kozić, and M. D. Petković, *Dynamic instability and critical velocity of a mass moving uniformly along a stabilized infinity beam,* International Journal of Solids and Structures **108**, 164 (2017).

V. Stojanović, M. D. Petković, and J. Deng, *Stability of vibrations of a moving railway vehicle along an infinite complex three-part viscoelastic beam/foundation system,* International Journal of Mechanical Sciences **136**, 155 (2018).

Z. Dimitrovová, *Semi-analytical solution for a problem of a uniformly moving oscillator on an infinite beam on a two-parameter visco-elastic foundation,* Journal of Sound and Vibration **438**, 257 (2019).

Q. Liu, M. Zhao, and C. Zhang, *Antiplane scattering of SH waves by a circular cavity in an exponentially graded half space,* International Journal of Engineering Science **78**, 61 (2014).

Q. Liu, M. Zhao, and Z. Liu, *Wave function expansion method for the scattering of SH waves by two symmetrical circular cavities in two bonded exponentially graded half spaces,* Engineering Analysis with Boundary Elements **106**, 389 (2019).

A. V. Metrikine and K. Popp, *Instability of vibrations of an oscillator moving along a beam on an elastic half-space,* European Journal of Mechanics A/Solids **18**, 331 (1999).

A. V. Metrikine, S. N. Verichev, and J. Blaauwendraad, *Stability of a two-mass oscillator moving on a beam supported by a visco-elastic half-space,* International Journal of Solids and Structures **42**, 1187 (2005).

D. M. Rote and Y. Cai, *Review of dynamic stability of repulsive-force Maglev suspension systems,* IEEE Transactions on Magnetics **38**, 1383 (2002).

A. S. Abdelrahman, J. Sayeed, and M. Z. Youssef, *Hyperloop transportation system: Analysis, design, control, and implementation,* IEEE Transactions On Industrial Electronics **65**, 7427 (2017).

R. Janzen, *Transpod ultra-high-speed tube transportation: Dynamics of vehicles and infrastructure,* Procedia Engineering **199**, 8 (2017).

M. Zhao, J. M. de Oliveira Barbosa, A. V. Metrikine, and K. N. van Dalen, *Semi-analytical solution for the 3D response of a tunnel embedded in an elastic half-space subject to seismic waves,* Soil Dynamics and Earthquake Engineering **174**, 108171 (2023).

E. Kausel, *Fundamental solutions in elastodynamics: a compendium* (Cambridge University Press, 2006).

S. K. Datta, A. H. Shah, and K. C. Wong, *Dynamic stresses and displacements in buried pipe,* Journal of Engineering Mechanics **110**, 1451 (1984).

A. J. B. Tadeu and E. Kausel, *Green's functions for two-and-a-half-dimensional elastodynamic problems,* Journal of Engineering Mechanics **126**, 1093 (2000).

A. Tadeu, J. António, and L. Godinho, *Green's function for two-and-a-half dimensional elastodynamic problems in a half-space,* Computational Mechanics **27**, 484 (2001).

M. Zhao, J. M. de Oliveira Barbosa, J. Yuan, A. V. Metrikine, and K. N. van Dalen, *Instability of vibrations of an oscillator moving at high speed through a tunnel embedded in soft soil,* Journal of Sound and Vibration **494**, 115776 (2021).

S. L. Kramer, *Geotechnical earthquake engineering* (Pearson Education India, 1996).

A. W. Leissa, *Vibration of Shells* (Nasa Washington, 1973).

H. A. Dieterman and A. Metrikine, *The equivalent stiffness of a half-space interacting with a beam. Critical velocities of a moving load along the beam,* European Journal of Mechanics A/Solids **15**, 67 (1996).

T. Lu, A. Metrikine, and M. Steenbergen, *The equivalent dynamic stiffness of a visco-elastic half-space in interaction with a periodically supported beam under a moving load,* European Journal of Mechanics-A/Solids , 104065 (2020).

A. R. M. Wolfert, H. A. Dieterman, and A. V. Metrikine, *Stability of vibrations of two oscillators moving uniformly along a beam on a viscoelastic foundation,* Journal of Sound and Vibration **211**, 829 (1998).

W. Soedel, *Vibrations of Shells and Plates* (CRC Press, 2004).

Z. Yuan, A. Boström, and Y. Cai, *Benchmark solution for vibrations from a moving point source in a tunnel embedded in a half-space,* Journal of Sound and Vibration **387**, 177 (2017).

M. F. M. Hussein, S. François, M. Schevenels, H. E. M. Hunt, J. P. Talbot, and G. Degrande, *The fictitious force method for efficient calculation of vibration from a tunnel embedded in a multi-layered half-space,* Journal of Sound and Vibration **333**, 6996 (2014).

A. V. Metrikine and A. C. W. M. Vrouwenvelder, *Surface ground vibration due to a moving train in a tunnel: Two-dimensional model,* Journal of Sound and Vibration **234**, 43 (2000).

ACKNOWLEDGEMENTS

I arrived in Delft on September 25th 2013 to start my PhD research. There has been many challenges for me during this journey, and I am very happy that I finally managed to finish my thesis. As I reflect on these years, I would like to take this opportunity to express my gratitude to many people who generously offered their help and support to me.

First and foremost, I would like to express my profound gratitude to my promotor Prof. Andrei Metrikine. Andrei, thank you for accepting my application for a PhD position and allowing me to become a member of the big family. I still vividly recall my first day at TU Delft when you accompanied me to introduce myself to our colleagues. Everyone is so kind and friendly, I felt warmly welcomed and my initial nervousness was alleviated. In the subsequent days, I was consistently impressed by your vast knowledge. You can always explain complex things in a clear and concise manner. Thank you for sitting downing in your office to derive formulae together, for coming up with great research ideas, for answering my questions, for training my presentation skills and for inviting me to the parties at your home. Additionally, I would like to thank you for arranging the financial support after the end of my Chinese scholarship.

I am deeply indebted to my daily supervisor and promotor Dr. Karel van Dalen for his invaluable guidance throughout my research journey. Karel, we had numerous meetings together to discuss the details of my research. I would like to express my sincere gratitude for your contribution and time. I learned from you to think rigorously, to write a scientific article in English, to communicate the ideas with people effectively, as well as to be a nice person. The spirit of enthusiasm, confidence and optimistic attitude that I see from you and Andrei inspired me and led me through the dark and frustrated moments. I am sure that the research and soft skills that I learnt from you guys will have a significant influence on my future career.

I feel grateful to all my colleagues from the research groups of Dynamics of Solids and Structures and Offshore Engineering. We always have lunch and coffee breaks together to talk about scientific problems, and to share the happy and sad things in life. Together, we attended conferences, savored refreshing beverages at Psor (especially during spring, surrounded by the beautiful cherry blossom trees), and particapated in well-organised Christmas dinners and group outings. Your company for sure made the life in Delft more enjoyable, and simultaneously contributed to the improvement of my English-speaking skills. My special thanks go to João. We arrived in Delft about the same time. We were first office mates and then became friends. Thanks for being involved in my research, for coming up with great ideas and for teaching me programming skills in Matlab. I learnt so much from you. Nikos, thanks for being a good office mate, and for inviting me to your home to enjoy the delicious Greek food. Kodo, thank you for defending my time when master students from the course of Structural Dynamics came to our office to ask a lot of questions regarding assignments, and for always giving me a ride to the group parties.

Chris, many thanks for cooking the traditional Dutch food and hosting delightful barbeques at your place. Eliz-Mari, thanks for the warm hospitality at your home, and for sharing some beautiful cloths with me. To my colleagues Hayo, Apostolos, Jeroen, Pim, William, Maxim, Antonio, Renate, Marnix, Frank Renting, Sergio, Peter, Dominik, Andrei Faragau, Andre Reinaldo Novgorodcev Junior, Francesca, Valentina, Cody, Thanasis, Evangelos, Tim, Timo, Marco, Mamin, Arvind, Federico, Alessandro, Ger, Frank Sliggers, Faraz and André, I appreciate your company and the knowledge you have shared.

I would like to acknowledge my colleagues at Movares Nederland B.V.: Wybo Gardien, Kareen Gasparotto, Herke Stuit, Shalaleh Hillebrand, Niels Lommers, Sander van der Burg, Anton Klip, Mark Wijnands, André Fredriksz and Paul Tulp. Working alongside you all in the pleasant atmosphere at Movares for one year and seven months has been a truly rewarding experience. Thanks for your interests on my PhD research. Special thanks go to Wybo and Kareen for their invaluable guidance in the field of modeling various structures and analysing the environmental vibrations induced by moving trains or cars.

Living in the Netherlands has been a relatively smooth experience for me, thanks in large part to the vibrant Chinese community in Delft. Tao and Yang are more than colleagues to me. You are like my older brothers, and I know that you are always there to help me if needed. I am lucky to have you guys as my close friends. Together, we traveled to different countries, cooked dinners, watched movies, played badminton as well as engaged in numerous scientific discussions. My life at Delft would not be so pleasant without your help and company. Yaxi, thanks for being a wonderful friend and for our outdoor runs during the challenging times of Covid. I enjoyed the delicious food prepared by you and Rui at your place. Yue Song, thanks for your willingness to share your research experience and for the memorable trip we took together to Prague. It was truly a fantastic time. Jiangyi, many thanks for your company during our exploration of Amsterdam on King's day and our shopping excursions in Den Haag. Before even arriving in the Netherlands, I had the pleasure of meeting Manxia, Chunhui, and Zhebin, who provided me with company and assistance, making my initial travel to a foreign country a pleasant experience and facilitating a smooth transition into this new phase of life. During my time engaging in sports, I have forged meaningful friendships. Juan, Zi and Wenjuan, many thanks for our shared sports activities at the Sport Center and for sharing joy in life in the changing room afterwards. Additionally, I appreciate the occasional indulgence in decious food, which added some extra calories to our bodies at the weekends. Lingling and tiantian, many thanks for the enjoyable online Zumba sessions we had during Covid. Your involvement added fun to life during those difficult times. I am thankful to Hengqian Yi, Yixin Lv, Fei Yan, Renfei Bu, Yueting Liu, Long Wu, Peiyao Luo, Chenjie Yu, Quanxin Jiang, Jun Yuan, Guanliang Chen, Shanshan Ren, Jian Fang, Yue Zhao, Jintao Yu, Xiang Fu, Die Yang, Zilong Wei, Kai Li, Shulan Shu, Xiaowei Ouyang, Bowei Huang, Qujiang Lei, Tianchi Tang, Liting Qiu, Dongyu Liu, Yaolu Liu and Mingzhao Zhuo. Your presence and friendship have contributed to making my stay in Delft truly enjoyable.

I am grateful to Johan for being a good friends for so many years. Thanks for your help ever since we shared the master student room after my arrival in Delft. I am especially thankful for your efforts in teaching Davide and me Dutch. Davide, thanks for

being able to learn Dutch together. Additionally, I want to thank Ali and Fariborz for our insightful conversations and the enjoyable Badminton matches we have played together at weekends.

I would like to express my heartfelt gratitude to my my master's supervisor Prof. Qijian Liu. Thank you for your advice, help and recommendation in pursuing a PhD position abroad. Furthermore, I am also grateful for the financial support provided by the Chinese Scholarship Council (CSC) during my PhD studies.

My deepest gratitude goes to my parents. Thanks for your unconditional love, support and understanding, especially for taking good care of me during my pregnancy and for taking good care of my daughter so that I have time to finish writing my thesis. My mom always encourage me and tell me not to have too much stress. Special thanks go to my younger brother and sister-in-law for your support and help. Last but not least, I am immensely grateful to my husband Jianhuan and our daughter Wanqiao. Jianhuan, thank you for your love, support, encouragement and guiding me in running Matlab codes on Cluster. Since the birth of our daughter, my life undergone significant changes. Although being a new mother can be tiring, the immense joy I feel motivates me even more to complete my PhD thesis. Thanks, my beloved baby.

Mingjuan Zhao
Beijing, Jan 2024

CURRICULUM VITÆ

Mingjuan ZHAO

10 September 1987	Born in Kaifeng, China.

EDUCATION

September 2006–June 2010	Bachelor in Civil Engineering Xinyang Normal University Faculty of Civil Engineering Department of Structural Engineering
September 2010–June 2013	Master in Civil Engineering Hunan University Faculty of Civil Engineering Department of Geotechnical Engineering
October 2013–present	PhD in Civil Engineering Delft University of Technology Faculty of Civil Engineering and Geosciences Department of Engineering Structures Section of Dynamics of Solids and Structures

WORK EXPERIENCE

September 2017–August 2018	Teacher assistant at Delft University of Technology Assist two courses of Structural Dynamics and Earthquakes Supervise two master students
September 2019–March 2021	Engineering advisor at Movares Nederland B.V. Work on project of earthquake-induced vibrations Work on project of train-induced vibrations Work on project of noise measurement and analysis

LIST OF PUBLICATIONS

JOURNAL PAPERS

1. **Mingjuan Zhao**, João Manuel de Oliveira Barbosa, Andrei V. Metrikine, Karel N. van Dalen, *Response of an elastic half-space with an embedded cylindrical cavity subject to a harmonic anti-plane shear wave: a comparison of methods*, prepare for submission.

2. **Mingjuan Zhao**, João Manuel de Oliveira Barbosa, Andrei V. Metrikine, Karel N. van Dalen, *Semi-analytical solution for the 3D response of a tunnel embedded in an elastic half-space subject to seismic waves*, Soil Dynamics and Earthquake Engineering **174**, 108171 (2023).

3. **Mingjuan Zhao**, João Manuel de Oliveira Barbosa, Jun Yuan, Andrei V. Metrikine, Karel N. van Dalen, *Instability of vibrations of an oscillator moving at high speed through a tunnel embedded in soft soil*, Journal of Sound and Vibration **494**, 115776 (2021).

4. Qijian Liu, Cheng Yue, **Mingjuan Zhao**, *Scattering of harmonic P1 and SV waves by a shallow lined circular tunnel in a poroelastic half-plane*, Soil Dynamics and Earthquake Engineering **158**, 107306 (2022).

5. Qijian Liu, **Mingjuan Zhao**, Zhongxian Liu, *Wave function expansion method for the scattering of SH waves by two symmetrical circular cavities in two bonded exponentially graded half spaces*, Engineering Analysis with Boundary Elements **106**, 389-396 (2019).

6. Qijian Liu, **Mingjuan Zhao**, Chao Zhang, *Antiplane scattering of SH waves by a circular cavity in an exponentially graded half space*, International Journal of Engineering Science **78**, 61-72 (2014).

7. Qijian Liu, **Mingjuan Zhao**, Lianhua Wang, *Scattering of plane P, SV or Rayleigh waves by a shallow lined tunnel in an elastic half space*, Soil Dynamics and Earthquake Engineering **49**, 52-63 (2013).

CONFERENCE PAPERS

1. **Mingjuan Zhao**, Karel N. van Dalen, João Manuel de Oliveira Barbosa, Andrei V. Metrikine, *Semi-analytical solution for the dynamic response of a cylindrical structure embedded in a homogeneous half-space*, Environmental Vibrations and Transportation Geodynamics **7**, 369-388 (2018).